TU Delft

Delft University of Technology

Control of the doubly-fed induction machine for wind turbine applications

Nguyen Tien, Hung

DOI
10.4233/uuid:54ea2136-ade7-4c0e-bf85-6d03a1a7af36

Publication date
2017

Document Version
Final published version

Citation (APA)
Nguyen Tien, H. (2017). *Control of the doubly-fed induction machine for wind turbine applications*. [Dissertation (TU Delft), Delft University of Technology]. https://doi.org/10.4233/uuid:54ea2136-ade7-4c0e-bf85-6d03a1a7af36

Important note
To cite this publication, please use the final published version (if applicable).
Please check the document version above.

Copyright
Other than for strictly personal use, it is not permitted to download, forward or distribute the text or part of it, without the consent of the author(s) and/or copyright holder(s), unless the work is under an open content license such as Creative Commons.

Takedown policy
Please contact us and provide details if you believe this document breaches copyrights.
We will remove access to the work immediately and investigate your claim.

This work is downloaded from Delft University of Technology.
For technical reasons the number of authors shown on this cover page is limited to a maximum of 10.

The linear control of doubly-fed induction machines in wind power systems normally encounters the problems in variations of the rotor mechanical angular speed and other time-varying parameters. However, better performance requirements against changes in the machine parameters and exogenous inputs are desired. This can be achieved by appropriate controller design. Furthermore, the robustness of the controlled system under the effects of grid voltage dips is an important aspect as well. This work focuses on the use of linear matrix inequalities for analysis and synthesis of current controllers for doubly fed induction machines in wind power systems. The design is aimed at improving the robust dynamic performance of the controlled system in a wide range of mechanical rotor speed variations and reducing the effect of stator voltage dips when the grid undergoes a fault. A rigorous robust analysis based on the integral quadratic constraints approach is presented for evaluating and comparing the robustness of the controlled system with respect to the changes in the machine inductances and the rotor angular speed for the linear parameter varying approach and a conventional design.

ISBN 978-94-6186-825-1

Control of the doubly-fed induction machine for wind turbine applications

Nguyen Tien Hung

TU Delft

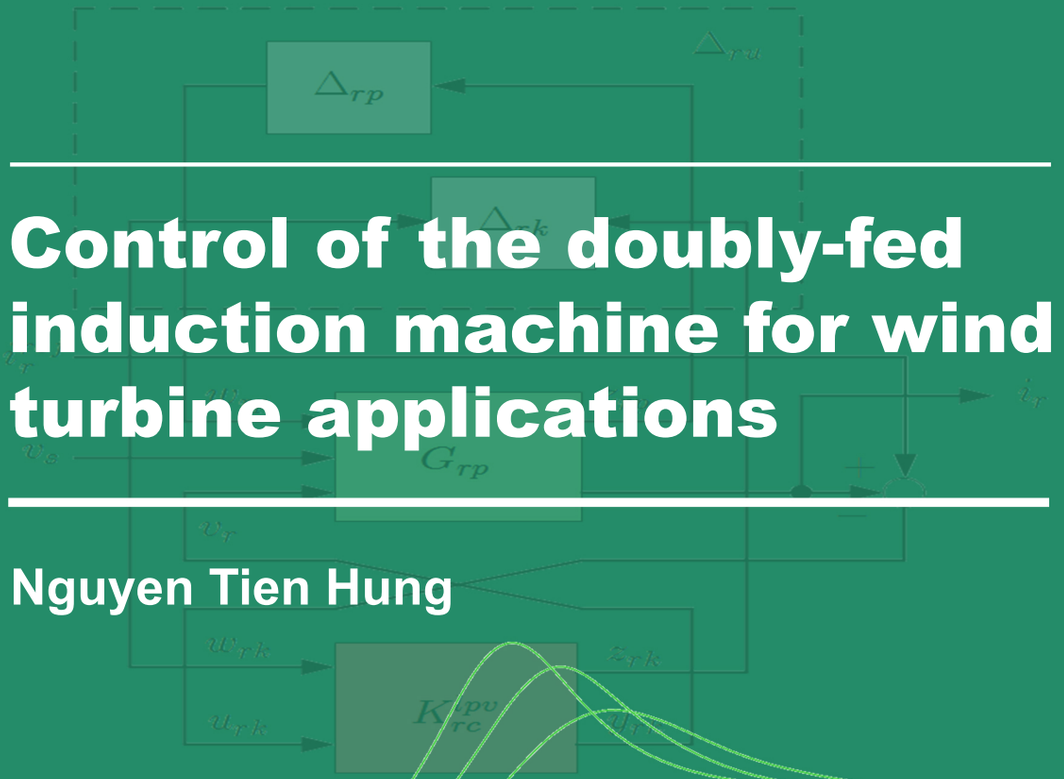

Control of the doubly-fed induction machine for wind turbine applications

Nguyen Tien Hung

CONTROL OF THE DOUBLY-FED INDUCTION MACHINE FOR WIND TURBINE APPLICATIONS

CONTROL OF THE DOUBLY-FED INDUCTION MACHINE FOR WIND TURBINE APPLICATIONS

Proefschrift

ter verkrijging van de graad van doctor
aan de Technische Universiteit Delft,
op gezag van de Rector Magnificus prof. ir. K.C.A.M. Luyben,
voorzitter van het College voor Promoties,
in het openbaar te verdedigen op maandag 26 June 2017 om 12.30 uur

door

Hung Tien NGUYEN

Master of Engineering in Automatization
Hanoi University of Science and Technology, Vietnam,
geboren te Thái Nguyên, Vietnam.

This dissertation has been approved by the

promotors: Prof. dr. ir. J. M. A. Scherpen, Prof. dr. C. W. Scherer and Prof. dr. ir. J. Hellendoorn

Composition of the doctoral committee:

Rector Magnificus,	chairman
Prof. dr. ir. J. M. A. Scherpen,	University of Groningen
Prof. dr. C. W. Scherer,	University of Stuttgart
Prof. dr. ir. J. Hellendoorn,	Delft University of Technology
Independent members:	
Prof. dr. ir. W. de Jong,	Delft University of Technology
Prof. dr. M. K. Camlibel,	University of Groningen
Prof. dr. B. Jayawardhana,	University of Groningen
Dr. H. Polinder,	Delft University of Technology
Prof. dr. G. V. Vdovin,	Delft University of Technology, reserve member

This research was funded by the Vietnamese Ministry of Education and Training.

Copyright © 2017 by Hung Tien Nguyen

ISBN 978-94-6186-825-1
Printed in The Netherlands

CONTENTS

Acknowledgements **xi**

1 Introduction **1**

1.1 Doubly-fed induction machines for wind turbine systems 1

1.2 Overview of the literature 3

1.3 Research objectives and contributions 5

1.4 Thesis outline 5

2 The system description **9**

2.1 The grid and DFIM models 9

2.1.1 Reference frames and transformations 9

2.1.2 Doubly-fed induction machine model 11

2.1.3 The state space model of the grid coupling 14

2.2 The control configuration 16

2.2.1 Wind energy generation systems 16

2.2.2 Operating regions and control principles 17

2.3 Power flow control with back-to-back converter 19

2.3.1 Slip power regulation 19

2.3.2 The rotor side control 20

2.3.3 The grid side control 21

2.4 Open-loop characteristics of doubly-fed induction machines 24

2.5 Summary 26

3 Conventional control scheme with deadbeat controllers **27**

3.1 Introduction 27

3.2 Multivariable deadbeat control for discrete-time systems 28

3.2.1 Dead-beat response 28

3.2.2 Deadbeat controllers 30

3.2.3 Input-output realization of the deadbeat response in the z-domain . 31
3.3 Deadbeat controllers design for DFIMs 33
3.3.1 The rotor side control 33
3.3.2 The grid side control 40
3.3.3 Simulation results 42
3.4 DFIM parameter uncertainties and robustness 44
3.4.1 DFIM parameter uncertainties 44
3.4.2 Robustness of the control system against parameter changes 45
3.4.3 The impact of stator voltage dips on the robustness of the control system 45
3.4.4 Discussions 46
3.5 Summary 50

4 LPV controller synthesis for affinely parameter-dependent systems 51
4.1 Introduction 51
4.2 Preliminaries 52
4.2.1 Notations 52
4.2.2 Linear matrix inequalities 52
4.2.3 The H_∞-norm 53
4.2.4 The bounded real lemma 53
4.3 H_∞ control of linear time-invariant systems 54
4.3.1 H_∞ performance 54
4.3.2 Sub-optimal H_∞ control 55
4.3.3 H_∞ controller synthesis 56
4.3.4 Mixed sensitivity H_∞ approach 57
4.4 Gain-scheduled H_∞ control for affinely parameter-dependent systems 59
4.4.1 Linear parameter varying systems 59
4.4.2 The polytopic approach to LPV controller synthesis 60
4.4.3 Gain-scheduled controller construction 62
4.5 Summary 63

5 Gain-scheduling design for doubly-fed induction machines 65
5.1 Introduction 65

5.2 The system representation . . . 65
5.3 H_∞ control of the LPV system . . . 69
5.3.1 The control configuration . . . 69
5.3.2 H_∞ loop shaping design . . . 70
5.3.3 Simulation results with the H_∞ current controller . . . 72
5.4 LPV control of DFIMs . . . 80
5.4.1 Synthesis of self-scheduled current controller . . . 80
5.4.2 Simulation results with the LPV current controller . . . 81
5.5 Robustness of the LPV current controller . . . 88
5.5.1 Robustness of the control system against parameter changes . . . 88
5.5.2 The impact of stator voltage dips on the robustness of the control system . . . 89
5.6 Discretization problem of predesigned LPV controllers . . . 90
5.7 Summary . . . 96

6 Robustness analysis **99**
6.1 Problem formulation . . . 99
6.1.1 Standard setup for robustness analysis . . . 100
6.2 Structured singular value analysis . . . 101
6.2.1 The system representation with uncertainties . . . 102
6.2.2 Robustness analysis . . . 105
6.3 IQC-based robust stability analysis . . . 105
6.3.1 The IQC framework . . . 106
6.3.2 Robustness against time-varying rate-bounded parametric uncertainties . . . 107
6.4 Robustness analysis of the controlled system . . . 111
6.4.1 Stability margins . . . 111
6.4.2 Rate-of-variations . . . 113
6.5 Robustness analysis of deadbeat current controller . . . 114
6.6 Summary . . . 119

7 Experimental results **121**
7.1 Introduction . . . 121
7.2 Experimental setup . . . 122

7.3 Experimental results with the LPV current controller . . . 124
7.3.1 The rotor current controller with the stator open circuit . . . 124
7.3.2 Grid synchronization testing . . . 126
7.3.3 The rotor current LPV controller with a closed circuit of the stator windings . . . 127
7.3.4 The closed-loop system with outer loops . . . 129
7.3.5 The system performance during the rotor speed variations . . . 131
7.3.6 Grid voltage dip tests . . . 135
7.4 Experimental results with the FRT current controller . . . 142
7.4.1 The rotor current controller with the stator open circuit . . . 144
7.4.2 The rotor current FRT controller with a closed circuit of the stator windings . . . 144
7.4.3 The system performance with the FRT controller during rotor speed variations . . . 145
7.4.4 Grid voltage dip tests with the FRT controller . . . 145
7.5 Summary . . . 146

8 Conclusions and recommendations 155
8.1 Conclusions . . . 155
8.2 Recommendations . . . 157

A Linear Fractional Representation of the system 159

B Electrical machine characteristics 167
B.1 Parameters for a real doubly-fed induction machine . . . 167
B.2 Parameters for a laboratory scale doubly-fed induction machine . . . 167
B.3 Induction motor . . . 168

C The experimental platform 169
C.1 The ALPHA-COMBO system . . . 169
C.2 The power module . . . 169

Bibliography 171

Summary 183

Samenvatting 185

List of Publications **187**

Propositions **189**

Curriculum Vitæ **191**

ACKNOWLEDGEMENTS

Taking me to the final destination is a bumpy road. It has been so long and, not a few times, I felt that it was still so far at the very end of the road. Though I can not estimate uncertainties on my left distance, I am extremely sure that my thesis would not be completed without the help of many people.

I am greatly indebted to my promoters and also daily supervisor, Prof. Carsten Scherer, and Prof. Jacquelien Scherpen, for giving me the opportunity of being a PhD student and for their support in the completion of this thesis even after many years since I left Delft. It was a great pleasure and honor to work with you. You were in DCSC for me every step of the way. I want you to know how much I value your support. Thank you both for being patient and helping me improve.

I would like to express my heartfelt gratitude and sincere appreciation to my co-promoter, Prof. Hans Hellendoorn, for providing me the chance to finalize my thesis in DCSC. You were always available whenever I need your help even in the most difficult times. I wholeheartedly appreciate everything you have done for me.

I am especially grateful to Dr. Volkmar Mueller at the Institute of Electrical Power Engineering, faculty of Electrical Engineering and Information Technologies, Dresden University of Technology, Germany for allowing me to carry out the experiments and for his help in providing favourable conditions for the experiments. I also specially thanks Dr. Phung Ngoc Lan and Nguyen Tran Duc Viet for their assistance during the experimental works. Special thanks go to Dr. Hakan Koroglu and Ronald Toth, at Delft Center for Systems and Control, Delft University of Technology, The Netherlands for many useful discussion and also for their help to write some Matlab scripts.

Many thanks to all my colleagues and friends in Delft who made my nearly five years easier. I still well remember happy and sad memories we shared when we were in a long distance from our families. Dear Dr. Pham Quang Tu and Tran Duc Thinh, thank you for your support when I was not in Delft.

I would like to thank the Vietnamese Government and all the staff members of the project 322 for the financial support and their incentives to follow our passion for the research. I am also grateful to all (former) CICAT staffs, especially Dr. Paul Althuis and Mrs. Veronique Van der Vast, for their help in implementing administration stuff and financial support.

My deepest gratitude goes to all members of my family for their unflagging love and support throughout my life. This dissertation is simply impossible without them. I was fortunate to have a wife, Le Thi Thu Huong, who has understood what I am interested in and the hard thing in my career. I am indebted to my wife and my son for their love and patience.

To all wonderful people I owe a deep sense of gratitude especially now that this thesis has been completed.

Delft, May 28, 2017
Nguyen Tien Hung

1

INTRODUCTION

1.1. DOUBLY-FED INDUCTION MACHINES FOR WIND TURBINE SYSTEMS

Since the 1970s when the price of fossil fuels boomed, wind energy has regained to be interesting for electricity generation. Over the last three decades and since the increasing interest towards the use of renewable energy sources and demands for clean energy, wind energy is the fastest growing renewable energy source worldwide. Statistics released by Global Wind Energy Council in March 2015 showed that the global installed capacity of grid-connected wind power in more than 80 countries around the world was approximately 370 GW (Gigawatts) [1]. The installed wind power capacity in the European Union increased by 227.8% in 2008 to reach a total amount of 128.8 GW in 2014 [2]. Wind energy installations in the United States increased from about 16,800 MW at the end of 2007 to more than 66,008 GW at the first quarter of 2015 [3, 4].

Wind turbines coupled with electrical generators convert wind energy into electric power and feed electricity into the utility grid. Power electronics enable the wind turbine systems working as an electric power plant in order to produce active power from wind energy. Groups of wind turbines establish "wind farms" or "wind power plants" that have grown in size from a few dozen up to several hundred megawatts of capacity. In 2014, wind turbines with a capacity of up to 8 MW (Megawatt) have been developed specifically for off-shore operation [1].

Wind energy conversion systems (WECSs) often use induction machines as generators equipped with wind turbines. Squirrel-cage induction machines are used in a simple and low cost wind turbine system (Fig. 1.1a). In this configuration, the stator windings are directly connected to the grid and the system is only working at near synchronous speed. Hence, this configuration is referred to as an approximately constant speed, constant frequency or fixed speed WECS in which the rotor speed may be varied from 1 to 2% from a nominal value. Since the system has to be operated in small-speed

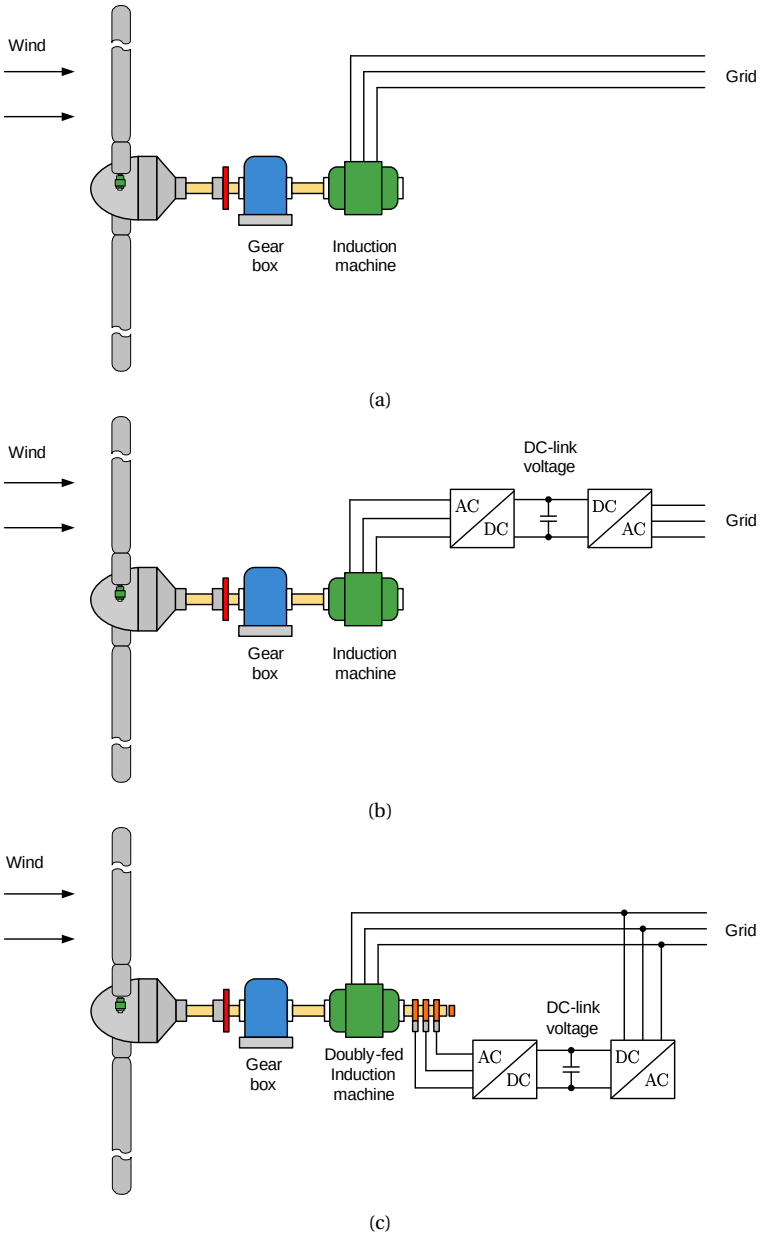

Figure 1.1: Fixed speed WECS with squirrel-cage induction machine (a), variable speed WECS with squirrel-cage induction machine (b), and variable speed WECS with doubly-fed induction machine (c).

variations around the synchronous speed while the wind velocity is fluctuating in a wide range, the energy capture by the wind turbine for producing electrical energy is not high.

In order to improve the energy capture from wind, we need a WECS in which the rotor shaft speed can be varied in a large range but the output electrical frequency is kept constant [5]. This can be done by using electronic equipment as presented in Fig. 1.1b. In this figure, a back-to-back converter is placed between the machine and the grid. The converter is aimed at converting the three-phase electrical power with varying frequency in the stator circuit of the machine into the three-phase electrical power with constant frequency in order to supply to the grid. The main advantage of this configuration is that it allows to control independently the active and reactive power of the machine [6, 7, 8]. However, this configuration still possesses a disadvantage since the converter has to handle the full power supply from the machine to the grid.

Another scheme for wind turbines is to use a variable speed configuration with pitch control and a slip ring induction machine. This electrical machine is supplied by two voltage source inverters in the stator and the rotor (Fig. 1.1c) that is a so-called doubly-fed induction machine (DFIM). Note that, similar to the variable speed WECS with squirrel-cage induction machines, the generator power is still fed to the grid at the stator side of the DFIM. As a result, besides an ability to handle large-speed variations around the synchronous speed, DFIMs are also considered as an attractive solution for WECS since only approximately 30% of the total generator power has to be handled by power converters [9, 10, 11, 12, 13]. This allows a reduction of the size of the power converter and, hence, of the cost of the overall system, especially at high-power levels [14]. The electrical energy efficiency of wind turbine systems equipped with doubly-fed induction generators in comparison to other wind turbine generator systems has been investigated in [15].

1.2. OVERVIEW OF THE LITERATURE

In the literature, conventional controller designs for DFIMs as described in [16, 17, 18, 19, 20, 21] are based on field or vector control. These control strategies rely on the assumption that the machine parameters are all time-invariant. In some cases, feed-forward terms are added to the output of the rotor current controllers for compensating cross coupling terms in the rotor current equations. Obviously, the performance for the designed current controllers could be very sensitive to any variations of parameter values, and a careful tuning is required in order to guarantee good performance over the whole operating range of the rotor speed.

Hence various techniques have been proposed as alternatives to these vector control schemes, such as direct power control (DPC) [22] and direct torque control (DTC) [23, 24]. As a typical feature, DPC does not require an inner current controller. This leads to a simplified control configuration and allows to obtain high dynamic responses. As a disadvantage, such control schemes produce large ripples in the active and reactive power at steady state. This issue has been addressed in [10, 25, 26, 27]. In [10], all feasible and smooth connections between two adjacent vector sequences were taken into account in the framework of a novel three-vector-based strategy for a predictive DPC to achieve both active power and reactive power ripple reduction with simple calculations. In [25], a combination of DPC and vector control is considered to result in a high dynamic response and lower power ripples. However, there were no experimental results

showing the robustness of the controlled system with respect to rotor speed variations in the operating range. Moreover, the performance of the controlled system when the voltage in the grid is temporarily dropped due to a fault has also not been presented in these works.

Additionally, the design of so-called finite response time (FRT or deadbeat-like) controllers in [28, 29] rely on the assumption that the mechanical angular speed is constant during each sampling period. The FRT controller is designed for every sampling cycle under the assumption that the DFIM model is linear time-invariant. The main drawbacks of this approach are the high on-line computational load and the fact that the adjustment of the FRT controller is ad-hoc since it is simply based on computing a new controller according to the actual measured rotor speed. As a result, the performance of the system can not be guaranteed over the entire operating range of the DFIM. The linear parameter-varying (LPV) control approach of [30, 31] provides a key solution to this problem, since the controller adaption is tailored towards obeying stability and performance for all admissible trajectories of the on-line measurable mechanical angular speed. However, it is emphasized that no digital implementation of the LPV design and no experimental results are reported in [30, 31].

It is well-known that the electrical parameters of the machine are strongly affected by temperature, magnetic saturation, and winding current modulus. These effects can deteriorate the controller performance when designed with nominal parameter values. Therefore, a better performance requirement against changes in the machine parameters and exogenous inputs is desired to be achieved by appropriate controller design for the DFIM. An H_∞ control approach for the DFIM control is proposed in [32, 33], and a sliding mode control approach is proposed in [34, 35, 36, 37]. In [34, 37] a flux sliding mode control is asserted to be more robust than those based on the conventional theory presented in [38, 39, 40]. However, the performance of the closed-loop system over a large operating range of the rotor speed as required in the WECS with the DFIM is not considered thoroughly in these studies.

Since the total power of installed wind turbine systems worldwide has constantly increased, the separation of wind turbines from the grid is only allowed under some specific situations [41, 42]. Otherwise, the unsupervised disconnection of wind turbines from the grid might lead to instabilities in the electric power distribution. Therefore the robustness of the controlled system under the effects of grid voltage sags is an important aspect of the controller design.

When the grid undergoes a fault, the sag in the grid voltage will result in an increase of the current in the stator windings of the DFIM. Because of the magnetic coupling between stator and rotor, this current will also flow into the rotor circuit and the power converter, which leads to a damage of the converter if nothing is done to protect it. On the other hand, the study in [43] shows that the dynamics of the DFIM has poorly damped poles if considering a Linear Time Invariant (LTI) model of the machine. This will cause oscillations in the flux if the DFIM is affected by grid disturbances. After such a disturbance occurs, an increased rotor voltage will be needed to control the rotor currents. When this required voltage exceeds the voltage limit of the converter, it is not possible any longer to control the current as desired [44, 45]. Therefore, the control system

should maintain operation and reduce oscillations as much as possible during grid voltage faults, and normal operation of the DFIM should be re-established as soon as the fault is cleared [46]. This issue has not been mentioned in the H_∞ and the sliding mode control approaches presented in [32, 33, 34, 35, 36, 37].

1.3. RESEARCH OBJECTIVES AND CONTRIBUTIONS

In this work, the focus of interest is to improve performance of the current control loop on the rotor side converter with respect to machine parameter variations and in view of the stator voltage disturbance, as well as to systematically analyze the robustness of the controlled system. Consequently, the main objectives that are also main contributions of this thesis are:

- To analyze some open-loop characteristics of the DFIM based on its derived model.
- To design a controller for the DFIM that achieves performance of the closed-loop system for large variations of the rotor angular speed around the synchronous speed. Furthermore, the designed controller should guarantee robustness against parameter changes as rate-bounded linear time-varying uncertainties as well as reduce the impact of stator voltage dips on the controlled system.
- To propose a method in order to replace the designed continuous-time controller by an equivalent discrete-time controller that guarantees stability of the resulting digital control system for a reasonable sampling frequency for implementation in an industrial digital control system.
- To propose a systematic method for robust stability analysis subject to rate-bounded linear time-varying parametric uncertainties in order to give stability margins for the controlled system with the designed controller.
- To validate the proposed control algorithm on a experimental setup.

1.4. THESIS OUTLINE

Having a model that is appropriate for controller design purpose is a very important task. For the DFIM control, the relevant physical variables that can be associated with state variables are the rotor currents, the active and reactive powers, the electrical torque, the power factor, and the rotor speed. The problem of modeling the grid and the DFIM is presented in Chapter 2. This chapter also gives an overview of the working principle of a WECS with doubly-fed induction machines and some investigations of open-loop characteristics of the DFIM.

An overview of a conventional controller design for the DFIM, the so-called deadbeat control technique, is given in Chapter 3. The deadbeat control technique is described not only in the state-space representation but also in the input-output representation of the closed-loop system. The application of the deadbeat control technique is then

employed to design the current controllers for both the generator and the grid sides. Robustness of the controlled system with respect to parameter variations with an assumption that the machine parameters are all time-invariant uncertainties and the impact of the stator voltage dips on the system performance are investigated via some simulation results.

The aim of Chapter 4 is to provide tools for linear parameter-varying (LPV) controller synthesis that is based on the linear matrix inequality (LMI) approach. First, we present H_∞ control for controller synthesis of linear time-invariant systems where H_∞-constraints are transformed into LMIs by using the so-called bounded real lemma. Then the synthesis technique is extended for a class of systems whose time-varying parameters are measured online with the LPV-design method. This approach is aimed at achieving exponential stability and a given performance level of the closed-loop system for all admissible parameter trajectories. We present in this chapter a general framework of the polytopic approach for synthesizing gain-scheduled H_∞ controllers for affine parameter-dependent systems.

In Chapter 5 we present the robust parameter-independent H_∞ and self-scheduled LPV controller designs for the DFIM based on the synthesis technique presented in Chapter 4. The requirement for the designed controller is to be able to ensure the desired objectives in the wide operating range of the rotor angular speed. In order to do so, the rotor mechanical angular speed is treated as a varying parameter or an uncertainty and a single robust parameter-independent H_∞ controller is designed for a frozen value of the rotor angular speed. The designed H_∞ controller guarantees the stability of the controlled system for the entire operating range. However, simulation results show that the performance of the closed-loop system with the H_∞ controller is deteriorated for both constant and fast parameter variations of rotor angular speeds. Since the rotor angular speed can be measured online, we adopt the framework of LPV controller synthesis in order to design a self-scheduled current controller for the DFIM. The simulation results of this approach validate a highly robust dynamic performance of the LPV controller for all admissible trajectories of the rotor angular speed over the operating range even for fast rotor angular speed variations. Furthermore, in comparison with conventional designs, the controlled system with the LPV current controller is more robust with respect to machine parameter variations and in the presence of the stator voltage disturbance. After that we present the trapezoidal technique that is used for the real-time implementation of the LPV controller in an industrial digital control system. This technique guarantees a good match of the responses of the continuous-time and the discrete-time system for a consistent sampling frequency.

Since the stator and rotor inductances as well as the mutual inductance vary with the machine flux due to the magnetic saturation and winding current modulus, Chapter 6 is devoted to presenting a rigorous robustness analysis for investigating the stability of the system against parameter variations for these inductances as linear time-varying parameters. In this chapter, the integral quadratic constraints (IQCs) approach is employed for robust stability analysis with these rate-bounded linear time-varying (LTV) parametric uncertainties. The LPV design achieves higher stability margins with respect to machine parameter uncertainties and to the rotor angular speed in comparison with that of the

conventional deadbeat design.

Chapter 7 presents the experimental validation of the LPV and the finite response time (FRT) current controllers proposed in Chapter 5 and Chapter 3, respectively. Via experimental results, a comparison of the performance of the controlled system achieved with two controllers is drawn. This comparison is made for both open and closed-loop circuits of the stator windings with the electrical torque and the reactive power control. The experiments show that the controlled system with the LPV current controller achieves much better performance in terms of settling time, overshoot and oscillations in the controlled variables in comparison with that of the FRT controller. Furthermore, the LPV controller guarantees the performance of the closed-loop system for frozen and varying rotor speeds around ±30% of the synchronous speed. In contrast, the performance of the closed-loop system with the FRT controller is deteriorated when the rotor speed is near and above the synchronous speed. When the grid undergoes a fault, the rotor currents with the LPV controller recover their nominal values faster than that of the deadbeat controller. The LPV controller also gives better damping of electrical torque and reactive power than the FRT controller during the fault.

Finally, Chapter 8 presents the research conclusions and discusses some recommendations for future work.

2

THE SYSTEM DESCRIPTION

The main part of this chapter is to derive models for the grid and DFIMs that are needed for controller design in the next chapters and as well for describing a working principle of wind turbines coupled with doubly-fed induction generators. Subsequently, the open-loop characteristics of DFIMs are investigated and the grid fault sensitivity is discussed for further analysis.

2.1. THE GRID AND DFIM MODELS

Before developing the differential equations for the grid and DFIM we will briefly introduce the necessary reference frames on which the differential equations of the grid and the DFIM are described and discuss the corresponding transformations.

2.1.1. REFERENCE FRAMES AND TRANSFORMATIONS

In order to reduce the complexity of the differential equations that describe the grid or DFIM behavior, three-phase quantities such as currents, voltages, or fluxes are described by new variables on a new two-phase orthogonal reference frame. This frame can be associated with the stator and it forms a fixed or stationary reference frame. Alternatively, this frame can be associated with other revolving components, for example the rotor or the stator flux, and it forms a rotating reference frame [47, 39]. The tools for changing the variables from stationary to rotating reference frames are Clarke's and Park's frame transformations [48, 49].

In modern electrical driver systems, all three phase variables can be transformed into a rotating reference frame, the so-called dq reference frame, with their two phase equivalents. Then the control computations are handled in terms of these dq variables for both their phase angles and modulus. In the literature, the control implementation based on dq variables in the chosen reference frame is referred to as *vector control*

[38, 50, 51]. In the following part of this section we will briefly discuss how to transform variables from the three-phase system to a dq reference frame for the vector control of the DFIM in the next chapters.

Let ξ_s stand for different three-phase quantities such as currents, voltages, or fluxes. The idealized instantaneous value ξ_s of the three-phase quantities denoted by ξ_{sa}, ξ_{sb}, and ξ_{sc} satisfies the equation

$$\xi_s = \frac{2}{3}\left(\xi_{sa}(t) + \xi_{sb}(t)e^{j120^0} + \xi_{sc}(t)e^{j240^0}\right)$$

where $\xi_{sa}(t) + \xi_{sb}(t) + \xi_{sc}(t) = 0$, and the subscript "s" is employed to denote quantities in a stationary reference frame.

Let us establish a new reference frame in the complex plane, denoted by $\alpha\beta$, in which the real α-axis is aligned with e^{j0^0} as shown in Fig. 2.1. Then

$$\xi_s^{\alpha\beta 0} = T_{sf}\xi_s^{abc} \tag{2.1}$$

where $\xi_s^{\alpha\beta 0} = \begin{pmatrix}\xi_{s\alpha} & \xi_{s\beta} & \xi_{s0}\end{pmatrix}^T$, $\xi_s^{abc} = \begin{pmatrix}\xi_{sa} & \xi_{sb} & \xi_{sc}\end{pmatrix}^T$. Note that ξ_{s0} is a zero component and only added for the matrix T_{sf} to be invertible.

The transformation matrix is given by [48]

$$T_{sf} = \frac{2}{3}\begin{pmatrix} 1 & -\frac{1}{2} & -\frac{1}{2} \\ 0 & \frac{\sqrt{3}}{2} & -\frac{\sqrt{3}}{2} \\ \frac{1}{2} & \frac{1}{2} & \frac{1}{2} \end{pmatrix}.$$

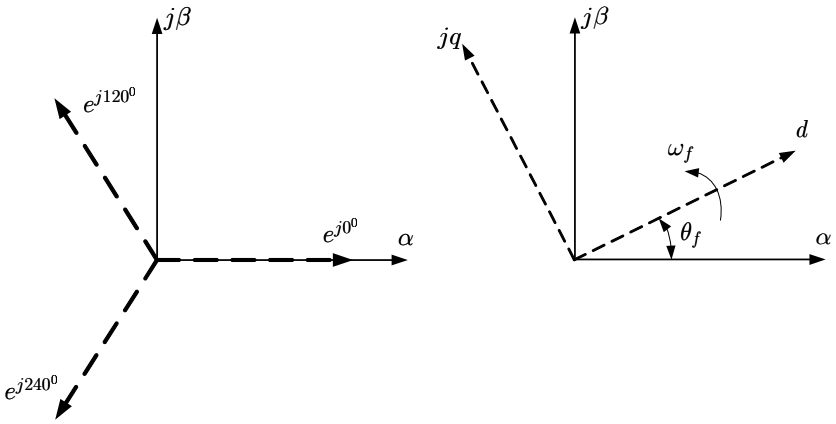

Figure 2.1: Frame transformations

In the general case, if we take $\alpha\beta$ as the stationary reference frame in the complex plane and dq as the new reference frame which is rotated with angle θ_f (see Fig. 2.1),

then the component $\xi_s^{\alpha\beta} = \begin{pmatrix} \xi_{s\alpha} & \xi_{s\beta} \end{pmatrix}^T$ of $\xi_s^{\alpha\beta 0}$ can be transformed into this new reference frame as

$$\xi_r^{dq} = T_{rf}\xi_s^{\alpha\beta} \tag{2.2}$$

where $\xi_r^{dq} = \begin{pmatrix} \xi_d & \xi_q \end{pmatrix}^T$. The real component of ξ_r^{dq} is on the d-axis while the imaginary component of ξ_r^{dq} is on the q-axis. The transformation matrix is given by [47, 48, 49]

$$T_{rf} = \begin{pmatrix} \cos\theta_f & \sin\theta_f \\ -\sin\theta_f & \cos\theta_f \end{pmatrix}.$$

Fig. 2.1 shows the representation of three-phase quantities on the $\alpha\beta$ reference frame (left) and the relationship between the $\alpha\beta$ and dq reference frames (right).

2.1.2. DOUBLY-FED INDUCTION MACHINE MODEL

In an induction machine, the stator variables are normally defined with respect to a stationary reference frame, while the rotor variables are defined with respect to a rotating reference frame with rotation speed being the electrical angular speed ω_r [18]. As discussed above, for current control of the DFIM that uses the vector control technique, it is necessary to transform the variables into a common rotating reference frame dq. The reference frame can be aligned with the stator flux vector [19, 52, 17, 18] or with the grid voltage vector [16, 29, 53, 54]. Since the DFIM works in parallel with the grid it is required to be synchronized with the grid. Therefore, choosing a dq reference frame with the d-axis oriented along the grid voltage vector might lead to some technical advantages [55]. This reference frame is independent of the machine parameters and the rotor speed measurement accuracy [16]. Hence it is adopted for the to-be-developed model and for the current control algorithms for the DFIM hereafter.

The voltage equations of the stator and the rotor can be written as follows:

$$v_s = R_s i_s + \frac{d\Psi_s}{dt}, \tag{2.3}$$

$$v_r = R_r i_r + \frac{d\Psi_r}{dt}. \tag{2.4}$$

Here, v_s and v_r are the stator and the rotor voltages, i_s and i_r are the stator and the rotor currents, R_s and R_r are the stator and the rotor resistances, Ψ_s and Ψ_r are the stator and the rotor fluxes.

The stator and the rotor fluxes are determined by

$$\begin{aligned} \Psi_s &= i_s L_s + i_r L_m, \\ \Psi_r &= i_r L_r + i_s L_m, \end{aligned} \tag{2.5}$$

where L_m is the magnetizing inductance, and L_s, L_r are the stator and the rotor self inductances. Note that, in a normal working condition, the machine parameters L_m, L_s, and L_r are considered to be constant in time. Let us denote the stator and the rotor

leakage inductances by $L_{\sigma s}$ and $L_{\sigma r}$. The stator and the rotor self inductances can be calculated as

$$\begin{aligned} L_s &= L_m + L_{\sigma s}, \\ L_r &= L_m + L_{\sigma r}. \end{aligned}$$

Let us establish an $\alpha\beta$ reference frame in which the real axis is aligned with the winding axis of phase a of the three-phase grid voltage with the phase sequence of abc. Let θ_s and θ_r be the angles between the real axis of the $\alpha\beta$ reference frame and the stator and rotor flux axes. The angular speeds of the rotating magnetic field in the stator ω_s and rotor ω_r can be expressed by

$$\omega_s = \frac{d\theta_s}{dt}, \quad \omega_r = \frac{d\theta_r}{dt}.$$

Note that

$$\omega_r = \omega_s - \omega_m \tag{2.6}$$

where ω_m is the mechanical angular speed of the rotor.

In this work, since the stator windings are connected to the grid, the stator frequency is identical to the grid frequency. Hence, ω_s is assumed to be constant throughout this thesis.

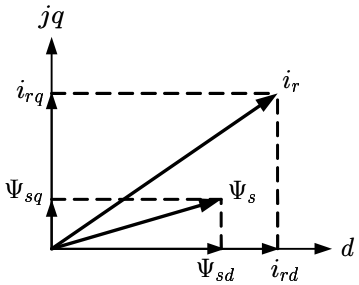

Figure 2.2: Phasor representation of the dq components of the stator flux and rotor current

In the dq reference frame (see Fig. 2.1), the rotor current and the stator flux can be represented as phasors in the complex plane by [56] (see Fig. 2.2)

$$i_r = i_{rd} + j i_{rq} \tag{2.7}$$
$$\Psi_s = \Psi_{sd} + j\Psi_{sq} \tag{2.8}$$

Similarly, the stator and the rotor voltages can be represented in the dq reference frame by

$$v_s = v_{sd} + j v_{sq}, \tag{2.9}$$
$$v_r = v_{rd} + j v_{rq}. \tag{2.10}$$

If applying the coordinate transformations (2.1) and (2.2) to equations (2.3) and (2.4) we obtain the following equations in the dq reference frame [57]:

$$\begin{aligned}
\frac{di_{rd}}{dt} &= -\left(\frac{a+1}{T_r}+\frac{a}{T_s}\right)i_{rd}+(\omega_s-\omega_m)i_{rq}+\frac{a}{L_m T_s}\Psi_{sd} \\
&\quad -\frac{a\omega_m}{L_m}\Psi_{sq}-\frac{a}{L_m}v_{sd}+\frac{a+1}{L_r}v_{rd}, \qquad (2.11)\\
\frac{di_{rq}}{dt} &= (\omega_m-\omega_s)i_{rd}-\left(\frac{a+1}{T_r}+\frac{a}{T_s}\right)i_{rq}+\frac{a\omega_m}{L_m}\Psi_{sd} \\
&\quad +\frac{a}{L_m T_s}\Psi_{sq}-\frac{a}{L_m}v_{sq}+\frac{a+1}{L_r}v_{rq}, \qquad (2.12)\\
\frac{d\Psi_{sd}}{dt} &= \frac{L_m}{T_s}i_{rd}-\frac{1}{T_s}\Psi_{sd}+\omega_s\Psi_{sq}+v_{sd}, \qquad (2.13)\\
\frac{d\Psi_{sq}}{dt} &= \frac{L_m}{T_s}i_{rq}-\omega_s\Psi_{sd}-\frac{1}{T_s}\Psi_{sq}+v_{sq} \qquad (2.14)
\end{aligned}$$

where $\sigma = 1-\frac{L_m^2}{L_s L_r}$ is the total leakage factor, and $a=\frac{1-\sigma}{\sigma}$.

In what follows, we will write $i_r=\begin{pmatrix} i_{rd} & i_{rq}\end{pmatrix}^T$, $\Psi_s=\begin{pmatrix}\Psi_{sd} & \Psi_{sq}\end{pmatrix}^T$, $v_s=\begin{pmatrix} v_{sd} & v_{sq}\end{pmatrix}^T$, and $v_r=\begin{pmatrix} v_{rd} & v_{rq}\end{pmatrix}^T$ when no confusion with i_r, ψ_s, v_s, and v_r in (2.7) - (2.10) can arise.

The outputs of the system are the rotor currents since they are easy to measure by current sensors. Hence, the compact form of equations (2.11), (2.12), (2.13), and (2.14) in combination with the output equation is expressed as

$$\begin{aligned}
\dot{x}_r &= A_r(\omega_m)x_r+B_s v_s+B_r v_r, \qquad (2.15)\\
y_r &= C_r x_r \qquad (2.16)
\end{aligned}$$

where $x_r=\begin{pmatrix} i_{rd} & i_{rq} & \Psi_{sd} & \Psi_{sq}\end{pmatrix}^T$, $y_r=i_r=\begin{pmatrix} i_{rd} & i_{rq}\end{pmatrix}^T$,

$$A_r(\omega_m)=\begin{pmatrix} -\left(\frac{a+1}{T_r}+\frac{a}{T_s}\right) & \omega_s-\omega_m & \frac{a}{L_m T_s} & -\frac{a\omega_m}{L_m} \\ \omega_m-\omega_s & -\left(\frac{a+1}{T_r}+\frac{a}{T_s}\right) & \frac{a\omega_m}{L_m} & \frac{a}{L_m T_s} \\ \frac{L_m}{T_s} & 0 & -\frac{1}{T_s} & \omega_s \\ 0 & \frac{L_m}{T_s} & -\omega_s & -\frac{1}{T_s}\end{pmatrix}, \qquad (2.17)$$

$$B_u=\left(\begin{array}{c|c} B_s & B_r\end{array}\right) = \left(\begin{array}{cc|cc} -\frac{a}{L_m} & 0 & \frac{a+1}{L_r} & 0 \\ 0 & -\frac{a}{L_m} & 0 & \frac{a+1}{L_r} \\ 1 & 0 & 0 & 0 \\ 0 & 1 & 0 & 0\end{array}\right), \qquad (2.18)$$

$$C_r=\begin{pmatrix} 1 & 0 & 0 & 0 \\ 0 & 1 & 0 & 0\end{pmatrix}. \qquad (2.19)$$

2.1.3. THE STATE SPACE MODEL OF THE GRID COUPLING

A simple circuit representation of the coupling to the grid is shown in Fig. 2.3a. The grid side converter is usually connected with the grid through a filter including an inductor L_c, a capacitor C_f, and a resistance R_f. The resistance of the inductor L_c is indicated by R_c.

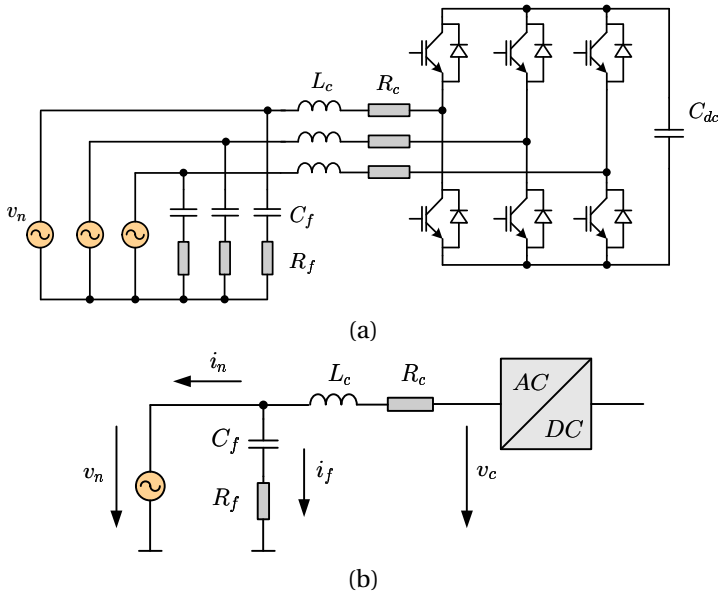

Figure 2.3: The grid side circuit (a) and the grid side model (b)

The following basic equations are corresponding to the equivalent circuit of the grid side circuit which is shown in Fig. 2.3b:

$$v_c = R_c i_c + L_c \frac{di_c}{dt} + v_n, \tag{2.20}$$

$$i_c = i_n + i_f. \tag{2.21}$$

Here, v_c and i_c are the voltage and current of the grid side converter, v_n and i_n are the voltage and current of the grid, and i_f is the current through the parallel branch of R_f and L_f of the filter. In practice, the filter current i_f is treated as a disturbance for the control loop since it can be considered as a constant in steady state.

Similarly in Section 2.1.2, the voltage of the grid v_n, the voltage of the grid side converter v_c, the grid current i_n, and the filter current i_f can be represented in the dq refer-

ence frame (Fig. 2.1) by

$$v_n = v_{nd} + j v_{nq}, \tag{2.22}$$
$$v_c = v_{cd} + j v_{cq}, \tag{2.23}$$
$$i_n = i_{nd} + j i_{nq}, \tag{2.24}$$
$$i_f = i_{fd} + j i_{fq}. \tag{2.25}$$

Applying the coordinate transformations (2.1) and (2.2) to equations (2.20) and (2.21) we obtain the following equations for variables in the dq reference frame [57]:

$$\frac{di_{nd}}{dt} = -\frac{1}{T_c} i_{nd} + \omega_s i_{nq} + \frac{1}{L_c} v_{cd} - \frac{1}{L_c}(v_{nd} + R_c i_{fd} - \omega_s L_c i_{fq}), \tag{2.26}$$
$$\frac{di_{nq}}{dt} = -\frac{1}{T_c} i_{nq} - \omega_s i_{nd} + \frac{1}{L_c} v_{cq} - \frac{1}{L_c}(v_{nq} + R_c i_{fq} + \omega_s L_c i_{fd}) \tag{2.27}$$

where $T_c = \frac{L_c}{R_c}$.

After some calculations with the assumption that $\frac{di_f}{dt} = 0$ [53], the equations (2.26) and (2.27) now read as

$$\frac{di_{nd}}{dt} = -\frac{1}{T_c} i_{nd} + \omega_s i_{nq} + \frac{1}{L_c} v_{cd} - \left(\zeta_{nd} v_{nd} - \zeta_{nq} v_{nq}\right), \tag{2.28}$$
$$\frac{di_{nq}}{dt} = -\frac{1}{T_c} i_{nq} - \omega_s i_{nd} + \frac{1}{L_c} v_{cq} - \left(\zeta_{nq} v_{nd} + \zeta_{nd} v_{nq}\right), \tag{2.29}$$

where ζ_{nd} and ζ_{nq} are constants defined as follows:

$$\zeta_{nd} = \frac{1}{L_c}\left(\frac{1 + \omega_s^2 R_f^2 C_f^2 + \omega_s^2 R_c R_f C_f^2 + \omega_s^2 L_c C_f}{\omega_s^2 R_f^2 C_f^2 + 1}\right),$$
$$\zeta_{nq} = \frac{1}{L_c}\left(\frac{\omega_s^3 L_c R_f C_f^2 - \omega_s R_c C_f}{\omega_s^2 R_f^2 C_f^2 + 1}\right).$$

Here and subsequently, we will write $v_n = \begin{pmatrix} v_{nd} & v_{nq} \end{pmatrix}^T$, $v_c = \begin{pmatrix} v_{cd} & v_{cq} \end{pmatrix}^T$, and $i_n = \begin{pmatrix} i_{nd} & i_{nq} \end{pmatrix}^T$ which differ from that of (2.22) - (2.24) for simplicity of notation. The state space model of the grid side circuit can hence be expressed by:

$$\dot{x}_n = A_n x_n + B_c v_c + B_n v_n, \tag{2.30}$$
$$y_n = C_n x_n \tag{2.31}$$

where $x_n = i_n = \begin{pmatrix} i_{nd} & i_{nq} \end{pmatrix}^T$, $y_n = \begin{pmatrix} i_{nd} & i_{nq} \end{pmatrix}^T$, $A_n = \begin{pmatrix} -\frac{1}{T_c} & \omega_s \\ -\omega_s & \frac{1}{T_c} \end{pmatrix}$, $B_n = \begin{pmatrix} -\zeta_{nd} & \zeta_{nq} \\ -\zeta_{nq} & -\zeta_{nd} \end{pmatrix}$, $B_c = \begin{pmatrix} \frac{1}{L_c} & 0 \\ 0 & \frac{1}{L_c} \end{pmatrix}$, $C_n = \begin{pmatrix} 1 & 0 \\ 0 & 1 \end{pmatrix}$.

2.2. THE CONTROL CONFIGURATION

2.2.1. WIND ENERGY GENERATION SYSTEMS

The overall control system of the wind energy generation system consists of two main parts: the wind turbine control and the DFIM control as shown in Fig. 2.4 [58]. The wind turbine control is aimed at providing the reference value for the active power or the electrical torque T_e^{ref} for the DFIM controller. This value is based on the measured wind speed and a lookup-table for optimizing the power output of the wind turbine. The other reference signal is the pitch angle θ_{pitch} that is directly delivered to the blade pitch angle actuator system.

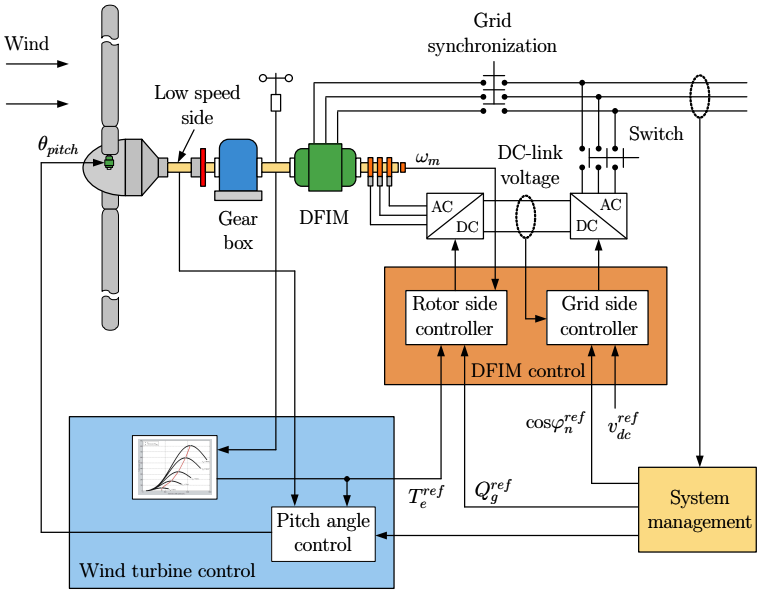

Figure 2.4: Variable speed wind turbine system

Section 2.2.2 gives a brief discussion of how to determine the maximum power which can be extracted by a wind turbine based on the input wind speed. By monitoring the wind turbine output power, the reference value of the electrical torque is calculated and given to the DFIM control stage. This is a topic addressed in detail in [54, 59, 60, 14].

In the regular configuration of variable speed wind turbines, the stator windings of the DFIM are directly connected to the grid and the rotor is connected with two converters, one on the grid side, the so-called Grid Side Converter (GSC), and the other on the rotor side, the so-called Rotor Side Converter (RSC), coupled by a DC-voltage link. The reference values of the reactive power Q_g^{ref} and the power factor $\cos\varphi_n^{ref}$ are given by the so-called system management unit which is responsible for the operation and control of transmission and distribution networks. Usually, these values are aimed at keeping the power factor of the power system at unity. The reference value of the DC-link voltage

v_{dc}^{ref} derives from the desired value of the active power flowing into the DC-link. The goal of the rotor side controller is to keep the electrical torque and reactive power of the DFIM at their reference values, while the grid side controller is aimed at maintaining the DC-link voltage and the power factor of the grid at given constant reference values.

In this work we only focus on the DFIM control. However, in order to give an overview of the working principle of a wind generation system, we will briefly present some concepts of the wind turbine control in the next section. The DFIM control problem setting is then presented in more detail in section 2.3. This also is the subject for the next chapters.

2.2.2. OPERATING REGIONS AND CONTROL PRINCIPLES

The mechanical power extracted by the wind turbine depends on the swept area of its blades which is proportional to the square of the rotor radius (the length of the blades) and the cube of the wind speed [59, 14, 61, 18]:

$$P_{tb} = \frac{1}{2}\rho\pi R_b^2 V_w^3 C_p. \tag{2.32}$$

Here, ρ is air density (kg/m^3), R_b is the rotor radius (m), V_w is upstream wind speed defined as wind speed at a considerable distance to the entrance of the rotor blades (m/s), C_p is the power coefficient of the wind turbine.

The characteristics of a wind turbine are available from turbine manufactures, in which C_p is the most important aerodynamic coefficient. In the literature, the theoretical maximum value of C_p is 0.593 [62, 63, 64]. This means that a wind turbine would not extract more than 59.3% of available wind power (known as the Betz limit). In practical designs, the values of C_p are often between 0.2 and 0.5 [61].

The value of C_p is determined by the relationship between the wind speed and the rotor speed of the turbine. This relationship is expressed by the ratio of the tangential speed at the tip of a blade and the upstream wind speed, known as tip-speed ratio (TSR). It is a non-dimensional factor defined as follows:

$$\lambda(t) = \frac{\omega_{tb}(t) R_b}{V_w(t)}. \tag{2.33}$$

Here, ω_{tb} is the turbine shaft angular speed on the low-speed side of the gear box.

At high wind speeds, the output power of the electrical generator can be limited by changing the blade pitch angle θ_{pitch}. Since the power coefficient C_p is dependent on the blade geometry, its value changes with variations of the pitch angle. In other words, C_p is a function of λ and θ_{pitch}:

$$C_p = f(\lambda, \theta_{pitch}).$$

Due to equation (2.32) and for a given wind turbine at a specific site where the air density ρ is a constant, the output power is dependent on the upstream wind speed and

C_p, i.e.

$$P_{tb} = \beta_{tb} V_w^3 C_p \tag{2.34}$$

where $\beta_{tb} = \frac{1}{2}\rho\pi R_b^2$ is a constant.

Thus, for a given wind turbine and a given input wind speed, if the rotor speed changes, the turbine power also changes corresponding to the variation of the value of C_p. This is illustrated in Fig. 2.5.

In order to optimize the obtained power for each given wind speed, the rotor speed must be controlled such that it matches as closely as possible the wind speed so as to maintain the optimal value of C_p. Furthermore, the rotor speed is also controlled to protect the generator and the power electronic equipment from overloading when the wind speed is too low or too high. The speed control requirements can be directly implemented by pitch control or yaw control, as well as indirectly by changing the speed of the electrical generators.

Since the rotor shaft of the generator is connected to the rotor shaft of the turbine through a gear box, the output power of the electrical generator is closely related to the relationship between the output power of the turbine and its rotor angular speed. An example of the ideal P_{tb} - ω_{tb} characteristic of a wind turbine which is depicted for different given wind speeds is shown in Fig. 2.5. The maximum power locus is plotted as a dotted line. The curve of the wind turbine power P_{tb} is plotted as a thick line.

In order to optimize the operating mode of the wind turbine, the rotor speed is controlled as follows [61] (see Fig. 2.5):

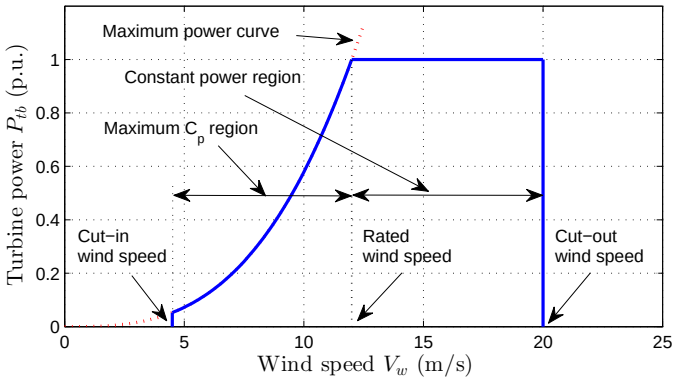

Figure 2.5: Operating regions of DFIM

- The lowest wind speed at which a wind turbine starts producing power is called the *cut-in* speed. When the input wind speed is below this value, the wind turbine is turned off.

- When the input wind speed is higher than the value of the cut-in speed but the generated power is still lower than the rated power of the generator, the rotor speeds of the generator are regulated so as to operate at a constant tip-speed ratio λ corresponding to the maximum C_p value adapting with the wind variations. This rotor speed region of the wind turbine is called *the maximum C_p region*.

- When the input wind speed continuously increases, the output power will approach the power limitation of the electrical generator. Then the blade pitch angle is regulated to operate at the tip-speed ratio λ corresponding to lower value of C_p. As a consequence, the extracted power is kept at the rated power to avoid over-loading of the generator. This rotor speed region of the wind turbine is called *the constant output power region*.

- When the input wind speed is too high, the turbine is turned off to protect the blades, the generator and other components of the system. The high wind speed at which the wind turbine is shut down is called the *cut-out* speed.

2.3. POWER FLOW CONTROL WITH BACK-TO-BACK CONVERTER

2.3.1. SLIP POWER REGULATION

The electrical power that is injected/extracted into/from the rotor circuit through slip-ring terminals is, in the context of this thesis, called slip power since it is related to the difference between the speed of the rotating magnetic field in the stator and the rotor speed. The power flow regulation is implemented via the two-side or back-to-back converter, that consists of the GSC and the RSC, as mentioned in Section 2.2. Because of having a bidirectional converter at the rotor side, the slip power can flow both from rotor to the grid and in the opposite direction.

In a conventional operation of DFIMs, the rotor speed is usually lower than the synchronous speed and the DFIM will operate as in motoring mode. In this case, if some amount of electrical power is injected to the rotor circuit, the operating mode of the machine will be changed into the generating mode [55]. Hence the generator power P_g is the sum of the power at the stator side P_s and the slip power P_{slip} [65]:

$$P_g = P_s + P_{slip}. \tag{2.35}$$

Note that if the rotor speed is lower than the synchronous speed the DFIM is said to be operated at sub-synchronous speed which supplies electrical power from the stator side to the grid.

When the input wind speed increases the power extracted by the wind turbine might be larger than the rated power of the generator or, in other words, the extracted power exceeds the power limitation of the generator. In this case, in order to avoid over-loading of the generator, the power coefficient C_p is reduced by controlling the blade pitch angle so as to keep the generated power at the rated value.

2.3.2. THE ROTOR SIDE CONTROL

The rotor side controller aims at controlling active and reactive power by regulating the electrical torque T_e and the reactive power Q_g.

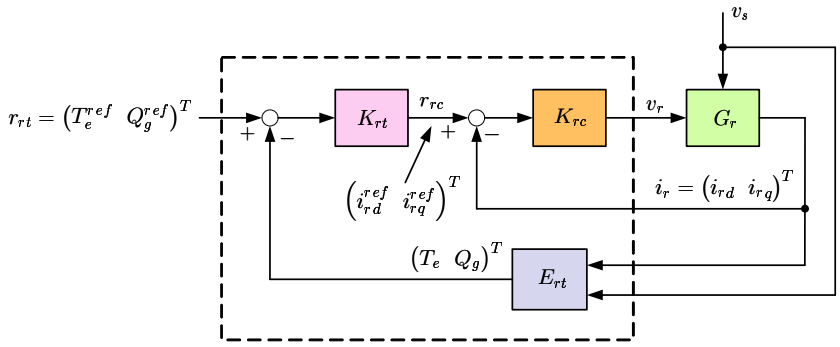

Figure 2.6: Block diagram of the rotor side control

In electrical machine control systems, current control plays a very important role since it is aimed at providing the required voltage vector for the power electronic circuit. Moreover, the performance of the whole system depends mainly on the performance of the current controllers. Therefore, electrical machine control systems usually consist of a inner loop with a current controller and a outer loop with other control variables such that the electrical torque, the rotor speed, or flux.

The control structure on the rotor side of the DFIM is treated in the same fashion, i.e., it has two loops (see Fig. 2.6) as mentioned above [18, 53, 66]. The inner loop with controller K_{rc} is called the rotor current control loop. The controller design goal of the rotor current controller K_{rc} is to achieve fast-response performance and robust tracking of the rotor currents. The outer loop with controller K_{rt} is called electrical torque control loop and is used for tracking the optimal values of the control input r_{rt} consisting of the electrical torque T_e^{ref} and the reactive power Q_g^{ref}, $r_{rt} = \left(T_e^{ref} \quad Q_g^{ref}\right)^T$. Based on the actual measured values of the wind speed and the characteristics of each particular wind turbine, the main control station will track the optimum torque from a look-up table and use it as the reference value r_{rt} for the power electronics control stage. The output signal r_{rc} of the controller K_{rt} gives the reference values of the rotor current components i_{rd}^{ref}, and i_{rq}^{ref} for the rotor current controller K_{rc}. In Fig. 2.6, G_r represents the model of the DFIM corresponding to equations (2.15) and (2.16), $y_g = \left(T_e \quad Q_g\right)^T$ is the controlled output that is estimated from the output $i_r = \left(i_{rd} \quad i_{rq}\right)^T$ of the rotor (see equations (2.36) and (2.37) below) by the block E_{rt}.

The electrical torque of the DFIM in the dq reference frame of the stator voltage, i.e.

$\Psi_{sd} = 0$, can be computed by

$$T_e = -\frac{3}{2} p \frac{L_m}{L_s} \Psi_{sq} i_{rd}. \tag{2.36}$$

Here p is the number of the machine pole-pair.

The reactive power can be obtained as

$$Q_g = -3 v_{sd} \frac{\Psi_{sq} - i_{rq} L_m}{L_s}. \tag{2.37}$$

Note that the q component of the stator flux Ψ_{sq} in (2.36) and (2.37) is defined in (2.14).

Controlling the reactive power Q_g can be implemented by regulating the power factor $\cos\varphi_g$. This factor can be computed as follows:

$$\cos\varphi_g = \frac{i_{sd}}{\sqrt{i_{sd}^2 + i_{sq}^2}}. \tag{2.38}$$

The equations (2.36), (2.37), and (2.38) show that the electrical torque and reactive power or the power factor of the DFIM can be regulated via the components of the rotor currents i_{rd} and i_{rq}.

The details of the control scheme of the rotor side converter are represented in Fig. 2.7. The dashed box in Fig. 2.7 is the same as that in Fig. 2.6 except that the torque and reactive power calculation block is now including the calculation of the rotor voltage phase angle θ_r, where $\theta_r = \int \omega_r dt$. Recall that ω_r is the (electrical) angular speed of the rotor. The controller outputs $v_r = \begin{pmatrix} v_{rd} & v_{rq} \end{pmatrix}^T$ are brought to the Pulse Width Modulation (PWM) block via a frame transformation block. The other blocks are used to transform the variables of the stator and the rotor currents, (i_s, i_r), as well as the stator voltages v_s to the corresponding reference frames and to calculate the stator voltage phase angle θ_s.

2.3.3. THE GRID SIDE CONTROL

Besides the ability of operating in both inverter and rectifier modes for indirectly transferring active and reactive power between the rotor circuit and the grid, the control action on the grid side is responsible for maintaining the DC-link voltage and the reactive power at given constant reference values. In order to perform these tasks, a structure on the grid side controller is proposed as shown in Fig. 2.8.

The control structure on the grid side is similar to the control structure on the rotor side. This control structure consists of two loops. The inner loop with controller K_{nc} is called the grid current control loop. The controller design goal for the grid current controller K_{nc} is to achieve fast-response performance and fast tracking of the grid currents. The outer loop with controller K_{np} is called the grid power flow control loop used for

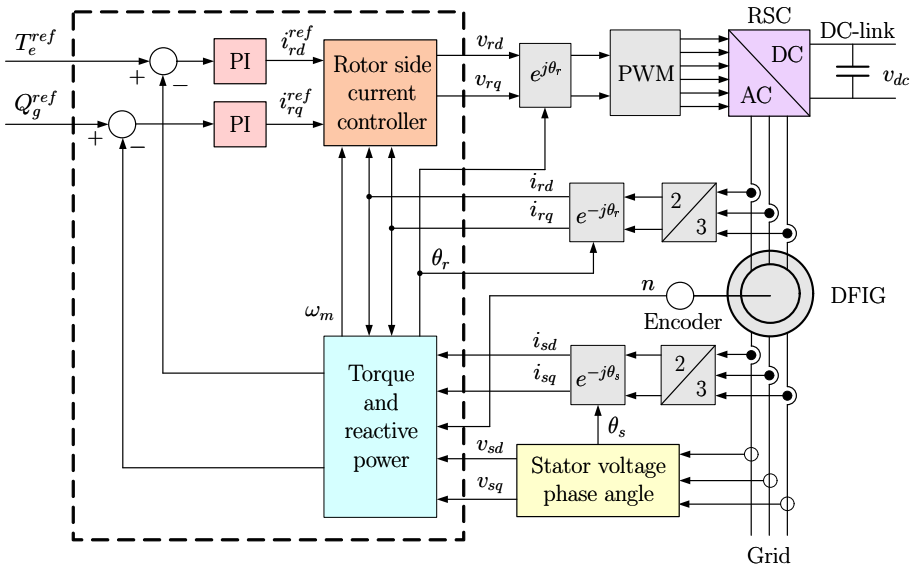

Figure 2.7: Rotor side control structure

controlling the DC-link voltage and the reactive power between the grid and converter via the power factor $\cos\varphi_n$ estimated by the block E_{np}. In Fig. 2.8, G_n represents the grid model (where subscript n stands for net or grid). The controlled outputs consist of the DC-link voltage measured on the DC circuit v_{dc} and the grid current $i_n = \begin{pmatrix} i_{nd} & i_{nq} \end{pmatrix}$. Here, i_{nd} and i_{nq} are components of the grid current that are on the reference frame aligned with the stator voltage v_s.

The DC-link voltage v_{dc} of the DC-link circuit can be computed as follows:

$$v_{dc} = v_{dc0} + \frac{1}{C_{dc}} \int (i_{nd} - i_{rd}) dt \tag{2.39}$$

where v_{dc0} is an initial value of v_{dc}, C_{dc} is the capacitor value in the DC-link circuit, i_{rq} is the q-component of the rotor current.

The power factor $\cos\varphi_n$ of the grid can be computed as follows:

$$\cos\varphi_n = \frac{i_{nd}}{\sqrt{i_{nd}^2 + i_{nq}^2}}. \tag{2.40}$$

Equation (2.39) show that the DC-link voltage can be controlled via the d-component of the grid current i_{nd}. In a real setup, the DC-link voltage should be kept at constant values irrespective of variations of the rotor current i_{rd}. The power factor $\cos\varphi_n$ can be controlled via the q-component of the grid current i_{nq}. This control technique is also mentioned in the literature, for instance in [17, 53, 29].

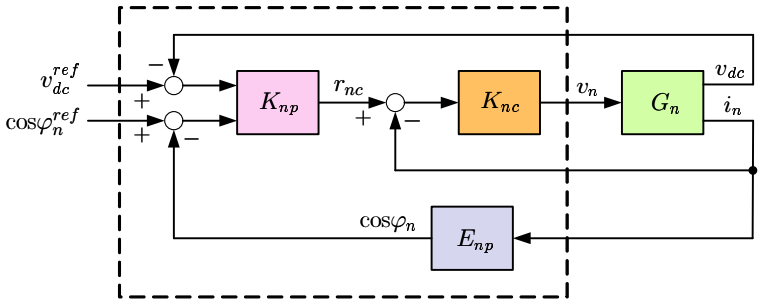

Figure 2.8: Block diagram of the grid side control

The details of the control scheme of the grid side converter are shown in Fig. 2.9. The dashed box in Fig. 2.9 is similar to that in Fig. 2.8. The controller outputs $v_n = \begin{pmatrix} v_{nd} & v_{nq} \end{pmatrix}^T$ are brought to the PWM block via a frame transformation block. The other blocks are used to transform the variables of the grid currents (i_{nd}, i_{nq}) to the corresponding reference frames and to calculate the grid voltage phase angle θ_n as well as the grid power factor $\cos\varphi_n$.

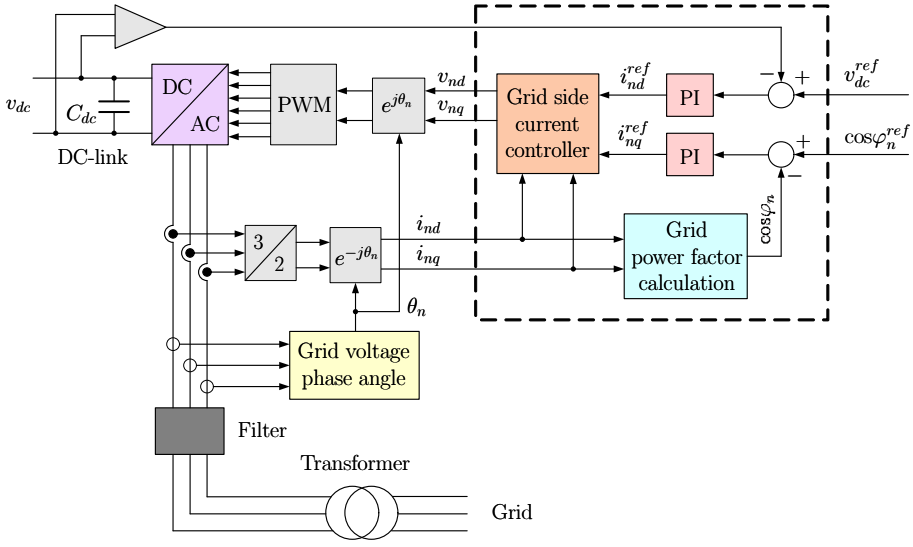

Figure 2.9: Grid side control structure

2.4. OPEN-LOOP CHARACTERISTICS OF DOUBLY-FED INDUCTION MACHINES

Let us rewrite equations (2.15) and (2.16) in matrix form as

$$\begin{pmatrix} \dot{x}_r \\ y_r \end{pmatrix} = \left(\begin{array}{c|cc} A_r(\omega_m) & B_s & B_r \\ \hline C_r & 0 & 0 \end{array}\right) \begin{pmatrix} x_r \\ v_s \\ v_r \end{pmatrix} \tag{2.41}$$

and analyze the system (2.41) with transfer matrix denoted by G_r as shown in Fig. 2.10.

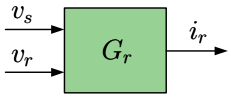

Figure 2.10: The plant model

Here, the rotor voltages v_r are the control inputs, the controlled outputs are the rotor current i_r, while the stator voltages v_s are considered as input disturbances, and the angular speed of the rotating magnetic field in the stator ω_s is considered to be constant as mentioned in section 2.1.2.

The frequency responses of the channels $v_r \to i_r$ and $v_s \to i_r$ are shown in Fig. 2.11 and 2.12. In Fig. 2.11a, the thick curves correspond to the channel $v_{rd} \to i_{rd}$ while the thin curves correspond to the channel $v_{rd} \to i_{rq}$. In Fig. 2.11b, the thick curves correspond to the channel $v_{rq} \to i_{rq}$ while the thin curves correspond to the channel $v_{rq} \to i_{rd}$. In Fig. 2.12a, the thick curves show the influence of the d component of the stator voltage v_{sd} on the output i_{rd} while the thin curves show the influence of the stator voltage v_{sd} on the output i_{rq}. In Fig. 2.12b, the thick curves show the influence of the q component of the stator voltage v_{sq} on the output i_{rq} while the thin curves show the influence of the stator voltage v_{sq} on the output i_{rd}.

The time responses of the rotor currents with respect to the rotor voltages v_r and the stator voltages v_s for some values of ω_m in its operating range are depicted in Fig. 2.13.

An analysis of the open-loop shows:

- The stator voltage v_s can be considered as an input disturbance [53, 67]. The Bode magnitude responses of the channel $v_s \to i_r$ exhibit resonances at the frequency near the stator voltage frequency $\omega_s = 2\pi f_s = 314.16$rad/s for the stator voltage frequency $f_s = 50$Hz (see Fig. 2.12). Hence, for disturbance attenuation, the sensitivity of the channel $v_s \to i_r$ should be reduced especially at around the stator voltage frequency. Alternatively, a feedforward compensation can be used in order to compensate for the stator voltage disturbance [53].

- Because of the magnetic coupling between the stator and rotor, variations of the stator voltage result in oscillations in the rotor current. As can be seen in Fig. 2.13,

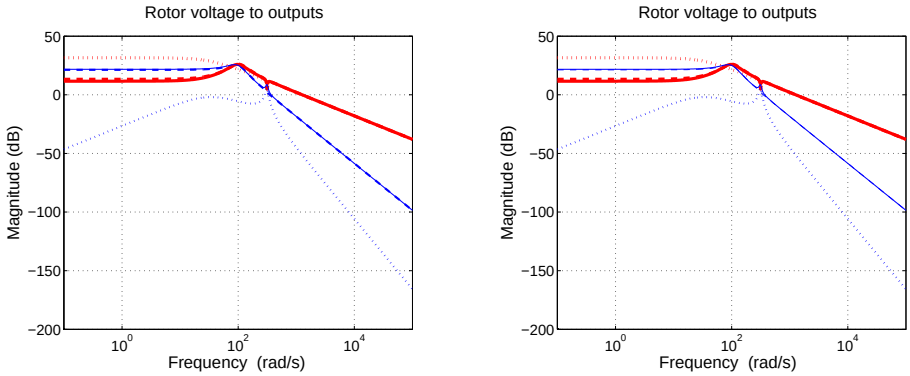

(a) (b)

Figure 2.11: Bode magnitude plot from the rotor voltages v_r to the rotor currents i_r. Dash lines: $\omega_m = 0.7\omega_s$, dotted line: $\omega_m = \omega_s$, and solid line: $\omega_m = 1.3\omega_s$

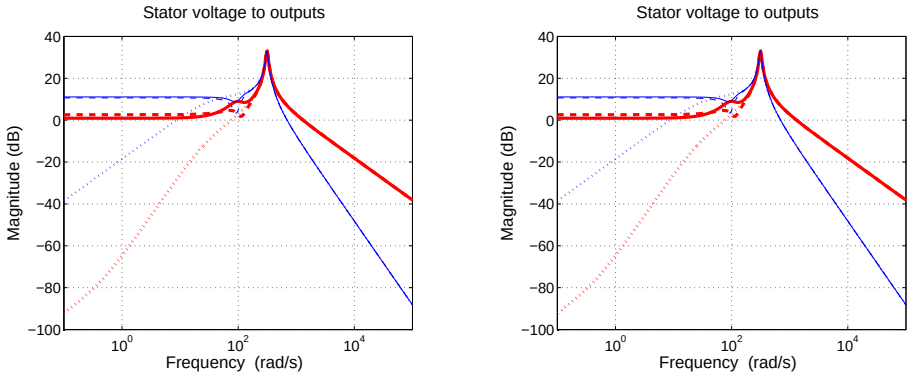

(a) (b)

Figure 2.12: Bode magnitude plot from the stator voltages v_s to the rotor currents i_r. Dash lines: $\omega_m = 0.7\omega_s$, dotted line: $\omega_m = \omega_s$, and solid line: $\omega_m = 1.3\omega_s$

the dynamics of the DFIM is poorly damped for the step changes of the stator voltages.

- In normal operation the stator voltage v_s is assumed to be constant. However, in some specific cases such as grid faults, the sag in the grid voltage could result in a significant influence on the performance of the system.

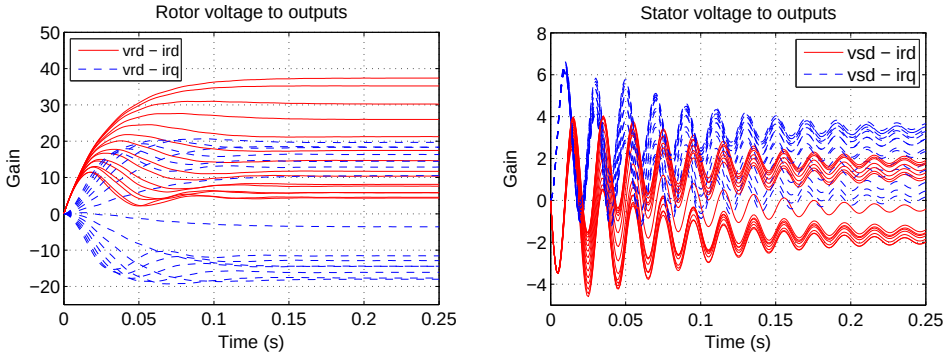

Figure 2.13: Open loop time response of the rotor currents i_r with respect to the rotor voltages v_r (left) and the stator voltages v_s (right) for 15 values of ω_m in the range of $[0.7\omega_s, 1.3\omega_s]$

2.5. SUMMARY

In this chapter, in order to derive the continuous models for both the DFIM and the grid, the required reference frames and transformations were introduced. A rotating reference frame which is independent of the machine parameters and the rotor speed measurement accuracy with the d-axis oriented along the grid voltage vector has been adopted. This reference frame has been used for the developed models and for the current control algorithms of both the rotor and the grid side controllers. Consequently, state-space models of the rotor and the grid side have been developed with respect to this rotating reference frame.

Subsequently, some basic concepts of a wind energy conversion systems have been presented. In order to optimize the power converted from wind energy into electrical energy, both from the stator and the rotor, same generic control strategies were sketched. Moreover, the rotor and the grid side control configurations as well as control objectives for each control loop were proposed. The control variables include i_{rd} and i_{rq} for the electrical torque and reactive power control on the rotor side, i_{nd} and i_{nq} for the DC-link voltage, and reactive power control on the grid side.

A preliminary open-loop analysis of the DFIM shows that the performance of the controlled system may considerably be affected from grid voltage disturbances, especially during grid faults. Hence, besides methods to enable fault ride-through and protection during low voltage periods, this phenomenon needs to be considered for controller design in the next chapters.

3

CONVENTIONAL CONTROL SCHEME WITH DEADBEAT CONTROLLERS

This chapter gives an overview of a conventional control for DFIMs with deadbeat controllers. The background of deadbeat control is given in the first part of the chapter. Then deadbeat control is applied to designing the current controllers for both the generator and the grid sides. The design is based on the DFIM and the grid models developed in the previous chapter. Further, DFIM parameter uncertainties and robustness of the controlled system are discussed. The impact of the stator voltage dips on the system performance is also investigated at the end of the chapter.

3.1. INTRODUCTION

A deadbeat controller is a classical feedback controller where the controller forces the state of a linear n-state discrete-time system to zero in a number of steps at most equal to n [68, 69]. If the controller can drive the system from any arbitrary initial condition to the origin of the state space with a minimum value of time steps equal to the controllability index of the system it is said to be a *minimum-time deadbeat controller*.

Deadbeat control is used for induction machine control in many electrical drive systems [70, 71, 72, 73, 74, 75]. Applications of this technique have been studied for the control of doubly-fed induction generators [53, 29]. In [73], one-sample deadbeat controllers are implemented for the stator flux and torque control of an induction machine. In [70], one and two-samples deadbeat controllers are proposed for current control of a PWM rectifier on the grid side. However, only simulation results are presented for the two-samples deadbeat controller design. Then a stability analysis of the two-samples deadbeat controller for the case of inaccurate model parameters is also given. In [53], a one-step deadbeat controller is designed for the inner current control loop of the rotor side converter. The simulation results show that the one-step deadbeat controller

obtains a good performance in terms of a good tracking and a fast response. However, robustness of the controlled system with respect to parameter variations as well as grid voltage dips are not discussed. The study in [29] shows, based on experimental results in this specific setup, that a longer time-step deadbeat controller is suitable for the control of the DFIM. Therefore, in [29], a three-step deadbeat controller is designed for both the rotor side and grid side converters. Since these controllers are not minimum-time deadbeat controllers, they are also called *finite response time controllers* [53, 29].

3.2. MULTIVARIABLE DEADBEAT CONTROL FOR DISCRETE-TIME SYSTEMS

3.2.1. DEAD-BEAT RESPONSE

Consider the discrete-time state space system

$$\begin{aligned} x[k+1] &= A_d x[k] + B_d u[k], \\ y[k] &= C_d x[k] + D_d u[k] \end{aligned} \tag{3.1}$$

where $x[k] \in \mathbb{R}^n$, $u[k] \in \mathbb{R}^m$.

It is assumed that the matrix A_d is non-singular, that the matrix B_d is of full column rank, and that the pair (A_d, B_d) is completely controllable, i.e., the matrix

$$\mathscr{C}_d = \begin{pmatrix} B_d & A_d B_d & \cdots & A_d^{n-1} B_d \end{pmatrix} \tag{3.2}$$

has full rank n.

Suppose that the state of the system (3.1) is x_0 at $k = 0$. Then the state at the kth sampling time is given by

$$\begin{aligned} x[k] &= A_d x[k-1] + B_d u[k-1] \\ &= A_d (A_d x[k-2] + B_d u[k-2]) + B_d u[k-1] \\ &= A_d^2 x[k-2] + (A_d B_d u[k-2] + B_d u[k-1]) \\ &= \vdots \\ &= A_d^k x_0 + \sum_{i=0}^{k-1} A_d^{k-i-1} B_d u[i] \end{aligned} \tag{3.3}$$

or

$$x[k] = A_d^k x_0 + \begin{pmatrix} B_d & A_d B_d & \cdots & A_d^{k-1} B_d \end{pmatrix} \begin{pmatrix} u[k-1] \\ u]k-2] \\ \vdots \\ u[0] \end{pmatrix}. \tag{3.4}$$

The system (3.1) is controllable if there exists an input that can transfer the state x_0

to the origin $x[k] = \mathbf{0}$, i.e.

$$\mathbf{0} = A_d^k x_0 + \begin{pmatrix} B_d & A_d B_d & \cdots & A_d^{k-1} B_d \end{pmatrix} \begin{pmatrix} u[k-1] \\ u[k-2] \\ \vdots \\ u[0] \end{pmatrix}. \tag{3.5}$$

Since A_d is invertible, it follows that

$$x_0 = -\begin{pmatrix} A_d^{-1} B_d & A_d^{-2} B_d & \cdots & A_d^{-k} B_d \end{pmatrix} \begin{pmatrix} u[0] \\ u[1] \\ \vdots \\ u[k-1] \end{pmatrix}. \tag{3.6}$$

Hence, all states can be steered to the origin for some choice of the input sequence $\{u[0], u[1], \cdots, u[k-1]\}$ if the matrix

$$\begin{pmatrix} A_d^{-1} B_d & A_d^{-2} B_d & \cdots & A_d^{-k} B_d \end{pmatrix} \text{ has full row rank } n. \tag{3.7}$$

If we denote by κ the smallest k for which (3.7) is true, then κ is called the controllability index of the pair (A_d, B_d). As a consequence, for $\kappa \leq q \leq n$,

$$\begin{pmatrix} A_d^{-1} B_d & A_d^{-2} B_d & \cdots & A_d^{-q} B_d \end{pmatrix} \text{ has full row rank } n.$$

This means that, under the control action of the input signal sequence $\{u[0], u[1], \cdots, u[k-1]\}$, all states can be steered to the origin in no more than q time steps [68].

Suppose we want to control the system by state-feedback

$$u[k] = -K_d x[k]$$

where $K_d \in \mathbb{R}^{m \times n}$ is the state feedback gain matrix. Then the closed-loop control system becomes

$$x[k+1] = (A_d - B_d K_d) x[k]. \tag{3.8}$$

Let K_d be chosen so that all the eigenvalues of $(A_d - B_d K_d)$ are zero, i.e.

$$\det(\lambda I - A_d + B_d K_d) = \lambda^n = 0. \tag{3.9}$$

Due to the Cayley-Hamilton theorem, it follows that

$$(A_d - B_d K_d)^n = \mathbf{0}. \tag{3.10}$$

Equation (3.10) implies that $(A_d - B_d K_d)$ is nilpotent with index n. Hence, from equation (3.8) and (3.10) we may conclude that [76]

$$x[n] = (A_d - B_d K_d)^n x[0] = \mathbf{0}. \tag{3.11}$$

The controller is said to be a q-step deadbeat controller if the system (3.8) is driven from any arbitrary state x_0 to the origin of the state space in at most q time steps. In case that $q = \kappa$, it is said to be a minimum-time deadbeat controller.

3.2.2. DEADBEAT CONTROLLERS

For the sake of simplicity, let us consider the deadbeat controller design problem for a single input only. One can refer, for example, to [77] for the multi-input systems.

Consider again equation (3.1) with the characteristic polynomial of A_d given by

$$p_{A_d} = (z-\lambda_1)(z-\lambda_2)\cdots(z-\lambda_n) = z^n + a_1 z^{n-1} + \cdots + a_{n-1}z + a_n. \tag{3.12}$$

We can find a nonsingular matrix $\mathcal{T}_d$ such that

$$\hat{B}_d = \mathcal{T}_d^{-1} B_d = \begin{pmatrix} 0 \\ 0 \\ \vdots \\ 0 \\ 1 \end{pmatrix}$$

and

$$\hat{A}_d = \mathcal{T}_d^{-1} A_d \mathcal{T}_d = \begin{pmatrix} 0 & 1 & 0 & \cdots & 0 \\ 0 & 0 & 1 & \cdots & 0 \\ \vdots & \vdots & \vdots & \ddots & \vdots \\ 0 & 0 & 0 & \cdots & 1 \\ -a_n & -a_{n-1} & -a_{n-2} & \cdots & -a_1 \end{pmatrix}.$$

Let us also define the new state $\hat{x}[k]$ by

$$x[k] = \mathcal{T}_d \hat{x}[k].$$

Then equation (3.1) can be written as

$$\begin{aligned} \hat{x}[k+1] &= \mathcal{T}_d^{-1} A_d \mathcal{T} \hat{x}[k] + \mathcal{T}_d^{-1} B_d u[k] = \hat{A}_d \hat{x}[k] + \hat{B}_d u[k] \\ &= \begin{pmatrix} 0 & 1 & 0 & \cdots & 0 \\ 0 & 0 & 1 & \cdots & 0 \\ \vdots & \vdots & \vdots & \ddots & \vdots \\ 0 & 0 & 0 & \cdots & 1 \\ -a_n & -a_{n-1} & -a_{n-2} & \cdots & -a_1 \end{pmatrix} \hat{x}[k] + \begin{pmatrix} 0 \\ 0 \\ \vdots \\ 0 \\ 1 \end{pmatrix} u[k]. \end{aligned} \tag{3.13}$$

If applying the state feedback controller K_d with

$$u[k] = -K_d x[k] = -K_d \mathcal{T}_d \hat{x}[k] = -\hat{K}_d \hat{x}[k]$$

where

$$\hat{K}_d = K_d \mathcal{T}_d = \begin{pmatrix} \varrho_n & \varrho_{n-1} & \cdots & \varrho_1 \end{pmatrix}, \tag{3.14}$$

the closed-loop system becomes

$$\hat{x}[k+1] = (\hat{A}_d - \hat{B}_d K_d \mathcal{T}_d)\hat{x}[k] = \boldsymbol{A}_d \hat{x}[k]$$

where

$$\boldsymbol{A}_d = \begin{pmatrix} 0 & 1 & 0 & \cdots & 0 \\ 0 & 0 & 1 & \cdots & 0 \\ \vdots & \vdots & \vdots & \ddots & \vdots \\ 0 & 0 & 0 & \cdots & 1 \\ -(a_n+\varrho_n) & -(a_{n-1}+\varrho_{n-1}) & -(a_{n-2}+\varrho_{n-2}) & \cdots & -(a_1+\varrho_1) \end{pmatrix}. \tag{3.15}$$

The characteristic polynomial of $\boldsymbol{A}_d$ is given by

$$p_{\boldsymbol{A}_d} = z^n + (a_1+\varrho_1)z^{n-1} + \cdots + (a_{n-1}+\varrho_{n-1})z + (a_n+\varrho_n). \tag{3.16}$$

Hence, $\varrho_1, \cdots, \varrho_n$ can be chosen to arbitrarily assign the characteristic polynomial (3.16) of the corresponding system matrix of (3.15).

Now let us choose the desired pole locations to be at the origin or, in other words, choose the desired eigenvalues to be zero $\lambda_1 = \lambda_2 = \cdots = \lambda_n = 0$. The characteristic equation with the desired eigenvalues equals

$$p_{\hat{A}_d} = z^n + (a_1+\varrho_1)z^{n-1} + \cdots + (a_{n-1}+\varrho_{n-1})z + (a_n+\varrho_n) = z^n.$$

Hence

$$a_1+\varrho_1 = a_2+\varrho_2 = \cdots = a_n+\varrho_n = 0$$

and

$$\boldsymbol{A}_d = \begin{pmatrix} 0 & 1 & 0 & \cdots & 0 \\ 0 & 0 & 1 & \cdots & 0 \\ \vdots & \vdots & \vdots & \ddots & \vdots \\ 0 & 0 & 0 & \cdots & 1 \\ 0 & 0 & 0 & \cdots & 0 \end{pmatrix}.$$

Thus, $\boldsymbol{A}_d = \hat{A}_d - \hat{B}_d K_d \mathcal{T}_d$ is a nilpotent matrix. Therefore, we have

$$\boldsymbol{A}_d^n = (\hat{A}_d - \hat{B}_d K_d \mathcal{T}_d)^n = 0.$$

In this fashion we achieve deadbeat control in n sampling steps.

It follows from equation (3.14) that the corresponding feedback gain should be chosen as

$$K_d = \begin{pmatrix} -a_n & -a_{n-1} & \cdots & -a_1 \end{pmatrix} \mathcal{T}_d^{-1}. \tag{3.17}$$

3.2.3. INPUT-OUTPUT REALIZATION OF THE DEADBEAT RESPONSE IN THE Z-DOMAIN

In this section we consider the response of a deadbeat system as a particular case of discrete-time systems. Let us assume that a linear discrete-time system is excited by the unit impulse signal

$$\tilde{u}(z) = \frac{1}{1-z^{-1}}. \tag{3.18}$$

Let k be some positive integer. A system is called to be finite response time if the output of the system follows a step input reference after k-time steps with no overshoot. In practice, if control algorithms are implemented on a digital system with an industrial computer or with a microprocessor-based system, a computation delay is unavoidable. However, in modern digital control systems, the amount of computation required for the control algorithm can be completed within one or several sampling periods. As a result, if the system is assumed to be FRT and if the algorithm is intended to be implemented on a modern digital system we assume that one step of hardware computation delay is taken into account. Therefore, the output response of the system can be represented as follows [78] (see Fig. 3.1):

$$\widetilde{y}(z) = \sum_{\vartheta=0}^{\infty} h_\vartheta z^{-\vartheta}. \tag{3.19}$$

where

$$h_\vartheta = \begin{cases} 0 & \text{for } \vartheta = 0, \\ \frac{\vartheta-1}{k} & \text{for } \vartheta = 1, \cdots, k, \\ 1 & \text{for } \vartheta = k+1, \cdots, \infty. \end{cases}$$

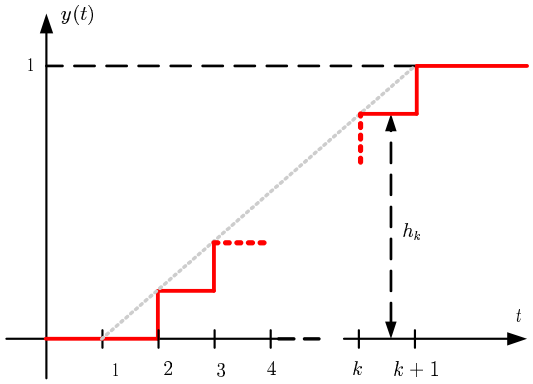

Figure 3.1: The output response of the FRT system

If $|z| < 1$, equation (3.19) can be written as

$$\begin{aligned} \widetilde{y}(z) &= \frac{z^{-(k+1)}}{1-z^{-1}} + \sum_{\vartheta=1}^{k} \frac{\vartheta-1}{k} z^{-\vartheta} \\ &= \left(z^{-(k+1)} + \left(1-z^{-1}\right) \sum_{\vartheta=1}^{k} \frac{\vartheta-1}{k} z^{-\vartheta} \right) \frac{1}{1-z^{-1}} \\ &= G_{db}(z)\widetilde{u}(z) \end{aligned}$$

where

$$G_{db}(z) = z^{-(k+1)} + \left(1 - z^{-1}\right) \sum_{\vartheta=1}^{k} \frac{\vartheta - 1}{k} z^{-\vartheta} \tag{3.20}$$

is the pulse transfer function of the system.

For a linear n-state discrete-time system, a deadbeat controller is expected to force the output of the system to follow the reference input after $(n+1)$-time steps $(k = n)$ including one step of hardware computation delay with no overshoot. In case the output response of the controlled system settles down in $(k+1)$-time steps where $k > n$, the system is no longer deadbeat but FRT.

In the literature, the properties of a deadbeat control are summarized as follows [77, 79]:

- The deadbeat control technique uses the sampling period as one design parameter.
- The control signal is significantly influenced by the sampling period T. In deadbeat control, the settling time is not larger than $(n+1)T$. Furthermore, if the sampling period is chosen small the control signal might be very large in order to force the control error to zero in a short time period.

3.3. DEADBEAT CONTROLLERS DESIGN FOR DFIMS

3.3.1. THE ROTOR SIDE CONTROL

Let us start by deriving the discrete-time state space model of DFIM. The basic equations (2.15) and (2.16) of the doubly-fed induction machine can be rewritten as follows:

$$\dot{x}_r = A_r(\omega_m)x_r + B_s v_s + B_r v_r = A_r(\omega_m)x_r + B_u u_r, \tag{3.21}$$

$$y_r = C_r x_r \tag{3.22}$$

where

$$A_r(\omega_m) = \left(\begin{array}{cc|cc} -\left(\frac{a+1}{T_r} + \frac{a}{T_s}\right) & \omega_s - \omega_m & \frac{a}{L_m T_s} & -\frac{a\omega_m}{L_m} \\ \omega_m - \omega_s & -\left(\frac{a+1}{T_r} + \frac{a}{T_s}\right) & \frac{a\omega_m}{L_m} & \frac{a}{L_m T_s} \\ \hline \frac{L_m}{T_s} & 0 & -\frac{1}{T_s} & \omega_s \\ 0 & \frac{L_m}{T_s} & -\omega_s & -\frac{1}{T_s} \end{array}\right) = \left(\begin{array}{c|c} A_{r11}(\omega_m) & A_{r12}(\omega_m) \\ \hline A_{r21} & A_{r22} \end{array}\right), \tag{3.23}$$

$$B_u = \begin{pmatrix} B_s & B_r \end{pmatrix} = \left(\begin{array}{cc|cc} -\frac{a}{L_m} & 0 & \frac{a+1}{L_r} & 0 \\ 0 & -\frac{a}{L_m} & 0 & \frac{a+1}{L_r} \\ \hline 1 & 0 & 0 & 0 \\ 0 & 1 & 0 & 0 \end{array}\right) = \left(\begin{array}{c|c} B_{s1} & B_{r1} \\ \hline B_{s2} & B_{r2} \end{array}\right). \tag{3.24}$$

This leads to

$$\dot{x_r} = \begin{pmatrix} A_{r11}(\omega_m) & A_{r12}(\omega_m) \\ A_{r21} & A_{r22} \end{pmatrix} \begin{pmatrix} i_r \\ \Psi_s \end{pmatrix} + \begin{pmatrix} B_{s1} & B_{r1} \\ B_{s2} & B_{r2} \end{pmatrix} \begin{pmatrix} v_s \\ v_r \end{pmatrix}. \tag{3.25}$$

Let us assume that ω_m is constant during a sampling period T. The discretization of state equation (3.21) is given as ([53, 77, 80])

$$x_r[k+1] = \tilde{\mathbf{A}}_r(\omega_m)\, x_r[k] + \tilde{\mathbf{B}}_s\, v_s[k] + \tilde{\mathbf{B}}_r\, v_r[k] \tag{3.26}$$

where

$$\tilde{\mathbf{A}}_r(\omega_m) = e^{A_r(\omega_m)T} = \sum_{\vartheta=0}^{\infty} (A_r(\omega_m))^{\vartheta} \frac{T^{\vartheta}}{\vartheta!}, \tag{3.27}$$

$$\tilde{\mathbf{B}}_{s,r} = \int_{kT}^{(k+1)T} e^{A_r \tau} d\tau B_{s,r} = \sum_{\vartheta=1}^{\infty} \frac{(A_r)^{\vartheta-1}}{\vartheta!} T^{\vartheta} B_{s,r}. \tag{3.28}$$

Using the first-order approximation of (3.27) and (3.28), equation (3.26) can now be rewritten as

$$x_r[k+1] = \mathbf{A}_r(\omega_m)\, x_r[k] + \mathbf{B}_s\, v_s[k] + \mathbf{B}_r\, v_r[k] \tag{3.29}$$

where

$$\mathbf{A}_r(\omega_m) = \left(\begin{array}{cc|cc} 1 - T\left(\frac{a+1}{T_r} + \frac{a}{T_s}\right) & (\omega_s - \omega_m)T & \frac{aT}{L_m T_s} & -\frac{a}{L_m}\omega_m T \\ (\omega_m - \omega_s)T & 1 - T\left(\frac{a+1}{T_r} + \frac{a}{T_s}\right) & \frac{a}{L_m}\omega_m T & \frac{aT}{L_m Ts} \\ \hline \frac{T}{T_s} & 0 & 1 - \frac{T}{T_s} & \omega_s T \\ 0 & \frac{T}{T_s} & -\omega_s T & 1 - \frac{T}{T_s} \end{array}\right) = \begin{pmatrix} \mathbf{A}_{r11}(\omega_m) & \mathbf{A}_{r12}(\omega_m) \\ \mathbf{A}_{r21} & \mathbf{A}_{r22} \end{pmatrix},$$

$$\mathbf{B}_s = \left(\begin{array}{cc} -\frac{a}{L_m}T & 0 \\ 0 & -\frac{a}{L_m}T \\ \hline \frac{T}{L_m} & 0 \\ 0 & \frac{T}{L_m} \end{array}\right) = \left(\begin{array}{c} \mathbf{B}_{s1} \\ \hline \mathbf{B}_{s2} \end{array}\right), \tag{3.30}$$

$$\mathbf{B}_r = \left(\begin{array}{cc} \frac{T}{\sigma L_r} & 0 \\ 0 & \frac{T}{\sigma L_r} \\ \hline 0 & 0 \\ 0 & 0 \end{array}\right) = \left(\begin{array}{c} \mathbf{B}_{r1} \\ \hline \mathbf{B}_{r2} \end{array}\right).$$

Consequently, the discretizing state space equation (3.29) of the DFIM can also be compactly expressed as

$$x_r[k+1] = \begin{pmatrix} \mathbf{A}_{r11}(\omega_m) & \mathbf{A}_{r12}(\omega_m) \\ \mathbf{A}_{r21} & \mathbf{A}_{r22} \end{pmatrix} \begin{pmatrix} i_r[k] \\ \Psi_s[k] \end{pmatrix} + \begin{pmatrix} \mathbf{B}_{s1} & \mathbf{B}_{r1} \\ \mathbf{B}_{s2} & \mathbf{B}_{r2} \end{pmatrix} \begin{pmatrix} v_s[k] \\ v_r[k] \end{pmatrix}. \tag{3.31}$$

Conventional designs, described for instance in [53, 29], are based on the current model of the DFIM, which means that only the first two equations, (2.11) and (2.12), of (2.15) are used for designing the controller. In conventional designs

$$\widetilde{i}_{rd} = (\omega_s - \omega_m) i_{rq}, \tag{3.32}$$
$$\widetilde{i}_{rq} = (\omega_m - \omega_s) i_{rd} \tag{3.33}$$

are considered as cross-coupling terms.

In the literature, the common features of the finite response time controller designs for DFIM are summarized as follows:

- The rotor angular speed ω_m is measured online at each sampling time and it is assumed to be equal to a constant during that sampling period. This means that the DFIM model is considered to be a linear time-invariant system within a sampling interval. Then a finite response time controller is also designed online for each sampling period based on this assumption on the plant [53, 29].

- As mentioned in section 2.3.2, the electrical torque and reactive power of the DFIM can be regulated via the components of the rotor currents i_{rd} and i_{rq}, respectively (see equations (2.36), and (2.37)). Therefore, the current controller should ensure a decoupling between the electrical torque and the reactive power forming the current components i_{rd} and i_{rq}. In [53, 15, 81, 17], the cross-coupling terms (3.32) and (3.33) in the rotor current equations that include the mechanical angular speed are eliminated by adding a feed-forward term to the output of the q-axis controller.

COMPENSATING STATOR VOLTAGE AND FLUX

Since the stator windings of the DFIMs are connected to the stiff power system, the stator voltages and flux are considered as disturbances. Their influence on the rotor currents can be compensated by a simple feedforward controller. The compensation is aimed at eliminating the terms $\mathbf{A}_{r12}\Psi_s$ and $\mathbf{B}_{s1}v_s$ in equation (3.31).

In order to do so, we use the variable transformation

$$\begin{pmatrix} v_s \\ \tilde{v}_r \end{pmatrix} = \begin{pmatrix} 0 & 0 \\ 0 & \mathbf{B}_{r1}^{-1}\mathbf{A}_{r12} \end{pmatrix}\begin{pmatrix} i_r \\ \Psi_s \end{pmatrix} + \begin{pmatrix} I & 0 \\ \mathbf{B}_{r1}^{-1}\mathbf{B}_{s1} & I \end{pmatrix}\begin{pmatrix} v_s \\ v_r \end{pmatrix}$$
$$= \begin{pmatrix} 0 & 0 \\ 0 & \boldsymbol{D}_f \end{pmatrix}\begin{pmatrix} i_r \\ \Psi_s \end{pmatrix} + \begin{pmatrix} I & 0 \\ \boldsymbol{D}_v & I \end{pmatrix}\begin{pmatrix} v_s \\ v_r \end{pmatrix} \tag{3.34}$$

where $\boldsymbol{D}_v = \boldsymbol{B}_{r1}^{-1}\boldsymbol{B}_{s1}$, and $\boldsymbol{D}_f = \boldsymbol{B}_{r1}^{-1}\boldsymbol{A}_{r12}$ are the disturbance matrices.

It follows that

$$\begin{pmatrix} v_s \\ v_r \end{pmatrix} = \begin{pmatrix} 0 & 0 \\ 0 & -\mathbf{B}_{r1}^{-1}\mathbf{A}_{r12} \end{pmatrix}\begin{pmatrix} i_r \\ \Psi_s \end{pmatrix} + \begin{pmatrix} I & 0 \\ -\mathbf{B}_{r1}^{-1}\mathbf{B}_{s1} & I \end{pmatrix}\begin{pmatrix} v_s \\ \tilde{v}_r \end{pmatrix}. \tag{3.35}$$

Thus, equation (3.31) now becomes

$$\begin{aligned} x_r[k+1] &= \begin{pmatrix} \mathbf{A}_{r11} & \mathbf{A}_{r12} \\ \mathbf{A}_{r21} & \mathbf{A}_{r22} \end{pmatrix}\begin{pmatrix} i_r[k] \\ \Psi_s[k] \end{pmatrix} \\ &\quad + \begin{pmatrix} \mathbf{B}_{s1} & \mathbf{B}_{r1} \\ \mathbf{B}_{s2} & \mathbf{B}_{r2} \end{pmatrix}\left\{\begin{pmatrix} 0 & 0 \\ 0 & -\mathbf{B}_{r1}^{-1}\mathbf{A}_{r12} \end{pmatrix}\begin{pmatrix} i_r[k] \\ \Psi_s[k] \end{pmatrix} + \begin{pmatrix} I & 0 \\ -\mathbf{B}_{r1}^{-1}\mathbf{B}_{s1} & I \end{pmatrix}\begin{pmatrix} v_s[k] \\ \tilde{v}_r[k] \end{pmatrix}\right\} \\ &= \begin{pmatrix} \mathbf{A}_{r11} & 0 \\ \mathbf{A}_{r21} & \mathbf{A}_{r22} - \mathbf{B}_{r2}\mathbf{B}_{r1}^{-1}\mathbf{A}_{r12} \end{pmatrix}\begin{pmatrix} i_r[k] \\ \Psi_s[k] \end{pmatrix} + \begin{pmatrix} 0 & \mathbf{B}_{r1} \\ \mathbf{B}_{s2} - \mathbf{B}_{r2}\mathbf{B}_{r1}^{-1}\mathbf{B}_{s1} & \mathbf{B}_{r2} \end{pmatrix}\begin{pmatrix} v_s[k] \\ \tilde{v}_r[k] \end{pmatrix}. \end{aligned}$$

Since $\mathbf{B}_{r2} = \begin{pmatrix} 0 & 0 \\ 0 & 0 \end{pmatrix}$ this results in the simpler form

$$x_r[k+1] = \begin{pmatrix} \mathbf{A}_{r11} & 0 \\ \mathbf{A}_{r21} & \mathbf{A}_{r22} \end{pmatrix}\begin{pmatrix} i_r[k] \\ \Psi_s[k] \end{pmatrix} + \begin{pmatrix} 0 & \mathbf{B}_{r1} \\ \mathbf{B}_{s2} & 0 \end{pmatrix}\begin{pmatrix} v_s[k] \\ \tilde{v}_r[k] \end{pmatrix} \tag{3.36}$$

or

$$x_r[k+1] = \widetilde{\mathbf{A}}_r x_r[k] + \widetilde{\mathbf{B}}_r \tilde{u}_r[k] \tag{3.37}$$

where

$$\widetilde{\mathbf{A}}_r = \left(\begin{array}{cc|cc} -\left(\frac{a+1}{T_r} + \frac{a}{T_s}\right) & \omega_s - \omega_m & 0 & 0 \\ \omega_m - \omega_s & -\left(\frac{a+1}{T_r} + \frac{a}{T_s}\right) & 0 & 0 \\ \hline \frac{L_m}{T_s} & 0 & -\frac{1}{T_s} & \omega_s \\ 0 & \frac{L_m}{T_s} & -\omega_s & -\frac{1}{T_s} \end{array}\right), \tag{3.38}$$

$$\widetilde{\mathbf{B}}_r = \left(\begin{array}{cc|cc} 0 & 0 & \frac{a+1}{L_r} & 0 \\ 0 & 0 & 0 & \frac{a+1}{L_r} \\ \hline 1 & 0 & 0 & 0 \\ 0 & 1 & 0 & 0 \end{array}\right), \tag{3.39}$$

$$\widetilde{u}_r = \begin{pmatrix} v_s \\ \widetilde{v}_r \end{pmatrix}. \tag{3.40}$$

Furthermore, from equation (3.35) we have

$$\begin{aligned} v_r &= -\mathbf{B}_{r1}^{-1}\mathbf{A}_{r12}\Psi_s + \begin{pmatrix} -\mathbf{B}_{r1}^{-1}\mathbf{B}_{s1} & I \end{pmatrix}\begin{pmatrix} v_s \\ \widetilde{v}_r \end{pmatrix} \\ &= \begin{pmatrix} -\mathbf{B}_{r1}^{-1}\mathbf{A}_{r12} & -\mathbf{B}_{r1}^{-1}\mathbf{B}_{s1} & I \end{pmatrix}\begin{pmatrix} \Psi_s \\ v_s \\ \widetilde{v}_r \end{pmatrix} \\ &= F_r \begin{pmatrix} \Psi_s \\ v_s \\ \widetilde{v}_r \end{pmatrix} \end{aligned} \tag{3.41}$$

where $F_r = \begin{pmatrix} -\mathbf{B}_{r1}^{-1}\mathbf{A}_{r12} & -\mathbf{B}_{r1}^{-1}\mathbf{B}_{s1} & I \end{pmatrix}$.

Hence, via the variable transformation, the actions of the stator voltage v_s on the control input of the system are compensated since the left upper term of the matrix $\widetilde{\mathbf{B}}_r$ in equation (3.39) is zero. The new discrete-time model of the DFIM with the control input $\widetilde{v}_r$ is now obtained by adding the term F_r to the input v_r. In this scenario, the term F_r plays the role of a feedforward compensator for the stator voltage and flux.

Pictorially, the above variable transformation can be illustrated as in Fig. 3.2.

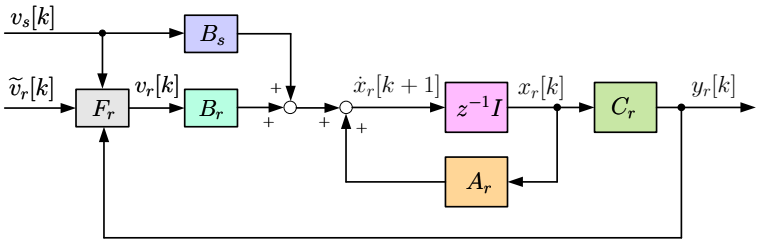

Figure 3.2: The DFIM model with the stator voltage and flux compensator

DEADBEAT CONTROLLER DESIGN FOR THE ROTOR SIDE CONVERTER

Since the design of the rotor current controller can only be based on the current model of the DFIM, we are only interested in the rotor current dynamic equations in (3.36).

As mentioned in [53, 29], the rotor angular speed ω_m is measured online and is considered to be a constant in each sampling interval. Therefore, the DFIM current model is a linear time-invariant system during the sampling period and a deadbeat controller is designed online within that time.

Decomposing equation (3.36) and considering only equations that consist of the current as state variables, it follows that

$$x_{rc}[k+1] = \mathbf{A}_{rc}x_{rc}[k] + \mathbf{B}_{rc}\tilde{v}_r[k] \tag{3.42}$$

where

$$\begin{aligned} \mathbf{A}_{rc} &= \mathbf{A}_{r11}, \quad x_{rc} = i_r = \begin{pmatrix} i_{rd} & i_{rq} \end{pmatrix}^T, \\ \mathbf{B}_{rc} &= \mathbf{B}_{r1}, \quad \tilde{v}_r = \begin{pmatrix} \tilde{v}_{rd} & \tilde{v}_{rq} \end{pmatrix}^T. \end{aligned}$$

Taking the z transform of equation (3.42) with assuming that the initial state is zero we obtain

$$zx_{rc} = \mathbf{A}_{rc}x_{rc} + \mathbf{B}_{rc}\tilde{v}_r \tag{3.43}$$

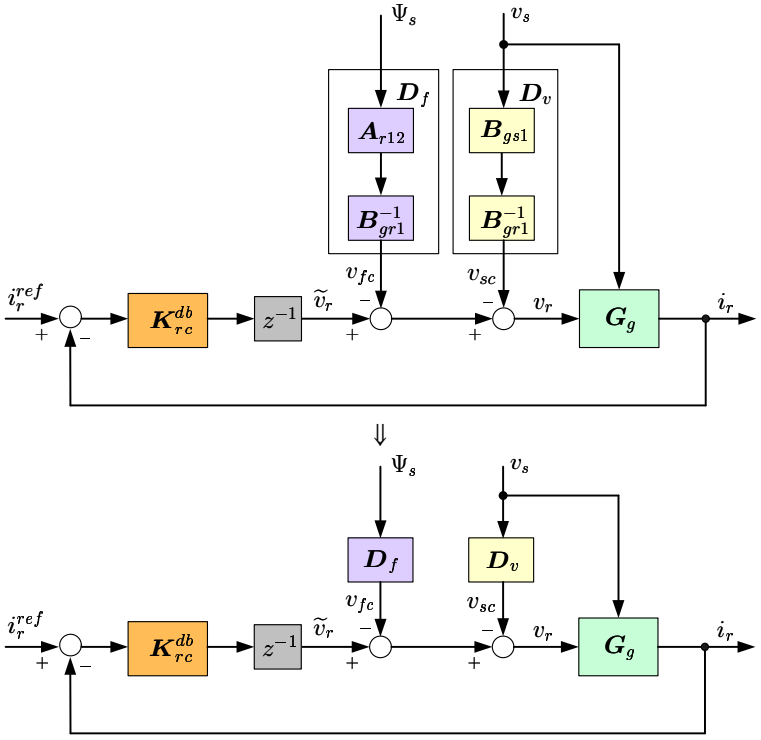

Figure 3.3: The controlled system with deadbeat current controller

Now, let K_{rc}^{db} be the feedback matrix of a deadbeat controller, and let i_r^{ref} and i_r denote the reference and the actual value of the rotor currents, respectively. Since, as

discussed above, there always exists one step of computing delay in digital controller implementations that is represented by the delay operator z^{-1} in Fig. 3.3, it follows that

$$\widetilde{v}_r = z^{-1}K_{rc}^{db}\left(i_r^{ref} - i_r\right). \tag{3.44}$$

Substituting equation (3.44) into equation (3.43) gives

$$\left(I - z^{-1}\mathbf{A}_{rc} + z^{-2}\mathbf{B}_{rc}K_{rc}^{db}\right) i_r = z^{-2}\mathbf{B}_{rc}K_{rc}^{db} i_r^{ref}.$$

The transfer function from the reference input i_r^{ref} to the output i_r is given as

$$G_{rc}^{db}(z) = \left(I - z^{-1}\mathbf{A}_{rc} + z^{-2}\mathbf{B}_{rc}K_{rc}^{db}\right)^{-1} z^{-2}\mathbf{B}_{rc}K_{rc}^{db}. \tag{3.45}$$

Hence, the K_{rc}^{db} controller is said to be FRT if (3.45) satisfies (3.20), i.e.

$$\left(I - z^{-1}\mathbf{A}_{rc} + z^{-2}\mathbf{B}_{rc}K_{rc}^{db}\right)^{-1} z^{-2}\mathbf{B}_{rc}K_{rc}^{db} = z^{-(k+1)} + \left(1 - z^{-1}\right)\sum_{\vartheta=1}^{k}\frac{\vartheta - 1}{k}z^{-\vartheta}.$$

It follows that [29]

$$K_{rc}^{db} = \mathbf{B}_{rc}^{-1}\left(I - z^{-1}\mathbf{A}_{rc}\right)\frac{\sum_{\vartheta=0}^{k-1} z^{-\vartheta}}{k - \sum_{\vartheta=2}^{k+1} z^{-\vartheta}} \tag{3.46}$$

where $k \geq 1$.

Thus, for a one-step deadbeat controller ($k = 1$) we have

$$K_{rc}^{db} = \mathbf{B}_{rc}^{-1}\left(I - z^{-1}\mathbf{A}_{rc}\right)\frac{1}{1 - z^{-2}}. \tag{3.47}$$

This implies that

$$i_r = z^{-2} i_r^{ref}.$$

Similarly, with a two-step deadbeat controller ($k = 2$) it follows that

$$K_{rc}^{db} = \mathbf{B}_{rc}^{-1}\left(I - z^{-1}\mathbf{A}_{rc}\right)\frac{1 + z^{-1}}{2 - z^{-2} - z^{-3}},$$

and

$$i_r = \frac{1}{2}\left(z^{-2} + z^{-3}\right) i_r^{ref}.$$

In order to evaluate the performance of the deadbeat control for wind turbine applications with DFIMs, the one-step deadbeat controller has been chosen for the rotor side control. The simulation results of the closed-loop system with deadbeat current controller on the rotor side will be given in Section 3.3.3.

3.3.2. THE GRID SIDE CONTROL

THE DISCRETE-TIME STATE SPACE MODEL OF THE GRID SIDE

Using the first-order approximation method, the first order discretization of the state equations (2.30) and (2.31) during a sampling period is given by

$$i_n[k+1] = \boldsymbol{A}_n i_n[k] + \begin{pmatrix}\boldsymbol{B}_n & \boldsymbol{B}_c\end{pmatrix}\begin{pmatrix}v_n[k]\\ v_c[k]\end{pmatrix} \tag{3.48}$$

where

$$\boldsymbol{A}_n = \begin{pmatrix}1-\frac{T}{T_c} & \omega_s T\\ -\omega_s T & 1-\frac{T}{T_c}\end{pmatrix},$$

$$\boldsymbol{B}_c = \begin{pmatrix}\frac{T}{L_c} & 0\\ 0 & \frac{T}{L_c}\end{pmatrix}, \quad \boldsymbol{B}_n = \begin{pmatrix}-\zeta_{nd}T & \zeta_{nq}T\\ -\zeta_{nq}T & -\zeta_{nd}T\end{pmatrix}.$$

COMPENSATING THE GRID VOLTAGE

The design procedure for the current deadbeat controller of the grid side converter is similar to that on the rotor side. Here the grid voltage is considered as a disturbance and a simple feedforward compensation is also used to eliminate its influence. The compensation is aimed at eliminating the term $\boldsymbol{B}_n v_{n,k}$ in equation (3.48).

Using the variable transformation

$$\begin{pmatrix}v_n\\ \widetilde{v}_c\end{pmatrix} = \begin{pmatrix}I & 0\\ \mathbf{B}_c^{-1}\mathbf{B}_n & I\end{pmatrix}\begin{pmatrix}v_n\\ v_c\end{pmatrix} = \begin{pmatrix}I & 0\\ \boldsymbol{D}_n & I\end{pmatrix}\begin{pmatrix}v_n\\ v_c\end{pmatrix}$$

where

$$\boldsymbol{D}_n = \mathbf{B}_c^{-1}\mathbf{B}_n = \begin{pmatrix}\frac{L_c}{T} & 0\\ 0 & \frac{L_c}{T}\end{pmatrix}\begin{pmatrix}-\zeta_{nd} & \zeta_{nq}\\ -\zeta_{nq} & -\zeta_{nd}\end{pmatrix} = \begin{pmatrix}-L_c\zeta_{nd} & L_c\zeta_{nq}\\ -L_c\zeta_{nq} & -L_c\zeta_{nd}\end{pmatrix}$$

it follows that

$$\begin{pmatrix}v_n\\ v_c\end{pmatrix} = \begin{pmatrix}I & 0\\ -\mathbf{B}_c^{-1}\mathbf{B}_n & I\end{pmatrix}\begin{pmatrix}v_n\\ \widetilde{v}_c\end{pmatrix}. \tag{3.49}$$

Then we have

$$i_n[k+1] = \mathbf{A}_n i_{n,k} + \begin{pmatrix}\mathbf{B}_n & \mathbf{B}_c\end{pmatrix}\begin{pmatrix}I & 0\\ -\mathbf{B}_c^{-1}\mathbf{B}_n & I\end{pmatrix}\begin{pmatrix}v_n[k]\\ \widetilde{v}_c[k]\end{pmatrix}.$$

Therefore

$$i_n[k+1] = \mathbf{A}_n i_n[k] + \mathbf{B}_c \widetilde{v}_c[k]. \tag{3.50}$$

Rewriting equation (3.50) in z-domain results in

$$z i_n = \mathbf{A}_n i_n + \mathbf{B}_c \widetilde{v}_c. \tag{3.51}$$

DEADBEAT CONTROLLER DESIGN FOR THE GRID SIDE CONVERTER

Similarly to the current deadbeat controller design for the rotor side converter, let K_{nc}^{db} be the feedback matrix of a deadbeat controller, and let i_n^{ref} and i_n denote the reference and the actual values of the grid currents, respectively (Fig. 3.4). Thus

$$\widetilde{v}_c \quad = \quad z^{-1} K_{nc}^{db} \left(i_n^{ref} - i_n \right). \tag{3.52}$$

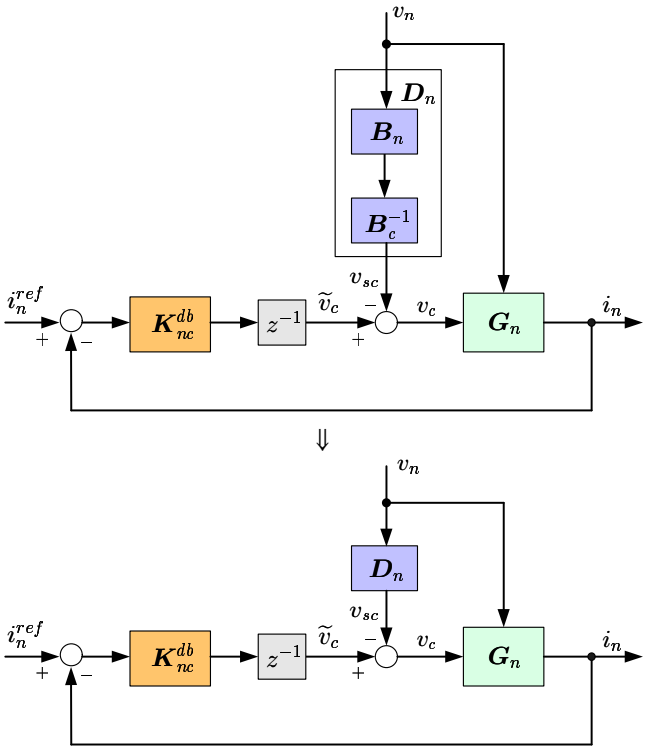

Figure 3.4: The grid side converter with deadbeat current controller

Substituting equation (3.52) into equation (3.51) leads to

$$\left(I - z^{-1}\mathbf{A}_n + z^{-2}\mathbf{B}_c K_{nc}^{db} \right) i_n \quad = \quad z^{-2}\mathbf{B}_c K_{nc}^{db} i_n^{ref}. \tag{3.53}$$

The transfer function from the reference input i_n^{ref} to the output i_n is given as

$$G_{nc}^{db}(z) = \left(I - z^{-1}\mathbf{A}_n + z^{-2}\mathbf{B}_c K_{nc}^{db} \right)^{-1} z^{-2}\mathbf{B}_c K_{nc}^{db}. \tag{3.54}$$

Thus, similarly to the current deadbeat controller design for the rotor side converter,

it follows that

$$K_{nc}^{db} = \mathbf{B}_n^{-1}\left(I - z^{-1}\mathbf{A}_c\right)\frac{\sum_{\vartheta=0}^{k-1} z^{-\vartheta}}{k - \sum_{\vartheta=2}^{k+1} z^{-\vartheta}} \tag{3.55}$$

where $k \geq 1$.

As mentioned in [29, 57], a one-step deadbeat current controller gives a good performance in terms of fast response and reduced steady-state error. The simulation results of the closed-loop system with one-step deadbeat current controllers on the rotor and grid sides are given in the next section.

3.3.3. SIMULATION RESULTS

Figs. 3.5 - 3.6 show the simulation results that are derived for the DFIM model with parameters presented in [66] (see Appendix B.1 for more details). The sampling time used for the simulations is $T_{samp} = 0.00004s$.

In the following simulation results, the negative sign of the angle φ_g of the power factor $\cos\varphi_g$ indicates that the DFIM delivers reactive power to the grid. Conversely, the positive sign of the angle φ_g indicates that the DFIM consumes reactive power from the grid. Similarly, the negative sign of electrical torque indicates that the DFIM consumes mechanical torque on its shaft in order to generate active power pumped into the grid.

The performance of the rotor side control with a one-step deadbeat current controller is shown in Fig. 3.5. The reference and simulated values of the electrical torque T_e of the DFIM are depicted in Fig. 3.5a. The initial value of the electrical torque is -1500Nm. Then it increases to -3500Nm at time 2.5s. After that it decreases to -2000Nm at time 5.5s. Meanwhile, the reference value of the angle φ_g of the power factor $\cos\varphi_g$ (Fig. 3.5b) increases from an initial value of 0.05 to -0.3 at time 2s, and then it decreases to 0.1 at time 5s. Fig. 3.5c and Fig. 3.5d show the roles of the currents i_{rd} and i_{rq} in controlling the electrical torque T_e and the angle φ_g of the power factor $\cos\varphi_g$. The d-component of the rotor current i_{rd} is used to control the electrical torque T_e, and the q-component of the rotor current i_{rq} is used to regulate the power factor $\cos\varphi_g$ via controlling φ_g. The variations of the dq-component of the stator currents i_{sd} and i_{sq} are shown in Fig. 3.5e and Fig. 3.5f.

The performance of the grid side control with a one-step deadbeat current controller is shown in Fig. 3.6. We can see from Fig. 3.6a that the DC-link voltage is kept at a constant value of 1000V in order to maintain the power exchange between the rotor circuit and the grid. Meanwhile, the reference value of the angle φ_n of the power factor $\cos\varphi_n$ increases from an initial value of -0.05 to -0.2 at time $4s$. Fig. 3.6c and Fig. 3.6d show the roles of the currents i_{nd} and i_{nq} in controlling the DC-link voltage v_{DC} and the angle φ_n of the power factor $\cos\varphi_n$. The d-component of the grid current i_{nd} holds a role to regulate the DC-link voltage v_{DC}, and the q-component of the grid current i_{rq} is used to control the angle φ_n.

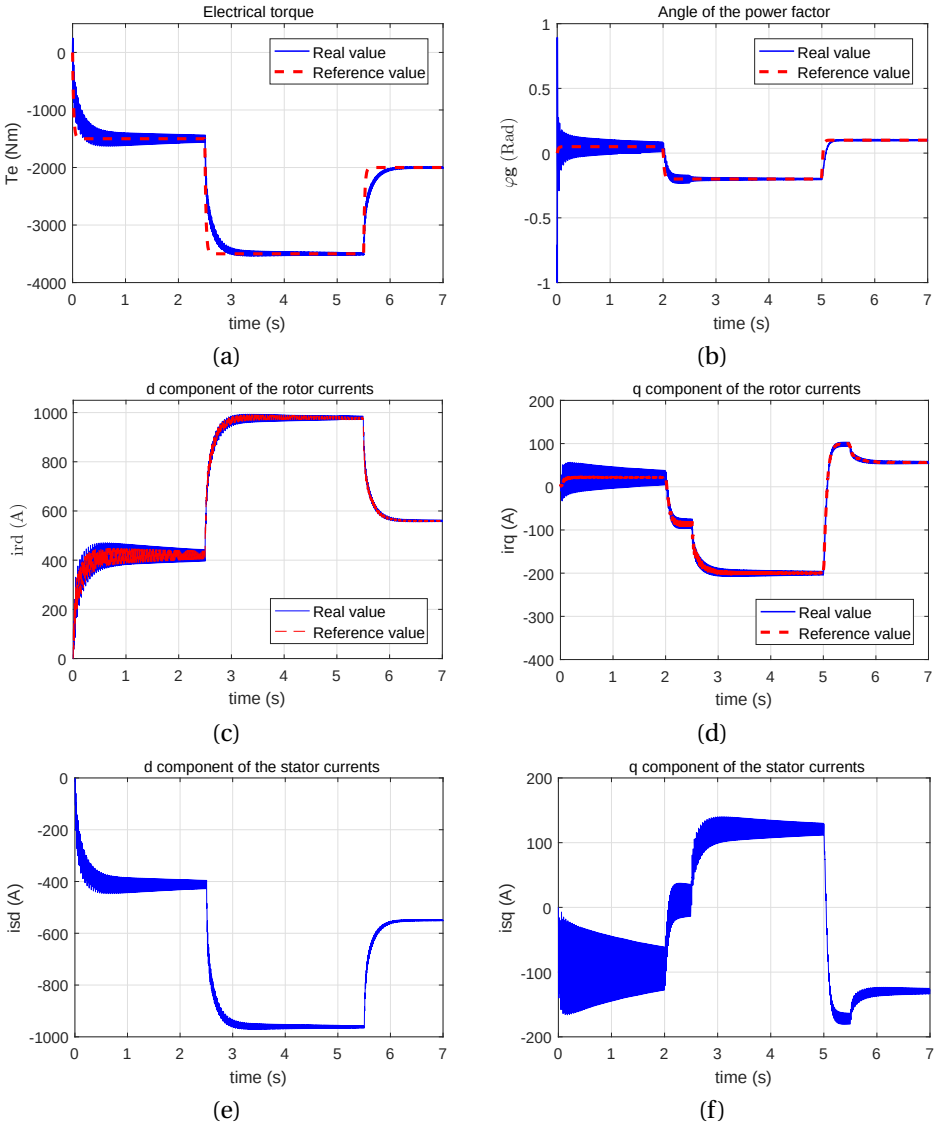

Figure 3.5: Performance of the rotor side control. (a) Electrical torque T_e, (b) the angle φ_g of the power factor $\cos\varphi_g$, (c) and (d) dq-component of the rotor currents, (e) and (f) dq-component of the stator currents

As can be seen in Fig. 3.5 and Fig. 3.6, for the case of perfect knowledge of the DFIM parameters, the closed-loop system with the deadbeat controller achieves good tracking of the rotor currents, the reference electrical torque, the DC-link voltage, and the power factor. This is due to the fact that the one-step deadbeat controller guarantees the short settling time of the output currents. However, this may also result in disadvantages in

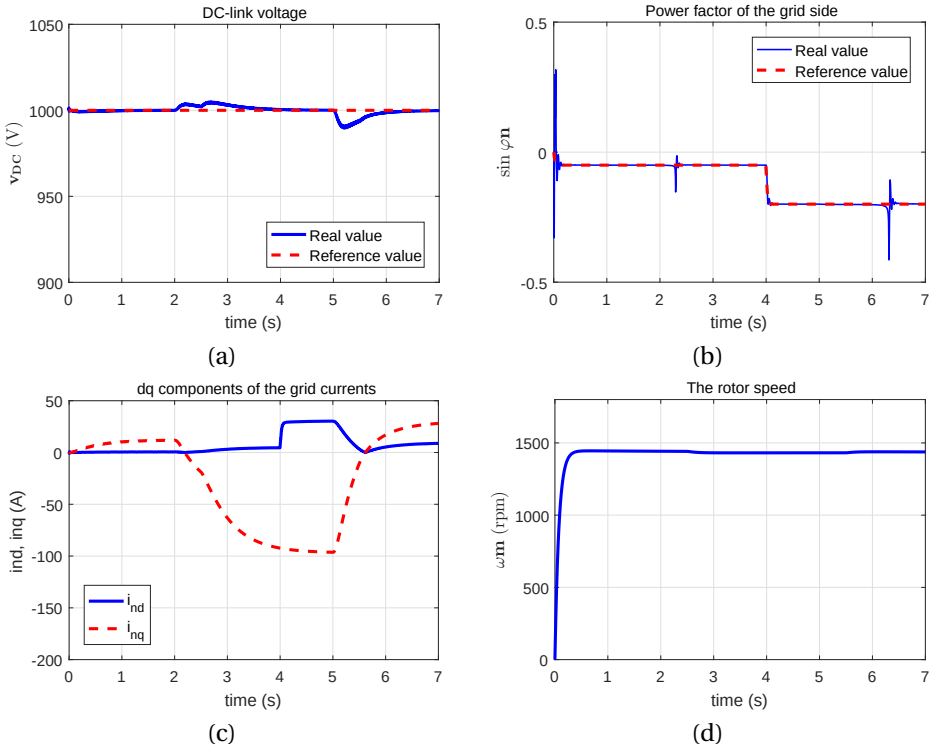

Figure 3.6: Performance of the grid side control. (a) DC-link voltage v_{DC}, (b) the angle φ_n of the power factor cosφ_n, (c) dq-component of the grid currents, and (d) the rotor speed in rotations per minute corresponding to ω_m

practical implementations since huge control efforts are required for deriving the tracking error to zero in a short time.

3.4. DFIM PARAMETER UNCERTAINTIES AND ROBUSTNESS

3.4.1. DFIM PARAMETER UNCERTAINTIES

The variations of the machine resistances are mainly due to machine temperature changes. Electrical machines are usually allowed to be operated in a wide range of the working temperature band. The winding temperature of a non-working machine is defined to be about 20^0C while the allowed maximum winding temperature might be going up to 170^0C depending on the machine class. The machine inductances, however, vary with the temperature and the machine flux due to magnetic saturation and winding current modulus [70].

Here are some remarks on the variations of the machine parameters:

- By simulation results, it was shown that changes in the values of R_s and R_r do not cause significantly changes in performance of the controlled system, or in other words, the closed-loop system is not sensitive to changes in the values of the resistances of the stator and the rotor.
- Since L_s, L_r, L_m, and the mechanical angular speed of the rotor ω_m are all bounded, the uncertainty set $\boldsymbol{\delta}$ of the parameter vector $\delta = (L_s, L_r, L_m, \omega_m)$ is a polytope with $2^{\text{size}(\delta)} = 2^4 = 16$ generators

$$\boldsymbol{\delta} = co\left\{\begin{pmatrix} L_s \\ L_r \\ L_m \\ \omega_m \end{pmatrix} : L_s \in \{\underline{L}_s, \overline{L}_s\}, L_r \in \{\underline{L}_r, \overline{L}_r\}, L_m \in \{\underline{L}_m, \overline{L}_m\}, \omega_m \in \{\underline{\omega}_m, \overline{\omega}_m\}\right\}$$

  However, the system matrices are not affinely dependent on L_s, L_r, and L_m (see equations (3.49) and (3.24)). Hence, a precise robustness analysis will be given only later (see Chapter 6).
- The machine parameters are all slowly time-varying parameters since their values depend on the characteristics of the machine which naturally vary slowly in time, namely temperature and magnetic saturation.

In the next section, we will investigate the robustness of the controlled system with respect to machine parameter variations as evaluated by simulation.

3.4.2. ROBUSTNESS OF THE CONTROL SYSTEM AGAINST PARAMETER CHANGES

The following simulations are carried out for which the machine inductances are treated as time-invariant parameters. Simulation results show that the system with a dead-beat controller stays stable if the mutual inductance L_m is smaller than 1.12% of its nominal values. Fig. 3.7 shows the performance of the system for tracking error of the electrical torque, the power factor, and the rotor current when L_m is set to 101.12% of its normal value.

Similarly, by taking different tests for different values of L_s we see from Fig. 3.8 that the system with dead-beat controller stays stable if L_s deviates by [97.9%, 101.12%] from its nominal values. The same test is performed for different values of L_r. We see from Fig. 3.9 that the system with dead-beat controller stays stable if the L_r deviates by [97.84%, 125%] from its nominal values.

Figs. 3.7, 3.8, and 3.9 show the performance degeneration in the sense of the tracking error of the electrical torque, the power factor, and the rotor current under the occurrence of the machine parameter variations as time-invariant uncertainties.

3.4.3. THE IMPACT OF STATOR VOLTAGE DIPS ON THE ROBUSTNESS OF THE CONTROL SYSTEM

The effect of grid voltage dips on the performance of the controlled system with the DFIG is mentioned in section 1.2. Here, the performance of the controlled system with the

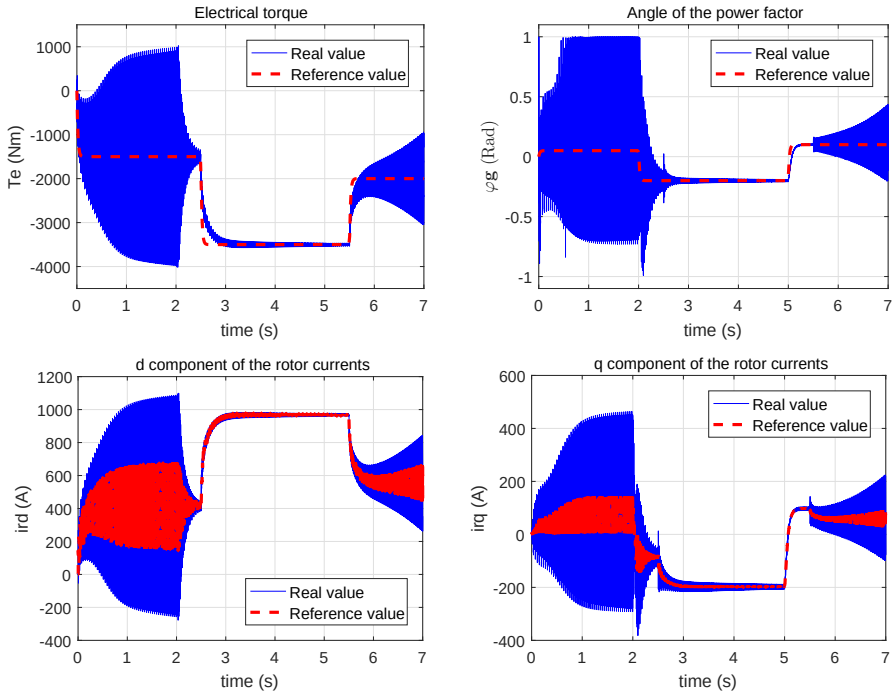

Figure 3.7: Performance of the controlled system when L_m increases by 1.12% of its normal value

current deadbeat controllers in the presence of grid voltage faults is demonstrated by some simulation results (Fig. 3.10). The grid voltage was dropped down to 25% of the normal voltage at time 7.5s. This phenomenon occurred in a period of 300 ms before it recovered to its rated value. After that, at time 8.5s, the grid voltage once again was dropped to 50% of the rated voltage during a period of 200 ms.

These simulation results show that the oscillations of torque and currents of the closed-loop system with the deadbeat controller are not well dampened at the grid voltage fault time. Recall that the effect of the stator voltage on the rotor current, as one of the natural characteristics of the DFIM, is depicted in Fig. 2.12). Since the deadbeat controller does not guarantee the transient oscillation suppression of the rotor current during a fault of the grid voltage, a high stability and robustness of the deadbeat controller in a real implementation is not expected when the grid voltage is faulty.

3.4.4. DISCUSSIONS

From a practical point of view, the controlled systems with deadbeat controllers have the following two main disadvantages [82, 83]:

- Robustness in the sense of the deadbeat response maintenance with respect to

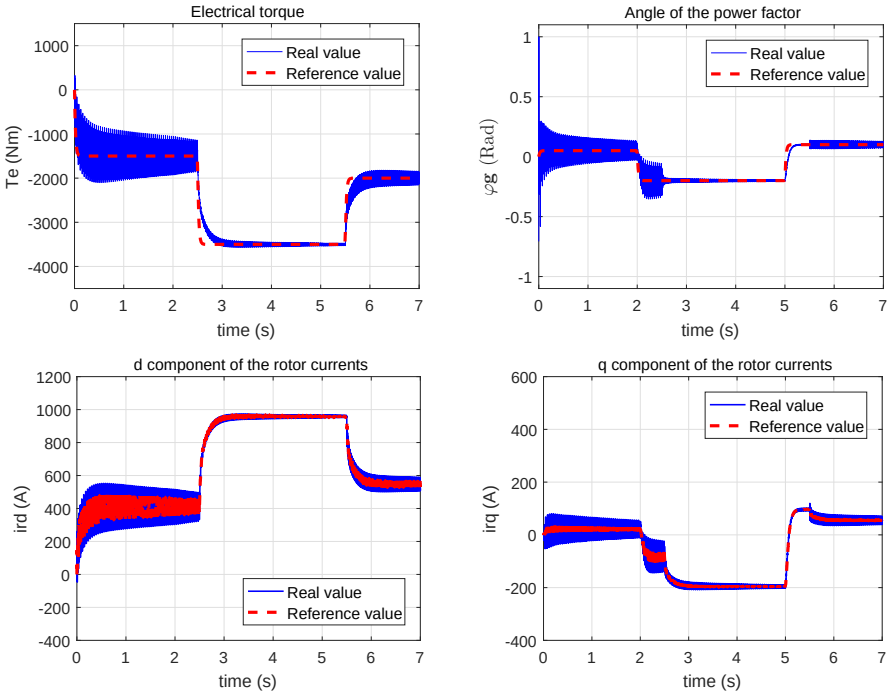

Figure 3.8: Performance of the controlled system when L_s decreases by 2.1% of its normal value

variations of plant parameters is not high. In principle, a small perturbation of the plant may lead to destroying the nominal deadbeat characteristics. In this case, the poles of the closed-loop system are not located at the origin of the z-plane and the behavior of the controlled systems becomes "nearly-deadbeat" [84].

- There is a trade-off between the settling time (deadbeat) and the robustness of the system: the greater the settling time, the better the robustness of the closed-loop system with respect to perturbations of the plant [85, 70]. Conversely, as mentioned in the earlier parts, very large reference control signals are required in order to obtain fast responses.

The robustness of the controlled system with deadbeat controllers could be enhanced by extending the number of deadbeat steps [29, 82] or by using other methods as in [86, 87, 88, 89, 84]. In [86], the design of robust-tracking deadbeat controllers is proposed using a two-degrees-of-freedom control configuration. Moreover, in [89], the H_∞-norm of the sensitivity function is used as the robustness index of the two-degrees-of-freedom control system in order to achieve both minimal-time deadbeat control and optimal robustness with only one controller. In [87], the robust deadbeat regulation problem is treated as an unconstrained optimization problem. In [88], the design of robust ripple-free deadbeat controllers is dealt with by minimizing of the maximum absolute tracking

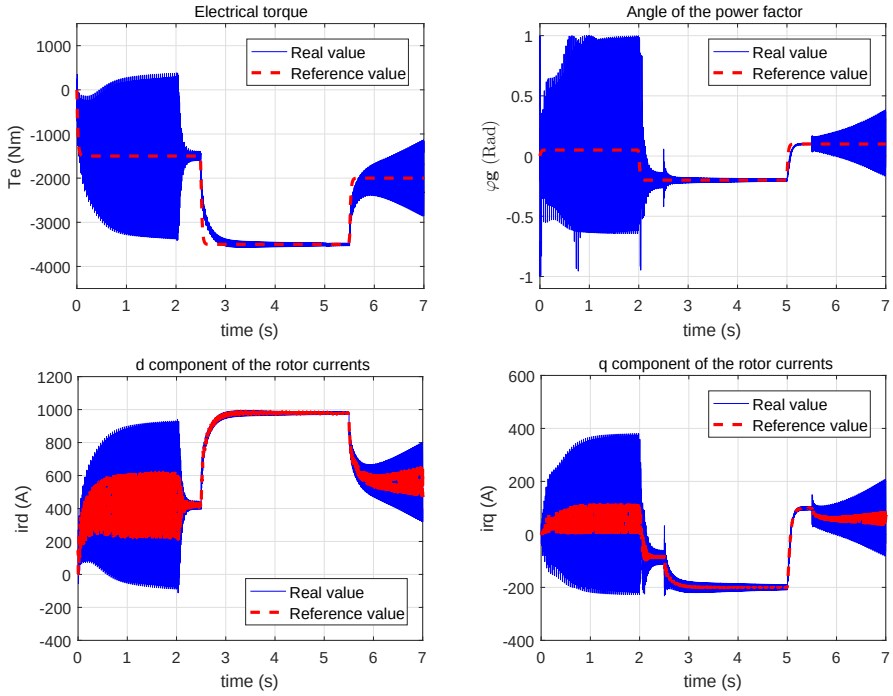

Figure 3.9: Performance of the controlled system when L_r decreases by 2.16% of its normal value

error in an l_∞ sense for any prescribed value of the settling time. In [84], a computational method for the robust deadbeat pole assignment with gain constraints is presented. The pole assignment is tackled using the Linear Matrix Inequality (LMI) framework. In some cases, the deadbeat steps may be chosen to be larger than the order of the system matrix A_d in equation (3.1). As a result, the deadbeat property is not maintained but a "deadbeat-like" behavior is expected, and this type of controllers is said to have *Finite Response Time* [29, 78]. However, robust stability of the system against parameter uncertainties is not fully studied in these literatures since the interest is mainly in maintaining deadbeat characteristics of the system regardless of parameter variations.

Another aspect in designing deadbeat controllers for DFIM is the decoupling. As mentioned earlier, the controlled system uses a simple feedforward compensator to reduce the influence of the stator voltages and flux disturbances by subtracting their values from the controller output (see Fig. 3.3) with

$$v_r = \widetilde{v}_r - v_{fc} - v_{sc}. \tag{3.56}$$

This strategy is similar to the case of a feedforward decoupling control scheme that is used for induction machines in [90, 91, 92, 93, 94, 95, 96, 97]. However, the perfor-

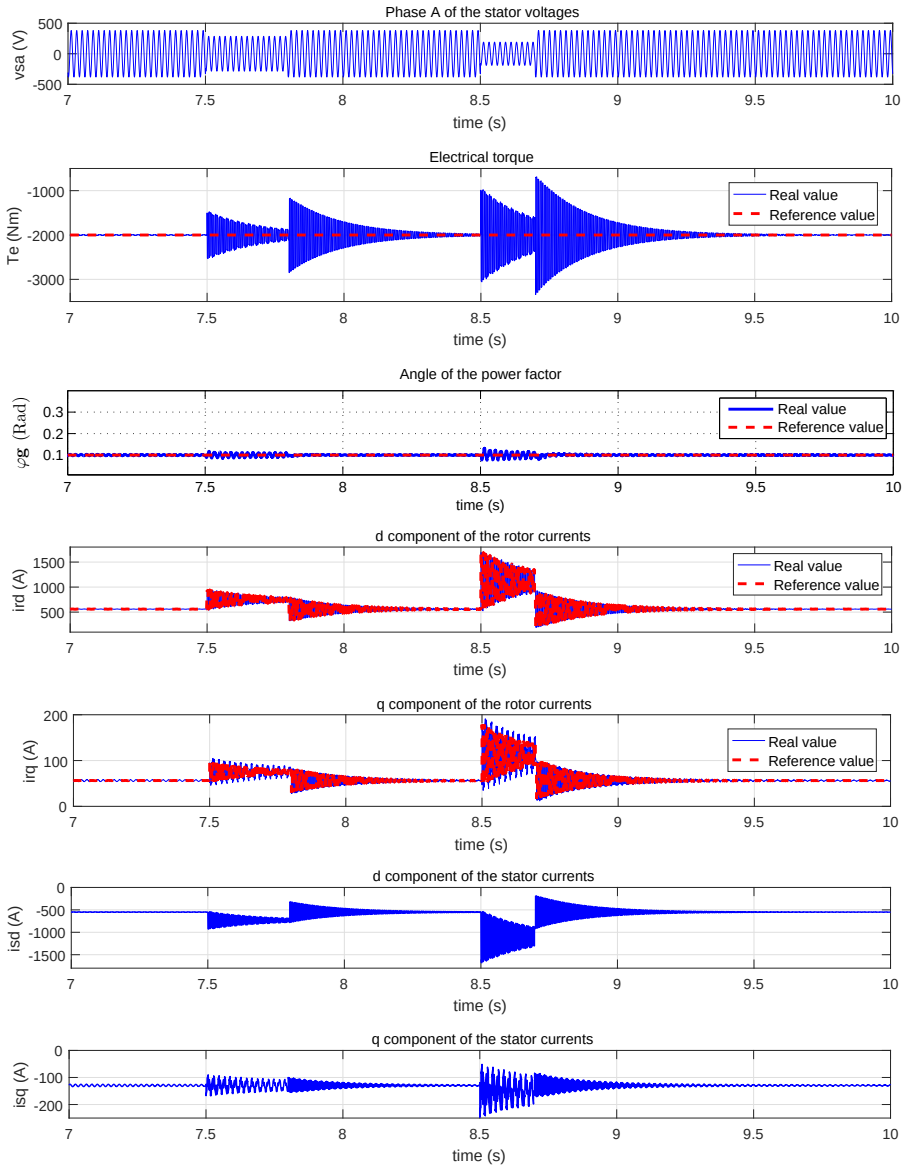

Figure 3.10: The performance of the system when grid voltage is faulty

mance of the feedforward compensation depends strongly on the accuracy of the machine inductances and the total leakage coefficient σ. Furthermore, the coupling term v_{fc} in (3.56) becomes larger as the generator speed ω_m increases. However, at over-synchronous speed, the stator flux begins to decrease and the machine operates in the

field-weakening region. Hence, the proportion of the back EMF does not increase with the mechanical rotor speed ω_m in this region. As a result, the stator flux disturbance is not perfectly canceled by the feedforward compensation over the operating range of the rotor speed.

In this study we do not focus on the control on the grid side converter. Hence, in view of these deficiencies, we will address techniques for designing the controller for the current control loop on the rotor side converter with performance improvement in Chapters 4 and 5. Furthermore, we will propose methods for systematic robustness analysis of the controlled system in order to investigate the stability with respect to parameter variations in Chapter 6.

3.5. SUMMARY

The first part of this chapter was aimed at presenting the preliminaries of the deadbeat control technique. First, the state-space approach to deadbeat control has been given. The deadbeat controller is directly obtained by transforming the system to a controllable canonical form. Alternatively, the deadbeat controller synthesis can be implemented via the input-output representation of the closed-loop system.

The application of the deadbeat control technique for designing both the rotor and the grid side converters was presented next. The discrete-time current model of DFIM was derived from its continuous-time model in the grid oriented dq reference frame with the assumption that the rotor mechanical angular speed ω_m is constant during a sampling period. This assumption allows to consider the DFIM model as a linear time-invariant system within that sampling time. This also allows to overcome the difficulty that arises from the nonlinearity characteristics of DFIM provided that the value of the rotor mechanical speed is available for online measurement. The cross-coupling components in the rotor current equations are compensated for by adding feed-forward terms to the output of the current controller. Then the current deadbeat controller is designed for each sampling period whose gain is automatically adjusted as a function of the rotor angular speed ω_m. In this scenario, the rotor angular speed ω_m is treated as the so-called scheduling parameter. The performance of the controlled system under normal operating conditions is illustrated by simulation results.

Robustness of the control system against parameter changes as well as the impact of stator voltage dips on the robustness of the control system are also considered by means of some simulation results. However, these robustness tests are only performed for the variations of individual machine parameters and are based on an assumption that the machine parameters are all time-invariant uncertainties. Hence, these simulations do not reflect the real substance of the machine parameters since they are all slowly time-varying uncertainties. As a consequence, in Chapter 4, and 5, a different synthesis approach will be applied in order to get better performance of the controlled system. In addition, systematic robust stability analysis methods subject to rate-bounded linear time-varying parametric uncertainties will be presented in Chapter 6.

4

LPV CONTROLLER SYNTHESIS FOR AFFINELY PARAMETER-DEPENDENT SYSTEMS

4.1. INTRODUCTION

In the deadbeat controller design, as mentioned in Chapter 3, the cross coupling terms in the rotor equations that include the mechanical angular speed ω_m are eliminated by adding a feed-forward term to the output of the q-axis controller [19, 15]. The rotor mechanical angular speed ω_m is treated as an scheduling parameter that is used for these compensators. However, the performance of the feed-forward compensation depends highly on the accurate knowledge of the machine parameters. We have seen that the deadbeat response is not robust against variations of plant parameters since the nominal deadbeat characteristics could be destroyed by a small perturbation of the plant.

In order to improve the system's performance against changes in the machine parameters and exogenous inputs, an H_∞ control approach for induction generators is proposed in [98, 99] and for induction motor control in [100, 101, 102, 32]. Recently, the LPV current control approach, which takes the parameter variations into account directly in the control design, is applied for an induction motor in [103, 104]. In [104], the electrical angular rotor speed and the estimated magnetizing current are considered to be varying parameters. The control objective is to track references for the magnetizing current and the angular electrical rotor speed. A quasi-LPV approach is applied in order to design a stator current controller and a speed controller. In [103], the same method is employed for the inner current control loop, and LPV controller synthesis is extended to a discrete time setting.

In this work, the problem is to improve performance of the current control loop on

the rotor side converter with respect to machine parameter variations and in view of the stator voltage disturbance, as well as to systematically analyze the robustness of the controlled system. The designed controller has to be able to ensure performance in the wide operating range of the rotor speed. Here, the rotor mechanical angular speed ω_m is treated as a varying parameter of the machine which can be measured online. We adopt the framework of linear parameter-varying (LPV) controller synthesis. A self-scheduled controller is designed for the inner current control loop in order to ensure that the controlled system satisfies the desired objectives for all admissible trajectories of the rotor speed in the operating range. The details of the controller design will be given in Chapter 5.

In this chapter we develop the necessary background for LPV controller synthesis as given in the next chapter. The presentation in this chapter is mainly based-on [105] and, in particular, it is especially focused on affine parameter-dependent systems. Since the synthesis is based-on the linear matrix inequality (LMI) approach, the first part of this chapter introduces preliminaries of LMIs, including a brief exposition of the bounded real lemma as a powerful tool for turning H_∞-constraints into LMIs. A subsequent section is devoted to discussing the classical small-gain based robust control for LTI uncertainties. Finally, the polytopic approach for synthesizing gain-scheduled H_∞ controllers, which is similar to classical H_∞ control except that both the plant and the controller are LPV systems, is presented as the most important part of this chapter.

4.2. PRELIMINARIES

4.2.1. NOTATIONS

Let $\mathscr{L}_2$ denote the space of square-integrable signals defined on the interval $[0,\infty)$. A matrix A is called symmetric if it is real and satisfies $A = A^T$. The set of all $m \times m$ symmetric matrices will be denoted by $\mathbb{S}^m$. A transfer function $M(s)$ with a state-space realization (A,B,C,D) will be denoted by

$$M = \left[\begin{array}{c|c} A & B \\ \hline C & D \end{array}\right].$$

4.2.2. LINEAR MATRIX INEQUALITIES

A linear matrix inequality has the form

$$F(x) = F_0 + \sum_{i=1}^{n} x_i F_i \prec 0 \tag{4.1}$$

where $x = (x_1,...,x_n)$ denotes the vector of decision variables and $F_i \in \mathbb{S}^n$, $i = 0,1,...,n$. Note that the inequality (4.1) means that $F(x)$ is a negative definite matrix, i.e.

$$v^T F(x) v \prec 0 \;\; \forall v \in \mathbb{R}^n, \;\; v \neq 0. \tag{4.2}$$

Moreover observe that F is an affine function, which implies that the set of $x \in \mathbb{R}^n$ satisfying (4.1) is convex. Both the problem of verifying feasibility of (4.1) or of optimizing a linear functional over this constraint are called LMI problems which can be solved in polynomial time with commercial software [106]. Let us finally stress that typical LMIs solvers allow to handle a finite system of LMIs

$$F_1(x) \prec 0, \ldots, F_N(x) \prec 0$$

described with affine symmetric-valued mappings $F_1(x), \ldots, F_N(x)$.

4.2.3. THE H_∞-NORM

Consider a linear input-output system Σ that is described by

$$\Sigma : \begin{cases} \dot{x} &= Ax + Bw \\ z &= Cx + Dw \end{cases} \tag{4.3}$$

and whose transfer matrix is given by

$$G(s) = C(sI - A)^{-1}B + D.$$

If A is stable and if we choose the initial condition $x(0)$ to be zero, Σ defines a linear map $w \to z$ on $\mathscr{L}_2$ with a finite energy gain defined as

$$\sup_{w \in \mathscr{L}_2, w \neq 0} \frac{\|Gw\|_2}{\|w\|_2}.$$

It is well-known that the energy-gain of Σ coincides with the H_∞-norm of the corresponding transfer matrix G given by

$$\|G\|_\infty = \sup_{\omega \in \mathbb{R}} \overline{\sigma}(G(j\omega))$$

where $\overline{\sigma}(M)$ stands for the largest singular value of the complex matrix matrix M.

4.2.4. THE BOUNDED REAL LEMMA

It is not possible to explicitly compute $\|G\|_\infty$ in terms of the realization matrices. Instead, one can characterize stability of G and the validity of the inequality

$$\| G \|_\infty < \gamma \tag{4.4}$$

as an LMI in some auxiliary matrix K and γ, which is one version of the celebrated bounded real lemma. Indeed, it can be shown [107] that A is stable and that (4.4) holds if and only if

$$D^T D - \gamma^2 I \prec 0$$

and there exits some $K^T = K \succ 0$ such that the Riccati inequality

$$A^T K + KA + C^T C + (KB + C^T D)(\gamma^2 I - D^T D)^{-1}(B^T K + D^T C) \prec 0 \tag{4.5}$$

is satisfied. By the Schur lemma (4.5), these conditions are equivalent to following system of LMIs [108]

$$K \succ 0, \quad \begin{pmatrix} A^T K + KA + C^T C & KB + C^T D \\ B^T K + D^T C & D^T D - \gamma^2 I \end{pmatrix} \prec 0. \tag{4.6}$$

This result is referred to as the bounded real lemma.

Yet another application of the Schur lemma allows to rewrite these inequalities with $R = K/\gamma$ into the following form [105, 109]:

$$R \succ 0, \quad \begin{pmatrix} A^T R + RA & RB & C^T \\ B^T R & -\gamma I & D^T \\ C & D & -\gamma I \end{pmatrix} \prec 0. \tag{4.7}$$

In this thesis, LMIs (4.7) are also expressed as

$$R \succ 0, \quad \left(\begin{array}{cc} I & 0 \\ A & B \\ \hline 0 & I \\ C & D \end{array}\right)^T \left(\begin{array}{cc|cc} 0 & R & 0 & 0 \\ R & 0 & 0 & 0 \\ \hline 0 & 0 & -\gamma I & 0 \\ 0 & 0 & 0 & \frac{1}{\gamma} I \end{array}\right) \left(\begin{array}{cc} I & 0 \\ A & B \\ \hline 0 & I \\ C & D \end{array}\right) \prec 0. \tag{4.8}$$

Note that (4.7) are LMI constraints on R and γ. This allows to determine the infimal γ for which (4.4) is true, and hence in turn the value $\|G\|_\infty$, by minimizing γ over the constraint (4.7) which is a standard LMI problem. Let us now show how this procedure of analysis can be successfully generalized to synthesizing controllers.

4

4.3. H_∞ CONTROL OF LINEAR TIME-INVARIANT SYSTEMS

4.3.1. H_∞ PERFORMANCE

A standard setup for H_∞ control is presented in Fig. 4.1, where w represents the generalized disturbances, z the controlled variable, u the control input and y the measurement output, while P is a linear time-invariant system described as

$$\begin{aligned} \dot{x} &= Ax + B_p w + Bu \\ z &= C_p x + D_p w + Eu \\ y &= Cx + Fw \end{aligned}$$

The goal in H_∞ control is to find a stabilizing LTI controller K that minimizes the H_∞ norm of the closed-loop system

$$\left\| \mathscr{F}_l(P,K) \right\|_\infty \tag{4.9}$$

where $\mathscr{F}_l(P,K)$ is lower linear fractional transformation of P and K, which is nothing but the closed-loop transfer function $w \to z$ in Figure 4.1.

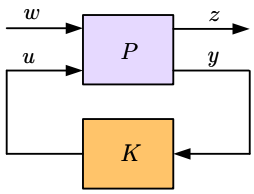

Figure 4.1: The interconnection of the system

In the literature, P is called a generalized plant if we can find at least one controller K that stabilizes P [110].

Minimization of (4.9) flattens the closed-loop responses in the frequency domain. In order to achieve certain desired shapes of the closed-loop transfer functions, such as dictated by requirements on bandwidth, weights are introduced. Instead of minimizing the H_∞ norm of (4.9) we rather consider minimizing the H_∞ norm of

$$\left\| \mathscr{F}_l(\widetilde{P}, K) \right\|_\infty \tag{4.10}$$

where $\mathscr{F}_l(\widetilde{P}, K) = W_z \mathscr{F}_l(P, K) W_w$ is the closed-loop transfer function $\widetilde{w} \to \widetilde{z}$ in Fig. 4.2, W_z and W_w are real-rational proper weighting functions with suitable band-pass characteristics.

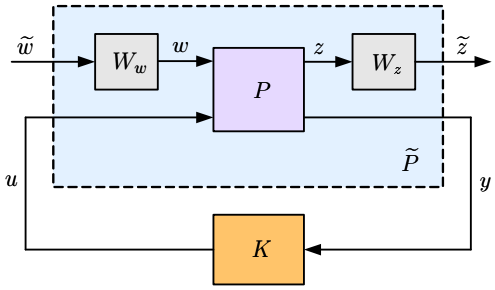

Figure 4.2: The weighted interconnection of the system

4.3.2. SUB-OPTIMAL H_∞ CONTROL

Let us now consider the following generalized plant P where weights are incorporated already:

$$\begin{pmatrix} \dot{x} \\ \hline z \\ y \end{pmatrix} = \left(\begin{array}{c|cc} A & B_p & B \\ \hline C_p & D_p & E \\ C & F & 0 \end{array}\right) \begin{pmatrix} x \\ \hline w \\ u \end{pmatrix}. \tag{4.11}$$

If the linear time-invariant controller K is expressed as

$$\left(\begin{array}{c|c} \dot{x}_c \\ \hline u \end{array}\right) = \left(\begin{array}{c|c} A_c & B_c \\ \hline C_c & D_c \end{array}\right)\left(\begin{array}{c|c} x_c \\ \hline y \end{array}\right), \tag{4.12}$$

the closed-loop system $\mathscr{F}_l(P,K)$ admits the following state-space description:

$$\left(\begin{array}{c|c} \dot{\xi} \\ \hline z \end{array}\right) = \left(\begin{array}{c|c} \mathscr{A} & \mathscr{B} \\ \hline \mathscr{C} & \mathscr{D} \end{array}\right)\left(\begin{array}{c|c} \xi \\ \hline w \end{array}\right) \tag{4.13}$$

where

$$\left[\begin{array}{c|c} \mathscr{A} & \mathscr{B} \\ \hline \mathscr{C} & \mathscr{D} \end{array}\right] = \left[\begin{array}{cc|c} A+BD_cC & BC_c & B_p+BD_cF \\ B_cC & A_c & B_cF \\ \hline C_p+ED_c & EC_c & D_p+ED_cF \end{array}\right]. \tag{4.14}$$

The H_∞ control problem is to find an LTI controller which renders $\mathscr{A}$ stable and such that

$$\left\| \left[\begin{array}{c|c} \mathscr{A} & \mathscr{B} \\ \hline \mathscr{C} & \mathscr{D} \end{array}\right] \right\|_\infty < \gamma \tag{4.15}$$

holds true [111], where $\gamma > 0$ is a given number that specifies the performance level. This is the so-called sub-optimal H_∞ problem.

4

4.3.3. H_∞ CONTROLLER SYNTHESIS

Using the bounded real lemma for (4.15), the matrix $\mathscr{A}$ is stable and (4.15) is satisfied if and only if the LMI

$$\left(\begin{array}{cc} I & 0 \\ \mathscr{A} & \mathscr{B} \\ \hline 0 & I \\ \mathscr{C} & \mathscr{D} \end{array}\right)^T \left(\begin{array}{cc|cc} 0 & \mathscr{X} & 0 & 0 \\ \mathscr{X} & 0 & 0 & 0 \\ \hline 0 & 0 & -\gamma I & 0 \\ 0 & 0 & 0 & \frac{1}{\gamma} I \end{array}\right) \left(\begin{array}{cc} I & 0 \\ \mathscr{A} & \mathscr{B} \\ \hline 0 & I \\ \mathscr{C} & \mathscr{D} \end{array}\right) \prec 0 \tag{4.16}$$

holds for some $\mathscr{X} \succ 0$. Unfortunately this inequality is not affine in $\mathscr{X}$ and in the controller parameters which are appearing in the description of $\mathscr{A}, \mathscr{B}, \mathscr{C}, \mathscr{D}$. However, a by now standard procedure [105, 109, 112, 113] allows to eliminate the controller parameters from these conditions, which in turn leads to convex constraints in the matrices X and Y that appear in the partitioning of

$$\mathscr{X} = \begin{pmatrix} X & U \\ U^T & * \end{pmatrix} \quad \text{and} \quad \mathscr{X}^{-1} = \begin{pmatrix} Y & V \\ V^T & * \end{pmatrix} \tag{4.17}$$

according to that of $\mathscr{A}$ in (4.14). One then arrives at the following synthesis LMIs for H_∞-design [114]:

$$\begin{pmatrix} Y & I \\ I & X \end{pmatrix} \succ 0 \tag{4.18}$$

$$\Phi_X^T \begin{pmatrix} XA + A^T X & XB_p & C_p^T \\ B_p^T X & -\gamma I & D_p^T \\ C_p & D_p & -\gamma I \end{pmatrix} \Phi_X \prec 0 \tag{4.19}$$

$$\Phi_Y^T \begin{pmatrix} AY + YA^T & B_p & YC_p^T \\ B_p^T & -\gamma I & D_p^T \\ C_p Y & D_p & -\gamma I \end{pmatrix} \Phi_Y \prec 0 \tag{4.20}$$

where Φ_X and Φ_Y are basis matrices for the subspaces

$$\ker\begin{pmatrix} C & F & 0 \end{pmatrix} \text{ and } \ker\begin{pmatrix} B^T & 0 & E^T \end{pmatrix} \tag{4.21}$$

respectively.

Note that these inequalities are defined by open-loop system parameters only, and that they depend affinely on the design variables X and Y. Hence we can directly minimize γ over these LMIs in order to compute the best possible level γ with (4.15) that can be achieved by a stabilizing controller.

After having obtained X and Y that satisfy (4.33)-(4.35) for some level γ, the controller parameters can be reconstructed by using the projection lemma [105]. This procedure for H_∞-synthesis is implemented in the robust control toolbox [106].

4.3.4. MIXED SENSITIVITY H_∞ APPROACH

CLOSED-LOOP TRANSFER FUNCTIONS

Fig. 4.3a shows a simple feedback control system. This interconnection can be recast into a standard setup for H_∞ control as depicted in Fig. 4.3b. For this control configuration, engineers are usually interested in some specific transfer functions. In particular, $S = (I + GK)^{-1}$ is the sensitivity function which describes the influence of the external disturbance w to the tracking error y. $T = (I + GK)^{-1}GK$ is the complementary sensitivity function which describes the influence of the reference signal w to the system output z. Finally, KS is the transfer function from w to the control input u that indicates control activity [115].

MIXED SENSITIVITY H_∞ PERFORMANCE

In general, performance of the closed-loop system that is specified by H_∞ norm of the channel $w \to z$ in (4.9) can be formulated as a multi-objective problem (see Fig. 4.4).

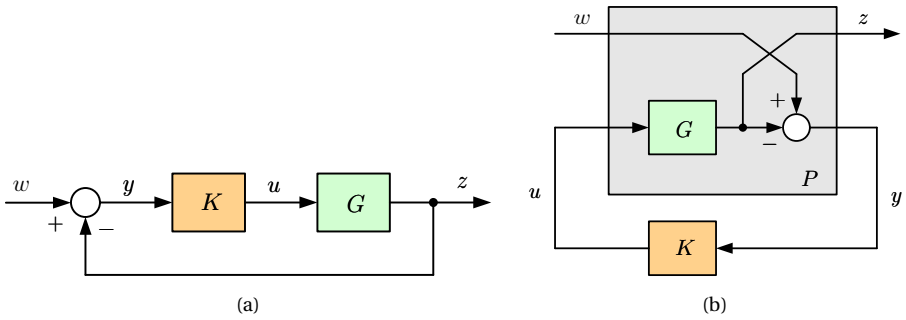

Figure 4.3: General feedback control configuration

This leads to the minimization of

$$\left\| \begin{matrix} (I+GK)^{-1} \\ K(I+GK)^{-1} \\ (I+GK)^{-1}GK \end{matrix} \right\|_\infty \quad \text{or} \quad \left\| \begin{matrix} S \\ KS \\ T \end{matrix} \right\|_\infty . \tag{4.22}$$

The multi-variable loop shaping with various specifications (4.22) is the so-called the mixed sensitivity H_∞ design approach.

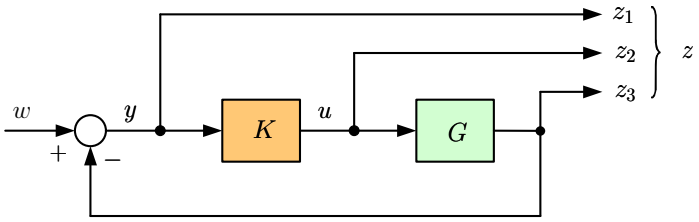

Figure 4.4: Mixed sensitivity H_∞ control

It is well-known in the literature that the transfer functions S, T, and KS need to be small in magnitude in order to achieve good command tracking and robust stability. However, the well-known constraint $S+T=I$ reveals that these requirements can not be achieved simultaneously over the whole frequency range. However, the use of frequency filters or weighting functions opens up the possibility to minimize the magnitudes of S, T, and KS over different frequency ranges [32]. Hence, in practice, instead of minimizing (4.22) one rather determines a stabilizing LTI controller K that minimizes the cost function

$$\left\| \begin{pmatrix} W_S S \\ W_P KS \\ W_T T \end{pmatrix} \right\|_\infty \tag{4.23}$$

where W_S, W_P, W_T are suitably chosen weighting functions (Fig. 4.5).

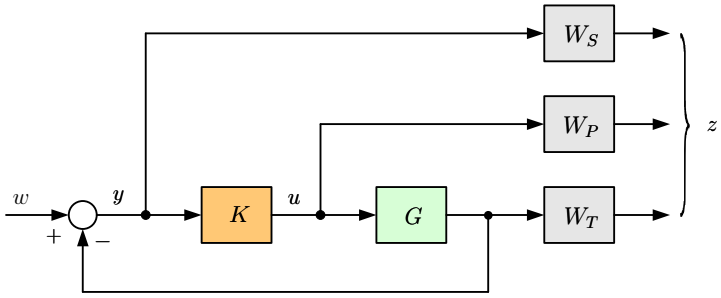

Figure 4.5: Mixed sensitivity H_∞ control

4.4. GAIN-SCHEDULED H_∞ CONTROL FOR AFFINELY PARAMETER-DEPENDENT SYSTEMS

H_∞ control as presented above provides a very powerful tool for controller synthesis of linear time-invariant systems in the presence of uncertainty. However, the design techniques become more complicated if considering uncertain linear time-varying systems. In this section we will present an extension of the sketched synthesis techniques for a class of systems whose state-space matrices are functions of time-varying parameters. These systems are referred to as Linear Parameter Varying (LPV) systems.

At the expense of conservativeness and possibly poor performance, the varying parameters can be treated as uncertainties and a single robust parameter-independent LTI controller can be designed for the entire operating range [111]. On the other hand, if the parameter value is measurable online, one might instead try to design a parameter-dependent controller in order to improve performance. The purpose of this section is to provide a brief overview of the corresponding so-called LPV-design procedure.

4.4.1. LINEAR PARAMETER VARYING SYSTEMS

Let us consider an LPV system that is described as

$$\left(\begin{array}{c} \dot{x} \\ \hline z_p \\ y \end{array}\right) = \left(\begin{array}{c|cc} A(\delta(t)) & B_p(\delta(t)) & B(\delta(t)) \\ \hline C_p(\delta(t)) & D_p(\delta(t)) & E(\delta(t)) \\ C(\delta(t)) & F(\delta(t)) & 0 \end{array}\right) \left(\begin{array}{c} x \\ \hline w_p \\ u \end{array}\right) \tag{4.24}$$

where $\delta(\cdot)$ varies in the so-called admissible set of parameter curves, the set of all continuous

$$\delta : [0,\infty) \to \mathbb{R}^m \text{ with } \delta(t) \in \boldsymbol{\delta} \text{ for all } t \geq 0 \tag{4.25}$$

where $A(\cdot)$, $B_p(\cdot)$, $B(\cdot)$, $C_p(\cdot)$, $D_p(\cdot)$, $E(\cdot)$, $C(\cdot)$, $F(\cdot)$ are affine functions of δ and $\boldsymbol{\delta}$ is a compact subset of $\mathbb{R}^m$.

Let us consider an LPV controller that is defined similarly as

$$\begin{pmatrix} \dot{x}_c(t) \\ u(t) \end{pmatrix} = \begin{pmatrix} A_c(\delta(t)) & B_c(\delta(t)) \\ C_c(\delta(t)) & D_c(\delta(t)) \end{pmatrix} \begin{pmatrix} x_c(t) \\ y(t) \end{pmatrix}. \tag{4.26}$$

The closed-loop system of (4.24) and (4.26) then admits the description

$$\begin{pmatrix} \dot{\xi}(t) \\ z_p(t) \end{pmatrix} = \begin{pmatrix} \mathscr{A}(\delta(t)) & \mathscr{B}(\delta(t)) \\ \mathscr{C}(\delta(t)) & \mathscr{D}(\delta(t)) \end{pmatrix} \begin{pmatrix} \xi(t) \\ w_p(t) \end{pmatrix} \tag{4.27}$$

where

$$\left(\begin{array}{c|c} \mathscr{A}(\delta) & \mathscr{B}(\delta) \\ \hline \mathscr{C}(\delta) & \mathscr{D}(\delta) \end{array}\right) = \left(\begin{array}{cc|c} A(\delta)+B(\delta)D_c(\delta)C(\delta) & B(\delta)C_c(\delta) & B_p(\delta)+B(\delta)D_c(\delta)F(\delta) \\ B_c(\delta)C(\delta) & A_c(\delta) & B_c(\delta)F(\delta) \\ \hline C_p(\delta)+E(\delta)D_c(\delta)C(\delta) & E(\delta)C_c(\delta) & D_p(\delta)+E(\delta)D_c(\delta)F(\delta) \end{array}\right). \tag{4.28}$$

The controlled system (4.27) is (internally and uniformly) exponentially stable [112] if there exists constants $\beta > 0$ and $\alpha > 0$ such that for all unforced system trajectory $\xi(.)$ (obtained with $w_p(.) = 0$) and for all admissible parameter curves the following property holds:

$$\left\|\xi(t)\right\| \leq \beta e^{-\alpha(t-t_0)} \left\|\xi(t_0)\right\| \text{ for all } 0 \leq t_0 \leq t.$$

4

For each parameter-trajectory the closed-loop system is time-varying. Therefore, we replace the H_∞-norm by the $\mathscr{L}_2$-gain as a performance criterion. Since we are interested in guaranteeing a certain level of performance over all admissible parameter trajectories $\delta(.)$, we actually consider the criterion

$$\sup_{\delta(.) \text{ admissible},\ w_p \in \mathscr{L}_2\{0\}} \frac{\left\|z_p\right\|_2}{\left\|w_p\right\|_2} < \gamma. \tag{4.29}$$

The resulting optimization problem is to search for an LPV controller that exponentially stabilizes the closed-loop system (4.27) and which renders (4.29) satisfied (for a minimal γ).

4.4.2. THE POLYTOPIC APPROACH TO LPV CONTROLLER SYNTHESIS

Suppose that the matrices in (4.24) are affine functions of the parameter vector that varies in the polytope $\boldsymbol{\delta}$ with vertices $\delta^1, ..., \delta^k$, that is

$$\delta(t) \in \boldsymbol{\delta} = \text{Co}\left\{\delta^1, ..., \delta^k\right\} \triangleq \left\{ \sum_{j=1}^{k} \lambda_j \delta^j, \quad \lambda_j \geq 0, \quad \sum_{j=1}^{k} \lambda_j = 1 \right\}. \tag{4.30}$$

The goal is to determine an LPV controller K_{lpv} as described in (4.26) with affine functions $A_c(\delta)$, $B_c(\delta)$, $C_c(\delta)$, $D_c(\delta)$ such that the closed-loop system (4.27) is exponentially stable and the $\mathscr{L}_2$-gain of $w_p \to z_p$ is bounded as in (4.29).

A characterization of robust stability and performance for the closed-loop system (4.27) is provided by the following theorem.

Theorem 4.4.1 *If there exists a constant matrix $\mathscr{X} \succ 0$ such that*

$$\left(\begin{array}{cc} I & 0 \\ \mathscr{A}(\delta) & \mathscr{B}(\delta) \\ \hline 0 & I \\ \mathscr{C}(\delta) & \mathscr{D}(\delta) \end{array}\right)^T \left(\begin{array}{cc|cc} 0 & \mathscr{X} & 0 & 0 \\ \mathscr{X} & 0 & 0 & 0 \\ \hline 0 & 0 & -\gamma I & 0 \\ 0 & 0 & 0 & \frac{1}{\gamma} I \end{array}\right) \left(\begin{array}{cc} I & 0 \\ \mathscr{A}(\delta) & \mathscr{B}(\delta) \\ \hline 0 & I \\ \mathscr{C}(\delta) & \mathscr{D}(\delta) \end{array}\right) \prec 0 \text{ for all } \delta \in \boldsymbol{\delta} \tag{4.31}$$

then the system (4.27) is exponentially stable and the $\mathscr{L}_2$ gain from w_p to z_p is bounded by γ. □

Proof: See [105].

Since the system (4.24) is affinely parameter-dependent on $\delta \in \boldsymbol{\delta}$, the state-space matrices of (4.24) range in the polytope of generating system matrices defined as follows [116]:

$$\begin{aligned} \begin{pmatrix} A(\delta(t)) & B_p(\delta(t)) & B_(\delta(t)) \\ C_p(\delta(t)) & D_p(\delta(t)) & E(\delta(t)) \\ C(\delta(t)) & F(\delta(t)) & 0 \end{pmatrix} \in \text{Co} \Bigg\{ & \begin{pmatrix} A^j & B_p^j & B^j \\ C_p^j & D_p^j & E^j \\ C^j & F^j & 0 \end{pmatrix} \\ \triangleq & \begin{pmatrix} A(\delta^j) & B_p(\delta^j) & B(\delta^j) \\ C_p(\delta^j) & D_p(\delta^j) & E(\delta^j) \\ C(\delta^j) & F(\delta^j) & 0 \end{pmatrix}, j = 1, ..., k \Bigg\}. \end{aligned}$$

In view of (4.28) let us make the following important observation: If

$$\begin{pmatrix} B \\ E \end{pmatrix} \text{ and } \begin{pmatrix} C & F \end{pmatrix} \text{ are parameter independent,}$$

the describing matrices for the closed-loop system (4.27) are also affine in the parameter δ. On one hand, this implies for all admissible parameter curves that

$$\begin{pmatrix} \mathscr{A}(\delta(t)) & \mathscr{B}(\delta(t)) \\ \mathscr{C}(\delta(t)) & \mathscr{D}(\delta(t)) \end{pmatrix} \in \text{Co} \left\{ \begin{pmatrix} \mathscr{A}^j & \mathscr{B}^j \\ \mathscr{C}^j & \mathscr{D}^j \end{pmatrix} \triangleq \begin{pmatrix} \mathscr{A}(\delta^j) & \mathscr{B}(\delta^j) \\ \mathscr{C}(\delta^j) & \mathscr{D}(\delta^j) \end{pmatrix}, \ j = 1, ..., k \right\}.$$

On the other hand, we infer for the analysis inequalities (4.31) that one can replace the search over the polytope $\boldsymbol{\delta}$ without loss of generality by the search over the extreme

points $\delta^1,...,\delta^k$ of this set. Consequently, condition (4.31) can be reduced to a finite set of LMIs since it is equivalent to

$$\left(\begin{array}{cc} I & 0 \\ \mathscr{A}(\delta^j) & \mathscr{B}(\delta^j) \\ \hline 0 & I \\ \mathscr{C}(\delta^j) & \mathscr{D}(\delta^j) \end{array}\right)^T \left(\begin{array}{cc|cc} 0 & \mathscr{X} & 0 & 0 \\ \mathscr{X} & 0 & 0 & 0 \\ \hline 0 & 0 & -\gamma I & 0 \\ 0 & 0 & 0 & \frac{1}{\gamma} I \end{array}\right) \left(\begin{array}{cc} I & 0 \\ \mathscr{A}(\delta^j) & \mathscr{B}(\delta^j) \\ \hline 0 & I \\ \mathscr{C}(\delta^j) & \mathscr{D}(\delta^j) \end{array}\right) \prec 0 \tag{4.32}$$

for all $j = 1,..,k$.

4.4.3. GAIN-SCHEDULED CONTROLLER CONSTRUCTION

After these preparations it is now possible to eliminate the controller parameters in (4.32). This leads to the following LMI conditions that guarantee the existence of a polytopic LPV controller [116, 117, 118]:

$$\begin{pmatrix} Y & I \\ I & X \end{pmatrix} \succ 0 \tag{4.33}$$

$$\Phi_x^T \begin{pmatrix} XA(\delta^j) + A(\delta^j)^T X & XB_p(\delta^j) & C_p(\delta^j)^T \\ B_p(\delta^j)^T X & -\gamma I & D_p(\delta^j)^T \\ C_p(\delta^j) & D_p(\delta^j) & -\gamma I \end{pmatrix} \Phi_x \prec 0 \tag{4.34}$$

$$\Phi_y^T \begin{pmatrix} A(\delta^j)Y + YA(\delta^j)^T & B_p(\delta^j) & YC_p(\delta^j)^T \\ B_p(\delta^j)^T & -\gamma I & D_p(\delta^j)^T \\ C_p(\delta^j)Y & D_p(\delta^j) & -\gamma I \end{pmatrix} \Phi_y \prec 0 \tag{4.35}$$

$$j = 1,...,k$$

where Φ_x and Φ_y are again basis matrices of the subspaces (4.21).

After obtaining X and Y over the constraint LMIs (4.33)-(4.35), one can reconstruct $\mathscr{X}$ and the controller parameters at each vertex δ^j with the help of the projection lemma [105]. Then a vertex controller K_j is any solution that satisfies (4.32) for the corresponding index j.

Finally, the actual LPV controller is implemented as follows: At time t one needs to determine coefficients $\lambda_1(t),...,\lambda_k(t)$ which represent $\delta(t)$ according to (4.30), and one uses

$$K_{lpv}(t) \triangleq \sum_{j=1}^{k} \lambda_j(t) K_j = \sum_{j=1}^{k} \lambda_j(t) \begin{pmatrix} A_{kj} & B_{kj} \\ C_{kj} & D_{kj} \end{pmatrix} \tag{4.36}$$

as the system matrix for simulation. Let us finally stress again this technique for designing LPV controllers is implemented in the robust control toolbox [106].

4.5. SUMMARY

We have presented the well-known gain-scheduled H_∞ controller synthesis procedure for affinely parameter-dependent systems and controllers. The goal of the gain-scheduled H_∞ controller design is to guarantee exponentially stability and an a priori given bound on the $\mathscr{L}_2$-gain of the performance channel for the closed-loop system and for all admissible parameter trajectories. This so-called polytopic synthesis procedure leads to controllers that are easy to implement for simple polytopic parameter regions, such as parameter boxes. However, we note that determining coefficients $\lambda_1(t), ..., \lambda_k(t)$ for complicated set $\boldsymbol{\delta}$ might not be simple since it relates to solving a linear programming problem according to (4.30). The described procedure will be directly applied in order to design the rotor current controller of the DFIM in the next chapter.

5

GAIN-SCHEDULING DESIGN FOR DOUBLY-FED INDUCTION MACHINES

5.1. INTRODUCTION

This chapter is devoted to gain-scheduling controller design for a doubly-fed induction machine based on the synthesis technique presented in Chapter 4. As an introduction to the LPV-design, a mixed loop shaping H_∞-design for the rotor current control loop at fixed frozen values of the mechanical angular speed is presented in the first part of the chapter. Then the self-scheduled linear parameter varying current controller is designed in the continuous-time domain where the mechanical angular speed is considered as a parameter that is online measurable. The design goal is to guarantee the required performance specifications over the operating range of the rotor speed. Performance and robustness of the controlled system with an LPV-current controller are demonstrated via some simulation results.

In the next part of the chapter, the continuous-time LPV controller is sampled to obtain a discrete-time controller in order to be implemented in a real digital control system. The chapter is concluded with a time-domain analysis of the closed-loop system with the discretized LPV-controller.

5.2. THE SYSTEM REPRESENTATION

In this thesis, the mechanical angular speed ω_m in (2.15) is considered as a time-varying parameter. This particular choice is motivated by the fact that ω_m, which causes the system to be nonlinear, can be measured online. The value of the rotor angular speed

ω_m varies by $\pm p_\omega$% around the synchronous speed ω_s, i.e.

$$\omega_m \in [\omega_{min}, \omega_{max}] = [(1-p_\omega)\omega_s, (1+p_\omega)\omega_s]. \tag{5.1}$$

An alternative way to represent the variation of the rotor angular speed is to express ω_m as an uncertainty element

$$\omega_m = \omega_{nom} + \omega_{var} = \omega_{nom}(1 + p_\omega \delta_\omega), \tag{5.2}$$

where ω_{nom} is the nominal speed, ω_{var} is the variation of the rotor angular speed ω_m around its nominal value, and δ_ω is the normalizing factor that maps the uncertain element into a normalized uncertain element such that $-1 \le \delta_\omega \le 1$.

In the normal operation of the DFIM, the nominal speed ω_{nom} is close to the synchronous speed ω_s. Hence, if we denote the ratio of the nominal speed and the synchronous speed by ζ, i.e.

$$\omega_{nom} = \zeta \omega_s,$$

we can write

$$\omega_{var} = \zeta \omega_s p_\omega \delta_\omega,$$

and

$$\delta_w = \frac{\omega_m - \zeta\omega_s}{\zeta\omega_s p_w}. \tag{5.3}$$

Here, ζ is a scaling factor that allows to present the variation of the rotor speed ω_m around the synchronous speed ω_s but the synchronous speed is not in the middle of the range of the rotor variation as in (5.1). Therefore, the deviation of the rotor speed by $\pm p_\omega$% from the nominal speed $\omega_{nom} = \zeta\omega_s$ can be expressed as

$$\omega_m \in [(1-p_\omega)\zeta\omega_s, (1+p_\omega)\zeta\omega_s]. \tag{5.4}$$

The representation of ω_m in (5.4) provides a flexible choice of the rotor speed range in the controller design for the DFIM. As a result, the matrices in (2.15) and (2.16) can now be rewritten as follows:

$$A_r(\omega_m) \quad = \quad A_{rs} + \delta_\omega A_{r\omega}$$

where

$$
\begin{aligned}
A_{rs} &= \begin{pmatrix} -\left(\frac{a+1}{T_r}+\frac{a}{T_s}\right) & \omega_s(1-\zeta) & \frac{a}{L_m T_s} & -\frac{a\zeta\omega_s}{L_m} \\ \omega_s(\zeta-1) & -\left(\frac{a+1}{T_r}+\frac{a}{T_s}\right) & \frac{a\zeta\omega_s}{L_m} & \frac{a}{L_m T_s} \\ \frac{L_m}{T_s} & 0 & -\frac{1}{T_s} & \omega_s \\ 0 & \frac{L_m}{T_s} & -\omega_s & -\frac{1}{T_s} \end{pmatrix}, \\
A_{r\omega} &= \begin{pmatrix} 0 & -\omega_s p_\omega & 0 & -\frac{a\omega_s p_\omega}{L_m} \\ \omega_s p_\omega & 0 & \frac{a\omega_s p_\omega}{L_m} & 0 \\ 0 & 0 & 0 & 0 \\ 0 & 0 & 0 & 0 \end{pmatrix},
\end{aligned} \tag{5.5}
$$

and

$$
B_u = B_{rs} + \delta_\omega B_{r\omega} \tag{5.6}
$$

where

$$
B_{rs} = \begin{pmatrix} -\frac{a}{L_m} & 0 & \frac{a+1}{L_r} & 0 \\ 0 & -\frac{a}{L_m} & 0 & \frac{a+1}{L_r} \\ 1 & 0 & 0 & 0 \\ 0 & 1 & 0 & 0 \end{pmatrix}, \tag{5.7}
$$

$$
B_{r\omega} = 0. \tag{5.8}
$$

Equation (2.15) now becomes (see also equation (3.21))

$$
\begin{aligned}
\dot{x}_r &= (A_{rs}+\delta_\omega A_{r\omega})x_r + (B_{rs}+\delta_\omega B_{r\omega})u_r \\
&= \begin{pmatrix} A_{rs} & B_{rs} \end{pmatrix}\begin{pmatrix} x_r \\ u_r \end{pmatrix} + \delta_\omega \begin{pmatrix} A_{r\omega} & B_{r\omega} \end{pmatrix}\begin{pmatrix} x_r \\ u_r \end{pmatrix} \\
&= \begin{pmatrix} A_{rs} & B_{rs} \end{pmatrix}\begin{pmatrix} x_r \\ u_r \end{pmatrix} + \tilde{w}_\omega
\end{aligned} \tag{5.9}
$$

where

$$
\tilde{w}_\omega = \delta_\omega \begin{pmatrix} A_{r\omega} & B_{r\omega} \end{pmatrix}\begin{pmatrix} x_r \\ u_r \end{pmatrix} = \delta_\omega \tilde{z}_\omega \tag{5.10}
$$

$$
\tilde{z}_\omega = \begin{pmatrix} A_{r\omega} & B_{r\omega} \end{pmatrix}\begin{pmatrix} x_r \\ u_r \end{pmatrix}. \tag{5.11}
$$

In (5.10) and (5.11), $\widetilde{w}_\omega$ and $\widetilde{z}_\omega$ represent the input and output signals of the disturbance channel corresponding to the time-varying parameter ω_m.

Equations (5.9), (5.10), and (5.11) in combination with equation (2.16) can now be expressed as

$$\begin{pmatrix} \dot{x}_r \\ \widetilde{z}_\omega \\ y_r \end{pmatrix} = \begin{pmatrix} A_{rs} & I_4 & B_{rs} \\ A_{r\omega} & Z_4 & B_{r\omega} \\ C_r & D_{rw} & D_{rr} \end{pmatrix} \begin{pmatrix} x_r \\ \widetilde{w}_\omega \\ u_r \end{pmatrix}, \tag{5.12}$$

$$\widetilde{w}_\omega = \widetilde{\Delta}_\omega \widetilde{z}_\omega, \quad \widetilde{\Delta}_\omega = \delta_\omega I_4 \tag{5.13}$$

where I_4 is an 4×4 unity matrix, Z_4 is an 4×4 zero matrix, $D_{rw} = D_{rr} = 0$. $\widetilde{\Delta}_\omega$ is also called the perturbation block.

Since the two last rows of the matrices $A_{r\omega}$ and $B_{r\omega}$ are zero, let $\widetilde{w}_\omega = \begin{pmatrix} w_\omega \\ * \end{pmatrix}$, $\widetilde{z}_\omega = \begin{pmatrix} z_\omega \\ * \end{pmatrix}$, and $\widetilde{\Delta}_\omega = \begin{pmatrix} \Delta_\omega & 0 \\ 0 & * \end{pmatrix}$ we can write

$$w_\omega = \Delta_\omega z_\omega \tag{5.14}$$

where w_ω, and z_ω are two 2×1 vectors, Δ_ω is a 2×2 matrix.

Equations (5.12) and (5.13) can be easily simplified as

$$\begin{pmatrix} \dot{x}_r \\ z_\omega \\ y_r \end{pmatrix} = \begin{pmatrix} A_{rs} & B_{ww} & B_{rs} \\ C_{ws} & D_{ww} & D_{wr} \\ C_r & D_{rw} & D_{rr} \end{pmatrix} \begin{pmatrix} x_r \\ w_\omega \\ u_r \end{pmatrix} \tag{5.15}$$

where

$$B_{ww} = \begin{pmatrix} 1 & 0 & 0 & 0 \\ 0 & 1 & 0 & 0 \end{pmatrix}^T, \quad C_{ws} = \begin{pmatrix} 0 & -\omega_s p_\omega & 0 & -a\omega_s p_\omega / L_m \\ \omega_s p_\omega & 0 & a\omega_s p_\omega / L_m & 0 \end{pmatrix},$$

$$D_{ww} = D_{wr} = 0.$$

Let G_{rc} be the transfer function with the state-space realization (5.15), i.e.

$$G_{rc} \triangleq \left[\begin{array}{c|c} A_{rc} & B_{rc} \\ \hline C_{rc} & D_{rc} \end{array}\right] = \left[\begin{array}{c|cc} A_{rs} & B_{ww} & B_{rs} \\ \hline C_{ws} & D_{ww} & D_{wr} \\ C_r & D_{rw} & D_{rr} \end{array}\right]. \tag{5.16}$$

The system can then be generally described by

$$\begin{pmatrix} z_\omega \\ y_r \end{pmatrix} = G_{rc} \begin{pmatrix} w_\omega \\ v_s \\ v_r \end{pmatrix} = \begin{pmatrix} G_{zw} & G_{zs} & G_{zr} \\ G_{rw} & G_{rs} & G_{rr} \end{pmatrix} \begin{pmatrix} w_\omega \\ v_s \\ v_r \end{pmatrix}, \tag{5.17}$$

where G_{rr} is the transfer function mapping v_r to y_r, and $G_{rn} = \begin{pmatrix} G_{rs} & G_{rr} \end{pmatrix}$ is the transfer function from $\begin{pmatrix} v_s \\ v_r \end{pmatrix}$ to y_r.

The linear fractional transformation (LFT) representation of the system is depicted as shown in Fig. 5.1.

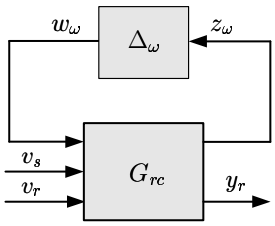

Figure 5.1: LFT representation of the system

5.3. H_∞ CONTROL OF THE LPV SYSTEM

In this section we start with H_∞-synthesis for the above mentioned frozen values of the rotor speed ω_m. Then the performance of the LTI controller designed for a fixed value of ω_m is evaluated with other constant values of ω_m as well as with a fast variation of the rotor speed along the parameter range. These design results give a motivation for the synthesis of self-scheduled current controller in the next section.

5.3.1. THE CONTROL CONFIGURATION

With the LFT representation of the plant as shown in Fig. 5.1 we can now derive a standard control structure for the synthesis of an H_∞-controller as depicted in Fig. 5.2. Here, G_{rc} is the LTI part of the plant as given in (5.16), Δ_ω is the uncertainty block as given in (5.14), K_{rc} is the H_∞ controller that is to be designed.

In this configuration, $i_r^{ref} = \begin{pmatrix} i_{rd}^{ref} & i_{rq}^{ref} \end{pmatrix}^T$ is the reference input, $v_r = \begin{pmatrix} v_{rd} & v_{rq} \end{pmatrix}^T$ is the controller output, $y_r = \begin{pmatrix} i_{rd} & i_{rq} \end{pmatrix}^T$ is the controlled output, and $e_r = \begin{pmatrix} e_{rcd} & e_{rcq} \end{pmatrix}^T = \begin{pmatrix} i_{rd}^{ref} - i_{rd} & i_{rq}^{ref} - i_{rq} \end{pmatrix}^T$ is the controller input which is equal to the tracking error. In this case, the transfer function from the reference input i_r^{ref} to the tracking error e_r will be $S_{rc} = (I + G_{rr}K_{rc})^{-1}$. The transfer function from reference inputs to controlled outputs is denoted by T_{rc}, i.e.

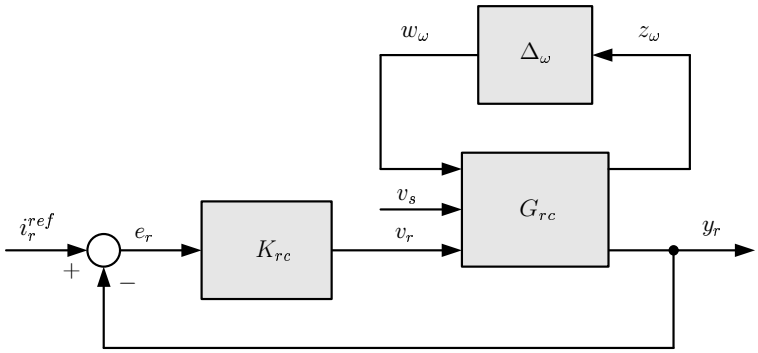

Figure 5.2: Structure of the closed-loop system in H_∞ design

$$\begin{pmatrix} i_{rd} \\ i_{rq} \end{pmatrix} = T_{rc} \begin{pmatrix} i_{rd}^{ref} \\ i_{rq}^{ref} \end{pmatrix} = \begin{pmatrix} T_{rc11} & T_{rc12} \\ T_{rc21} & T_{rc22} \end{pmatrix} \begin{pmatrix} i_{rd}^{ref} \\ i_{rq}^{ref} \end{pmatrix}. \tag{5.18}$$

5.3.2. H_∞ LOOP SHAPING DESIGN

The interconnection of the system used for the controller synthesis is shown in Fig. 5.3. The external control input w_{rc} consists of stator voltages and reference rotor currents $w_{rc} = \begin{pmatrix} v_{sd} & v_{sq} & i_{rd}^{ref} & i_{rq}^{ref} \end{pmatrix}^T$. The controller output is $v_r = \begin{pmatrix} v_{rd} & v_{rq} \end{pmatrix}^T$. The controller input or tracking error is $e_r = \begin{pmatrix} e_{rcd} & e_{rcq} \end{pmatrix}^T = \begin{pmatrix} i_{rd}^{ref} - i_{rd} & i_{rq}^{ref} - i_{rq} \end{pmatrix}^T$. The controlled variable is $z_{rc} = \begin{pmatrix} z_{rtd} & z_{rtq} & z_{rsd} & z_{rsq} \end{pmatrix}^T$. Note that the components v_{sd} and v_{sq} of the external control inputs are considered as disturbances and their influences on the controlled outputs must be reduced as much as possible.

The weighting function $W_{rs} = \begin{pmatrix} W_{rsd} & 0 \\ 0 & W_{rsq} \end{pmatrix}$ is used to shape the transfer function from the external control input w_{rc} to the tracking error e_r. W_{rs} is kept large over the low frequency range for tracking. The weighting function $W_{rt} = \begin{pmatrix} W_{rtd} & 0 \\ 0 & W_{rtq} \end{pmatrix}$ is used to shape the transfer function from the external control input w_{rc} to the controlled output y_r. The selection of the weighting function W_{rt} is not only intended to keep the closed loop bandwidth at a desired value, but also to reject the effects of the components v_{sd} and v_{sq} on the controlled outputs as discussed above. Note that a large bandwidth corresponds to a faster rise time but the system is more sensitive to noise and to parameter variations [115].

The standard H_∞ control problem is to find a stabilizing LTI controller K_{rc} at fixed frozen values of $\omega_m = \zeta\omega_s$ such that the H_∞-norm of the channel $w_{rc} \rightarrow z_{rc}$ is smaller

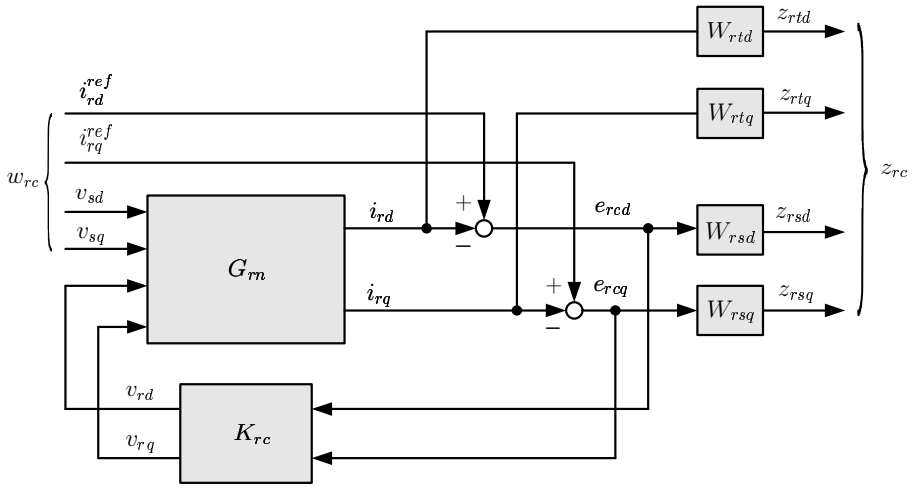

Figure 5.3: The interconnection of the system

than a given number γ:

$$\left\| \begin{bmatrix} W_{rs} S_{rc} \\ W_{rt} T_{rc} \end{bmatrix} \right\|_\infty \leq \gamma.$$

The design objectives are specified as follows:

- The bandwidth of the controlled system is larger than 10^3rad/s for good reference tracking, but less than 10^4rad/s for good sampling behavior (see section 5.6).
- The overshoot of set-point responses for the rotor current input signals at the outputs of the closed-loop system is not larger than 20%.
- As mentioned before, the stator voltage v_s is considered as disturbances. Its influence on the controlled outputs and control errors must be reduced as much as possible.

The set of DFIM parameters that is given in Appendix B.1 is applied for the controller synthesis. These parameters are relevant for a 620kW DFIM in a wind turbine system. Note that for the experiments as presented in Chapter 7, however, a DFIM of a laboratory-scale power (4kW) with parameters given in Appendix B.2 will be used for all experiments.

During the controller design stage, a trial-and-error-repetition technique is used in order to achieve the desired performance specifications by adjusting the weighting functions. The design steps are repeated until we are able to meet the required performance

specifications. Finally, the following weighting functions were obtained (for the parameter set given in Appendix B.1):

$$W_{rs} = \begin{pmatrix} W_{rsd} & 0 \\ 0 & W_{rsq} \end{pmatrix} = \begin{pmatrix} \frac{925}{s+0.15} & 0 \\ 0 & \frac{625}{s+2.5} \end{pmatrix}, \tag{5.19}$$

$$W_{rt} = \begin{pmatrix} W_{rtd} & 0 \\ 0 & W_{rtq} \end{pmatrix} = \begin{pmatrix} \frac{0.1s}{s+1.15} & 0 \\ 0 & \frac{0.155s+0.45}{s+1.25} \end{pmatrix}. \tag{5.20}$$

For the chosen frozen value of $\omega_m = 0.9\omega_s$ (at under-synchronous speed), the controlled system with the H_∞ current controller for the above given weighting functions achieves a norm of 0.36.

5.3.3. SIMULATION RESULTS WITH THE H_∞ CURRENT CONTROLLER

Fig. 5.4 shows the frequency responses of the controlled system with the H_∞ current controller and the inverse of the weighting functions W_{rtd}, and W_{rtq} (see equations (5.19) and (5.20)). Figs. 5.4a,b show the relevant magnitude plots of the complementary sensitivity and sensitivity functions of the closed-loop system with the performance requirements achieved by W_{rt} and W_{rs}. In Fig. 5.4a, the thick-dashed-dotted curve shows the response of the output i_{rd} with respect to the reference inputs i_{rd}^{ref}. This curve corresponds to the transfer function T_{rc11} (see equation (5.18)). Similarly, the thick-solid curve shows the response of the output i_{rq} with respect to the reference inputs i_{rq}^{ref} and it corresponds to the transfer function T_{rc22}. Meanwhile the thick-dashed curve shows the influence of the reference input i_{rq}^{ref} on the output i_{rd} corresponding to the transfer functions T_{rc12}, and the thick-dotted curve shows the influence of the reference input i_{rd}^{ref} on the output i_{rq} corresponding to the transfer functions T_{rc21}. The inverse of the weighting functions W_{rtd}, and W_{rtq} (see Fig. 5.3) are depicted by the solid and dashed lines in Fig. 5.4a, while the inverse of the weighting functions W_{rsd}, and W_{rsq} are depicted by the solid and dashed lines in Fig. 5.4b, respectively. The performance of the reference inputs to the control errors as well as the influence of the stator voltage v_s on the controlled outputs and controller inputs are shown in Figs. 5.4c,d with the same line styles.

It is clear from Fig. 5.4 that the sensitivity and complementary sensitivity functions are below the inverse of the performance weighting functions. The bandwidths corresponding to the channels $i_{rd}^{ref} \rightarrow i_{rd}$ and $i_{rq}^{ref} \rightarrow i_{rq}$ are about 6×10^3rad/s. The gains of the frequency responses of the stator voltages to controlled outputs and controller inputs are all smaller than −10db. This indicates that the controlled system has good disturbance rejection with respect to the stator voltage v_s. The overshoots of the channels $i_{rd}^{ref} \rightarrow i_{rd}$ and $i_{rq}^{ref} \rightarrow i_{rq}$ are about 15% and hence satisfy the performance requirement as mentioned above as well. Moreover, the gains corresponding to the frequency responses of the channels $i_{rd}^{ref} \rightarrow i_{rq}$ and $i_{rq}^{ref} \rightarrow i_{rd}$ are smaller than −22dB. This means that the cross-coupling interaction between i_{rd} and i_{rq} remains quite small, or in other words, the rotor current components can be considered to have no influence on each an-

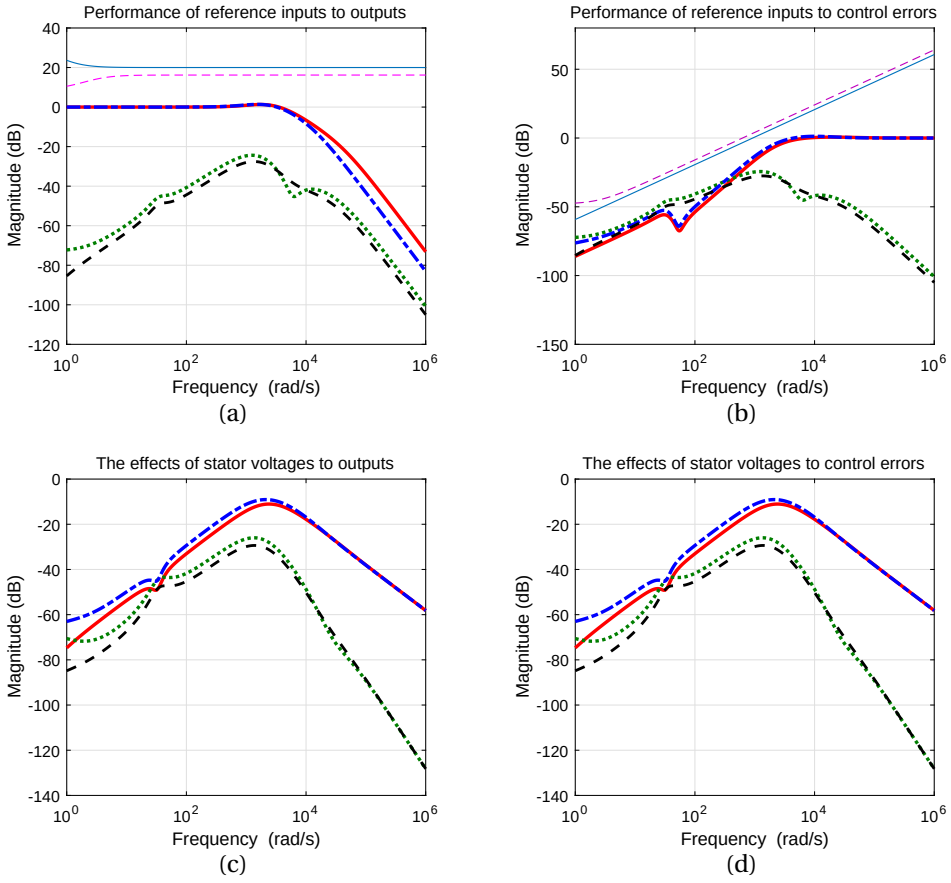

Figure 5.4: Performance of the controlled system with H_∞ current controller in the frequency domain for $\omega_m = 0.9\omega_s$.

other. As a result, the characteristics of the electrical torque and power factor responses are not deteriorated.

Fig. 5.5 shows the time responses of the controlled system for a step input. The solid line in Fig. 5.5a shows the response of the output i_{rd} with respect to the reference input i_{rd}^{ref} and it corresponds to the transfer function T_{rc11} in equation (5.18). The dashed line shows the response of the output i_{rq} with respect to the reference input i_{rq}^{ref} and it corresponds to the transfer function T_{rc22} in equation (5.18). The dotted curve shows the influence of the reference input i_{rq}^{ref} on the output i_{rd} corresponding to the transfer function T_{rc12}, and the dash-dotted curve shows the influence of the reference input i_{rd}^{ref} on the output i_{rq} corresponding to the transfer function T_{rc21}. The solid line in Fig. 5.5b

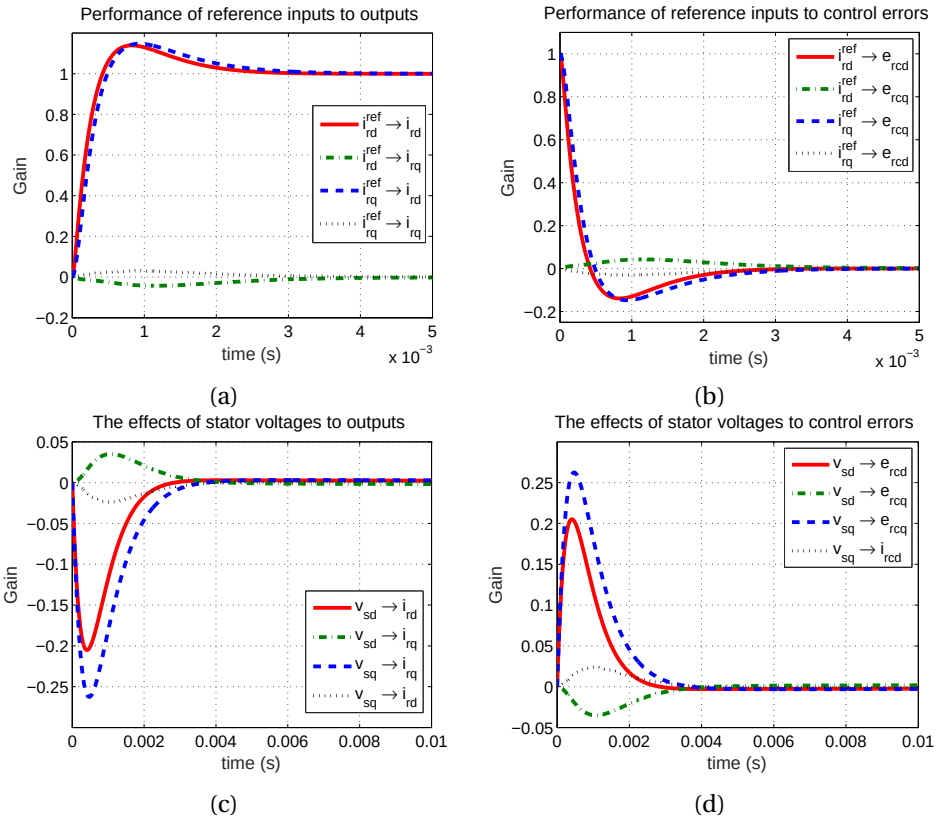

Figure 5.5: Performance of the controlled system with H_∞ current controller in the time domain for $\omega_m = 0.9\omega_s$.

5

shows the response of the control error e_{rcd} with respect to the reference input i_{rd}^{ref}. The dashed line shows the response of the control error e_{rcq} with respect to the reference input i_{rq}^{ref}. The dotted curve shows the influence of the reference input i_{rq}^{ref} on the control error r_{rcd}, and the dash-dotted curve shows the influence of the reference input i_{rd}^{ref} on the control error e_{rcq}. The influences of the stator voltages v_s on the controlled outputs and control errors are also show in Figs. 5.5c,d with the same line styles.

Note that the H_∞ current controller is designed with a fixed frozen value of the rotor angular speed ω_m. Hence, the obtained performance is not guaranteed for the whole region of variation of ω_m. However, we can further investigate the performance of the closed-loop system with the H_∞ controller designed for the frozen value $\omega_m = 0.9\omega_s$ for other angular rotor speeds. In the following investigation, we consider the performance of the controlled system with the rotor speed variations by ±30% from the rotor nominal speed $\omega_{nom} = \zeta\omega_s = 0.9\omega_s$ ($\zeta = 0.9$), i.e. $\omega_m \in [0.63\omega_s, 1.17\omega_s]$. In order to do so we synthesized two H_∞ controllers for the frozen parameter values $\omega_m = 0.63\omega_s$ and

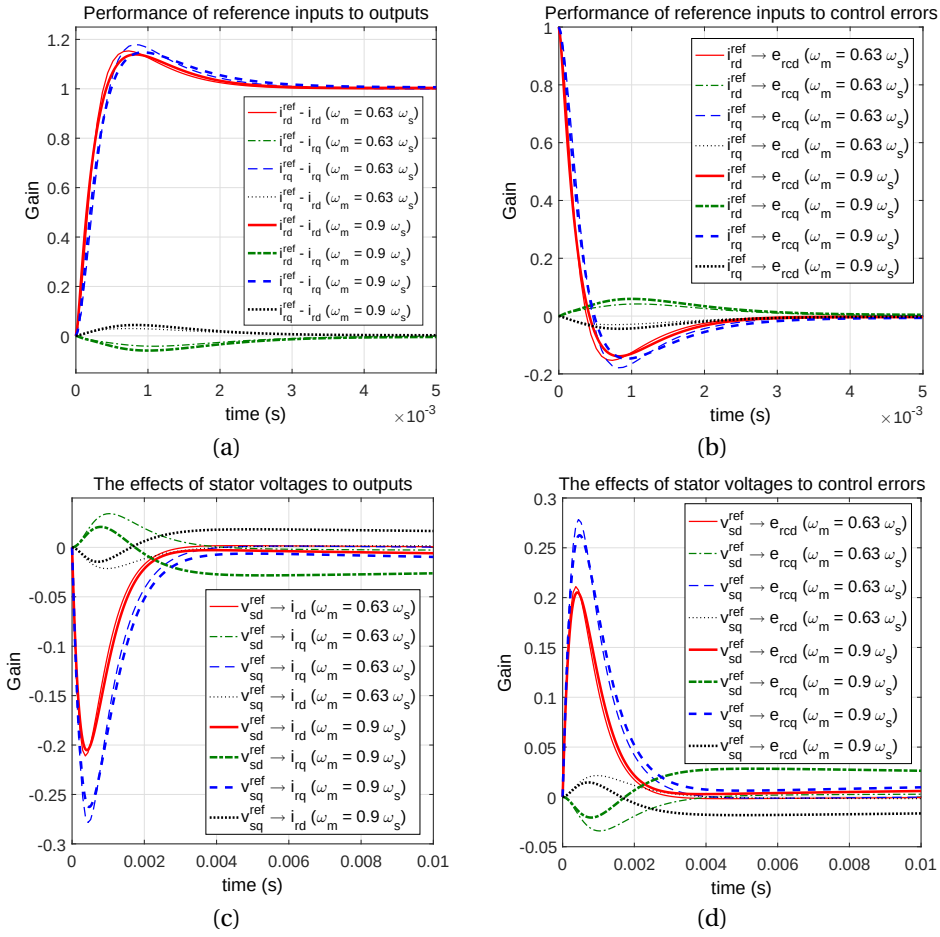

Figure 5.6: Performance of the controlled system with H_∞ current controller for frozen value $\omega_m = 0.9\omega_s$ for $\omega_m = 0.63\omega_s$.

$\omega_m = 1.17\omega_s$ using the same weighting functions as in (5.19) and (5.20). Then we plot the time responses of the closed-loop system with the H_∞ controller designed for the frozen value $\omega_m = 0.9\omega_s$ applying for the case where $\omega_m = 0.63\omega_s$ and $\omega_m = 1.17\omega_s$, respectively. The time responses of the closed-loop system with the local H_∞ controllers designed for the frozen values $\omega_m = 0.63\omega_s$ and $\omega_m = 1.17\omega_s$ are also plotted on each figure for the purpose of comparison of the achieved performance among these H_∞ controllers.

Fig. 5.6 shows the performance of the closed-loop system at $\omega_m = 0.63\omega_s$ with two H_∞ controllers designed for the frozen value $\omega_m = 0.9\omega_s$ and $\omega_m = 0.63\omega_s$, respectively. The thick lines are related to the designed H_∞ controller for the frozen value $\omega_m = 0.9\omega_s$.

The thin-lines are related to the local H_∞ controller designed for $\omega_m = 0.63\omega_s$. As can be seen from Fig. 5.6a, the time responses of the outputs i_{rd} and i_{rq} with respect to the step change of the reference inputs i_{rd}^{ref} and i_{rq}^{ref}, respectively, of the closed-loop system with the H_∞ controller designed for the frozen value $\omega_m = 0.9\omega_s$ are maintained for the frozen values $\omega_m = 0.63\omega_s$ if compared with that in Fig. 5.5. In addition, these curves are almost the same with that of the local H_∞ controller designed for $\omega_m = 0.63\omega_s$. The same conclusion can also be drawn for the curves related to the time responses of the control errors e_{rcd}, e_{rcq} with respect to the step change of the reference inputs i_{rd}^{ref}, i_{rq}^{ref} (Fig. 5.6b), and the influences of the stator voltages v_{sd}, v_{sq} on the controlled outputs i_{rd}, i_{rq} (Fig. 5.6c) and control errors e_{rcd}, e_{rcq} (Fig. 5.6d), respectively. However, the remarkable difference in the performance among these H_∞ controllers is indicated by their cross-coupling interactions. The effects of the stator voltages v_{sd} and v_{sq} to the outputs i_{rq}, i_{rd} (Fig. 5.6c) and to the control errors e_{rcq}, e_{rcd} (Fig. 5.6d), respectively, in the case of the H_∞ controller designed for the frozen value $\omega_m = 0.9\omega_s$ are larger than that of the local H_∞ controller designed for $\omega_m = 0.63\omega_s$.

The performance of the closed-loop system at $\omega_m = 1.17\omega_s$ with two H_∞ controllers designed for the frozen value $\omega_m = 0.9\omega_s$ and $\omega_m = 1.17\omega_s$, respectively, is shown in Fig. 5.7. The thick lines are related to the designed H_∞ controller for the frozen value $\omega_m = 0.9\omega_s$. The thin lines are related to the local H_∞ controller designed for $\omega_m = 1.17\omega_s$. Similarly to the previous simulation, the time responses of the closed-loop system with the H_∞ controller designed for the frozen value $\omega_m = 0.9\omega_s$ and the local H_∞ controller designed for $\omega_m = 1.17\omega_s$ corresponding to the step change of the reference inputs i_{rd}^{ref}, i_{rq}^{ref}, and to the effect of stator voltages v_{sd}, v_{sq} are almost the same, except their cross-coupling interactions. In the case of the H_∞ controller designed for the frozen value $\omega_m = 0.9\omega_s$, the influences of the stator voltages v_{sd} and v_{sq} to the outputs i_{rq}, i_{rd} (Fig. 5.7c) and to the control errors e_{rcq}, e_{rcd} (Fig. 5.7d) are larger than that of the local H_∞ controller designed for $\omega_m = 1.17\omega_s$.

Obviously, the performance of the the H_∞ controller designed for the frozen value $\omega_m = 0.9\omega_s$ for other rotor angular speeds are not maintained because of the cross-coupling interactions between the stator voltages v_{sd}, v_{sq} and the outputs i_{rq}, i_{rd} as well as the stator voltages v_{sd}, v_{sq} and the control errors e_{rcq}, e_{rcd}. This may cause a large tracking error for the controlled system since the stator voltages v_{sd} and v_{sq} are the input disturbances.

In order to evaluate the performance of the closed-loop system with an H_∞ controller designed for different frozen values of ω_m for other rotor angular speeds in the face of the stator voltage action, we performed the simulations with the set value of $i_{rd} = 700A$ and the set value of $i_{rq} = 300A$ as shown in Fig. 5.8. The time responses of the d (Fig. 5.8a) and q (Fig. 5.8b) components of the rotor currents achieved by the designed H_∞ controller for the frozen value $\omega_m = 0.63\omega_s$ are plotted by the solid curves. While the dashed and and the dotted curves show the performance of this controller for the value $\omega_m = 0.9\omega_s$, and $\omega_m = 1.17\omega_s$, respectively. These figures reveal that the tracking errors of the d and q components of the rotor currents achieved by this controller are increased for $\omega_m = 0.9\omega_s$ and $\omega_m = 1.17\omega_s$. This is because of the cross-coupling interactions be-

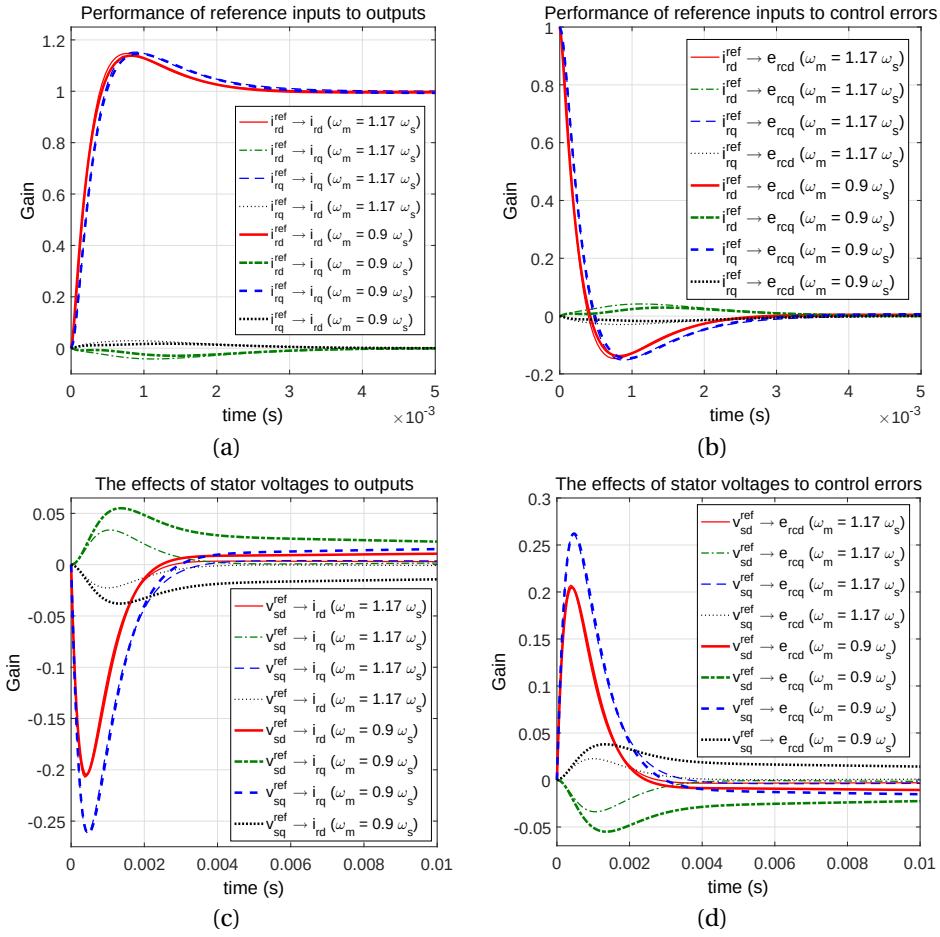

Figure 5.7: Performance of the controlled system with H_∞ current controller for frozen value $\omega_m = 0.9\omega_s$ for $\omega_m = 1.17\omega_s$.

tween the stator voltages v_{sd}, v_{sq} and the outputs i_{rq}, i_{rd} as well as the stator voltages v_{sd}, v_{sq} and the control errors e_{rcq}, e_{rcd} become larger for bigger rotor angular speeds as presented in the previous simulation. Figs. 5.8c and 5.8d show the time responses of the d and q components of the rotor currents achieved by the designed H_∞ controller for the frozen value $\omega_m = 0.9\omega_s$ (dashed curves) for the value $\omega_m = 0.63\omega_s$ (solid curves), and $\omega_m = 1.17\omega_s$ (dotted curves), respectively. Figs. 5.8e and 5.8f show the time responses of the d and q components of the rotor currents achieved by the designed H_∞ controller for the frozen value $\omega_m = 1.17\omega_s$ (dotted curves) for the value $\omega_m = 0.63\omega_s$ (solid curves), and $\omega_m = 0.9\omega_s$ (dashed curves), respectively. These figures reveal that performance of the H_∞ controller designed for a frozen value of ω_m is not guaranteed for these other values of ω_m.

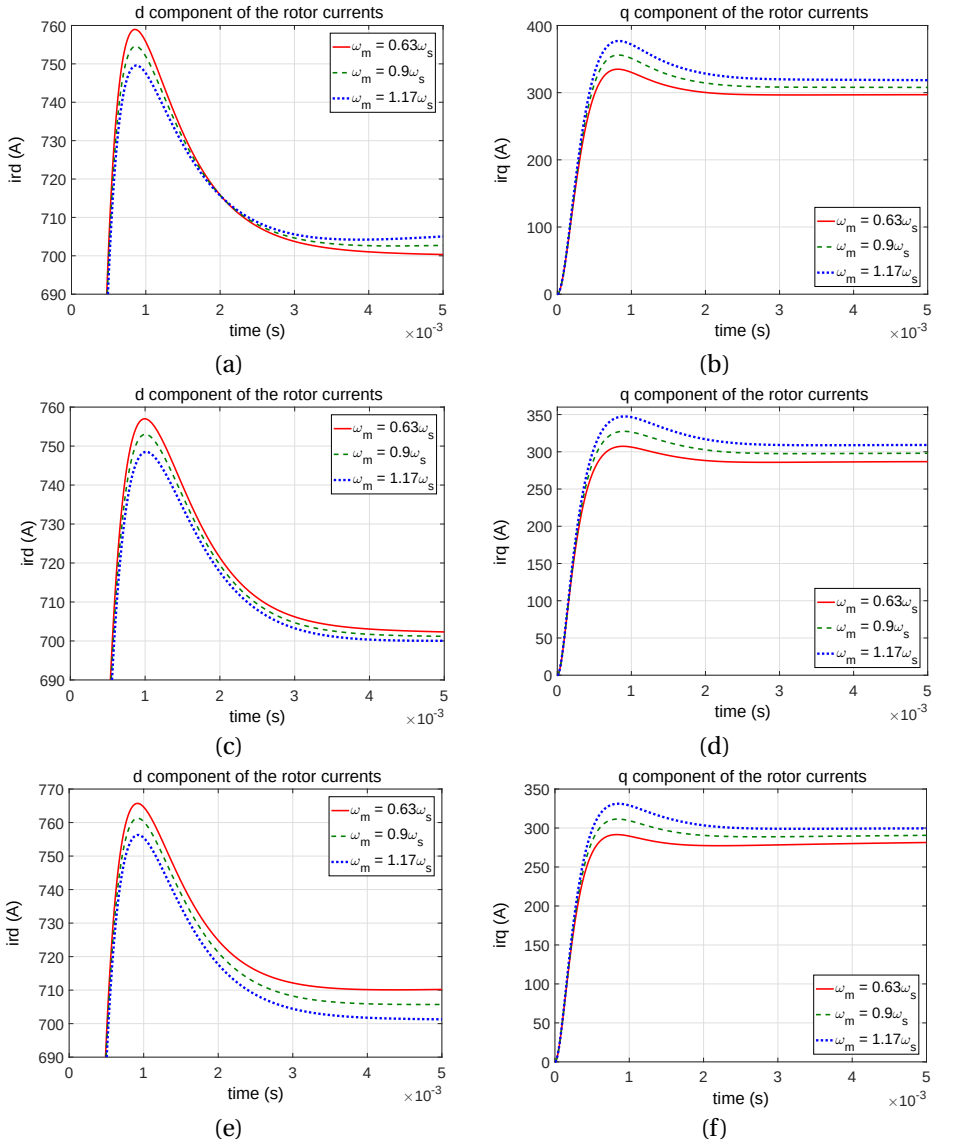

Figure 5.8: Performance of the controlled system with H_∞ current controllers designed for $\omega_m = 0.63\omega_s$ (a, b), for $\omega_m = 0.9\omega_s$ (c, d), and for $\omega_m = 1.17\omega_s$ (e, f) at different constant values of ω_m.

For further investigation, we carry out a simulation with the H_∞ controller designed for a frozen value of ω_m in which the rotor speed is suddenly changed between its extreme points in the parameter interval. We consider three local H_∞ controllers designed for the frozen values $\omega_m = 0.63\omega_s$, $\omega_m = 0.9\omega_s$, and $\omega_m = 1.17\omega_s$ as above. The parameter

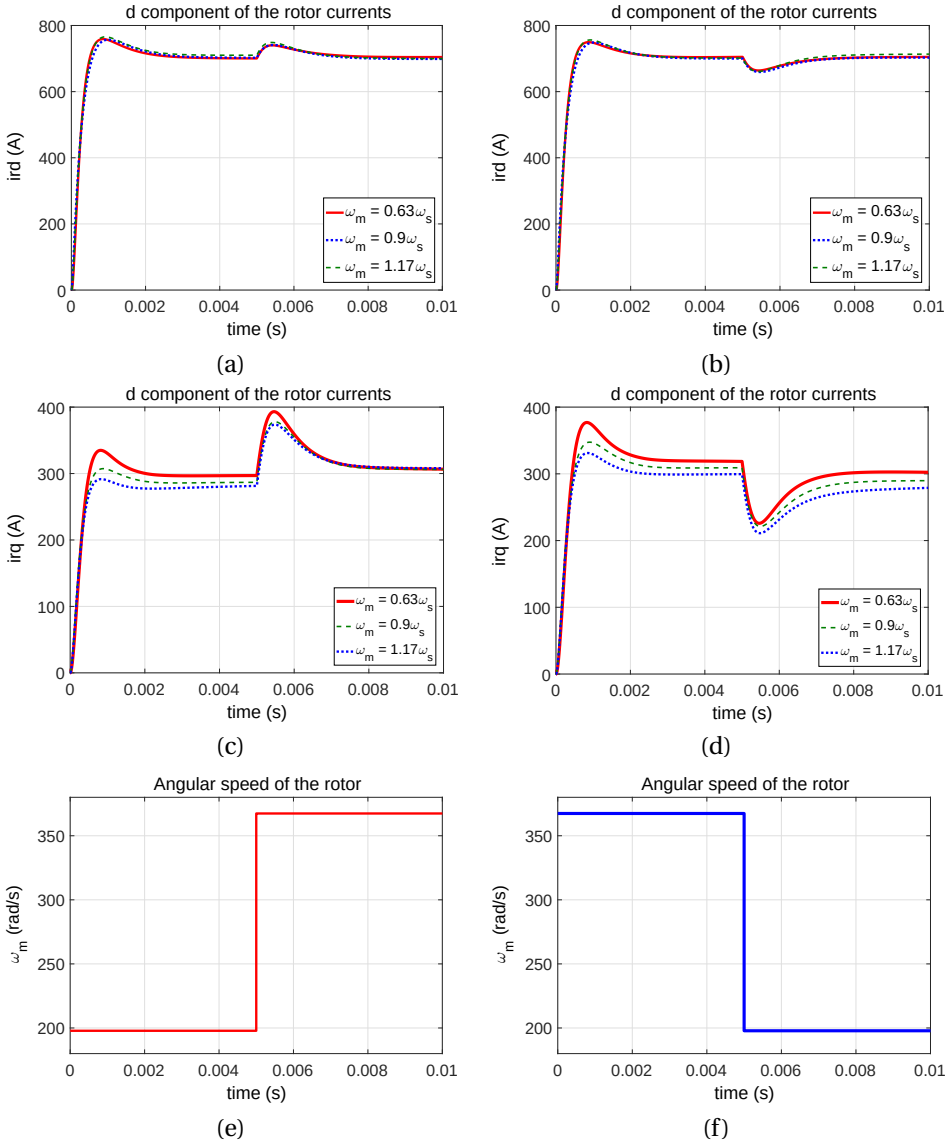

Figure 5.9: Performance of the controlled system with three H_∞ current controllers designed for $\omega_m = 0.63\omega_s$, $\omega_m = 0.9\omega_s$, and $\omega_m = 1.17\omega_s$, respectively, with fast variations of the rotor speed.

trajectory is given by the step change of the rotor speed. Figs. 5.9a,c,e show the behaviors of the d and q components of the rotor currents when the rotor angular speed increases from 70% to 130% of its nominal speed $\omega_{nom} = 0.9\omega_s$, where $\omega_s = 2\pi f_s = 314.15$(rad/s), $f_s = 50Hz$. Conversely, the behaviors of the d and q components of the rotor currents

when the rotor angular speed decreases from 130% down to 70% of its nominal speed are shown in Figs. 5.9b,d,f. These figures reveal that the H_∞ controllers do not guarantee tracking during the fast parameter transition. The control error increases along the parameter trajectory and reaches the largest value at the end of it.

Via these simulation results we can conclude that the performance of the H_∞ controller designed for a frozen value of ω_m is not guaranteed for other rotor angular speeds both for constant and fast parameter variations. In order to get a better performance level for the controlled system, the designed controller has to adapt to changes of the rotor angular speed. In that sense, the rotor angular speed can be adopted as a gain-scheduling parameter. This is related to the framework of the LPV controller synthesis as presented in Section 4.4. As a result, in the next section, we will deal with the synthesis of self-scheduled current controller for DFIMs based on considering the rotor angular speed as an uncertain online measurable parameter.

5.4. LPV CONTROL OF DFIMS

5.4.1. SYNTHESIS OF SELF-SCHEDULED CURRENT CONTROLLER

The gain-scheduled controller synthesis is similar to classical H_∞ synthesis, but both the plant and the controller are LPV systems.

The LPV-design approach (see Section 4.4) is to find a stabilizing controller $K_{rc}^{lpv}(\omega_m)$ of the form

$$\begin{pmatrix}\dot{x}_c(t)\\ u_c(t)\end{pmatrix} = \begin{pmatrix}A_c(\omega_m(t)) & B_c(\omega_m(t))\\ C_c(\omega_m(t)) & D_c(\omega_m(t))\end{pmatrix}\begin{pmatrix}x_c(t)\\ y_c(t)\end{pmatrix} \tag{5.21}$$

such that the closed-loop system of (5.15) and (5.21), denoted as

$$\begin{pmatrix}\dot{\xi}_{rc}(t)\\ z_{rc}(t)\end{pmatrix} = \begin{pmatrix}\mathscr{A}_{rc}(\omega_m(t)) & \mathscr{B}_{rc}(\omega_m(t))\\ \mathscr{C}_{rc}(\omega_m(t)) & \mathscr{D}_{rc}(\omega_m(t))\end{pmatrix}\begin{pmatrix}\xi_{rc}(t)\\ w_{rc}(t)\end{pmatrix},$$

is internally stable and the $\mathscr{L}_2$-gain of the channel $w_{rc} \to z_{rc}$ is smaller than a specified bound γ for all trajectories of $\omega_m(t) \in [\omega_{min}, \omega_{max}] = [(1-p_\omega)\zeta\omega_s, (1+p_\omega)\zeta\omega_s]$.

We employ the Linear Matrix Inequality (LMI) Control Toolbox in Matlab [119] in order to compute the vertex controllers

$$K_{rc1} = \begin{pmatrix}A_{Krc1} & B_{Krc1}\\ C_{Krc1} & D_{Krc1}\end{pmatrix}, \quad K_{rc2} = \begin{pmatrix}A_{Krc2} & B_{Krc2}\\ C_{Krc2} & D_{Krc2}\end{pmatrix}$$

in a polytopic controller description as given in (4.36). Then the controller is implemented as follows: for a value $\omega_m(t)$ measured at time t, we use

$$K_{rc}(t) = \frac{1-p(t)}{2}K_{rc1} + \frac{p(t)+1}{2}K_{rc2} \tag{5.22}$$

where $p(t) = \frac{\omega_m(t)-\zeta\omega_s}{\zeta\omega_s p_w}$ for simulating the controller dynamics. This choice is to ensure that (4.30) will be guaranteed when the rotor speed varies by $\pm p_\omega$% from its nominal speed.

5.4.2. SIMULATION RESULTS WITH THE LPV CURRENT CONTROLLER

Similarly as for the deadbeat and H_∞ control cases, the following simulation results are obtained for the DFIM model with parameters presented in Appendix B.1.

Fig. 5.10 - Fig. 5.12 show the frequency and time responses of the controlled system with the LPV current controller for 3 values of ω_m in the range (5.4) with $\zeta = 0.9$, and $p_\omega = 30\%$. Here, the same weighting functions as in (5.19) and (5.20) are employed for the LPV controller synthesis. The controlled system with LPV current controller achieves a norm of 0.5092.

Note that, since the norm of the controlled system with the LPV controller is rather close to that of the H_∞ controller in section 5.3.2, there is not much conservatism.

Similarly as for H_∞-synthesis, the complementary sensitivity and sensitivity functions of the closed-loop system with the performance requirements specified by W_{rt} and W_{rs} are shown in Fig. 5.10 where the inverse weighting functions are depicted by the thick-dashed and thin-dashed lines. In Fig. 5.10a, the thick-solid line shows the response corresponding to the value of $\omega_m = 0.9\omega_s$ for the channel $i_{rd}^{ref} \rightarrow i_{rd}$. The thick-dashed-dotted and the thick-dotted lines correspond with $\omega_m = 0.63\omega_s$, and $\omega_m = 1.17\omega_s$, respectively. Meanwhile, the thin-solid line shows the response corresponding to the value of $\omega_m = 0.9\omega_s$ for the channel $i_{rd}^{ref} \rightarrow i_{rq}$. The thin-dashed-dotted and the thin-dotted lines correspond with $\omega_m = 0.63\omega_s$, and $\omega_m = 1.17\omega_s$, respectively. In Fig. 5.10b, the response corresponding to the value of $\omega_m = 0.9\omega_s$ for the channel $i_{rq}^{ref} \rightarrow i_{rq}$ is depicted by the thick-solid line. The thick-dashed-dotted and the thick-dotted lines correspond with $\omega_m = 0.63\omega_s$, and $\omega_m = 1.17\omega_s$, respectively. The response corresponding to the value of $\omega_m = 0.9\omega_s$ for the channel $i_{rq}^{ref} \rightarrow i_{rd}$ is depicted by the thin-solid line whereas the thin-dashed-dotted and the thin-dotted lines correspond with $\omega_m = 0.63\omega_s$, and $\omega_m = 1.17\omega_s$, respectively.

In Fig. 5.10c, the thick-solid line shows the response corresponding to the value of $\omega_m = 0.9\omega_s$ for the channel $i_{rd}^{ref} \rightarrow e_{rcd}$. The thick-dashed-dotted and the thick-dotted lines correspond with $\omega_m = 0.63\omega_s$, and $\omega_m = 1.17\omega_s$, respectively. Meanwhile, the thin-solid line shows the response corresponding to the value of $\omega_m = 0.9\omega_s$ for the channel $i_{rd}^{ref} \rightarrow e_{rcq}$. The thin-dashed-dotted and the thin-dotted lines correspond with $\omega_m = 0.63\omega_s$, and $\omega_m = 1.17\omega_s$, respectively. In Fig. 5.10d, the response corresponding to the value of $\omega_m = 0.9\omega_s$ for the channel $i_{rq}^{ref} \rightarrow e_{rcq}$ is depicted by the thick-solid line. The thick-dashed-dotted and the thick-dotted lines correspond with $\omega_m = 0.63\omega_s$, and $\omega_m = 1.17\omega_s$, respectively. The response corresponding to the value of $\omega_m = 0.9\omega_s$ for the channel $i_{rq}^{ref} \rightarrow e_{rcd}$ is depicted by the thin-solid line whereas the thin-dashed-dotted and the thin-dotted lines correspond with $\omega_m = 0.63\omega_s$, and $\omega_m = 1.17\omega_s$, respectively.

The influences of the stator voltage v_s on the controlled outputs and control errors

are shown in Fig. 5.11 with the same line styles.

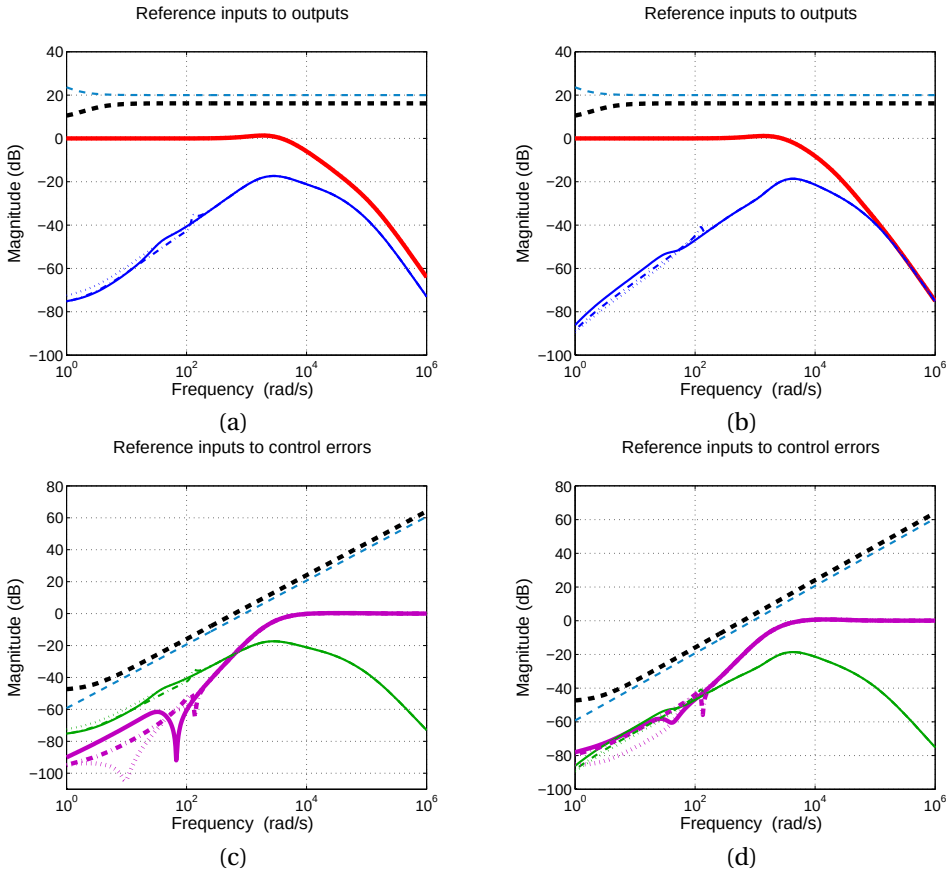

Figure 5.10: Performance of the controlled system with LPV current controller in the frequency domain for 3 values of ω_m in the range (5.4) with $\zeta = 0.9$, and $p_\omega = 30\%$.

Fig. 5.12 shows the time responses of the controlled system for a step input. The solid line in Fig. 5.12a shows the response of the output i_{rd} with respect to the reference input i_{rd}^{ref}. The dash-dotted line shows the response of the output i_{rq} with respect to the reference input i_{rq}^{ref}. The dotted curve shows the influence of the reference input i_{rq}^{ref} on the output i_{rd}, and the dashed curve shows the influence of the reference input i_{rd}^{ref} on the output i_{rq}. The solid line in Fig. 5.12b shows the response of the control error e_{rcd} with respect to the reference input i_{rd}^{ref}. The dash-dotted line shows the response of the control error e_{rcq} with respect to the reference input i_{rq}^{ref}. The dotted line shows the influence of the reference input i_{rq}^{ref} on the control error e_{rcd}, and the dashed line shows the influence of the reference input i_{rd}^{ref} on the control error e_{rcq}. The influences

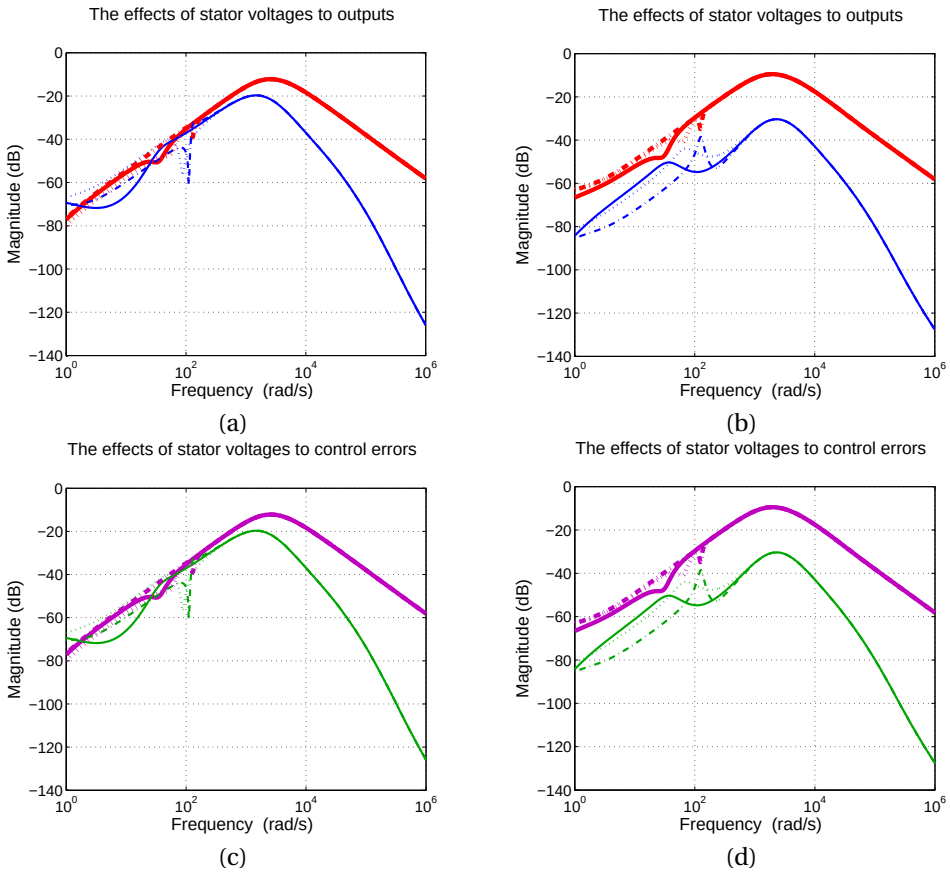

Figure 5.11: Performance of the controlled system with LPV current controller in the frequency domain for 3 values of ω_m in the range (5.4) with $\zeta = 0.9$, and $p_\omega = 30\%$.

of the stator voltages v_s on the controlled outputs and control errors are also show in Fig. 5.12c,d with the same line styles.

As can be seen in Figs. 5.10 - 5.12, the achieved performance of the controlled system with the LPV current controller satisfies the required performance specifications as mentioned in section 5.3. The performance for 3 values of ω_m over the interval (5.4) with $\zeta = 0.9$, and $p_\omega = 30\%$ is almost the same with that of the local design for the H_∞ controller at $\omega_m = 0.9\omega_s$ (see Fig. 5.5). Hence, unlike changing of performance of the H_∞ controller designed for a frozen value of ω_m for other rotor angular speeds as shown in Fig. 5.6 and 5.7, the performance obtained by the LPV design almost does not change with variations of the rotor angular speed in the given range. Note that the performance obtained by the local design for the H_∞ controller at $\omega_m = 0.9\omega_s$ (see Fig. 5.5) is a theoretical lower bound of the best performance achievable by the LPV design at the corresponding value of the rotor angular speed. Therefore, this simulation result reveals that

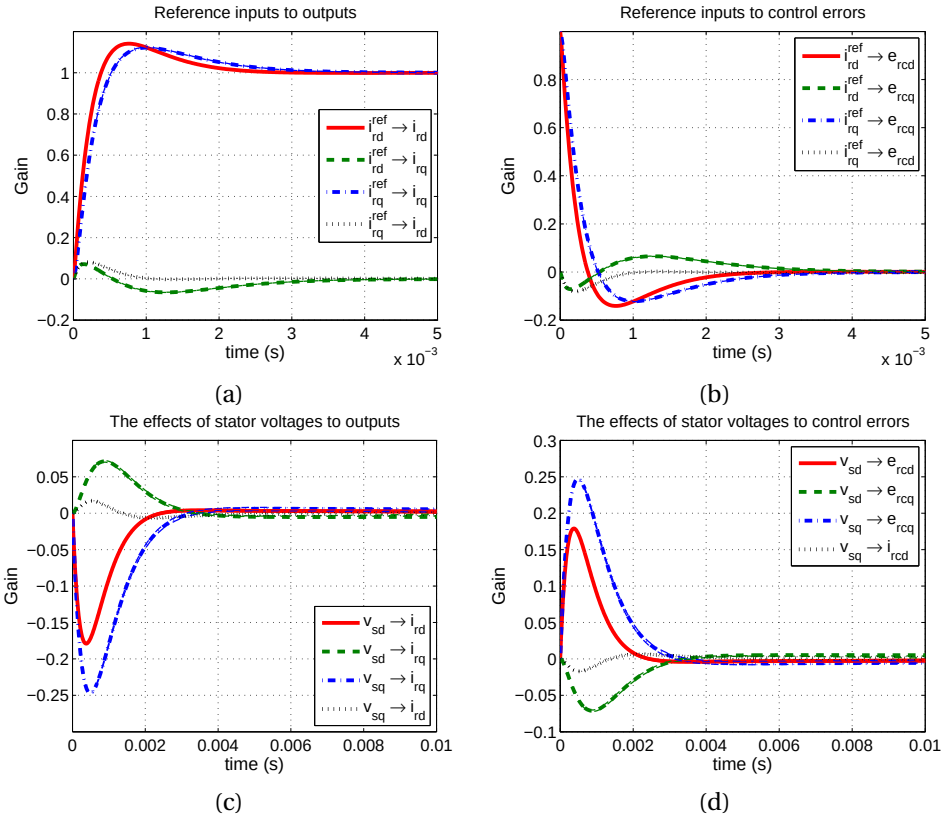

Figure 5.12: Performance of the controlled system with LPV current controller in the time domain for 3 values of ω_m in the range (5.4) with $\zeta = 0.9$, and $p_\omega = 30\%$.

5

the actual conservatism introduced in the performance of the LPV controller is negligible in comparison with the H_∞ controller designed at frozen values of the rotor angular speed.

For further comparison, we also performed the simulations with the set value of $i_{rd} = 700A$ and the set value of $i_{rq} = 300A$ in the face of the stator voltage action as shown in Fig. 5.13. The time responses of the d (Fig. 5.13a) and q (Fig. 5.13b) components of the rotor currents achieved by the LPV controller at the value $\omega_m = 0.63\omega_s$ are plotted by the solid curves. While the dashed and and the dash-dotted curves show the performance of this controller for the value $\omega_m = 0.9\omega_s$, and $\omega_m = 1.17\omega_s$, respectively. These figures reveal that the LPV controller guarantees tracking errors of the d and q components of the rotor currents for these other values of the rotor speed. This is a confirmation of the results obtained by the design method since the LPV controller achieves effective disturbance suppression of the stator voltage as shown in Fig. 5.12.

Simulation results of the LPV controller for fast variations of the rotor speed along

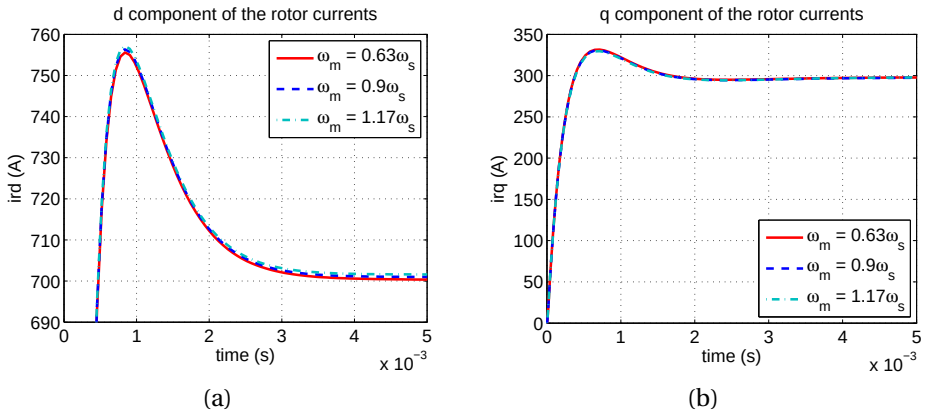

Figure 5.13: Performance of the controlled system with LPV current controller for frozen value $\omega_m = 0.63\omega_s$ at different constant values of ω_m.

the whole parameter interval are shown in Fig. 5.14. Figs. 5.14a,c,e show the behaviors of the d and q components of the rotor currents when the rotor angular speed increases from 70% to 130% of the nominal speed of the rotor $\omega_{nom} = 0.9\omega_s$, where $\omega_s = 2\pi f_s = 314.15(\text{rad/s})$, $f_s = 50Hz$. Conversely, the behaviors of the d and q components of the rotor currents when the rotor angular speed decreases from 130% down to 70% of the nominal speed of the rotor are shown in Figs. 5.14b,d,f. These figures reveal that the LPV controller guarantees performance in the presence of infinitely fast parameter transitions.

In conclusion, the performance of the LPV controller is guaranteed over the whole interval even for fast variations of the rotor angular speed. Since the DFIM is required to work well in a wide range of the rotor speed, guaranteeing the performance of the controlled system over the operating interval of the rotor speed is the most important feature of the LPV controller being is superior to that of the H_∞ controller. Especially, when the grid experiences a fault causing the significant changes of the rotor speed, the LPV controller still guarantees performance while this is not the case for the H_∞ controller. Hence, self-scheduled LPV controller design is really necessary to achieve a good performance for the control of DFIMs.

In order to make a comparison with the simulation results obtained in the deadbeat control case, the following simulations are performed with the LPV controller for the same reference values as in Section 3.3.3. Figs. 5.15a,b shows the reference and simulated values of the electrical torque T_e, and the angle φ_g of the power factor $\cos\varphi_g$ of the DFIM. Figs. 5.15c,d shows the reference and simulated values of the d and q components of the rotor current required to regulate the electrical torque and the power factor of the machine. The responses of the d and q components of the stator current are shown in Figs. 5.15e,f. Recall that the sign of the electrical torque T_e and the angle φ_g of the power factor $\cos\varphi_g$ indicates the direction of power flows or the operating mode of the DFIM only (see Section 3.3.3 for more explanations about these simulations).

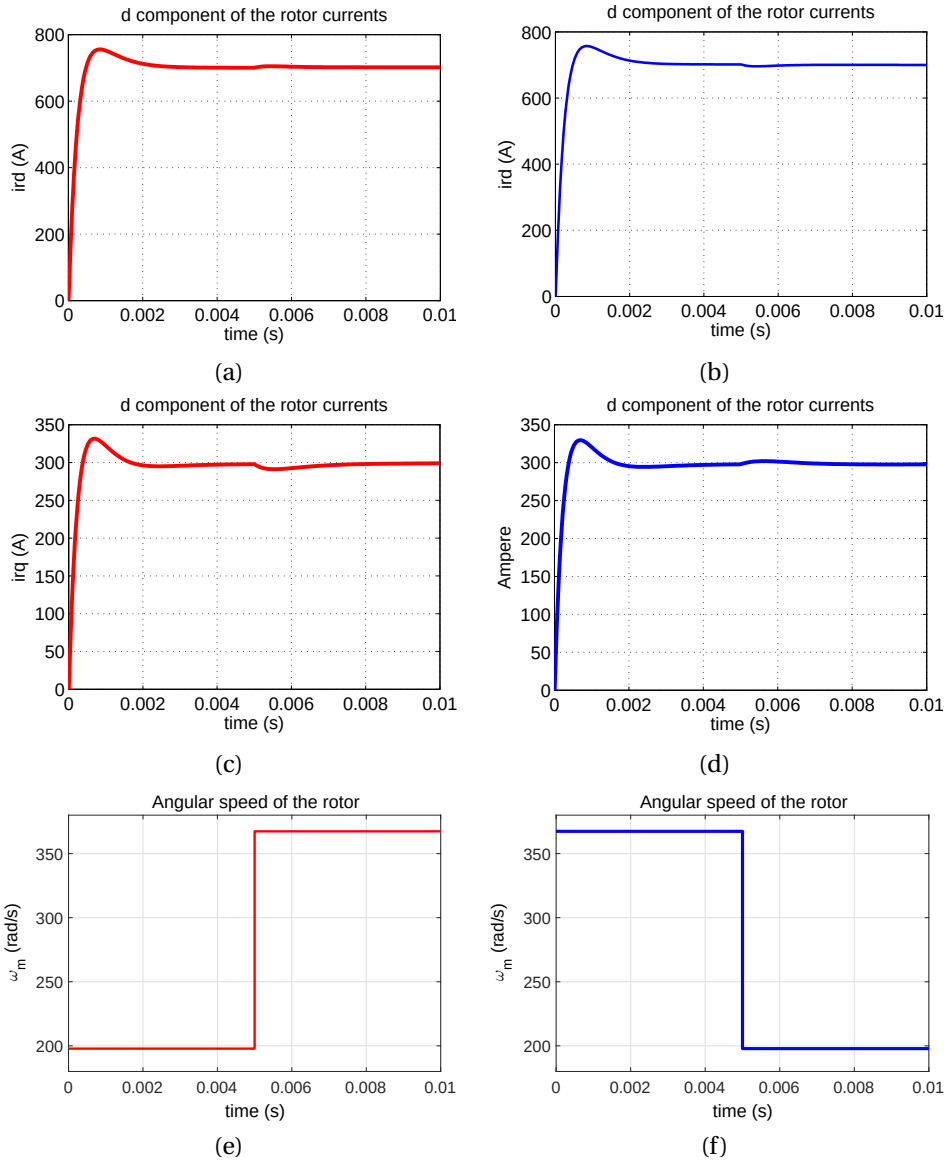

Figure 5.14: Performance of the controlled system with LPV current controller for frozen value $\omega_m = \omega_s$ for others.

As can be seen in Fig. 5.15, the closed-loop system with the LPV controller exhibits a better performance in comparison with that of the deadbeat controller case as presented in Section 3.3.3. The rotor current ripples in the dq channels are reduced for the LPV controller case. As a result, the ripples in the electrical toque and power factor are also

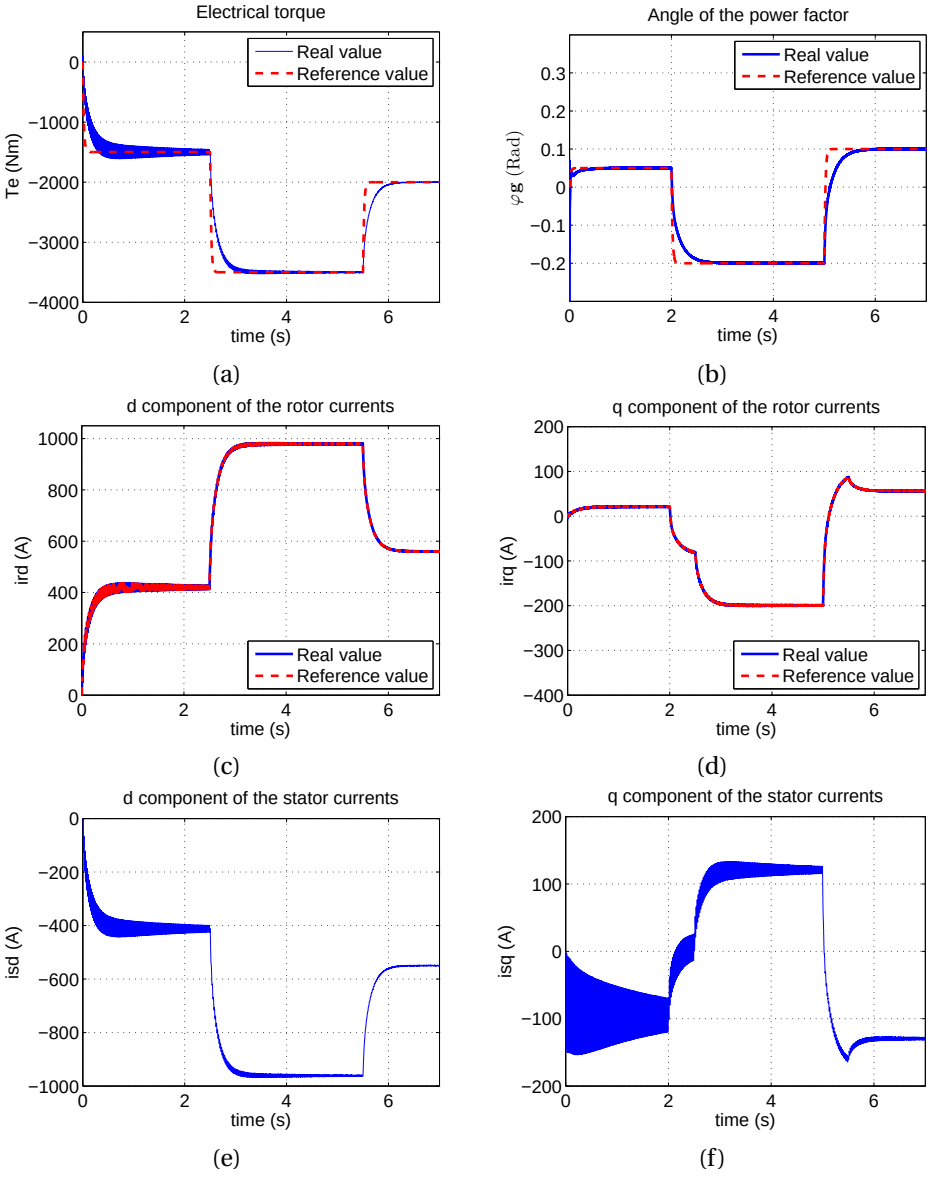

Figure 5.15: Performance of the rotor side control. (a) Electrical torque T_e, (b) angle φ_g of the power factor $\cos\varphi_g$, (c) and (d) dq-component of the rotor currents, (e) and (f) dq-component of the stator currents

lessened, especially for the power factor. Because of the magnetic coupling between the stator and the rotor magnetic fields, reducing the rotor current ripples contributes to decreasing the stator current ripples a little bit as shown in Figs. 5.15e,f.

The LPV controller design was based on the full model of the DFIM without using simple feedforward controllers as in the deadbeat case. This avoids the high sensitivity of the feedforward controller to the accuracy of machine parameters in case the DFIM parameters are exactly specified. Furthermore, the LPV controller achieves a good suppression of the cross-coupling interactions between the stator voltage and the rotor current as well as the control error the whole region of variation of the rotor speed as presented above (see Fig. 5.12). Hence, robustness of the controlled system with the LPV controller is expected not only in the normal operation but also in a faulty condition of the stator voltage.

The design of the continuous-time LPV current controller for DFIMs is also presented in [120, 121].

5.5. ROBUSTNESS OF THE LPV CURRENT CONTROLLER

The above simulation results are performed for the normal operation of the rotor speed and for the ideal values of the machine parameters as well as for the constant value of the stator voltage v_s. In this case, the controlled system with the LPV controller obtains better results in comparison with that of the deadbeat control case (see Fig. 3.5) since the fluctuations in the power factor and the rotor currents are smaller. Performance of the closed-loop system with the LPV controller with respect to robustness against parameter changes as well as the impact of stator voltage dips on the robustness of the controlled system will be further investigated by means of some simulation results.

5.5.1. ROBUSTNESS OF THE CONTROL SYSTEM AGAINST PARAMETER CHANGES

Simulation results show that the system with the self-scheduled current controller stays stable if the mutual inductance L_m is smaller than 102.4% of its nominal value. Fig. 5.16 shows the performance of the system when L_m increases to 102.4% of its normal value.

Similarly, by varying the values of L_s and L_r we see form Fig. 5.17 and Fig. 5.18 that the system with the self-scheduled current controller stays stable if L_s deviates by [95.8%, 150%] and L_r deviates by [95.68%, 150%] of their nominal values.

Obviously, the performance of the controlled system with the designed LPV current controller is maintained for different tests with different values of the machine parameters in the ranges given above. In addition, these simulation results show, in comparison with those presented in Fig. 3.7, 3.8, and 3.9, that the controlled system with the self-scheduled current controller is far more robust than that of the system with the deadbeat current controller in the presence of parameter variations. This will be confirmed by a rigorous analysis which is presented in Chapter 6.

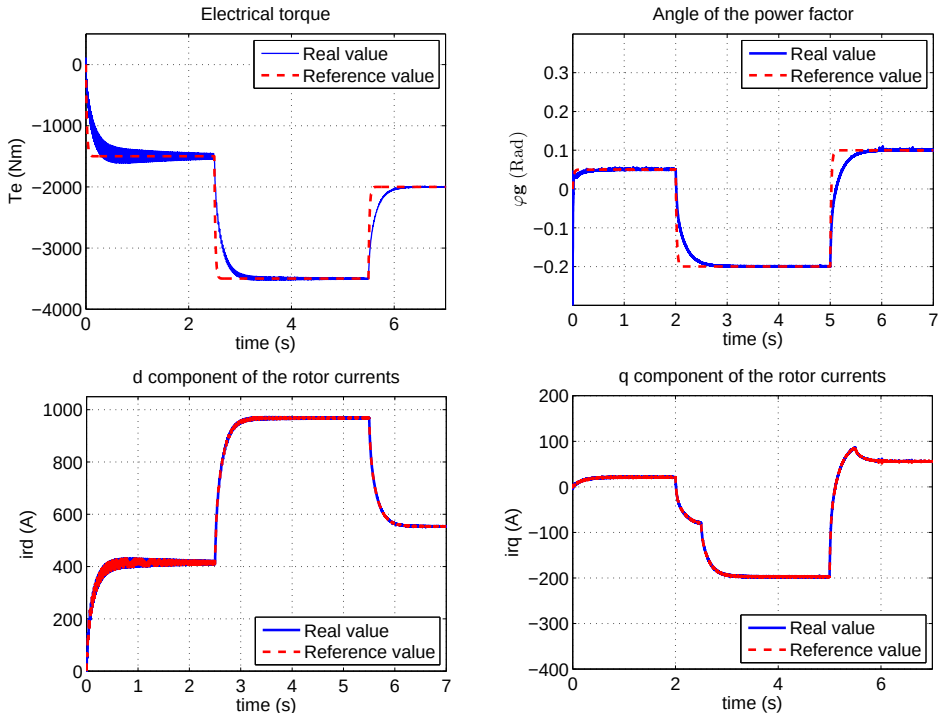

Figure 5.16: L_m increases to 102.4% of its normal value

5

5.5.2. THE IMPACT OF STATOR VOLTAGE DIPS ON THE ROBUSTNESS OF THE CONTROL SYSTEM

The effect of the grid voltage dips on the performance of the controlled system with DFIM is mentioned in section 1.2. Here, the performance of the controlled system with the LPV current controllers in the presence of grid voltage faults is demonstrated by some simulation results (Fig. 5.19). The grid voltage was dropped down to 25% of the normal voltage. This phenomenon occurred in a period of 300 msec before it recovered to its rated value. After that, the grid voltage once again was dropped to 50% of the rated voltage during 200 msec. The graphs show, in comparison with the performance of the deadbeat control in the presence of grid voltage faults presented in Fig. 3.10, that the oscillations of torque and currents in the case of self-scheduled LPV control were remarkably dampened at the grid voltage fault time. The reason for this is that the LPV design guarantees a good attenuation of the stator voltage.

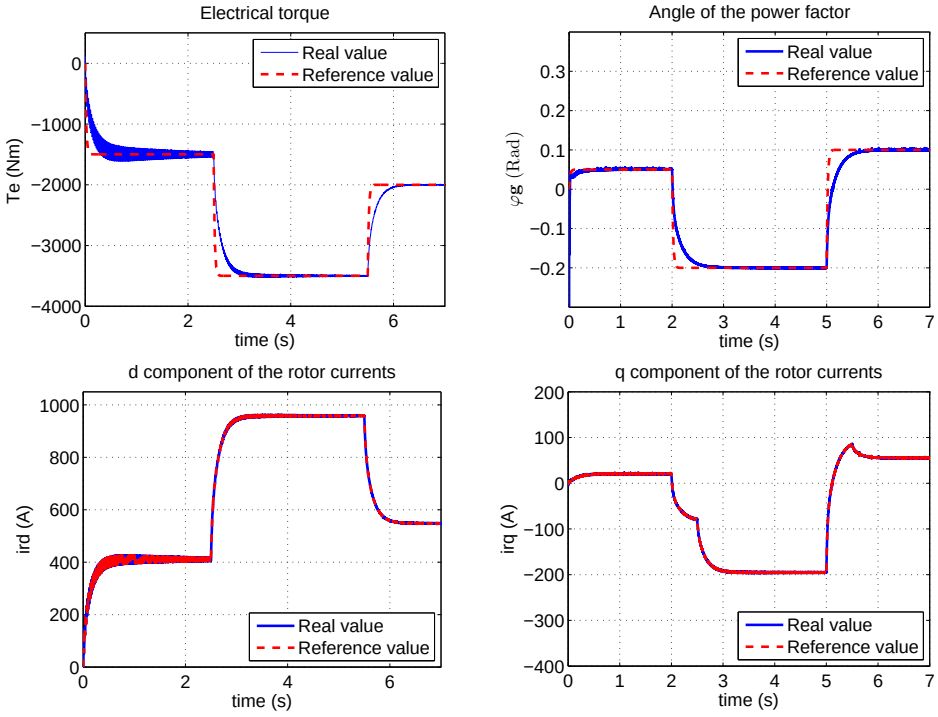

Figure 5.17: L_s decreases by 4.2% of its normal value

5.6. DISCRETIZATION PROBLEM OF PREDESIGNED LPV CONTROLLERS

5

Unlike a direct digital design method, such as for example used in [103], the designed continuous-time controller has to be replaced with an equivalent discrete-time controller in order to be implemented in an industrial digital control system. The continuous-to-discrete time design technique requires that the sampling frequency is very high so as to obtain a good digital approximation and to retain system stability. Otherwise the resulting discrete-time controlled system may be unstable even if the original continuous-time controlled is stable. Moreover, the states of the original closed-loop system may not closely match those of the discrete-time controlled open-loop system even if the discrete-time controlled system is stable [122].

In fact, the real maximal sampling frequency depends on the particular digital control system and it can not be arbitrary large. This drawback of the sampling frequency limitation is overcome by taking the closed-loop performance into account. In [123], the input and the feedback gains are modified to make the response of the sampled-data model as close to that of the original system as possible. In [124], the stability of the resulting control system is guaranteed by minimizing the H_∞-norm of the error transfer

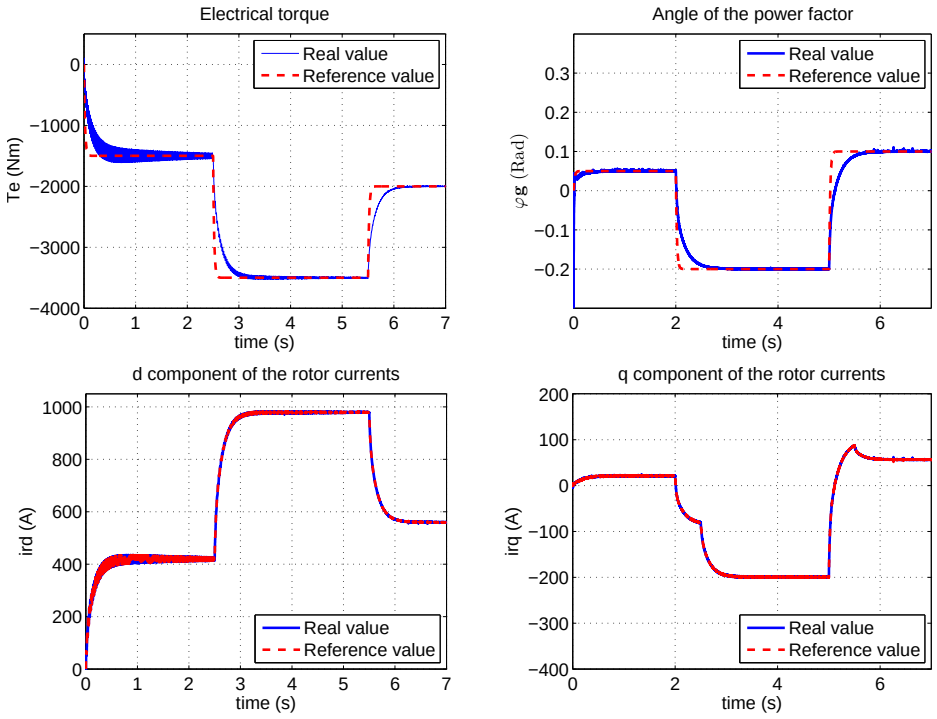

Figure 5.18: L_r decreases by 4.32% of its normal value

function. The so-called digital redesign technique based on closed-loop performance [125] or on minimizing a local quadratic performance index [122] is applied to achieve the same goal. Recently, new discretization methods of continuous-time controllers taking account of the inter-sample behavior of the resulting sampled-data system have been presented in [126].

Unfortunately, these techniques are not directly applicable to LPV controllers because of their limitation to time-varying systems [127]. Therefore, some extensions of these techniques need to be investigated.

Let us consider again the LPV controller designed in Section 5.4, see equation (5.21), with the generalized state-space form

$$K_{rc}^{lpv}(\omega_m) : \begin{cases} \dot{x}_c(t) &= A_c(\omega_m(t))x_c(t) + B_c(\omega_m(t))y_c(t) \\ u_c(t) &= C_c(\omega_m(t))x_c(t) + D_c(\omega_m(t))y_c(t) \end{cases} \tag{5.23}$$

where $\omega_m(t) \in \Omega$ stands for time-varying parameter vector in an interval Ω.

The objective here is to design a discrete-time LPV controller K_{rc}^{d} such that the performance of the closed-loop system matches that of the closed-loop system with the

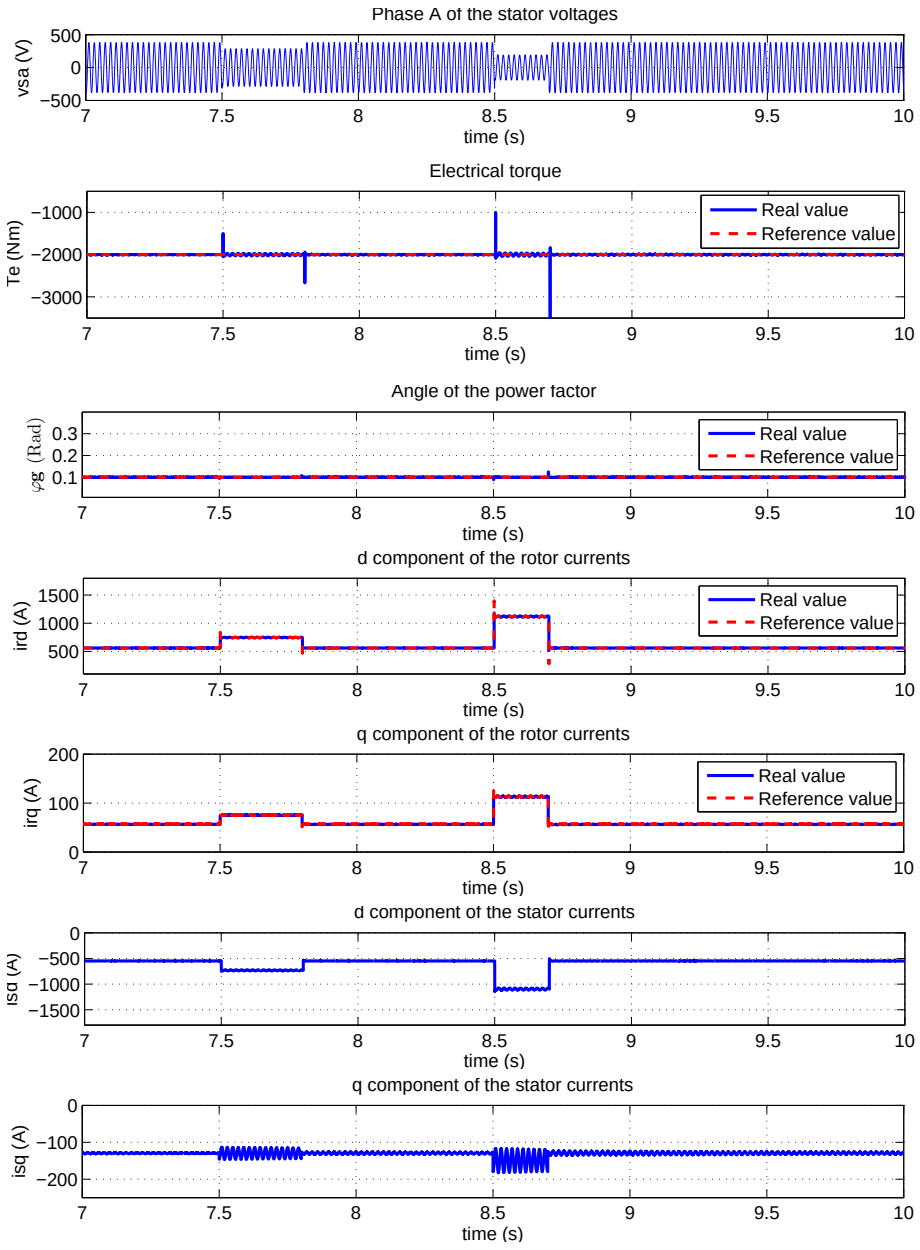

Figure 5.19: The performance of the system when grid voltage is faulty

continuous-time LPV controller as good as possible.

In this thesis, the trapezoidal technique is used for the real-time implementation of

the LPV controller since it guarantees a good match of the responses of the continuous-time and the discrete-time system for a reasonable sampling rate. The following discussion of this method is mainly based on [127].

Suppose the state vector of the controller at time kT is given by $x_{c,k} = x(kT)$. If the scheduled parameter that is measured online between the time interval $[kT,(k+1)T]$ is considered to be equal to its value at time kT, i.e. $\omega_m(t) = \omega_{m,k}$, then it follows at time $(k+1)T$ that

$$x_{c,k+1} = x_{c,k} + \int_{kT}^{(k+1)T} \left[A_c(\omega_m(\tau))x_c(\tau) + B_c(\omega_m(\tau))y_c(\tau)\right] d\tau. \tag{5.24}$$

The integral (5.24) is approximated using the trapezoidal rule [127] resulting in

$$x_{c,k+1} \approx x_{c,k} + \frac{T}{2}\left(A_c(\omega_{m,k})x_{c,k} + B_c(\omega_{m,k})y_{c,k} + A_c(\omega_{m,k+1})x_{c,k+1} + B_c(\omega_{m,k+1})y_{c,k+1}\right).$$

If we assume that the matrix

$$\left(I - \frac{T}{2}A_c(\omega_m)\right) \text{ is invertible for all } \omega_m \in \Omega, \tag{5.25}$$

we can solve for $x_{c,k+1}$ as

$$x_{c,k+1} = \Phi^{-1}_{\omega_{m,k+1}}\left[\Upsilon_{\omega_{m,k}}x_{c,k} + \tfrac{T}{2}\left(B_c(\omega_{m,k})y_{c,k} + B_c(\omega_{m,k+1})y_{c,k+1}\right)\right] \tag{5.26}$$

where $\Phi_{\omega_{m,k+1}} = \left(I - \frac{T}{2}A_c(\omega_{m,k+1})\right)$, and $\Upsilon_{\omega_{m,k}} = \left(I + \frac{T}{2}A_c(\omega_{m,k})\right)$.

In order to get a standard discrete-time system representation for (5.26) the following change of variables is used

$$z_{c,k+1} \triangleq \tfrac{1}{\sqrt{T}}\left(I - \tfrac{T}{2}A_c(\omega_{m,k+1})\right)x_{c,k+1} - \tfrac{\sqrt{T}}{2}B_c(\omega_{m,k+1})y_{c,k+1}. \tag{5.27}$$

Then substituting equation (5.26) into equation (5.27) gives

$$\begin{aligned} z_{c,k+1} &= \frac{1}{\sqrt{T}}\Phi_{\omega_{m,k+1}}\left\{\left[\Phi^{-1}_{\omega_{m,k+1}}\Upsilon_{\omega_{m,k}}x_{c,k} + \frac{T}{2}\left(B_c(\omega_{m,k})y_{c,k} + B_c(\omega_{m,k+1})y_{c,k+1}\right)\right]\right\} \\ &\quad - \frac{\sqrt{T}}{2}B_c(\omega_{m,k+1})y_{k+1} \\ &= \frac{1}{\sqrt{T}}\Upsilon_{\omega_{m,k}}x_{c,k} + \frac{\sqrt{T}}{2}B_c(\omega_{m,k})y_{c,k}. \end{aligned} \tag{5.28}$$

On the other hand, from (5.27) it follows that

$$x_{c,k} = \sqrt{T}\left(I - \tfrac{T}{2}A_c(\omega_{m,k})\right)^{-1}\left(z_{c,k} + \tfrac{\sqrt{T}}{2}B_c(\omega_{m,k})y_{c,k}\right). \tag{5.29}$$

Substituting equation (5.29) into equation (5.28) leads to

$$z_{c,k+1} = \tfrac{1}{\sqrt{T}}\Upsilon_{\omega_{m,k}}\sqrt{T}\Phi^{-1}_{\omega_{m,k}}\left(z_{c,k} + \tfrac{\sqrt{T}}{2}B_c(\omega_{m,k})y_{c,k}\right) + \tfrac{\sqrt{T}}{2}B_c(\omega_{m,k})y_{c,k}$$

where $\Phi_{\omega_{m,k}} = \left(I - \frac{T}{2} A_c(\omega_{m,k})\right)$.

Hence

$$\begin{aligned} z_{c,k+1} &= \Upsilon_{\omega_{m,k}} \Phi^{-1}_{\omega_{m,k}} z_{c,k} + \frac{\sqrt{T}}{2} \left[\left(I + \frac{T}{2} A_c(\omega_{m,k})\right) \Phi^{-1}_{\omega_{m,k}} + I \right] B_c(\omega_{m,k}) y_{c,k} \\ &= \Upsilon_{\omega_{m,k}} \Phi^{-1}_{\omega_{m,k}} z_{c,k} + \frac{\sqrt{T}}{2} \left[2\Phi^{-1}_{\omega_{m,k}} \right] B_c(\omega_{m,k}) y_{c,k}. \end{aligned}$$

This leads us to a standard discrete-time system of (5.26) as follows

$$z_{c,k+1} = \left(I + \frac{T}{2} A_c(\omega_{m,k})\right) \Phi^{-1}_{\omega_{m,k}} z_{c,k} + \sqrt{T} \Phi^{-1}_{\omega_{m,k}} B_c(\omega_{m,k}) y_{c,k}. \tag{5.30}$$

Similarly, the output equation can be expressed as

$$u_{c,k} = C(\omega_{m,k}) x_{c,k} + D(\omega_{m,k}) y_{c,k}. \tag{5.31}$$

Substituting equation (5.29) into equation (5.31) gives

$$u_{c,k} = C_c(\omega_{m,k}) \left[\sqrt{T} \Phi^{-1}_{\omega_{m,k}} \left(z_{c,k} + \frac{\sqrt{T}}{2} B_c(\omega_{m,k}) y_{c,k} \right) \right] + D_c(\omega_{m,k}) y_{c,k}.$$

Thus

$$u_{c,k} = \sqrt{T} C_c(\omega_{m,k}) \Phi^{-1}_{\omega_{m,k}} z_{c,k} + \left[\frac{T}{2} C_c \Phi^{-1}_{\omega_{m,k}} B_c(\omega_{m,k}) + D_c(\omega_{m,k}) \right] y_{c,k}. \tag{5.32}$$

Equations (5.30) and (5.32) are used to construct the discrete-time LPV controller.

The weighting functions in (5.19) and (5.20) are chosen for the LPV controller synthesis. Note that if we denote the spectral radius of a matrix by $\rho(\cdot)$, the invertibility condition (5.25) is guaranteed if the sampling time T satisfies [127]

$$T < 2\rho(A_c(\omega_m))^{-1}, \quad \forall \omega_m \in \Omega. \tag{5.33}$$

5

As mentioned before, the chosen sampling frequency needs to be consistent with the computing capability of the specific digital control system. For a continuous-time system and a corresponding discrete-time system, a higher sampling frequency produces a higher accuracy of the approximation of the two systems. This is illustrated in Fig. 5.20. Figs. 5.20a,b show the time responses of the continuous-time LPV current controller with the step changes of the rotor currents i_{rd} and i_{rq}, respectively. The time responses of the equivalent discrete-time LPV current controller are presented in Figs. 5.20c - 5.20g with different sampling frequencies. Figs. 5.20c,d present the time responses of the equivalent discrete-time LPV current controller with the sampling frequency of 4kHz corresponding to sampling time of $0.00025s$ (or $250ms$). Figs. 5.20e,f present the time responses of the equivalent discrete-time LPV current controller with the sampling frequency of 8kHz corresponding to sampling time of $0.000125s$ (or $125ms$). Meanwhile, Figs. 5.20g,h show the time responses of the equivalent discrete-time LPV current controller with the sampling frequency of 16kHz corresponding to sampling time of $0.00004s$ (or $40ms$).

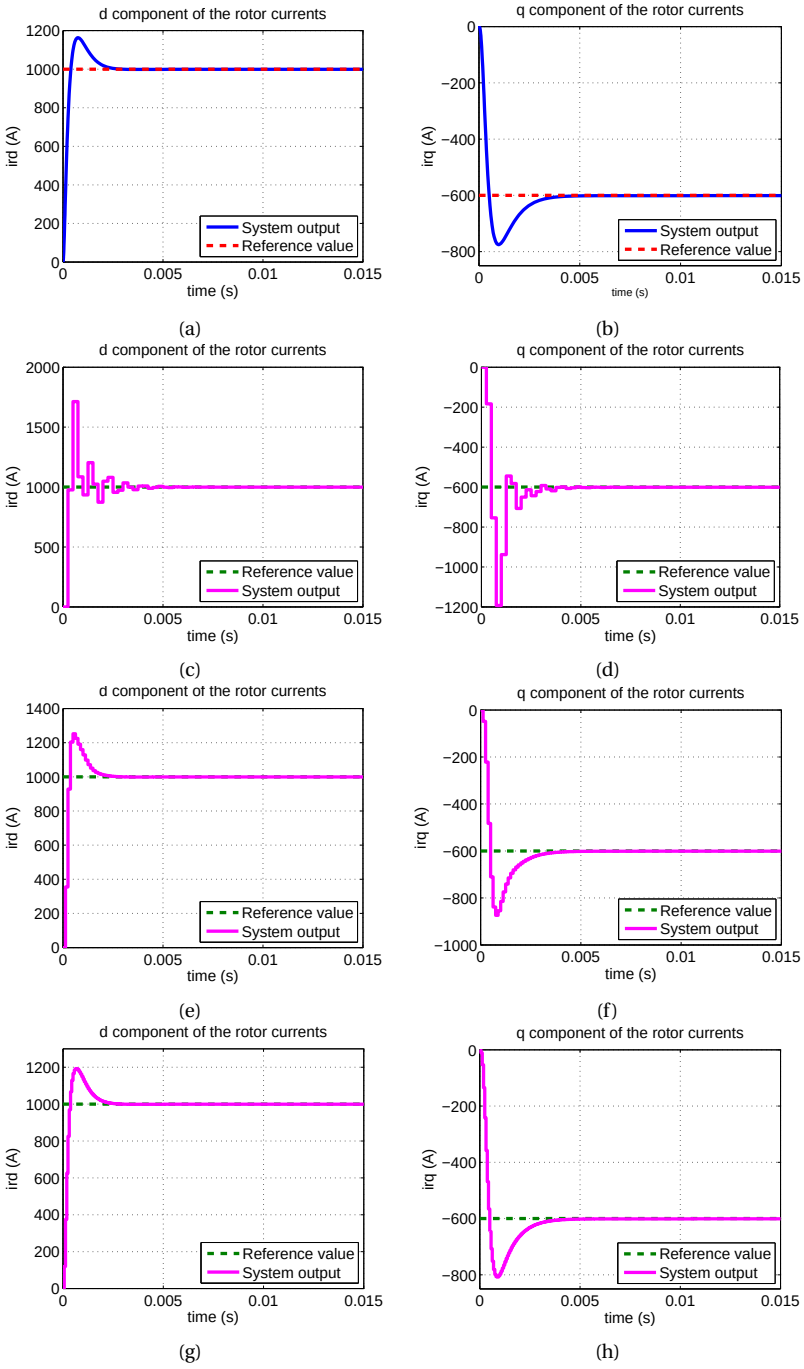

Figure 5.20: Time responses of the continuous-time and discrete-time LPV current controller with the step changes of the rotor currents. (a, b) continuous-time LPV controller, (c, d) discrete-time LPV controller with 4kHz sampling frequency, (e, f) discrete-time LPV controller with 8kHz sampling frequency, (g, h) discrete-time LPV controller with 16kHz sampling frequency

As can be seen in Fig. 5.20, although obtaining larger overshoots, the time responses of the equivalent discrete-time LPV current controller with the sampling frequency of 8kHz and 16kHz are considered to be a good approximation in comparison with that of the continuous-time LPV current controller. The closed-loop simulations lead to almost the same results as those shown in Fig. 5.15. Hence, these simulation results are not repeated here. On the other hand, the performance of the closed-loop system with the discrete-time LPV current controller corresponding to the sampling frequency of 4kHz is not close to that of the closed-loop system with the continuous-time LPV controller. Hence, the designed LPV current controller is only suitable for digital control systems with sampling frequency larger or equal to 8kHz.

In the real experimental setup presented in chapter 7 the maximal Pulse Width Modulation (PWM) frequency is specified at 8kHz by the manufacturer. However, the PWM frequency of 8kHz is too high to be implemented in the power module since it may lead to exceeding the power limit of the experimental system. Hence, the sampling frequency is set to 4kHz corresponding to a sampling time of $0.00025s$. As a result, the LPV controller is redesigned for this particular case of the laboratory test model in order to get a better approximation of the resulting discrete-time LPV controller. More details of the new design of the LPV controller will be given in Chapter 7.

The problem concerning the discretization of the continuous-time LPV controllers and the implementation in a real setup is also presented in [121, 128].

5.7. SUMMARY

In this chapter we presented the application of LPV control framework to the design of the rotor side current controller. First, H_∞ controllers are designed for different frozen values of the rotor angular speed. However, simulation results show that the performance of the H_∞ controller designed for a frozen value of ω_m is not guaranteed for other rotor angular speeds both for constant and fast parameter variations. Hence, in order to improve performance of the controlled system with respect to the rotor angular speed variations, a self-scheduled LPV current controller is designed in continuous-time domain. This design is based on viewing the mechanical angular speed as an uncertain yet online measurable parameter and on subsuming the problem into the framework of the LPV controller synthesis. The design objective is to achieve high robust dynamic performance for all admissible trajectories of the rotor speed in the operating range. After that, the existing continuous-time controller is replaced with an equivalent discrete-time controller that guarantees stability of the resulting digital control system for a consistent sampling frequency. This indirect discrete-time LPV controller design is significantly affected by the selected discretization method and the selected sampling interval. But this method also has advantages since it can be applied to any continuous-time design method and the bandwidth of the closed-loop system is known in advance.

Via simulation, it was shown that the designed LPV controller achieves the required performance specifications over the operating range of the rotor speed, and that the designed LPV controller can be implemented in a digital real time setup with sampling frequency larger or equal to 8kHz. In addition, robustness of the controlled system against

parameter changes as well as the impact of stator voltage dips on the robustness of the control system are also considered by means of some substantial simulation results. The controlled system with the LPV current controller is more robust with respect to machine parameter variations and in the presence of the stator voltage disturbance if compared to the conventional design with the deadbeat current controller.

However, as discussed in chapter 3, robustness of the system is not guaranteed only by simulation. Furthermore, since the stator and rotor inductances L_s, L_r, and the mutual inductance L_m are time-varying parameters, a rigorous robustness analysis is needed to investigate the stability of the system against parameter variations for both time-invariant and time-varying uncertainty cases. This will be the topic of the next chapter.

6

ROBUSTNESS ANALYSIS

Robustness of controlled systems could be demonstrated by means of simulation for several given values of the respective uncertain parameters [129, 32, 101]. Since such simulation results are not sufficient to confirm robustness with certainty, the structured singular value tool is adopted for robustness analysis against Linear Time-Invariant (LTI) uncertainties [130]. For Linear Time-Varying (LTV) parametric uncertainties, robustness analysis can be based on parameter-dependent Lyapunov functions if the system is, for example, depending affinely on slowly-varying parameters [131, 132]. As an extension of the classical multiplier theory, the Integral Quadratic Constraints (IQCs) approach [133, 134] provides a flexible way for robust stability analysis with both rate-bounded LTV parametric and dynamic uncertainties.

6.1. PROBLEM FORMULATION

In the DFIM model, the stator and rotor inductances L_s, L_r, and the mutual inductance L_m vary with the machine flux due to the magnetic saturation and winding current modulus [70]. As will be presented in the next sections, robust stability analysis can be performed for a common variation of all parameters. However, an investigation of closed-loop stability/performance subject to variations of individual machine parameters (while fixing the other three) is also useful in providing information about robustness of the controlled system in the controller design process. Figs. 6.1 and 6.2 depict, for instance, information on the performance of the controlled system for the LPV current controller with respect to rotor inductance variations in the range from 95% to 125% of its nominal value. Figs. 6.1a - 6.1d show the Bode plots of the transfer functions from the reference inputs i_r^{ref} to the outputs i_r, the reference inputs i_r^{ref} to the control errors e_r, the stator voltages v_s to the outputs i_r and the stator voltages v_s to the control errors e_r. Fig. 6.2a,b depict the step responses from the reference inputs i_r^{ref} to outputs i_r and control errors e_r, respectively. It can be observed that, in the face of the uncertainty, the perfor-

mance characteristics undergo some changes. Although the overshoots become larger, the system seems to remain robustly stable. This motivates a theoretically sound robust stability analysis as presented next.

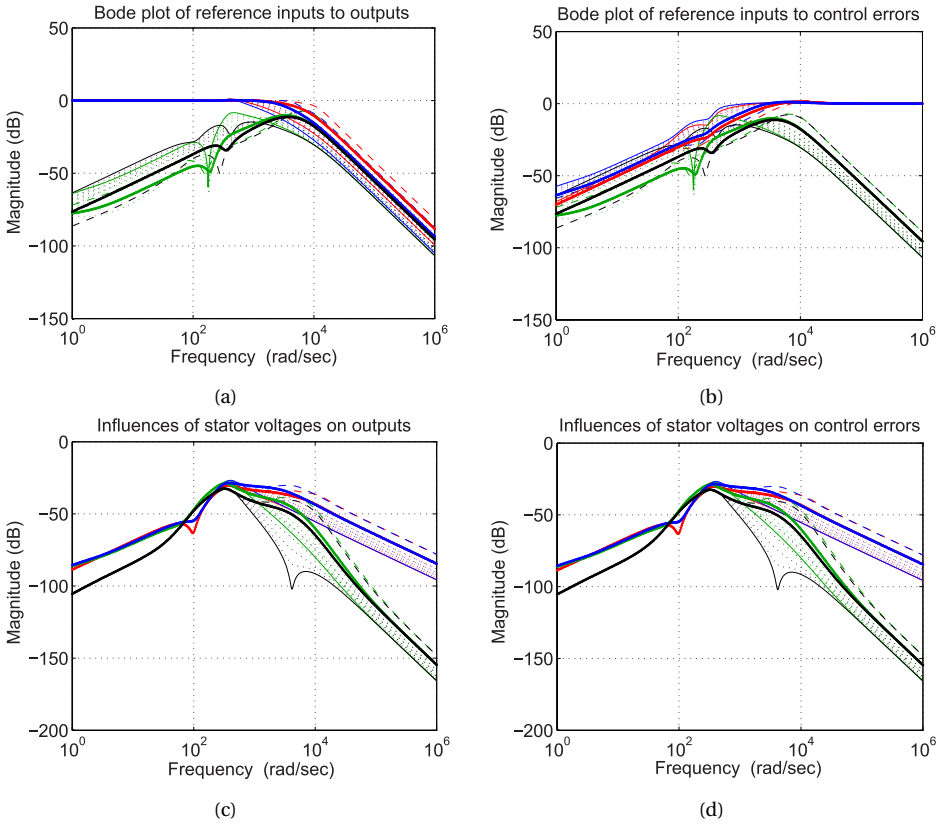

Figure 6.1: Performance of the controlled system with the LPV current controller subject to the rotor inductance variations from 95% to 125% of its nominal value in the frequency domain. Thick lines, dashed lines, solid lines, and dotted lines correspond with nominal, minimum, maximum, and intermediate values of the varying parameter, respectively.

6.1.1. STANDARD SETUP FOR ROBUSTNESS ANALYSIS

In this section $\mathscr{L}_c^{m\times n}$ denotes the set of all causal linear operators that map $L_2^n[0,\infty)$ into $L_2^m[0,\infty)$. Recall that, roughly, an operator is causal if the past output (at any current time) is not affected by any modification of the future of the input signal.

Let us now consider the standard setup for stability analysis as given in Fig. 6.3 where $M \in \mathscr{RH}_\infty^{p\times p}$ is a known causal linear time-invariant operator and $\Delta \in \mathscr{L}_c^{p\times p}$ is a general causal operator. For some set of uncertainties $\mathbf{\Delta} \subset \mathscr{L}_c^{p\times p}$ we say that M is robustly stable

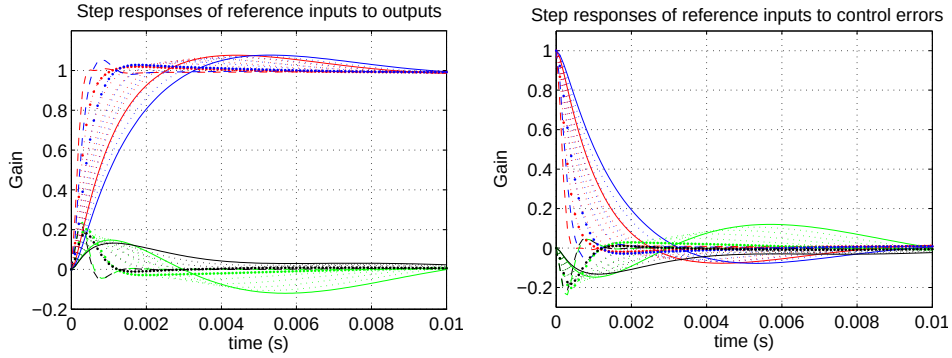

(a) (b)

Figure 6.2: Performance of the controlled system with the LPV current controller subject to the rotor inductance variations from 95% to 125% of its nominal value in the time domain. Thick lines, dashed lines, solid lines, and dotted lines correspond with nominal, minimum, maximum, and intermediate values of the varying parameter, respectively.

against $\mathbf{\Delta}$ if the feedback interconnection of M and Δ in Fig. 6.3 is well-posed ($I - M\Delta$ has a causal inverse) and stable ($(I - M\Delta)^{-1}$ has finite energy-gain) for all $\Delta \in \mathbf{\Delta}$.

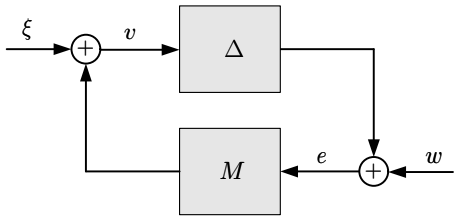

Figure 6.3: The standard setup for robust stability analysis

6.2. STRUCTURED SINGULAR VALUE ANALYSIS

The structured singular value, denoted by μ, is a powerful tool for robustness analysis against linear time-invariant (LTI) structured uncertainties [135, 136, 137].

For the standard set up as depicted in Fig. 6.3 and in view of the fact that we are considering parametric uncertainties, we define the structure of the uncertainty block in the scope of robustness analysis for the DFIM control as

$$\mathbf{\Delta} = \left\{\Delta = \text{diag}(\delta_1 I_{r_1}, ..., \delta_u I_{r_u}) : \delta_i \in \mathbb{R},\ i = 1, ..., u\right\} \tag{6.1}$$

where I_{r_i} is an $r_i \times r_i$ identity matrix. The size of the uncertainty $\Delta \in \mathbf{\Delta}$ is measured in

terms of the largest singular value as $\overline{\sigma}(\Delta)$. Since Δ is diagonal, let us recall that

$$\overline{\sigma}(\Delta) = \max_{i=1,\dots,u} |\delta_i|. \tag{6.2}$$

From the Nyquist theorem it is well-known that, for a stable system M in Fig. 6.3, the feedback interconnection is well-posed and stable if and only if

$$\det(I - M(j\omega)\Delta) \neq 0, \quad \forall \omega \in \mathbb{R} \cup \{\infty\}, \ \forall \Delta \in \mathbf{\Delta}. \tag{6.3}$$

Definition 6.2.1 *The structured singular value $\mu_{\mathbf{\Delta}}(\boldsymbol{M})$ of the complex matrix $\boldsymbol{M}$ with respect to the structure set $\mathbf{\Delta}$ is defined as the smallest $\overline{\sigma}(\Delta)$ that renders the matrix $I - \boldsymbol{M}\Delta$ singular, i.e.*

$$\mu_{\mathbf{\Delta}}(\boldsymbol{M}) = \frac{1}{inf\{\overline{\sigma}(\Delta) : \ \Delta \in \mathbf{\Delta}, \ \det(I - \boldsymbol{M}\Delta) = 0\}}, \tag{6.4}$$

and $\mu_{\mathbf{\Delta}}(\boldsymbol{M}) = 0$ if there is no $\Delta \in \mathbf{\Delta}$ such that $\det(I - \boldsymbol{M}\Delta) = 0$.

In view of (6.3), well-posedness and robust stability of the interconnection in Fig. 6.3 is hence guaranteed for all $\Delta \in \mathbf{\Delta}$ with

$$\overline{\sigma}(\Delta) < \left(\sup_{\omega \in \mathbb{R} \cup \{\infty\}} \mu_{\mathbf{\Delta}}(M(j\omega)) \right)^{-1}.$$

In the literature [110, 138, 139, 140], it is shown that exact calculation of the structured singular value is a very hard problem. Fortunately, lower and upper bounds can be computed efficiently with the μ-tools in Matlab [141].

If the DFIM parameters are considered to be time-invariant parametric uncertainties, then μ-analysis can be used to validate the robustness of the system as presented below.

6.2.1. THE SYSTEM REPRESENTATION WITH UNCERTAINTIES

In order to employ the μ-tools for robustness analysis of the controlled system with respect to the machine inductance uncertainties, we first pull the uncertainties out of the plant to get the standard $M - \Delta$ configuration as shown in Fig. 6.3.

Recalling that $a = \frac{1-\sigma}{\sigma}$, $\sigma = 1 - \frac{L_m^2}{L_s L_r}$, $T_s = \frac{L_s}{R_s}$, and $T_r = \frac{L_r}{R_r}$ (see chapter 2) the equations

in (2.17) and (2.18) read as

$$A_{rc} = \begin{pmatrix} \frac{-L_s^2R_r - L_m^2R_s}{\mathscr{E}_{rc}} & \omega_s - \omega_m & \frac{L_mR_s}{\mathscr{E}_{rc}} & -\frac{L_sL_m\omega_m}{\mathscr{E}_{rc}} \\ \omega_m - \omega_s & \frac{-(L_s^2R_r - L_m^2R_s}{\mathscr{E}_{rc}} & \frac{(L_sL_m\omega_m}{\mathscr{E}_{rc}} & \frac{L_mR_s}{\mathscr{E}_{rc}} \\ \frac{L_mR_s}{L_s} & 0 & -\frac{R_s}{L_s} & \omega_s \\ 0 & \frac{L_mR_s}{L_s} & -\omega_s & -\frac{R_s}{L_s} \end{pmatrix}, \tag{6.5}$$

$$B_{rc} = \begin{pmatrix} -\frac{L_sL_m}{\mathscr{E}_{rc}} & 0 & \frac{L_s^2}{\mathscr{E}_{rc}} & 0 \\ 0 & -\frac{L_sL_m}{\mathscr{E}_{rc}} & 0 & \frac{L_s^2}{\mathscr{E}_{rc}} \\ 1 & 0 & 0 & 0 \\ 0 & 1 & 0 & 0 \end{pmatrix} \tag{6.6}$$

where $\mathscr{E}_{rc} = L_s(L_sL_r - L_m^2)$.

Since the matrices of the state-space description in (2.17), and (2.18) depend rationally on the machine inductances L_s, L_r, and L_m, it is not difficult to obtain a Linear Fractional Representation (LFR) of the plant.

Equations (2.15) and (2.16) can now be expressed as

$$\boldsymbol{E}_{rc}\dot{x}_r = \boldsymbol{A}_{rc}x_r + \boldsymbol{B}_{rc}v_{rs}, \tag{6.7}$$

$$y_r = C_{rc}x_r \tag{6.8}$$

where

$$\boldsymbol{A}_{rc} = \begin{pmatrix} -L_s^2R_r - L_m^2R_s & -\mathscr{E}_{rc}(\omega - \omega_s) & L_mR_s & -L_mL_s\omega \\ \mathscr{E}_{rc}(\omega - \omega_s) & -L_s^2R_r - L_m^2R_s & L_mL_s\omega & L_mR_s \\ L_m(L_sL_r - L_m^2)R_s & 0 & -(L_sL_r - L_m^2)R_s & \mathscr{E}_{rc}\omega_s \\ 0 & L_m(L_sL_r - L_m^2)R_s & -\mathscr{E}_{rc}\omega_s & -(L_sL_r - L_m^2)R_s \end{pmatrix},$$

$$\boldsymbol{B}_{rc} = \begin{pmatrix} -L_mL_s & 0 & L_s^2 & 0 \\ 0 & -L_mL_s & 0 & L_s^2 \\ \mathscr{E}_{rc} & 0 & 0 & 0 \\ 0 & \mathscr{E}_{rc} & 0 & 0 \end{pmatrix},$$

$$\boldsymbol{E}_{rc} = \mathscr{E}_{rc}I_4 = \begin{pmatrix} \mathscr{E}_{rc} & 0 & 0 & \\ 0 & \mathscr{E}_{rc} & 0 & 0 \\ 0 & 0 & \mathscr{E}_{rc} & 0 \\ 0 & 0 & 0 & \mathscr{E}_{rc} \end{pmatrix}.$$

As discussed in Section 3.4, through simulation results it was shown that the closed-loop system is not sensitive to changes in the values of the resistances of the stator and the rotor. Hence, in this section, we are interested in robustness of the system against the machine inductances only.

Let $L_s = L_{sn} + L_{sv}$, $L_r = L_{rn} + L_{rv}$, $L_m = L_{mn} + L_{mv}$, where L_{rn}, L_{sn}, and L_{mn} are nominal values of the rotor, the stator and mutual inductances, $L_{sv} = \delta_s p_s$, $L_{rv} = \delta_r p_r$,

and $L_{mv} = \delta_m p_m$ express variations of the inductances, p_s, p_r, and p_m represent the relative perturbations of L_s, L_r, and L_m, respectively, and

$$-1 \leq \delta_r, \delta_s, \delta_m \leq 1. \tag{6.9}$$

We obtain the following LFR of the plant

$$\left(\begin{array}{c} \dot{x}_r \\ \hline z_r \\ \hline y_r \end{array}\right) = \left(\begin{array}{c|c|c} A_{rcs} & B_{rcu} & B_{rcv} \\ \hline C_{rcu} & D_{rsu} & D_{rcv} \\ \hline C_{rcs} & 0 & 0 \end{array}\right) \left(\begin{array}{c} x_r \\ \hline w_r \\ \hline v_{rs} \end{array}\right) \tag{6.10}$$

while the uncertainty block $\Delta_r \in \mathbb{R}^{48\times 48}$ admits the following description

$$w_r = \Delta_r z_r = \text{diag}\left(\delta_s I_8, \delta_r I_{12}, \delta_m I_{28}\right) z_r. \tag{6.11}$$

The details in constructing the LFT representation of the uncertain plant as well as the structure of the involved matrices are presented in Appendix A.

Let P_r be the transfer function from $\begin{pmatrix} w_r^T & v_{rs}^T \end{pmatrix}^T$ to $\begin{pmatrix} z_r^T & y_r^T \end{pmatrix}^T$ with the state-space realization of (A.3), i.e.

$$P_r \triangleq \left[\begin{array}{c|cc} A_{rcs} & B_{rcu} & B_{rcv} \\ \hline C_{rcu} & D_{rcu} & D_{rcv} \\ C_{rcs} & 0 & 0 \end{array}\right].$$

The LFR representation of the DFIM model with inductance uncertainties is depicted as Fig. 6.4.

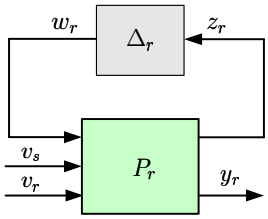

Figure 6.4: LFT representation of DFIM with the inductance uncertainties.

With the DFIM model with inductance uncertainties as depicted in Fig. 6.4, we can easily close the loop with the LPV current controller at a fixed value of the rotor angular speed ω_m (see Fig. 6.5a) and get the standard setup for μ analysis as depicted in Fig. 6.5b, where M_r is the transfer function from w_r to z_r.

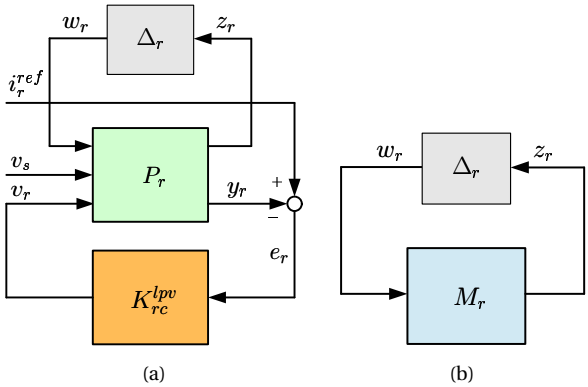

Figure 6.5: The standard M-Δ configuration with the controller K_{rc} (a) and the standard setup for μ analysis (b).

6.2.2. ROBUSTNESS ANALYSIS

The uncertainty structure fits into the framework of Section 6.2. Since M_r is known to be stable and due to the normalization (6.9), robust stability is guaranteed if the structured singular value satisfies $\mu_{\mathbf{\Delta}}(M_r(j\omega)) < 1$ for all $\omega \in \mathbb{R} \cup \{\infty\}$.

In order to guarantee operation of the controlled system, the designed controller is expected to maintain stability when the inductances vary around 5% - 10% of their nominal values.

Robust stability of the controlled system up to 5% uncertainty in the stator inductance, 7% uncertainty in the rotor inductance, and 5% uncertainty in the mutual inductance at speed $\omega_m = 300$rad/s is investigated by setting $p_s = 0.05L_s$, $p_r = 0.07L_r$, and $p_m = 0.05L_m$. The frequency responses of the upper and lower bounds of the structured singular value μ over the frequency interval $[0, 1000]$ are shown in Fig. 6.6. The maximum value of μ is 0.77 which means that the controlled system remains stable as long as the deviations of L_s, L_r and L_m from their nominal values obey the above bounds.

6.3. IQC-BASED ROBUST STABILITY ANALYSIS

In case that $\Delta \in \mathscr{L}_c^{p\times p}$ in the standard set-up in Fig. 6.3 is a general causal and bounded uncertainty, one cannot apply the structured singular value test for robustness analysis. We are particularly interested in the problem of analyzing robustness against rate-bounded time-varying parametric uncertainties as appearing in our DFIM model. An effective solution for such problems is to use the IQC approach for robust stability analysis as presented next.

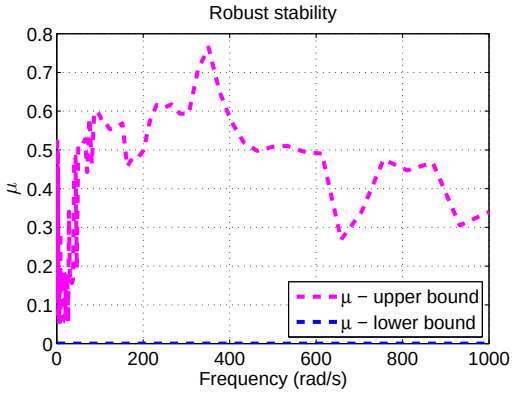

Figure 6.6: Robust stability analysis with 5% uncertainty in the stator inductance, 7% uncertainty in the rotor inductance, and 5% uncertainty in the mutual inductance.

6.3.1. THE IQC FRAMEWORK

In this section we first formulate the general IQC stability theorem which is based on a frequency-domain inequality that involves so-called multipliers. Next, by using the swapping lemma [134, 142, 143], we develop a class of multipliers which is tailored to robustness analysis for rate-bounded parametric uncertainties. With the help of the Kalman-Yakubovich-Popov lemma, one can translate the to-be-verified frequency-domain inequality into an LMI. Since both the values and the rate-of-variation of the parameters are contained in a polytope, it is finally shown how robustness analysis can be carried out on the basis of the so-called convex-hull relaxation.

In the configuration of Fig. 6.3 let us first suppose that $\Delta \in \mathscr{L}_c^{p\times p}$ is a general causal and bounded uncertainty. Under the assumption of well-posedness, the following results provides a computational test for verifying stability.

Theorem 6.3.1 (IQC stability theorem [133]) *Let* $\Pi = \begin{pmatrix} \Pi_{11} & \Pi_{12} \\ \Pi_{12}^* & \Pi_{22} \end{pmatrix}$ *be an IQC multiplier, a rational matrix-valued function that is Hermitian and bounded on the extended imaginary axis and that satisfies*

$$\int_{-\infty}^{\infty} \begin{pmatrix} \hat{z}(j\omega) \\ \tau\widehat{\Delta z}(j\omega) \end{pmatrix}^* \Pi(j\omega) \begin{pmatrix} \hat{z}(j\omega) \\ \tau\widehat{\Delta z}(j\omega) \end{pmatrix} \geq 0 \quad \forall \tau \in [0,1], \ \ \forall z \in L_2^p[0,\infty). \tag{6.12}$$

Then the feedback system of Fig. 6.3 is stable if the following conditions hold:

(i) $I - \tau M\Delta$ *has a casual inverse for all* $\tau \in [0,1]$ *(well-posedness).*
(ii) The following frequency-domain inequality holds:

$$\begin{pmatrix} M(j\omega) \\ I_p \end{pmatrix}^* \Pi(j\omega) \begin{pmatrix} M(j\omega) \\ I_p \end{pmatrix} < 0 \quad \forall \omega \in [0,\infty]. \tag{6.13}$$

The verification of the frequency domain inequality (6.13) can be transformed into checking the feasibility of an LMI by employing the following version of the Kalman-Yakubovich-Popov (KYP) lemma [144].

Lemma 6.3.2 *For $A \in \mathbb{R}^{n\times n}$, $B \in \mathbb{R}^{n\times m}$, $C \in \mathbb{R}^{k\times n}$, $D \in \mathbb{R}^{k\times m}$, $P = P^T \in \mathbb{R}^{k\times k}$, with $\det(j\omega I - A) \neq 0$ for all $\omega \in \mathbb{R}$, the following two statements are equivalent:*

(i) There exists a matrix $K = K^T \in \mathbb{R}^{n\times n}$ such that

$$\begin{pmatrix} I & 0 \\ A & B \end{pmatrix}^T \begin{pmatrix} 0 & K \\ K & 0 \end{pmatrix} \begin{pmatrix} I & 0 \\ A & B \end{pmatrix} + \begin{pmatrix} C & D \end{pmatrix}^T P \begin{pmatrix} C & D \end{pmatrix} \prec 0.$$

(ii) For all $\omega \in [0,\infty]$ one has

$$[C(j\omega I - A)^{-1}B + D]^* P [C(j\omega I - A)^{-1}B + D] \prec 0$$

We will see that the KYP lemma 6.3.2 is a useful tool for numerically checking robust stability by solving a semi-definite program.

6.3.2. ROBUSTNESS AGAINST TIME-VARYING RATE-BOUNDED PARAMETRIC UNCERTAINTIES

In this work we apply a particular IQC test for time-varying parametric uncertainties. For this purpose let us consider the set of all operators Δ_r that are defined by multiplication with the structured matrix

$$\operatorname{diag}(\delta_1(t) I_{r_1}, \ldots, \delta_u(t) I_{r_u}) \tag{6.14}$$

in which the time-varying parameter $\delta_i(t)$ and its rate-of-variation $\dot{\delta}_i(t)$ are suitably bounded for $t \geq 0$ and $i = 1, \ldots, u$. The development relies on the so-called swapping lemma [134, 142], or more specifically on the following generalized version of this auxiliary result as given in [143, 145].

Lemma 6.3.3 (Swapping lemma) *For a given transfer matrix $G_l = diag(G_1, \ldots, G_u)$ with $G_i = \left[\begin{array}{c|c} A_{G_i} & B_{G_i} \\ \hline C_{G_i} & D_{G_i} \end{array}\right] \in \mathscr{RH}_\infty^{l_i \times r_i}$, $A_{G_i} \in \mathbb{R}^{k_i \times k_i}$ (Hurwitz), $B_{G_i} \in \mathbb{R}^{k_i \times r_i}$, $C_{G_i} \in \mathbb{R}^{l_i \times k_i}$, $D_{G_i} \in \mathbb{R}^{l_i \times r_i}$ introduce, for $i = 1, \ldots, u$,*

$$G_{B_i} \triangleq \left[\begin{array}{c|c} A_{G_i} & B_{G_i} \\ \hline I & 0 \end{array}\right], \; G_B \triangleq diag(G_{B_1}, \ldots, G_{B_u}), \; G_{er} \triangleq \begin{pmatrix} G_l \\ G_B \end{pmatrix}$$

and

$$G_{C_i} \triangleq \left[\begin{array}{c|c} A_{G_i} & I \\ \hline C_{G_i} & 0 \end{array}\right], \; G_C \triangleq diag(G_{C_1}, \ldots, G_{C_u}), \; G_{el} \triangleq \begin{pmatrix} G_l & G_C \\ 0 & I \end{pmatrix}.$$

If Δ_l and V_{Δ_k} denote the operators defined by multiplication with

$$diag(\delta_1(t) I_{l_1}, \ldots, \delta_u(t) I_{l_u}) \;\; and \;\; diag(\dot{\delta}_1(t) I_{k_1}, \ldots, \dot{\delta}_u(t) I_{k_u})$$

and if introducing

$$\Delta_{er} \triangleq \begin{pmatrix} \Delta_r \\ V_{\Delta_k} G_B \end{pmatrix} \text{ and } \Delta_{el} \triangleq \begin{pmatrix} \Delta_l & 0 \\ 0 & V_{\Delta_k} \end{pmatrix}$$

then

$$G_{el}\Delta_{er} = \Delta_{el} G_{er}. \tag{6.15}$$

Note that (6.15) is expressed as an operator composition identity. It reveals the commutation property of the linear operators G_{el} and G_{er} with the time-varying uncertainties Δ_{er} and Δ_{el}, respectively as illustrated in Fig. 6.7.

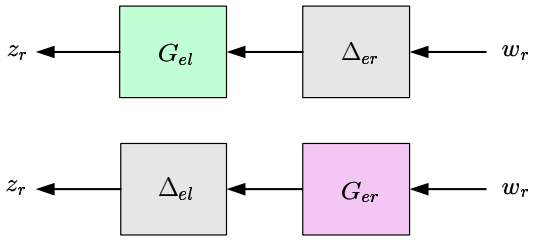

Figure 6.7: Illustration of commutation property (6.15).

This preparation allows us to present the key idea of the suggested approach. Obviously, the interconnection in Fig. 6.3 is well-posed and stable for $\Delta = \Delta_r$ iff the same holds true for the pair

$$M_e \triangleq \begin{pmatrix} M & 0_{r_e \times k_e} \end{pmatrix} \text{ and } \Delta_{er} = \begin{pmatrix} \Delta_r \\ V_{\Delta_k} G_B \end{pmatrix}$$

with $r_e = \sum_{i=1}^{u} r_i$, and $k_e = \sum_{i=1}^{u} k_i$. This motivates us to determine a suitable set of IQC multipliers for Δ_{er}. With real matrices $X_e = X_e^T$, Y_e, $U_e = U_e^T$ we choose the multiplier structure as

$$\Pi_e = \begin{pmatrix} G_{er} & 0 \\ 0 & G_{el} \end{pmatrix}^* \begin{pmatrix} X_e & Y_e \\ Y_e^T & U_e \end{pmatrix} \begin{pmatrix} G_{er} & 0 \\ 0 & G_{el} \end{pmatrix} = \begin{pmatrix} G_{er}^* X_e G_{er} & G_{er} Y_e G_{el} \\ G_{el}^* Y_e^T G_{er} & G_{el}^* U_e G_{el} \end{pmatrix}.$$

For any z of finite energy (and compatible dimension) we exploit (6.15) to infer

$$\begin{pmatrix} G_{er} & 0 \\ 0 & G_{el} \end{pmatrix} \begin{pmatrix} I \\ \Delta_{er} \end{pmatrix} z = \begin{pmatrix} G_{er} \\ G_{el}\Delta_{er} \end{pmatrix} z = \begin{pmatrix} G_{er} \\ \Delta_{el} G_{er} \end{pmatrix} z = \begin{pmatrix} I \\ \Delta_{el} \end{pmatrix} G_{er} z.$$

We then clearly infer that (6.12) holds true in case that

$$\begin{pmatrix} I \\ \tau\Delta_{el}(t) \end{pmatrix}^T \begin{pmatrix} X_e & Y_e \\ Y_e^T & U_e \end{pmatrix} \begin{pmatrix} I \\ \tau\Delta_{el}(t) \end{pmatrix} \geq 0 \text{ for all } t \geq 0,\ \tau \in [0,1], \tag{6.16}$$

where, with some abuse of notation, we denote the matrix which defines Δ_{el} by

$$\Delta_{el}(t) = \begin{pmatrix} \mathrm{diag}(\delta_1(t) I_{l_1}, ..., \delta_u(t) I_{l_u}) & 0 \\ 0 & \mathrm{diag}(\dot{\delta}_1(t) I_{k_1}, ..., \dot{\delta}_u(t) I_{k_u}) \end{pmatrix}. \tag{6.17}$$

Whenever we have found matrices $X_e = X_e^T$, Y_e, $U_e = U_e^T$ with (6.16), we can then apply Theorem 6.13 and guarantee stability by the frequency-domain inequality

$$\begin{pmatrix} G_{er}(j\omega) M_e(j\omega) \\ G_{el}(j\omega) \end{pmatrix}^* \begin{pmatrix} X_e & Y_e \\ Y_e^T & U_e \end{pmatrix} \begin{pmatrix} G_{er}(j\omega) & 0 \\ 0 & G_{el}(j\omega) \end{pmatrix} \begin{pmatrix} M_e(j\omega) \\ I \end{pmatrix} \prec 0 \quad \forall \omega \in [0, \infty]. \tag{6.18}$$

It is remarkable to observe that (6.16) and (6.18) for $\omega = \infty$ do actually imply that $I - M_e(\infty)\Delta_{el}(t) = I - M(\infty)\Delta_r(t)$ is non-singular for all $t \geq 0$, which means that the configuration in Fig. 6.3 is actually well-posed. Therefore, there is in fact no need to verify well-posedness separately.

If we introduce the state-space realization of the outer factor as

$$\begin{pmatrix} G_{er} M_e \\ G_{el} \end{pmatrix} = \left[\begin{array}{c|c} A_L & B_L \\ \hline C_L & D_L \end{array}\right] \text{ with stable } A_L \in \mathbb{R}^{d \times d}, \tag{6.19}$$

the KYP lemma reduces verification of (6.18) to the existence of a solution $K = K^T$ of the LMI

$$\begin{pmatrix} I & 0 \\ A_L & B_L \end{pmatrix}^T \begin{pmatrix} 0 & K \\ K & 0 \end{pmatrix} \begin{pmatrix} I & 0 \\ A_L & B_L \end{pmatrix} + \begin{pmatrix} C_L^T \\ D_L^T \end{pmatrix} \begin{pmatrix} X_e & Y_e \\ Y_e^T & U_e \end{pmatrix} \begin{pmatrix} C_L & D_L \end{pmatrix} \prec 0. \tag{6.20}$$

Let us finally describe the concrete construction of the LMI tests that are used for computations in the sequel. For this purpose suppose that $\mathbf{\Delta}$ is the set of all multiplication operators defined with (6.14) where the parameter values $\delta_i(t)$ and their rate-of-variations $\vartheta_i(t) = \dot{\delta}_i(t)$ are, for $t \geq 0$, contained in the hyper-rectangular region

$$\mathscr{R}_i = \left\{ (x_i, y_i) : x_i \in [\underline{\delta}_i, \overline{\delta}_i], y_i \in [\underline{\vartheta}_i, \overline{\vartheta}_i] \right\} = \mathrm{co}\, \mathscr{R}_i^c \tag{6.21}$$

with $\underline{\delta}_i \leq 0 \leq \overline{\delta}_i$, $\underline{\vartheta}_i \leq 0 \leq \overline{\vartheta}_i$ and

$$\mathscr{R}_i^c = \left\{ (\delta_i^{(1)}, \vartheta_i^{(1)}),\ (\delta_i^{(2)}, \vartheta_i^{(2)}),\ (\delta_i^{(3)}, \vartheta_i^{(3)}),\ (\delta_i^{(4)}, \vartheta_i^{(4)}) \right\}$$

for $i = 1, ..., u$.

With the finite set of generators

$$\Delta_{el}^c \triangleq \{ \mathrm{diag}(\delta_1^{(i_1)} I_{l_1}, ..., \delta_u^{(i_u)} I_{l_v}, \vartheta_1^{(i_1)} I_{k_1}, ..., \vartheta_u^{(i_u)} I_{k_v}) :\ (\delta_i^{(i_i)}, \vartheta_i^{(i_i)}) \in \mathscr{R}_i^c,\ i = 1, ..., u \}$$

we then infer that the matrices (6.17) actually satisfy the constriant

$$\Delta_{el}(t) \in \mathrm{co}\left(\Delta_{el}^c\right) \text{ for } t \geq 0.$$

Hence, a simple convexity argument implies that (6.16) holds true if

$$U_{e_1} \preceq 0,\ \ U_{e_2} \preceq 0,\ \ \begin{pmatrix} I \\ \Delta_{el} \end{pmatrix}^T \begin{pmatrix} X_e & Y_e \\ Y_e^T & U_e \end{pmatrix} \begin{pmatrix} I \\ \Delta_{el} \end{pmatrix} \succeq 0 \quad \forall \Delta_{el} \in \Delta_{el}^c, \tag{6.22}$$

where U_{e_1} and U_{e_2} denote the left-upper and right-lower diagonal blocks of U_e of dimensions $\sum_{i=1}^u l_i$ and $\sum_{i=1}^u k_i$ respectively.

Finally, it remains to specify the dynamics G_l. For this purpose we recall that, with any pole location $p_i > 0$, linear combinations of the stable transfer functions 1, $(s+p_i)^{-1}$,...,$(s+p_i)^{-q_i}$ can apporoximate any function in $\mathscr{RH}_\infty$ arbitrarily closely in the $\mathscr{H}_\infty$-norm, if only the integer q_i is chosen sufficiently large. The density property of these basis functions hence motivates the generic choice

$$G_i(s) = \begin{pmatrix} I_{r_i} \\ (s+p_i)^{-1} I_{r_i} \\ \cdots \\ (s+p_i)^{-q_i} I_{r_i} \end{pmatrix} \text{ with minimal realization } \left[\begin{array}{c|c} A_{G_i} \otimes I_{r_i} & B_{G_i} \otimes I_{r_i} \\ \hline C_{G_i} \otimes I_{r_i} & D_{G_i} \otimes I_{r_i} \end{array}\right]$$

where

$$\left(\begin{array}{c|c} A_{G_i} & B_{G_i} \\ \hline C_{G_i} & D_{G_i} \end{array}\right) = \left(\begin{array}{ccccc|c} -p_i & 0 & \cdots & \cdots & 0 & 1 \\ 1 & -p_i & \ddots & \vdots & \vdots & 0 \\ 0 & 1 & \ddots & \ddots & \vdots & \vdots \\ \vdots & \ddots & \ddots & -p_i & 0 & \vdots \\ 0 & \cdots & \cdots & 1 & -p_i & 0 \\ \hline & & 0 & & & 1 \\ & & I_{q_i} & & & 0 \end{array}\right) \tag{6.23}$$

for $i = 1,...,u$. After fixing q_i we can then construct realizations of G_l, G_{er}, G_{el} and hence of (6.19) as required for the implementation of the LMI (6.20). Note that q_i defines the parameters

$$l_i = (q_i+1)r_i \ \text{ and } \ k_i = q_i r_i$$

which specifies the dimensions of the matrices Δ_{le}, X_e, Y_e and U_e in (6.22). This constructions leads us to the following main result of this section.

6

Theorem 6.3.4 ([145]) *The configuration in Fig. 6.3 is well-posed and stable for all $\Delta \in \mathbf{\Delta}$ if there exist symmetric matrices K, X_e, U_e and a real matrix Y_e which satisfy (6.22) and (6.20).*

It is to be stressed that (6.22) and (6.20) form a finite system of standard LMIs that can be directly implemented. Clearly the choice of q_i influences the McMillan degree of G_i and, hence, the size of the LMI (6.20). Care has to be taken in choosing q_i not too large in practice. It is important to emphasize that we explicitly allow for $q_i = 0$ which implies $G_i(s) = I_{r_i}$ and $l_i = r_i$ as well as $k_i = 0$. Then the robustness test does not involve any bound on the rate-of-variation of the parameter and is based on a static multiplier. This corresponds to the situation that the parameteric uncertainties can actually vary arbitrarily fast in time.

6.4. ROBUSTNESS ANALYSIS OF THE CONTROLLED SYSTEM

6.4.1. STABILITY MARGINS

For constructing the LFR of the uncertain system, we can use the same technique as presented in Appendix A. However, the size of uncertainty sets is large if no reduction method is applied to yield reduced-order uncertainty matrices. Hence we employ the Robust Control Toolbox in Matlab [146] in order to extract certain and uncertain components of the system. When we use the numerical reduction method in the robust control toolbox, which is similar to truncated balanced realizations, we note that the order of the uncertainty matrices will be reduced significantly.

In general, the LFT representation of the plant is depicted as in Fig. 6.8, where the uncertainty matrix Δ_{rp} of the uncertain plant can be described as

$$\Delta_{rp} = \text{diag}\left(\delta_s I_{r_s}, \delta_r I_{r_r}, \delta_m I_{r_m}, \delta_\omega I_{r_\omega}\right), \tag{6.24}$$

in which r_s, r_r, r_m, and r_ω are the dimensions of the uncertainty blocks corresponding to the machine inductances L_s, L_r, L_m, and the rotor speed ω_m, respectively. The sizes of the resulting uncertainty matrices for the different parameters are summarized in Table 6.1. Note that the tests for the stability margin of the closed-loop system are performed for L_s, L_r, L_m, and ω_m, respectively as well as for the combination of each machine inductance with the rotor speed ω_m. Other combinations with more than two parameters result in very large uncertainty matrices. As a result, the time consumed for solving optimization problems is increased considerably.

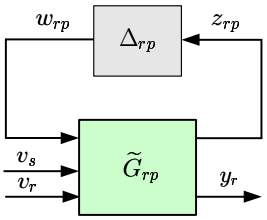

Figure 6.8: General LFT representation of the plant

The LFT representation of the LPV controller is constructed similarly. From the polytopic controller description (5.22) we have

$$K_{rc}^{lpv} = \frac{\omega_s(1+p_\omega)-\omega_m}{2\omega_s p_\omega} K_{rc1} + \frac{\omega_m-\omega_s(1-p_\omega)}{2\omega_s p_\omega} K_{rc2}. \tag{6.25}$$

Hence, the LFT representation of the LPV controller with respect to the rotor speed ω_m in (6.25) can be depicted as in Fig. 6.9, where the resulting uncertainty matrix Δ_{rk} is described as follows:

Table 6.1: Uncertainties and matrices

Uncertainties	Uncertainty matrix Δ_{rp} size
L_s	4×4 ($r_s=4$, $r_r=0$, $r_m=0$, $r_\omega=0$)
L_r	2×2 ($r_s=0$, $r_r=2$, $r_m=0$, $r_\omega=0$)
L_m	6×6 ($r_s=0$, $r_r=0$, $r_m=6$, $r_\omega=0$)
ω_m	2×2 ($r_s=0$, $r_r=0$, $r_m=0$, $r_\omega=2$)
L_s and ω_m	8×8 ($r_s=4$, $r_r=0$, $r_m=0$, $r_\omega=4$)
L_r and ω_m	6×6 ($r_s=0$, $r_r=2$, $r_m=0$, $r_\omega=4$)
L_m and ω_m	10×10 ($r_s=0$, $r_r=0$, $r_m=6$, $r_\omega=4$)

$$\Delta_{rk}=\delta_\omega I_6. \tag{6.26}$$

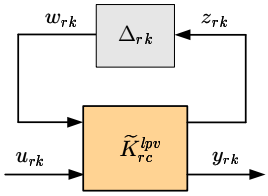

Figure 6.9: LFT representation of the LPV controller with respect to the rotor speed

The LFR of the plant and the LPV rotor current controller as well as the interconnection of the closed-loop system is depicted in Fig. 6.10.

Based on the configuration depicted in Fig. 6.10 we can easily construct the standard configuration as in Fig. 6.3 for testing robust stability of the LPV-controlled system within the above given IQC-framework.

For this purpose, we describe the machine inductances, the rotor mechanical speed ω_m, and their variations as uncertainties in a convex hull as in (6.21). The result in Theorem 6.3.4 is then implemented with the help of YALMIP, a toolbox [147] for rapid prototyping of optimization problems. The obtained results are summarized in Table 6.2. For the purpose of investigating the stability margin of the controlled system in the face of only one parameter variation, the tests 1, 2, 3, and 4 are performed for L_s, L_r, L_m, ω_m, and their variations, respectively. The LFR of the closed-loop system is constructed with the help of the robust control toolbox, while the corresponding region-of-variation (6.21) is re-constructed for each of the respective parameter variations. The results show that the closed-loop system remains stable when L_s varies from 90.5% to 117.33% of its nominal value while its rate varies in $[0, 0.645]$. The same conclusions are drawn, with the respective numerical results in Table 6.2, for variations in L_r, L_m and ω_m respectively. Note that the stability region for the mechanical rotor speed ω_m is quite large, even if

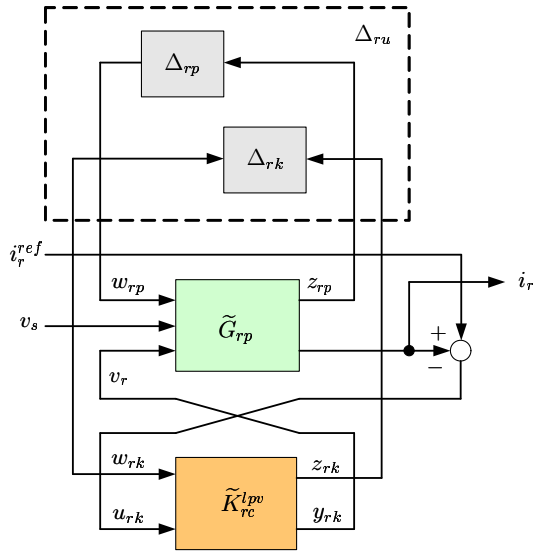

Figure 6.10: The interconnection of the closed-loop controlled system

allowing for very fast variations. This is indeed consistent with the controller design algorithm which is based on the assumption of arbitrary fast variation. The tests 5, 6, and 7 are performed in the same fashion but for the uncertainties of ω_m in combination with L_s, L_r, and L_m, respectively. It is interesting to observe that, in these cases, the stability of the system is no longer guaranteed for arbitrary fast variation of the mechanical rotor speed ω_m. Its rate-of-variation has to be decreased to $[0,125]$ in the tests 5, 7 and to $[0,250]$ in the test 6, respectively, while its range-of-variation decrease to $[65\%,135\%]$. Still, these margins for the mechanical rotor speed ω_m are in line with the practical need of tolerating up to $[70\%,130\%]$ of its nominal synchronous speed value.

6.4.2. RATE-OF-VARIATIONS

The analysis results presented in Table 6.2 are obtained by, first, letting the rate-of-variation $\dot{\delta}_s$, $\dot{\delta}_r$, $\dot{\delta}_m$, and $\dot{\delta}_\omega$ be zero. After that we find the maximum values of $\dot{\delta}_s$, and/or $\dot{\delta}_r$, $\dot{\delta}_m$, $\dot{\delta}_\omega$ such that the system remains stable.

In the following tests we further evaluate the stability margin of the system with respect to rate-of-variations of the parameters. The stability margins with respect to rate-of-variations on L_s, L_r, and L_m are shown in Figs. 6.11, 6.12, and 6.13. Obviously, the stability margins decrease when the rate of variation increases.

Table 6.2: Stability margins for LPV controller

Tests	Uncertainties	Uncertainty matrix size	Stability margins	
			Ranges of variation	Rates
1	L_s	4×4	90.50% – 111.73%	0 – 0.645
2	L_r	2×2	90.50% – 111.72%	0 – 0.042
3	L_m	6×6	92.50% – 105.10%	0 – 0.033
4	ω_m	8×8	26.5% – 173.5%	0 – 600000
5	L_s and ω_m L_s ω_m	 4×4 10×10	 91% – 109% 65% – 135%	 0 – 0.01 0 – 125
6	L_r and ω_m L_r ω_m	 2×2 10×10	 90.50% – 109.50% 65.00% – 135.00%	 0 – 0.01 0 – 250
7	L_m and ω_m L_m ω_m	 6×6 10×10	 93% – 105% 65% – 135%	 0 – 0.01 0 – 125

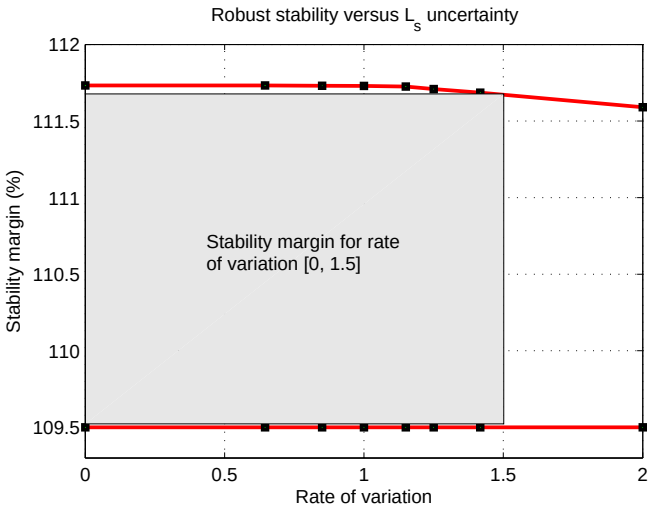

Figure 6.11: The stability margins decrease when the rate of variation of L_s increases

6.5. ROBUSTNESS ANALYSIS OF DEADBEAT CURRENT CONTROLLER

The robustness analysis for the deadbeat current controller designed in Chapter 3 is carried out in the same fashion as presented in Section 6.4. Recall that, in the deadbeat controller design, the rotor angular speed ω_m is treated as the scheduling parameter and the deadbeat controller is computed online for each sampling period. Furthermore, the dis-

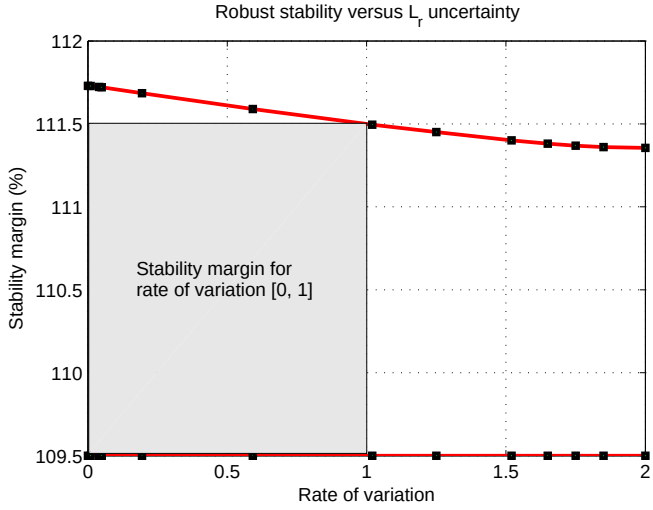

Figure 6.12: The stability margins decrease when the rate of variation of L_r increases

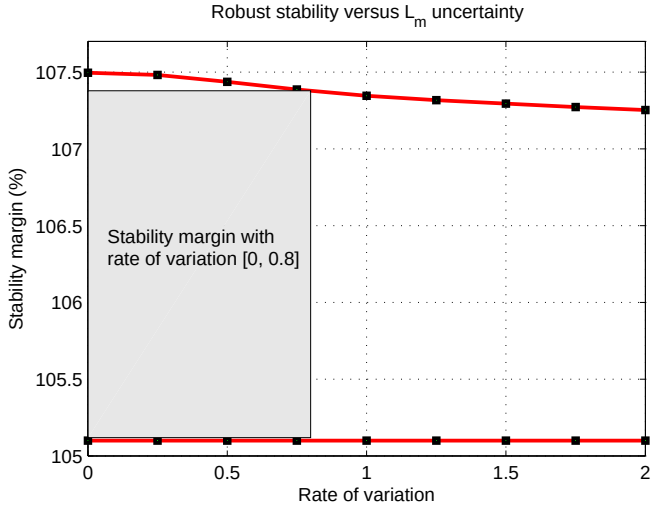

Figure 6.13: The stability margins decrease when the rate of variation of L_m increases

turbance matrix $\boldsymbol{D}_f$ in (3.34) is also a parameter-dependent transfer matrix. Hence, for the purpose of robustness analysis, we need to derive an LFT representations for both the deadbeat controller K_{rc}^{db} and the parameter-dependent transfer matrix $\boldsymbol{D}_f$. Note that the robustness analysis for the deadbeat current controller is implemented in the discrete-time domain.

Let u_{kd} be the controller input and y_{kd} the controller output. From equation (3.48) we have

$$\begin{aligned} y_{kd} &= K_{rc}^{db} u_{kd} = \mathbf{B}_{rc}^{-1}\left(I - z^{-1}\mathbf{A}_{rc}\right)\frac{1}{1-z^{-2}}u_{kd} \\ &= \begin{pmatrix} \dfrac{\frac{\sigma L_r}{T} - z^{-1}\frac{\sigma L_r}{T}\left[1 - T\left(\frac{a+1}{T_r} + \frac{a}{T_s}\right)\right]}{1-z^{-2}} & -\dfrac{\sigma L_r(\omega_s - \omega_m)}{1-z^{-2}} \\ \dfrac{\sigma L_r(\omega_s - \omega_m)}{1-z^{-2}} & \dfrac{\frac{\sigma L_r}{T} - z^{-1}\frac{\sigma L_r}{T}\left[1 - T\left(\frac{a+1}{T_r} + \frac{a}{T_s}\right)\right]}{1-z^{-2}} \end{pmatrix} u_{kd} \end{aligned}$$

With $\omega_m = \omega_{mn} + \delta_\omega p_\omega$ we can write

$$\begin{aligned} y_{kd} &= \begin{pmatrix} \dfrac{\frac{\sigma L_r}{T} - z^{-1}\frac{\sigma L_r}{T}\left[1 - T\left(\frac{a+1}{T_r} + \frac{a}{T_s}\right)\right]}{1-z^{-2}} & -\dfrac{\sigma L_r(\omega_s - \omega_{mn})}{1-z^{-2}} \\ \dfrac{\sigma L_r(\omega_s - \omega_{mn})}{1-z^{-2}} & \dfrac{\frac{\sigma L_r}{T} - z^{-1}\frac{\sigma L_r}{T}\left[1 - T\left(\frac{a+1}{T_r} + \frac{a}{T_s}\right)\right]}{1-z^{-2}} \end{pmatrix} u_{kd} \\ &\quad + \delta_\omega \begin{pmatrix} 0 & -\dfrac{\sigma L_r p_\omega}{1-z^{-2}} \\ \dfrac{\sigma L_r p_\omega}{1-z^{-2}} & 0 \end{pmatrix} u_{kd} \\ &= E_{dw}u_{kd} + \delta_\omega F_{dw}u_{kd} = E_{dw}u_{kd} + w_{kd} \end{aligned}$$

where

$$\begin{aligned} w_{kd} &= \delta\omega F_{dw}u_{kd} = \delta_\omega z_{kd}, \\ z_{kd} &= F_{dw}u_{kd}. \end{aligned}$$

Thus

$$\begin{aligned} \begin{pmatrix} z_{kd} \\ y_{kd} \end{pmatrix} &= \begin{pmatrix} 0 & F_{dw} \\ I & E_{dw} \end{pmatrix}\begin{pmatrix} w_{kd} \\ u_{kd} \end{pmatrix}, \\ w_{kd} &= \begin{pmatrix} \delta_\omega & 0 \\ 0 & \delta_\omega \end{pmatrix} z_{kd} = \Delta_{kd} z_{kd}. \end{aligned}$$

The LFT representation of the deadbeat controller with respect to the rotor speed ω_m uncertainty can be depicted as in Fig. 6.14.

The LFT representation of the parameter-dependent transfer matrix $\boldsymbol{D}_f$ is constructed similarly. Let u_{df} be the input, y_{df} be the output. We have

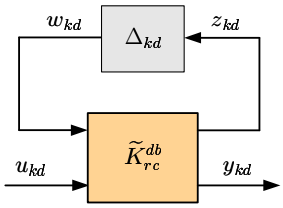

Figure 6.14: LFT representation of the deadbeat controller with respect to the rotor speed

$$
\begin{aligned}
y_{df} &= \boldsymbol{D}_f u_{df} = \begin{pmatrix} \frac{L_m^2}{L_s^2} R_s & -\frac{L_m^2}{L_s} \omega_m \\ \frac{L_m^2}{L_s} \omega_m & \frac{L_m^2}{L_s^2} R_s \end{pmatrix} u_{df} \\
&= \begin{pmatrix} \frac{L_m^2}{L_s^2} R_s & -\frac{L_m^2}{L_s} \omega_{mn} \\ \frac{L_m^2}{L_s} \omega_{mn} & \frac{L_m^2}{L_s^2} R_s \end{pmatrix} u_{df} + \delta_\omega \begin{pmatrix} 0 & -\frac{L_m^2}{L_s} p_\omega \\ \frac{L_m^2}{L_s} p_\omega & 0 \end{pmatrix} u_{df} \\
&= D_{fn} + \delta_\omega D_{fp} = D_{fn} + w_{df}
\end{aligned}
$$

where

$$
\begin{aligned}
w_{df} &= \delta\omega D_{fp} u_{df} = \delta_\omega z_{df}, \\
z_{df} &= D_{fp} u_{df}.
\end{aligned}
$$

Finally, we obtain

$$
\begin{aligned}
\begin{pmatrix} z_{df} \\ y_{df} \end{pmatrix} &= \begin{pmatrix} 0 & D_{fp} \\ I & D_{fn} \end{pmatrix} \begin{pmatrix} w_{df} \\ u_{df} \end{pmatrix}, \\
w_{df} &= \begin{pmatrix} \delta_\omega & 0 \\ 0 & \delta_\omega \end{pmatrix} z_{df} = \Delta_{df} z_{df}.
\end{aligned}
$$

Fig. 6.15 shows the LFT representation of the parameter-dependent transfer matrix $\boldsymbol{D}_f$ with respect to the rotor speed ω_m uncertainty.

The interconnection of the closed-loop system with the deadbeat controller is depicted in Fig. 6.16. Based on this control configuration we can easily construct the standard setup as in Fig. 6.3 for testing robust stability of the LPV-controlled system within the above given IQC-framework. The corresponding region-of-variation (6.21) is also re-constructed for each of the respective parameter variations.

The obtained results are summarized in Table 6.3. The results show that the closed-loop system remains stable when L_s varies from 95.1% to 107.33% of its nominal value

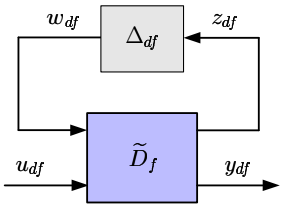

Figure 6.15: LFT representation of the parameter-dependent transfer matrix $\boldsymbol{D}_f$ with respect to the rotor speed

Table 6.3: Stability margins for deadbeat controller

Tests	**Uncertainties**	**Uncertainty matrix size**	**Stability margins**	
			Ranges of variation	Rates
1	L_s	4×4	95.10% – 107.33%	0 – 0.01
2	L_r	2×2	95.30% – 107.17%	0 – 0.01
3	L_m	6×6	94.30% – 102.50%	0 – 0.01
4	ω_m	6×6	73.20% – 126.80%	0 – 2000
5	L_s and ω_m			
	L_s	4×4	97.40% – 105.59%	0 – 0.01
	ω_m	8×8	94.90% – 105.10%	0 – 9
6	L_r and ω_m			
	L_r	2×2	98.50% – 101.50%	0 – 0.01
	ω_m	8×8	95.50% – 104.50%	0 – 9
7	L_m and ω_m			
	L_m	8×8	97.54% – 101.20%	0 – 0.01
	ω_m	8×8	95.70% – 104.30%	0 – 10

while its rate varies in $[0, 0.01]$. The same conclusions are drawn for variations in L_r, L_m, and ω_m, respectively as well as for the combination of the rotor speed ω_m with each machine inductance.

We can conclude, according to the analysis results in Table 6.3, that the deadbeat controller achieves smaller stability margins in comparison with that of the LPV controller case. The stability region for the mechanical rotor speed ω_m is remarkably decreased in comparison with that of the LPV controller implementation, especially in its rate of variation. This is also true for the tests with the uncertainties of ω_m in combination with L_s, L_r, and L_m, respectively. Its rate-of-variation decreases to $[0, 9]$ in the tests 5, 6 and to $[0, 10]$ in the test 7, respectively, while its range-of-variation decrease to $[194.9\%, 105.1\%]$ in test 5, to $[195.6\%, 104.5\%]$ in test 6, and to $[195.7\%, 104.3\%]$ in test 7, respectively.

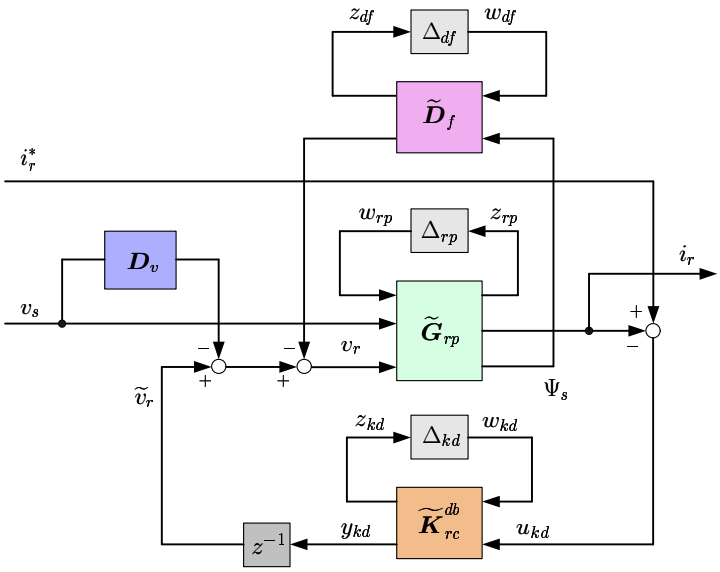

Figure 6.16: The interconnection of the closed-loop controlled system with deadbeat rotor current controller

6.6. SUMMARY

In this chapter, the machine inductances are considered as uncertainties. The system, therefore, is rational parameter-dependent and the LFT representations with the uncertainties have been derived. Then these parameters were considered as time-invariant uncertainties and a μ-analysis was used for verifying the robust stability.

In the next step, the IQC-based robust stability test has been applied for both the controlled system with the LPV and deadbeat controllers that were designed on the basis of the nominal model of the doubly-fed induction generator. Robust stability of the controlled system is tested by considering the machine inductances and the rotor mechanical angular speed as slowly time-varying parameters. The stability analysis has been implemented within the IQC framework which allows to include bounds on both the values and the rate-of-variation of the parameters. Robustness margins have been given to prove that the controlled system remains stable in the face of slowly time-varying parametric uncertainties of the machine. The test results listed in Tables 6.2 and 6.3 show that the LPV controller achieves higher stability margins in comparison with that of the deadbeat controller case. For the LPV controller implementation, the stability region for the mechanical rotor speed ω_m is very large. This indicates that the LPV design guarantees a good performance in terms of robustness with respect to machine parameter uncertainties and to the rotor speed.

7

EXPERIMENTAL RESULTS

7.1. INTRODUCTION

This chapter aims at presenting an experimental validation of the LPV controller design method that is developed in Chapter 5. First, the performance of the current control loop with the LPV current controller is tested when the stator circuit of the stator windings is not connected to the grid. This means that the performance of the current control loop is evaluated when it is not influenced by the stator voltage v_s as an input disturbance as well as without energy exchange between the stator circuit and the grid. Then these factors are taken into account in the next experiments with a closed stator winding circuit. After that the experiments are carried out with closing the outer loop of the electrical torque control. Since the self-scheduled LPV controller is designed to adapt to rotor speed variations, experimental results with changing rotor speeds are very important in order to verify the performance of the system. Therefore, the experimental results have been taken in the rotor speed range of ±30% of synchronous speed, i.e. from 1050rpm to 1950rpm with the synchronous speed at 1500rpm. In the next test, robustness of the controlled system is also investigated in the presence of stator voltage dips of 50% of its normal value.

In the last section of this chapter, the same experiments are also carried out with the finite response time (FRT or deadbeat-like) controller in order to compare performance between the LPV control and the conventional design with the FRT controller.

In the laboratory test model, an 11kW induction motor was used as the prime mover. A 4kW DFIM working in generator mode was used for all experiments. The technical characteristics of these electrical machines are presented in Appendix B.

For the laboratory-scale test model of the DFIM, a new LPV current controller is designed with the same method that is developed in Chapter 5. In addition, the LPV controller design is required to guarantee a good approximation of the resulting discrete-time LPV controller, consistently with the chosen sampling frequency of 4kHz corre-

sponding to a sampling time of $0.00025s$ as discussed in section 5.6.

The same philosophy presented in Section 5.4 is applied for the design of a continuous-time LPV gain-scheduling current controller in accordance with the design objective as presented in Section 5.3.

Trial-and-error iteration is used for choosing weighting functions for the LPV controller design until the desired performance specifications are achieved and the invertibility condition for discretization (5.25) is guaranteed with the sampling time $T = 0.00025s$. As a result, the following weighting functions are chosen for synthesis of a continuous-time LPV gain-scheduling current controller:

$$W_{rs} = \begin{pmatrix} \frac{650}{s+0.05} & 0 \\ 0 & \frac{950}{s+1.05} \end{pmatrix}$$

$$W_{rt} = \begin{pmatrix} \frac{0.01}{s+0.95} & 0 \\ 0 & \frac{0.01s+0.03}{s+0.95} \end{pmatrix}$$

In order to be implemented in the experimental platform, the designed continuous-time LPV controller is replaced by an equivalent sampled discrete-time controller with the same method presented in Section 5.6.

7.2. EXPERIMENTAL SETUP

The controllers have been implemented on the experimental test platform at the Institute of Electrical Power Engineering, faculty of Electrical Engineering and Information Technologies, Dresden University of Technology, Germany. This platform is based on the multi processors ALPHA-COMBO system manufactured by the company dSPACE. A rapid control prototyping structure used for the hardware interface and the controller implementation has been developed by the author of [29]. We are very grateful to all the people at Dresden University for the possibility to make use of the laboratory setup for our controller implementations. All our experimental results could not have been obtained without the help of Dr. Volkmar Müller, Dr. Phung Ngoc Lan, Mr. Nguyen Tran Duc Viet, and many others.

The block diagram of the overall experimental setup is depicted in Fig. 7.1. The setup contains three main modules including the electrical machine module, the ALPHA-COMBO module, and the power module. The electrical machine module includes the DFIG coupled to the induction motor as actually shown in Fig. 7.2. The ALPHA-COMBO module, whose technical details can be found in Appendix C, is the combination of the DSpace Multi-processors system and peripheral cards. The power module consists of the rotor side and the grid side converters that form back-to-back converters as already presented in Fig. 2.4. The appearance of the ALPHA-COMBO system, the power module, and the other switching devices that are assembled on the same panel are shown as in Fig. 7.3.

In the laboratory, experiments of the stator voltage dips are implemented by grid symmetrical faults created by short circuits of resistors. Switching these resistors is real-

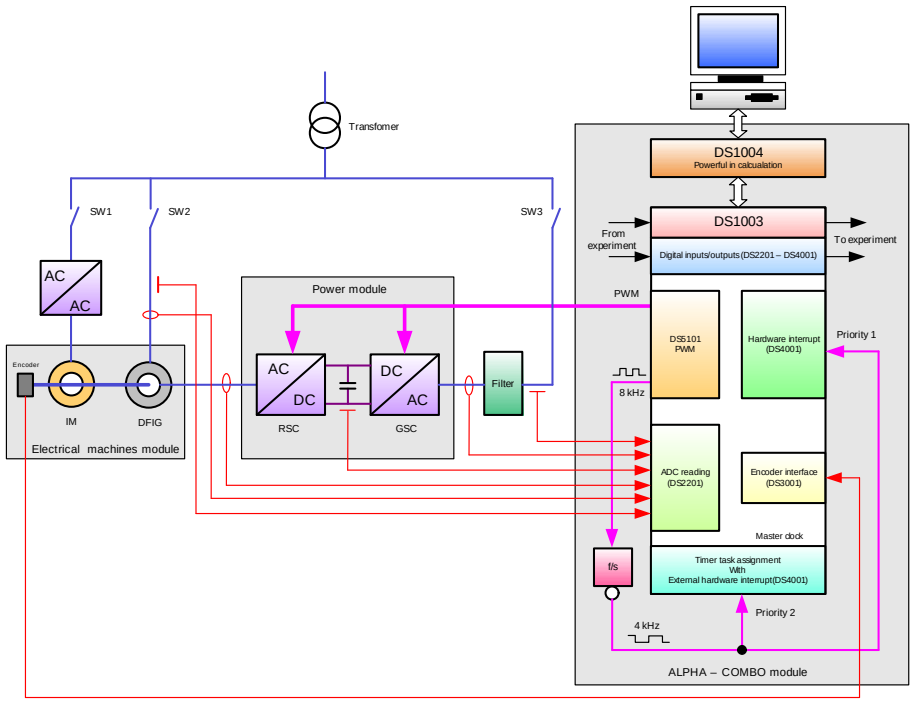

Figure 7.1: The experimental setup

ized by a power electronic equipment using thyristors as shown in Fig. 7.4. The switching times are specified by software based on the Matlab realtime environment.

All experimental tests are performed via a user-friendly interface. This interface is designed with the Control Desk software package of DSpace for each experimental test. Via this user interface we can observe the time-evolution of components of the stator voltages and currents, the rotor voltages and currents, the electrical torque, the reactive power, the rotor speed as well as other electrical components. Moreover, we can handle on/off operations of contactors by clicking on the selection buttons on the user interface. The status of the contactors, system errors etc. are also displayed on the user interface. The capture tool of the Control Desk software package allows to specify capture time intervals and expected variables whose values will be save in data files. Fig. 7.5 shows an example of the user interface designed by the Control Desk software package.

More technical details of the experimental platform are presented in Appendix C.

Note that the PWM (Pulse Width Modulation) frequency defined for the power module is 8KHz corresponding to a sampling time of 0.000125s. However, the realized frequency for the ALPHA-COMBO module is chosen at 4KHz. Therefore, the PWM frequency is divided by 2 and fed to the external hardware as the master clock signal as well as for Analog to Digital Converters (ADC) operation.

Figure 7.2: Doubly-fed induction generator and induction motor

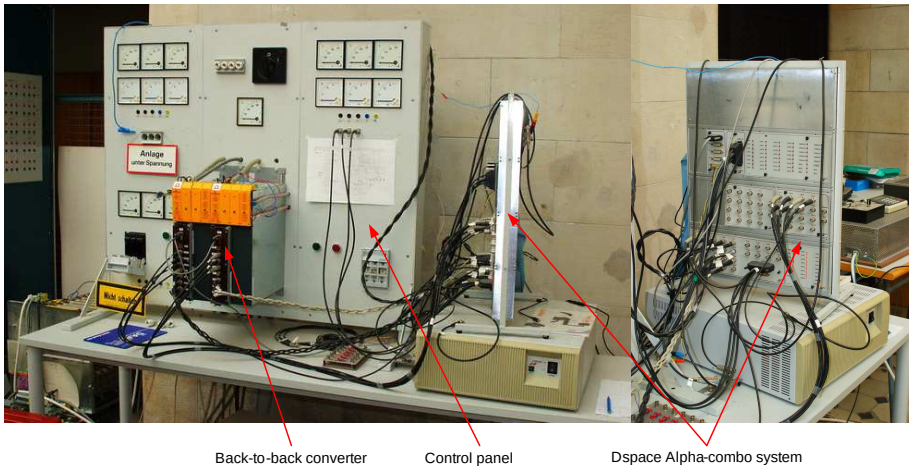

Figure 7.3: The ALPHA-COMBO system and the power module

7

7.3. EXPERIMENTAL RESULTS WITH THE LPV CURRENT CONTROLLER

7.3.1. THE ROTOR CURRENT CONTROLLER WITH THE STATOR OPEN CIRCUIT

Let us start by describing the first experimental results if the stator winding circuit is open, i.e. the stator windings are not connected to the grid. In this fashion the stator voltages need not be regulated so as to be identical to the grid voltage in phase and in

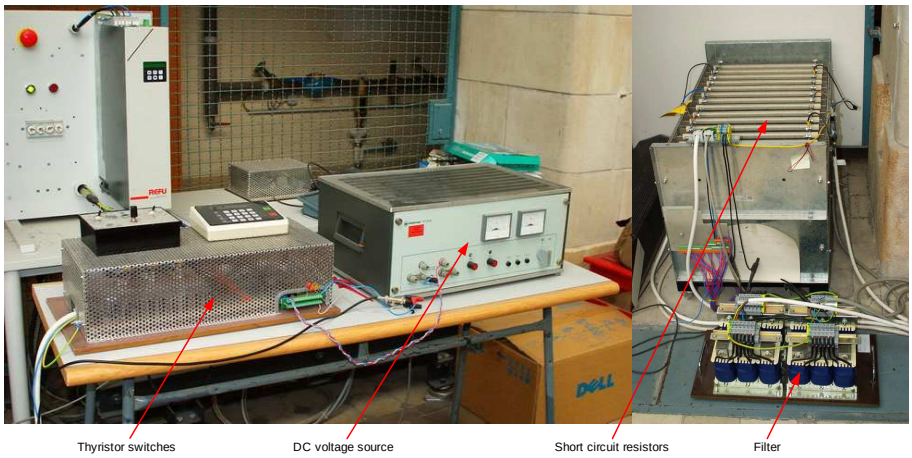

Figure 7.4: The experimental equipment for grid voltage dip tests

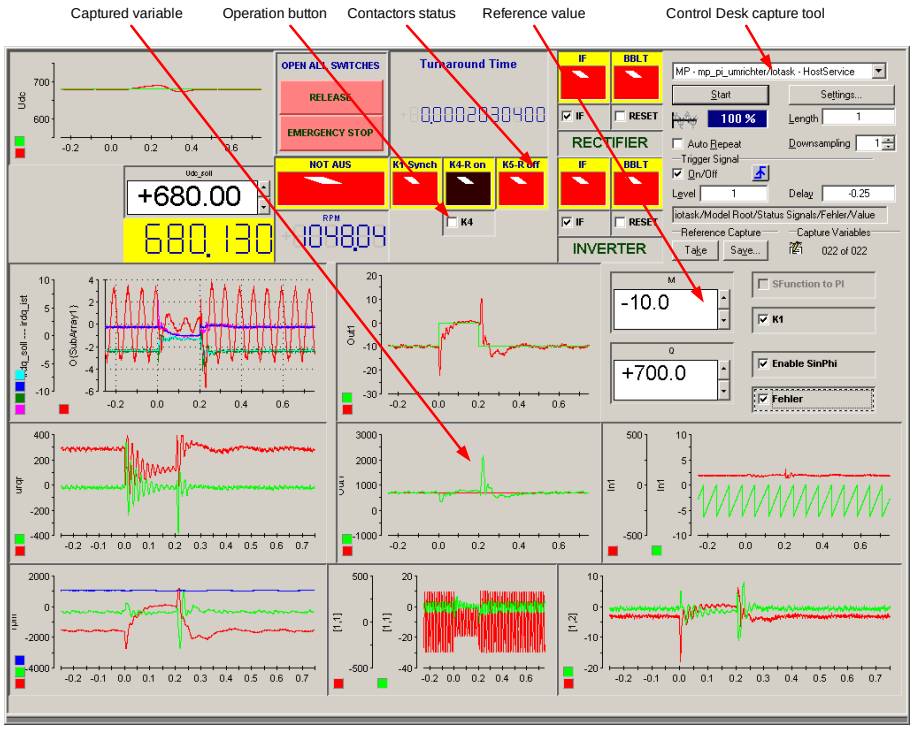

Figure 7.5: The Control Desk interface

amplitude. Since this experiment does not require any energy exchange between the stator circuit and the grid, it is easier to implement in comparison to other experiments. But it is a good first step for testing how the newly designed LPV controller behaves.

In this test, the rotor speed can be set to any value from 1050rpm up to 1950rpm or, in other words, within the range of ±30% of the synchronous speed at 1500rpm.

Fig. 7.6 shows the performance of the inner current-control loop with the LPV controller corresponding to step changes of the rotor currents i_{rd} and i_{rq}. The rotor speed is set to 1350 rpm. The reference value of the d-component of the rotor currents is set to perform a sudden step from $0A$ to $1.5A$ while the q-component of the rotor current is kept at $0A$ as shown in the left hand side of Fig. 7.6. Similarly, as on the right hand side of Fig. 7.6, the reference value of the q-component of the rotor current is set to perform a sudden step from $0A$ to $-2A$ while the d-component of the rotor currents is kept at $0A$.

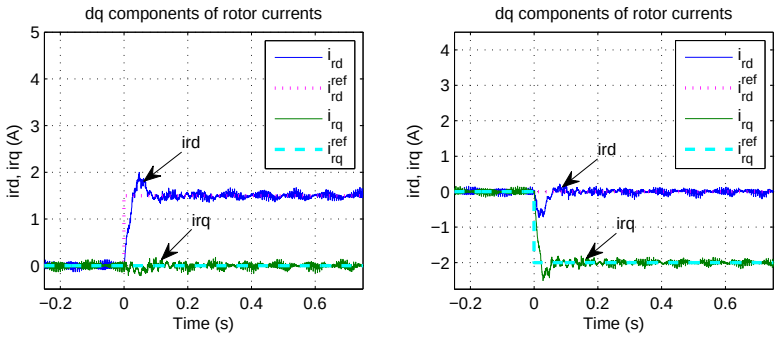

Figure 7.6: Performance of the inner current-control loop with the LPV controller corresponding to step changes of the rotor currents

As we can see from Fig. 7.6 the LPV controller achieves a good tracking of the references although the current measurements are corrupted by noise. The ripples of the rotor currents are quite small since the input of the plant is not effected by disturbances of the stator voltage (because the stator circuit is open). These experimental results agree with the simulations shown in Fig. 5.10 that a good performance is obtained by the LPV design without cross-coupling interactions between the stator voltage and the rotor current. Since the designed LPV controller works well if the stator circuit is open, further experimental tests can be carried out if the stator circuit is closed.

In the next steps, the stator windings are connected to the grid by following a special procedure that is called grid synchronization (see next section). Then the performance of the controlled system is tested in the presence of stator voltage disturbances.

7.3.2. GRID SYNCHRONIZATION TESTING

In this test, the stator voltages should be regulated so as to be equivalent to the grid voltage in phase and in amplitude. When these conditions are obtained, the stator windings

can be connected to the grid without causing current inrush because the electrical potential difference between the grid and stator voltage vectors is zero.

The stator windings are connected to the grid via three-coupled electrical lamps (high resistors) that are connected in parallel to the terminals of the contactor (see Fig. 7.7). These electrical lamps are needed for inducing the stator flux in order to generate the stator voltage and power. When the stator and the grid voltages are gradually equivalent in phase and amplitude, these electrical lamps are dimmed out because the voltage drop in each coupled electrical lamp tends to zero.

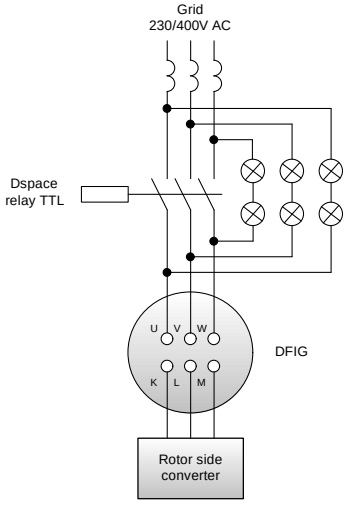

Figure 7.7: The electrical lamps are used for synchronization procedure

During the grid synchronization operation the amplitude of the stator voltage is automatically regulated by the q-component of the rotor current, while the d-component of the rotor current should be kept at zero [29, 148, 149, 150]. The performance of the LPV current controller during the grid connected operation is shown in Fig. 7.8. As we can see in this figure, the rotor currents follow their reference values after only $0.2s$ in the presence of the stator voltage (see Fig. 7.8a). As a consequence, the grid connected conditions are now met. The stator voltage is equal to the grid voltage in amplitude, phase and frequency (see Fig. 7.8b).

More details of the starting procedure can be found in [29, 148, 149, 150].

7.3.3. THE ROTOR CURRENT LPV CONTROLLER WITH A CLOSED CIRCUIT OF THE STATOR WINDINGS

The following experiments are performed so as to investigate the performance of the inner current-control loop when the stator circuit is connected to the grid in order to feed the electrical power from the stator to the grid. The references of the rotor current com-

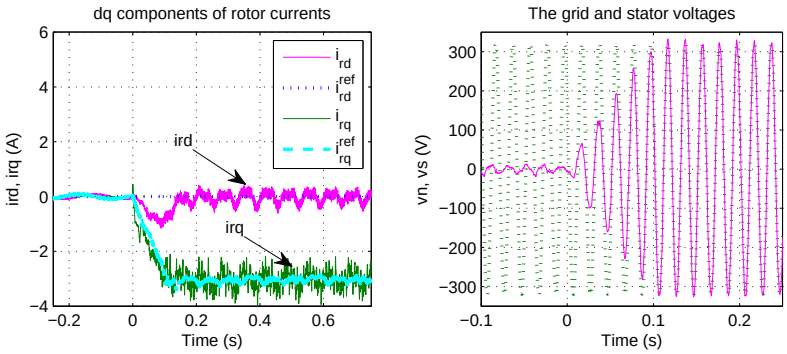

(a) (b)

Figure 7.8: Synchronization testing with the new LPV controller design

ponents are the same as in case of the stator open circuit, but at different values of the rotor speed and in the presence of stator voltage disturbances. In the next tests, three values of the rotor speed around the synchronous speed will be taken for the experiments.

Figs. 7.9 - 7.11 show the performance of the inner current-control loop corresponding to step changes of the rotor currents i_{rd} and i_{rq}. In Fig. 7.9, the rotor speed is set to the designed lowest operating speed (see equation (5.4)). Since the synchronous speed of the system is 1500rpm, the lowest under-synchronous speed in the LPV controller design is 1050rpm corresponding to a -30% offset from synchronous speed. The reference value of the q-component of the rotor currents is kept at $0A$ while the d-component of the rotor currents is set to perform a sudden step from $0A$ to $1.5A$ in Fig. 7.9a and from $1.5A$ to $1A$ in Fig. 7.9b. Similarly, the reference value of the d-component of the rotor currents is kept at $0A$ while the q-component of the rotor currents is set to perform a sudden step from $0A$ to $-2A$ in Fig. 7.9c and from $-2A$ to $-1A$ in Fig. 7.9d. As we can see from Fig. 7.9, the rotor currents contain more noisy measurements than that of the stator circuit open (see Fig. 7.6) because of the grid voltage disturbances. The LPV controller still achieves a good tracking of the references. However, because of the magnetic coupling between the stator and rotor circuit, the noise in the rotor currents will result in noise in the electrical torque and reactive power of the generator.

The same tests are performed for the controlled system with step changes of the reference values of the rotor currents at 1350rpm of the rotor speed (near-synchronous speed) as in Fig. 7.10 and at 1800rpm of the rotor speed (over-synchronous speed) as in Fig. 7.11. The experimental results show that the performance of the controlled system is guaranteed at the different rotor speeds. Note that, at a high rotor speed, the amplitude of the rotor voltage is at a low value. Consequently, the rotor winding impedance is also low, which leads to higher low-order harmonics. This causes a larger harmonic in the rotor currents and thus the oscillations in the machine flux as well as in the electrical torque [151]. Hence, the higher rotor speed results in more oscillations in the controlled

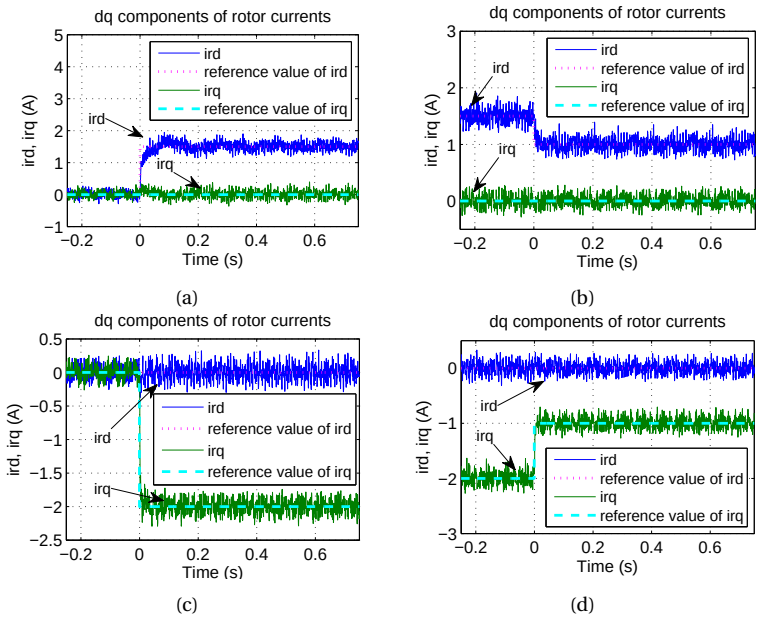

Figure 7.9: Performance of the inner current-control loop with the LPV controller corresponding to step changes of the rotor currents at 1050rpm of the rotor speed

variables if the controlled system is not robust with respect to noise and if the flux oscillation is not well damped. However, the above experimental results show that the LPV controller guarantees good performance of the closed-loop system even when the speed of the rotor is set above the synchronous speed (see Fig. 7.11).

Note that very similar responses observed in Figs. 7.9 - 7.11 indicate that the performance of the closed-loop system with the LPV controller is guaranteed for the different fixed values of the rotor speed around the synchronous speed. These experimental results are consistent with the full-scale simulations shown in Fig. 5.13.

7.3.4. THE CLOSED-LOOP SYSTEM WITH OUTER LOOPS

The outer loop with controller K_g is used for tracking the optimal values of the electrical torque T_e^{ref} and the reactive power Q_g^{ref} as presented in Fig. 2.6. The performance of the controlled system depicted in Fig. 2.6 is tested with step changes of the reference values for the electrical torque T_e and the reactive power Q_g at different rotor speeds.

The following experiments are carried out for three values of the rotor speed around the synchronous speed. These tests are presented in Figs. 7.12 - 7.17.

Fig. 7.12 shows the test results with the rotor speed set at 1050rpm (under-synchronous speed). In Figs. 7.12a - 7.12d, the test is carried out with step changes of the reference values of the reactive power Q_g from 0VAr to 700VAr (see equation (2.37)). After that, as

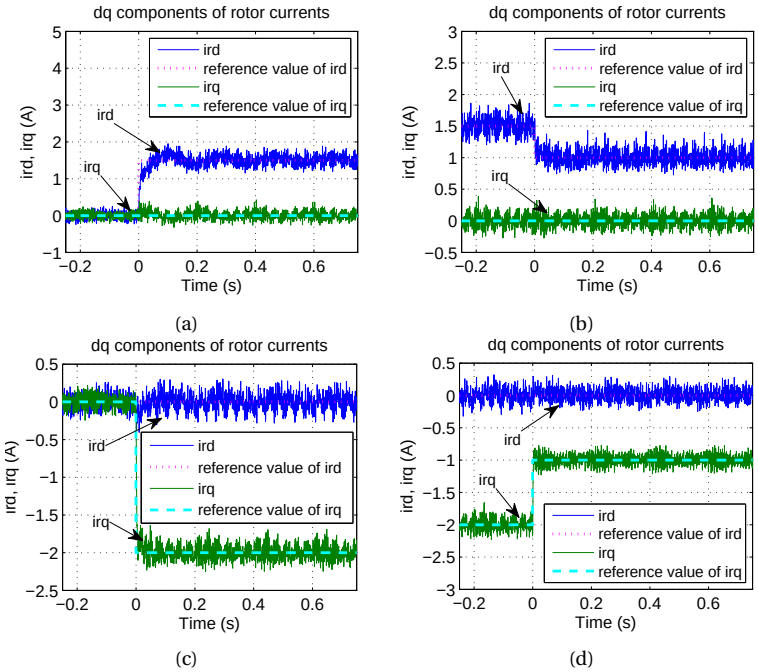

Figure 7.10: Performance of the inner current-control loop with the LPV controller corresponding to step changes of the rotor currents at 1350rpm of the rotor speed

shown in Figs. 7.12e - 7.12h, the reference values of the reactive power is dropped from 700VAr to 300VAr.

The same tests are performed for the controlled system with step changes of the reference values of the reactive power Q_g at 1350rpm of the rotor speed (near-synchronous speed) as in Fig. 7.14 and at 1800rpm of the rotor speed (over-synchronous speed) as in Fig. 7.16. The experimental results show that the tracking and decoupling of the electrical torque and reactive power are very good for the different fixed values of the rotor speed around the synchronous speed with the presence of noisy measurements. The ripples in the measured rotor current, the electrical torque, and the reactive power, compared to the experimental results with FRT controller in [29], are considerably smaller. Note that rotor speed oscillations are due to changes in the set-point of the the electrical toque developed by the machine since the rotor speed depends mainly on the difference between electrical and mechanical torque. These experimental results show a substantial improvement in performance in comparison with that of the experimental results with the FRT controller presented in [29].

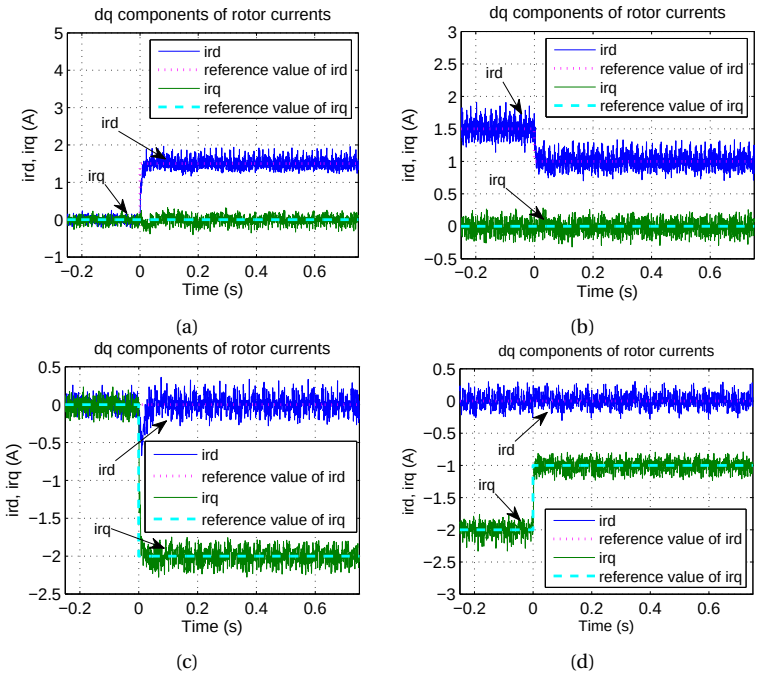

Figure 7.11: Performance of the inner current-control loop with the LPV controller corresponding to step changes of the rotor currents at 1800rpm of the rotor speed

7.3.5. THE SYSTEM PERFORMANCE DURING THE ROTOR SPEED VARIATIONS

Since the above tests are only implemented with different fixed values of the rotor speeds they do not give any information about the performance of the system during rotor speed changes. The following experiments are aimed at an investigation of this scenario.

In the following experimental test, the rotor speed of the DFIM is adjusted by the prime mover that is an 11kW induction motor as mentioned above. The prime mover plays the role of a wind turbine whose shaft is coupled to the shaft of the DFIM. Note that, because of large moment of inertia, the response of the rotor speed to step changes in the speed reference is usually slow.

Figs. 7.18 - 7.23 show how the reactive power Q_g, electrical torque T_e, and dq-component of the rotor currents change during variations of the rotor speeds. In Fig. 7.18, the performance of the controlled system with the LPV controller is given in the step changes of the rotor speed from $1050rpm$ to $1350rpm$. Meanwhile, the reactive power Q_g and the electrical torque T_e are kept at constants of $700Var$ and $-10Nm$, respectively. The rotor speed increases its value from $1050rpm$ to $1350rpm$ in about $2.1s$. During and after the speed transient period, the values of the reactive power Q_g and the electrical torque T_e are almost the same as their previous values at fixed values of the rotor speed ($1050rpm$ and $1350rpm$), as presented in Figs. 7.12 - 7.15. In Fig. 7.19, the

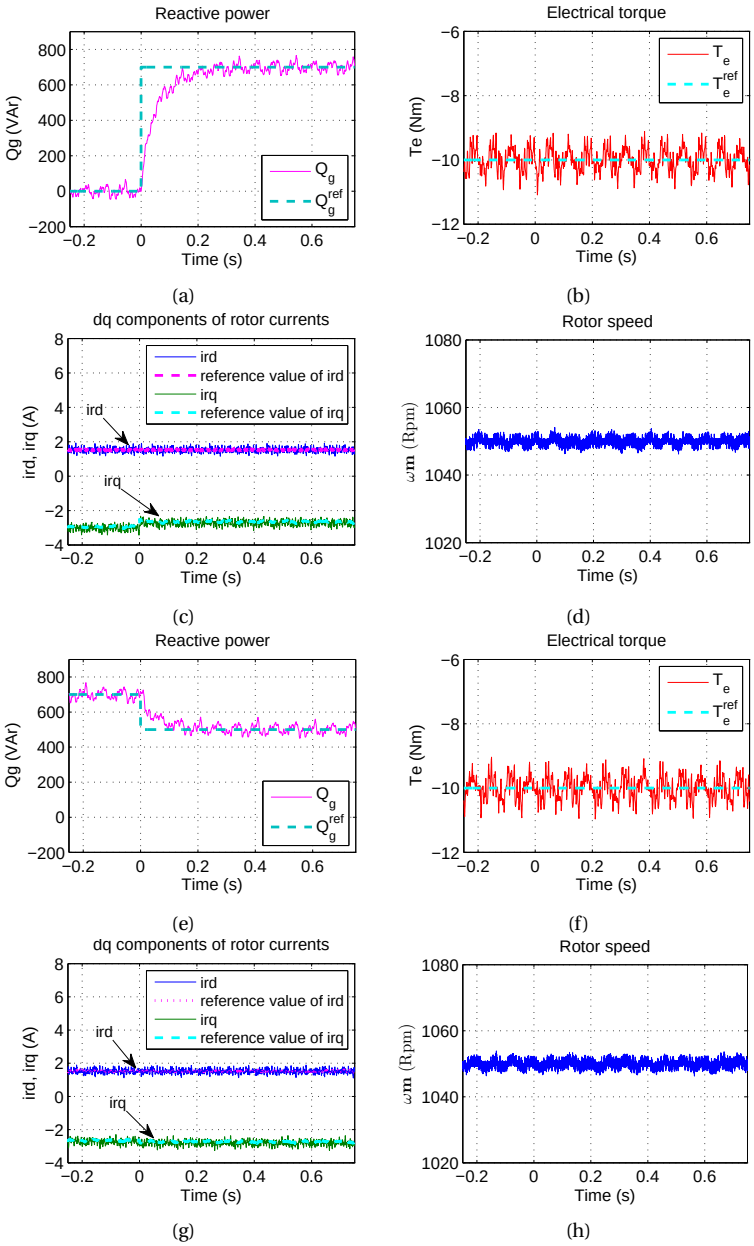

Figure 7.12: Performance of the LPV control system with step changes of reactive power from $0VAr$ to $700VAr$ at under-synchronous speed (1050rpm)

same performance is obtained with the step changes of the rotor speed from $1350rpm$

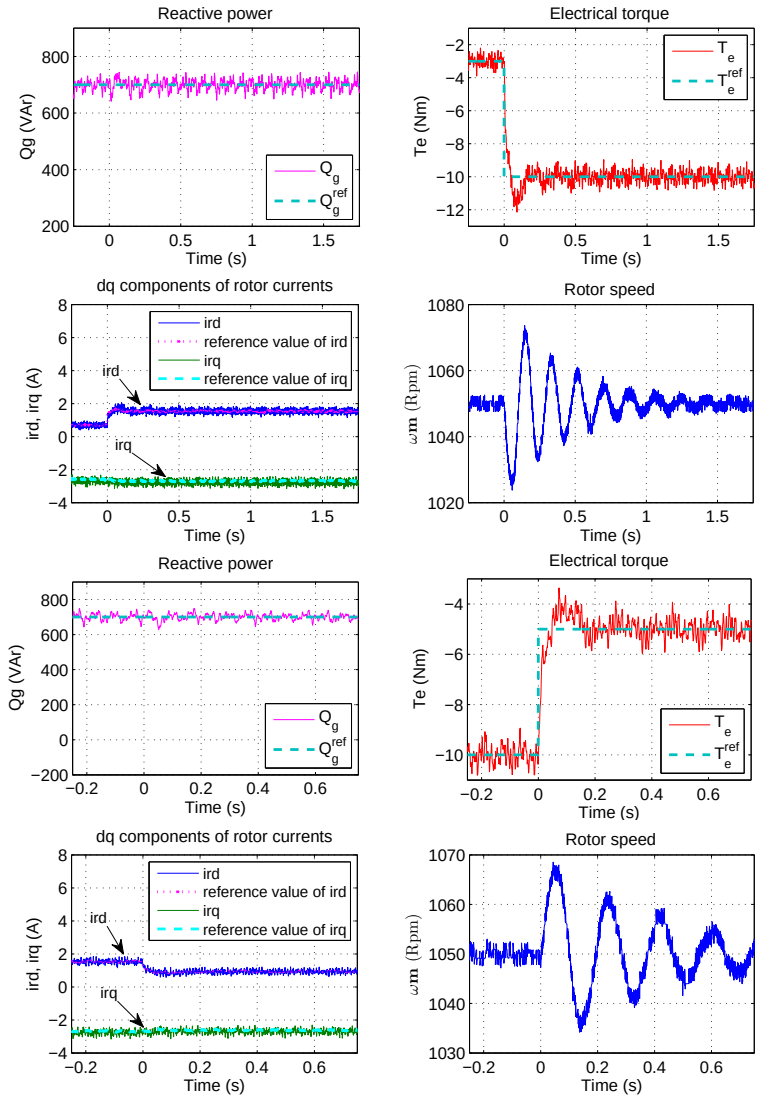

Figure 7.13: Performance of the LPV control system with step changes of electrical torque from $-3Nm$ to $-10Nm$ at under-synchronous speed (1050rpm)

down to $1050rpm$. Similarly, the tests are also performed for other step changes of the rotor speed for under the synchronous speed as given in Fig. 7.20, and for over the synchronous speed as given in Figs. 7.21 - 7.23.

These results show an important point that the performance of the controlled system is guaranteed during the rotor speed changes in the whole operating region from

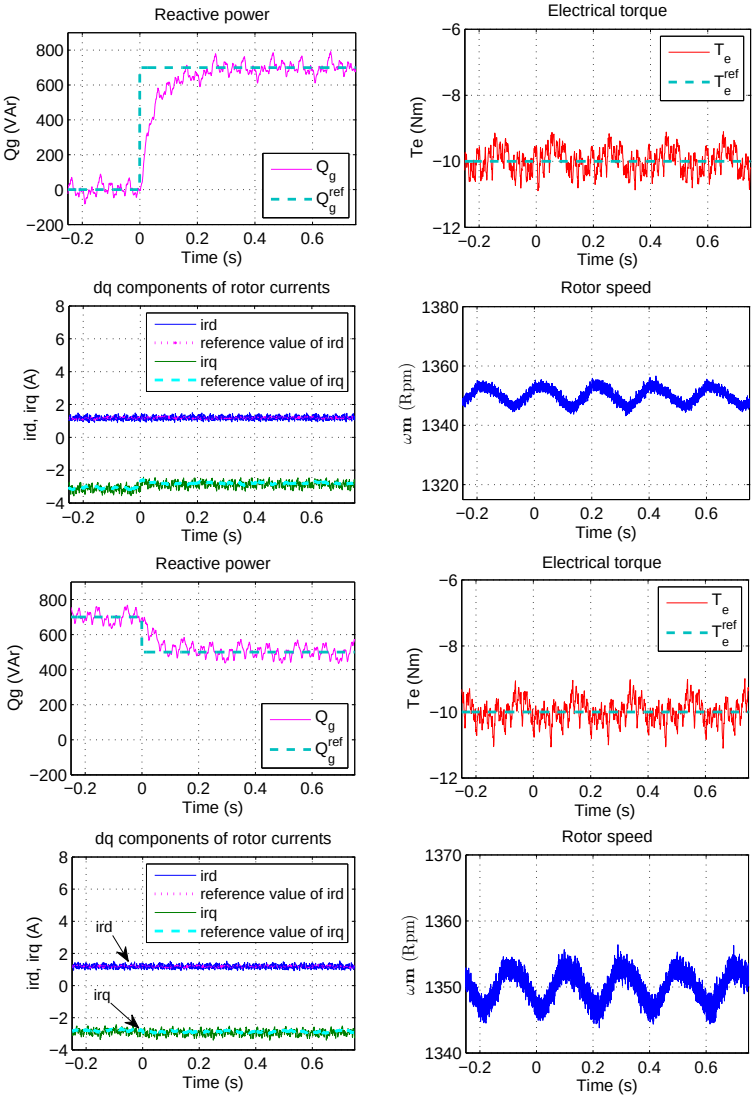

Figure 7.14: Performance of the LPV control system with step changes of reactive power from $0 VAr$ to $700 VAr$ at near-synchronous speed (1350rpm)

7

$1050 rpm$ to $1950 rpm$ as expected from the full-scale simulation results shown in Fig. 5.14.

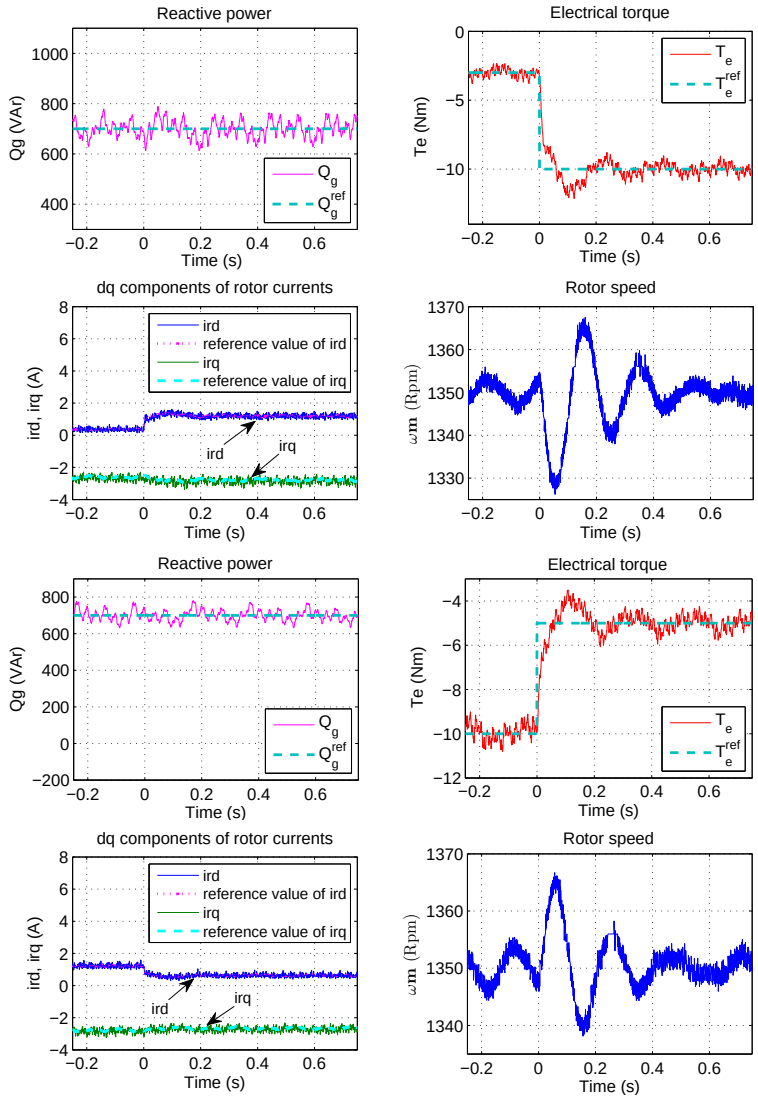

Figure 7.15: Performance of the LPV control system with step changes of electrical torque from $-3Nm$ to $-10Nm$ at near-synchronous speed (1350rpm)

7

7.3.6. GRID VOLTAGE DIP TESTS

In the laboratory, symmetrical grid voltage dips are realized with a short circuit of resistors only. The grid voltage is dropped down to 50% of its rated value and this phenomenon occurs in a period of 200 msec before it recovers to its nominal value. Figs. 7.24 - 7.26 show the system performance when the grid undergoes faults corresponding

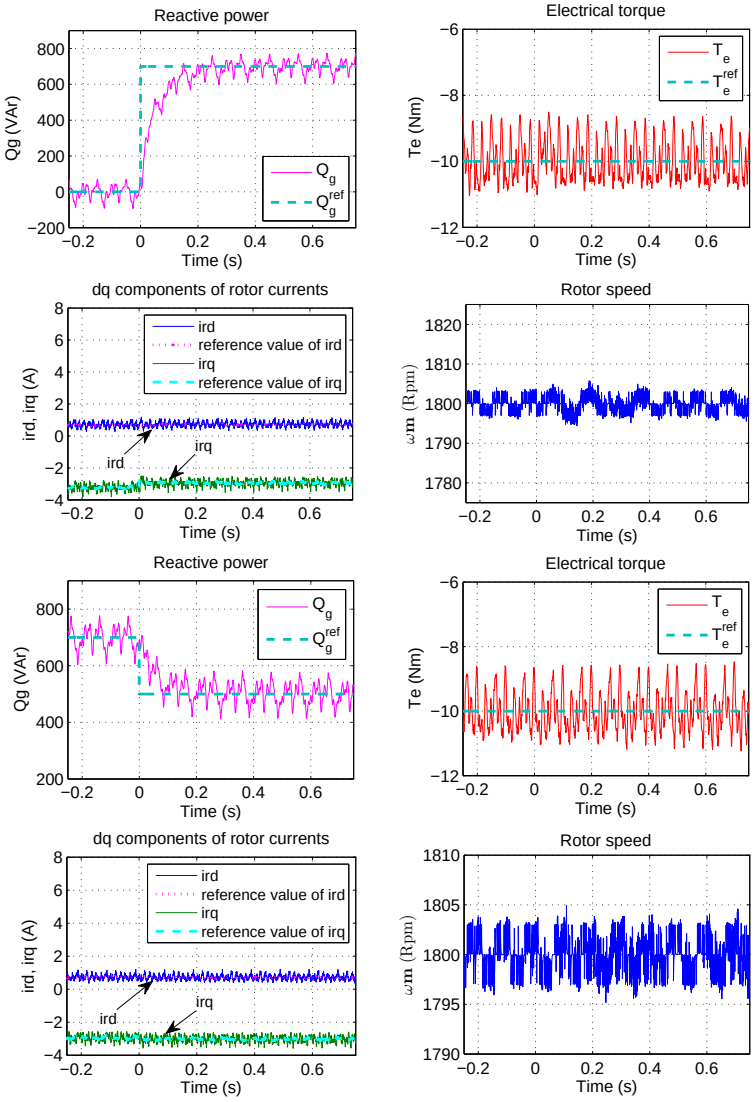

Figure 7.16: Performance of the LPV control system with step changes of reactive power from $0VAr$ to $700VAr$ at over-synchronous speed (1800rpm)

to under, near, and over-synchronous speeds of the rotor. As can be seen from these figures, the overshoots of the controlled variables get larger with larger values of the rotor speed. We note that these tests only verify the robustness of the controlled system in the presence of grid voltage dips. The tests are performed without additional hardware to ride through the faults as in [152, 153]. Therefore, the rotor currents will be very large if grid dips occur when the rotor is running at a very high speed. Because of that the rotor

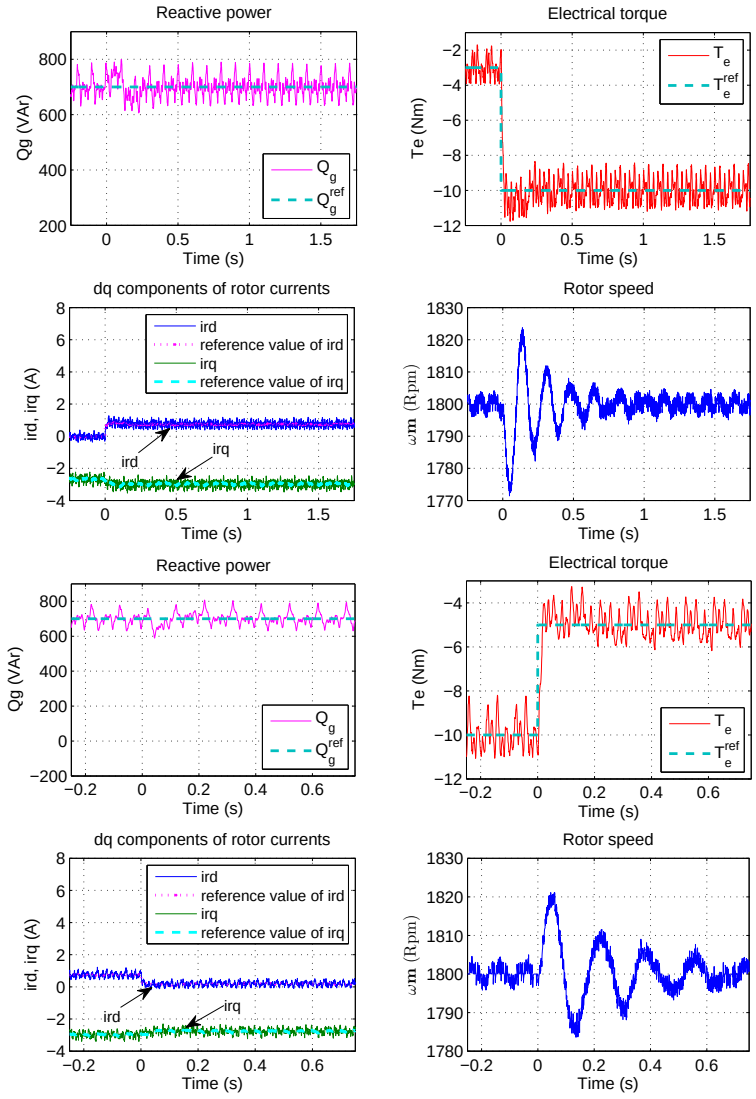

Figure 7.17: Performance of the LPV control system with step changes of electrical torque from $-3Nm$ to $-10Nm$ at over-synchronous speed (1850rpm)

speed is only set to the maximum value of 1800rpm to avoid exceeding the current limit of the converter in transient periods.

Figs. 7.24c, 7.25c, and 7.26c show that the oscillations of the rotor currents are well damped after only about 40ms corresponding to two sampling periods after the fault is cleared.

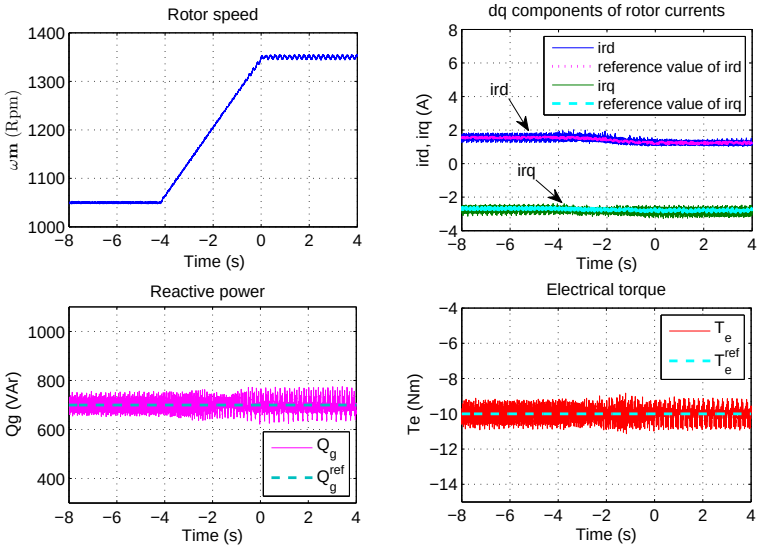

Figure 7.18: Performance of the controlled system with LPV controller for changes of the rotor speed from $1050rpm$ to $1350rpm$

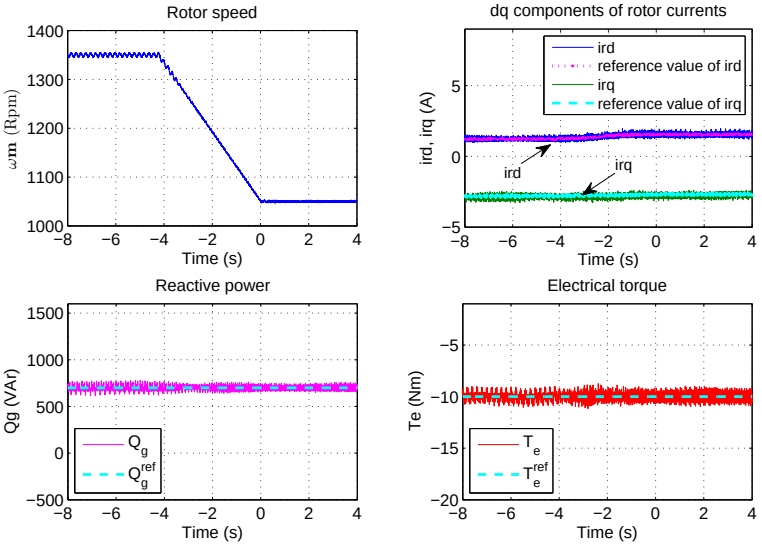

Figure 7.19: Performance of the controlled system with LPV controller for changes of the rotor speed from $1350rpm$ to $1050rpm$

In the next section, the same tests are performed for the FRT controller in order to make a comparison between the experimentally achieved performance with the LPV and

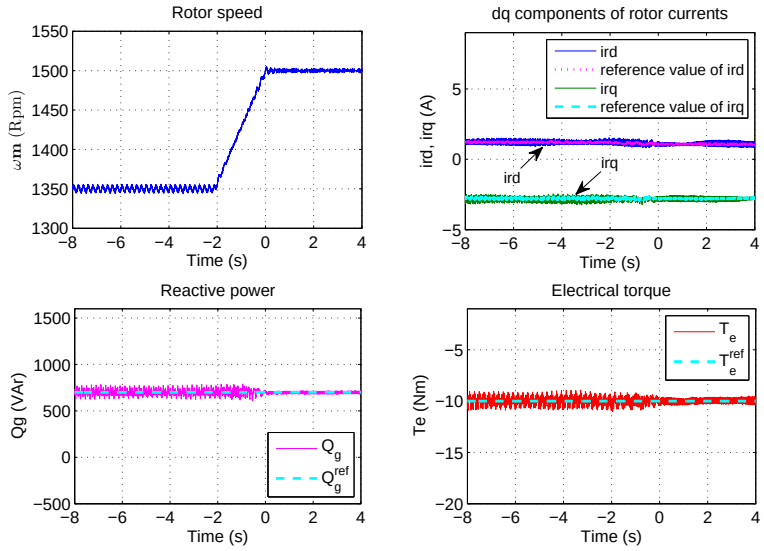

Figure 7.20: Performance of the controlled system with LPV controller for changes of the rotor speed from 1350rpm to 1500rpm

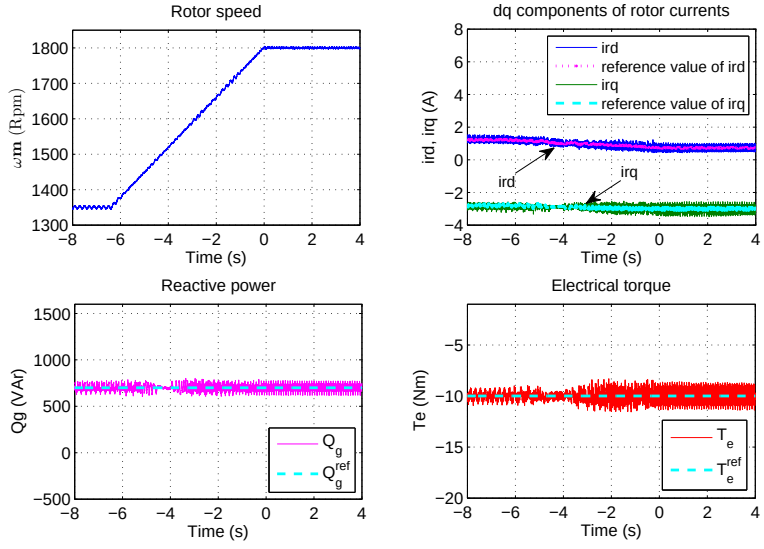

Figure 7.21: Performance of the controlled system with LPV controller for changes of the rotor speed from 1350rpm to 1800rpm

FRT controllers. We will start with the current control loop in which the test is carried out for the stator circuit being open as well as the closed-circuit of the stator windings. Then

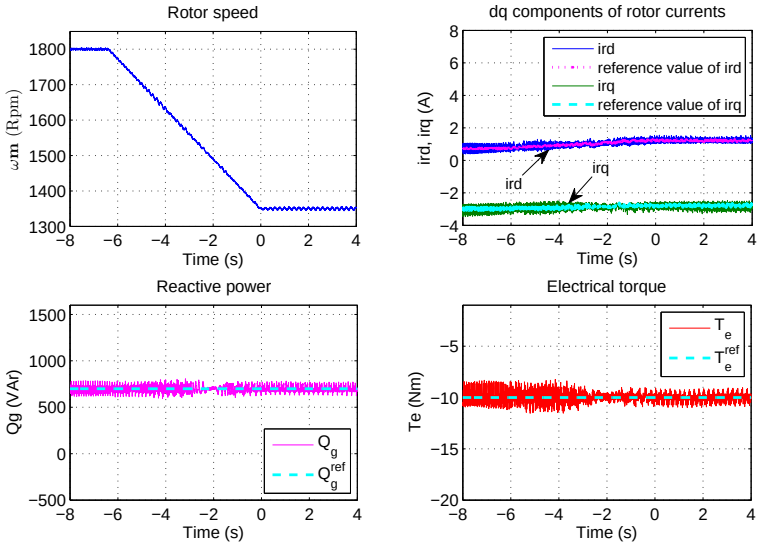

Figure 7.22: Performance of the controlled system with LPV controller for changes of the rotor speed from $1800rpm$ to $1350rpm$

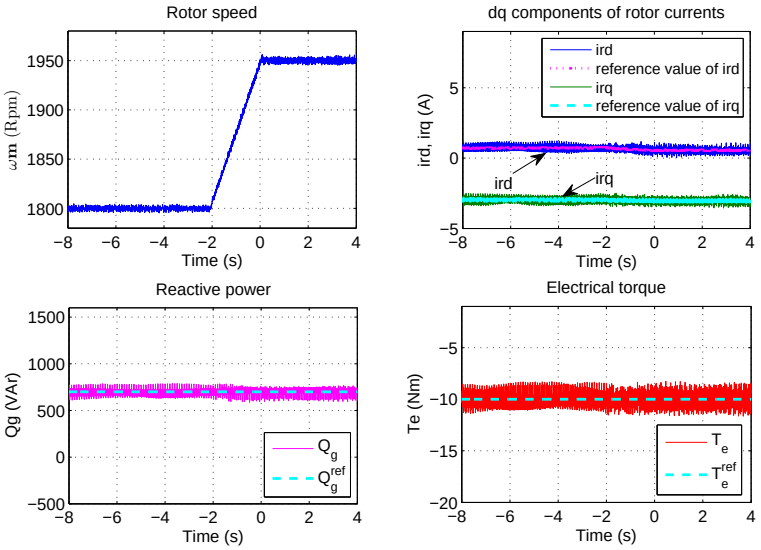

Figure 7.23: Performance of the controlled system with LPV controller for changes of the rotor speed from $1800rpm$ to $1950rpm$

performance of the closed-loop system with the outer loop is tested with the electrical torque and reactive power control. After that further experiments will be performed in

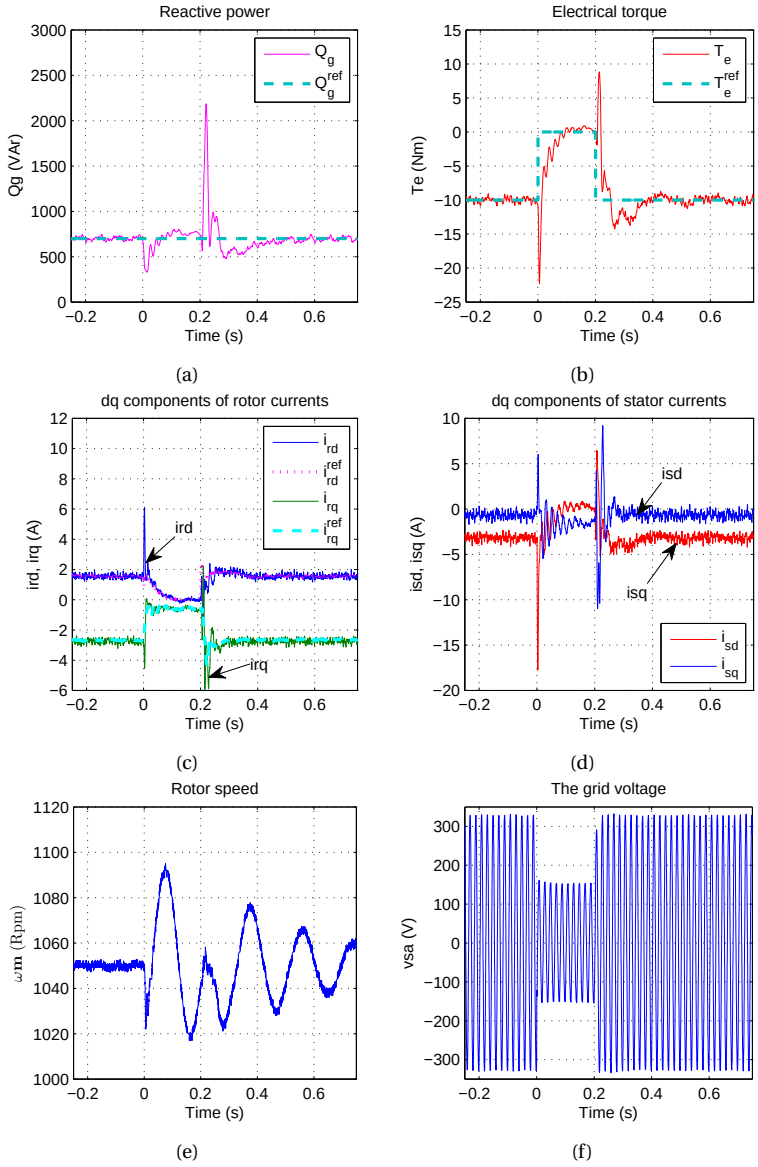

Figure 7.24: The grid voltage dips test at a fixed under-synchronous speed ($1050 rpm$) of the rotor with the LPV current controller

order to validate performance of the system with the rotor speed changes, and robustness of the controlled system with stator voltage dips. Through these experimental tests, the significant performance improvement of the closed-loop system with LPV controller is confirmed in comparison with that with FRT controller.

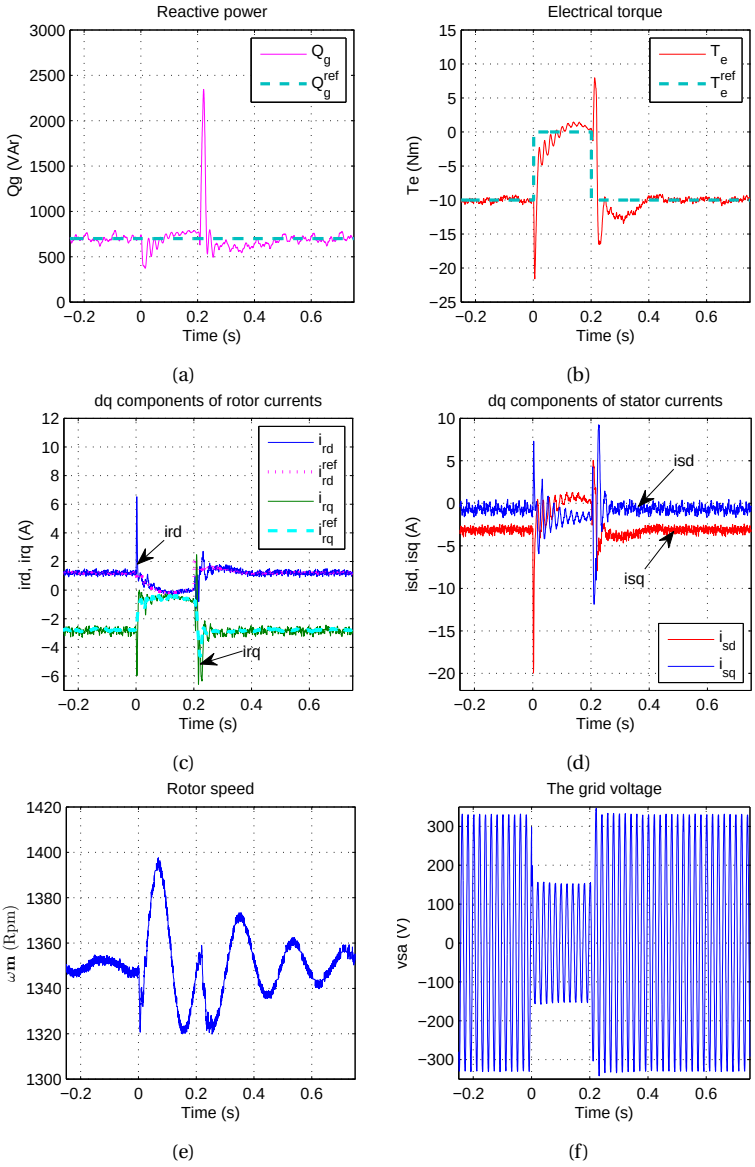

Figure 7.25: The grid voltage dips test at a fixed near-synchronous speed ($1350 rpm$) of the rotor with the LPV current controller

7.4. EXPERIMENTAL RESULTS WITH THE FRT CURRENT CONTROLLER

By implementing different types of the deadbeat and FRT controllers as presented in Chapter 3 on the experimental test platform, a three-step FRT controller (see equation

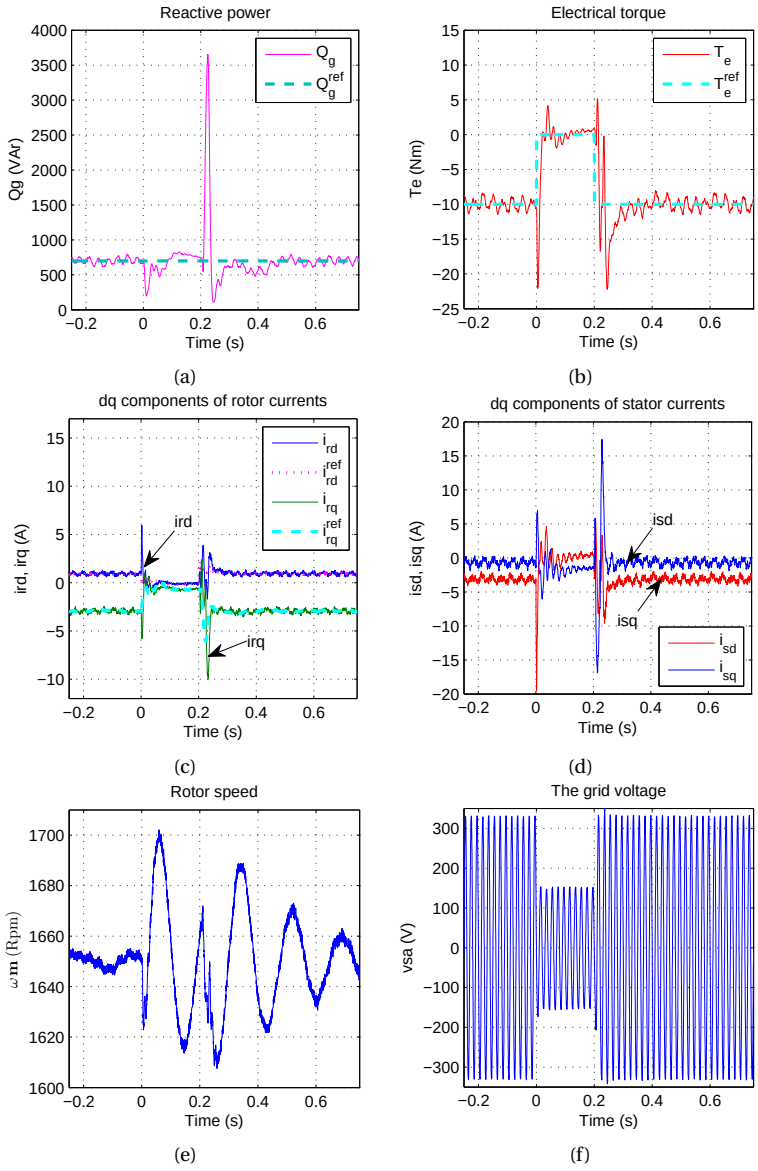

Figure 7.26: The grid voltage dips test at a fixed over-synchronous speed ($1800 rpm$) of the rotor with the LPV current controller

(3.46) with $k = 3$), turns out to be a best choice, in the sense of experimental results, for the current control loop of the DFIM [29]. The three-step FRT controller achieves better performance in terms of reference tracking, disturbance attenuation, and less overshoot than that of the others among the deadbeat type controllers.

7.4.1. THE ROTOR CURRENT CONTROLLER WITH THE STATOR OPEN CIRCUIT

Similar to the LPV controller implementation, performance of the inner current-control loop with the FRT controller is tested with step changes of the rotor currents i_{rd} from $0A$ to $-2A$, and i_{rq} from $0A$ to $-2A$, respectively, while the rotor speed is kept at 1350 rpm. For more explanations of the experiment we refer to the experimental test for the rotor current controller with the stator circuit open as shown in Fig. 7.6.

The experimental results show, as in Fig. 7.27, that the FRT controller achieves a good tracking of the references. However the settling time and overshoot are larger than that of the LPV control case (see Fig. 7.6). We found that one can get a shorter settling time for the same reference values for the one or two-step deadbeat controller case (equation (3.46) with $k = 1$ or $k = 2$) but the overshoot, in turn, becomes larger.

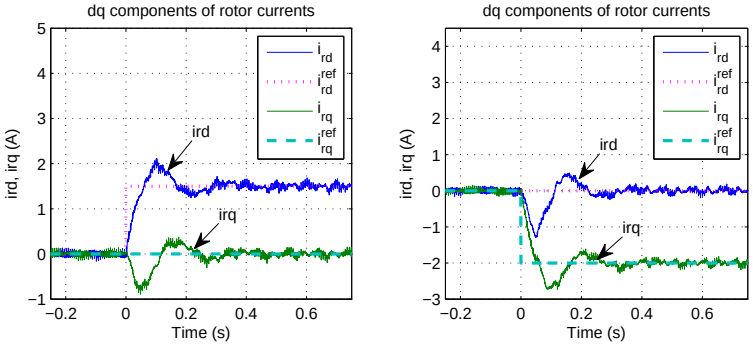

Figure 7.27: Performance of the inner current-control loop with the FRT controller corresponding to step changes of the rotor currents

7.4.2. THE ROTOR CURRENT FRT CONTROLLER WITH A CLOSED CIRCUIT OF THE STATOR WINDINGS

In this experiment, performance of the controlled system with the FRT current controller is tested with step changes of the reference values for the electrical torque T_e and the reactive power Q_g at different rotor speeds. Fig. 7.28 shows the test results with the rotor speed set to 1050rpm. In Figs. 7.28a - 7.28d, the test is carried out with step changes of the reference values of the reactive power Q_g from 0VAr to 700VAr. Then the reference values of the reactive power is dropped from 700VAr to 300VAr as shown in Figs. 7.28e - 7.28h. The same test is performed for the controlled system with step changes of the reference values of the reactive power Q_g at 1350rpm of the rotor speed as shown in Fig. 7.30.

As can be seen in Fig. 7.28 and Fig. 7.30, the performance of the controlled system with the FRT current controller in terms of tracking response and settling time is good at 1050rpm of the rotor speed, although the fluctuations in the characteristic curves that are given in Fig. 7.28 and Fig. 7.30 are larger than that of the LPV control case as shown in

Fig. 7.12 and Fig. 7.14. However the performance of the system becomes worse at higher rotor speed. Obviously, the closed-loop system with the FRT controller shows significant oscillations in the controlled variables in comparison with that of the LPV controller case (see Fig. 7.12 and Fig. 7.14). Since the performance of the closed-loop system with the FRT controller becomes worse when the rotor speed is increased, no further closed-loop performance test at higher rotor speeds is performed. The reason for this is that the controlled system with the FRT controller is not robust with respect to noise and the flux oscillation is not as well damped as in the LPV controller implementation. As a result, the higher rotor speed results in more oscillations in the controlled variables.

7.4.3. THE SYSTEM PERFORMANCE WITH THE FRT CONTROLLER DURING ROTOR SPEED VARIATIONS

Similar to the LPV control case, the following experiments are aimed at investigating the performance of the system during rotor speed changes.

Fig. 7.32 and Fig. 7.33 show the reactive power Q_g, electrical torque T_e, and dq components of the rotor currents curves with respect to the variation of the rotor speed from $1050rpm$ to $1350rpm$ and from $1350rpm$ to $1500rpm$, respectively. As can be seen in these figures, the performance of the closed-loop system with the FRT controller is degraded when the rotor speed is increased. In contrast, the performance of the closed-loop system with the LPV controller is guaranteed during the rotor speed changes in the whole operating region of ±30% synchronous speed, i.e. from $1050rpm$ to $1950rpm$.

7.4.4. GRID VOLTAGE DIP TESTS WITH THE FRT CONTROLLER

As mentioned above, a high rotor speed induces more oscillations in the controlled variables of the closed-loop system with the FRT controller. Especially, a higher over current will occur during the fault if the rotor speed is at a high value before a stator voltage fault [154]. The following grid voltage dip tests are only carried out at under-synchronous speed ($1050rpm$) and at near-synchronous speed ($1350rpm$) of the rotor to avoid exceeding the current limit of the converter in transient periods.

Figs. 7.34 - 7.35 show the system performance when the grid undergoes faults. The grid voltage drops down to 50% of its rated value and this phenomenon occurs at a time instant of 200 msec before it recovers to its nominal value. The experimental results show that the oscillations of the rotor currents are not well damped after the fault clearance. For the LPV controller and when the fault is cleared, we recall that the rotor currents quickly recover their normal values after only about two sampling periods (see Fig. 7.24 and Fig. 7.25). The slow settling to the normal values the controlled variables of the closed-loop system with the FRT controller leads to significant fluctuations of the reactive power and the electrical torque after the fault. This phenomenon becomes more serious if the rotor speed is larger or equal to the synchronous speed since the performance of the closed-loop system is not guaranteed for this situation as presented above. In brief, the controlled system with the FRT controller is not robust with respect to the presence of stator voltage dips, especially at high rotor speeds.

7.5. SUMMARY

This chapter presents experimental results of the LPV and the FRT (deadbeat-like) current controllers proposed in Chapter 5 and Chapter 3, respectively. These results confirm the performance of the controlled system with the current controllers for both open and closed-loop circuits of the stator windings with the outer loop of electrical torque control. The experimental results show that the LPV controller achieves much better performance in comparison with that of the FRT controller. The LPV controller implementation leads to fast tracking of the reference values with less overshoot. The LPV controller also induces less oscillations in the controlled variables in comparison with that of the FRT controller. Moreover, the most important feature of the LPV controller implementation is that the LPV controller guarantees the performance of the closed-loop system for the different fixed values of the rotor speed around the synchronous speed 1500rpm as well as over the operating range of the rotor speed from 1050rpm to 1950rpm. This means that the controlled system with the LPV current controller exhibits good behavior for frozen and varying rotor speeds around ±30% of the synchronous speed and under various circumstance. In case of grid dips, the experimental results for the LPV controller show that the oscillations of the rotor currents are well damped after the fault clearance. In contrast, for the FRT controller, the rotor currents only recover their nominal values slowly when the fault is cleared.

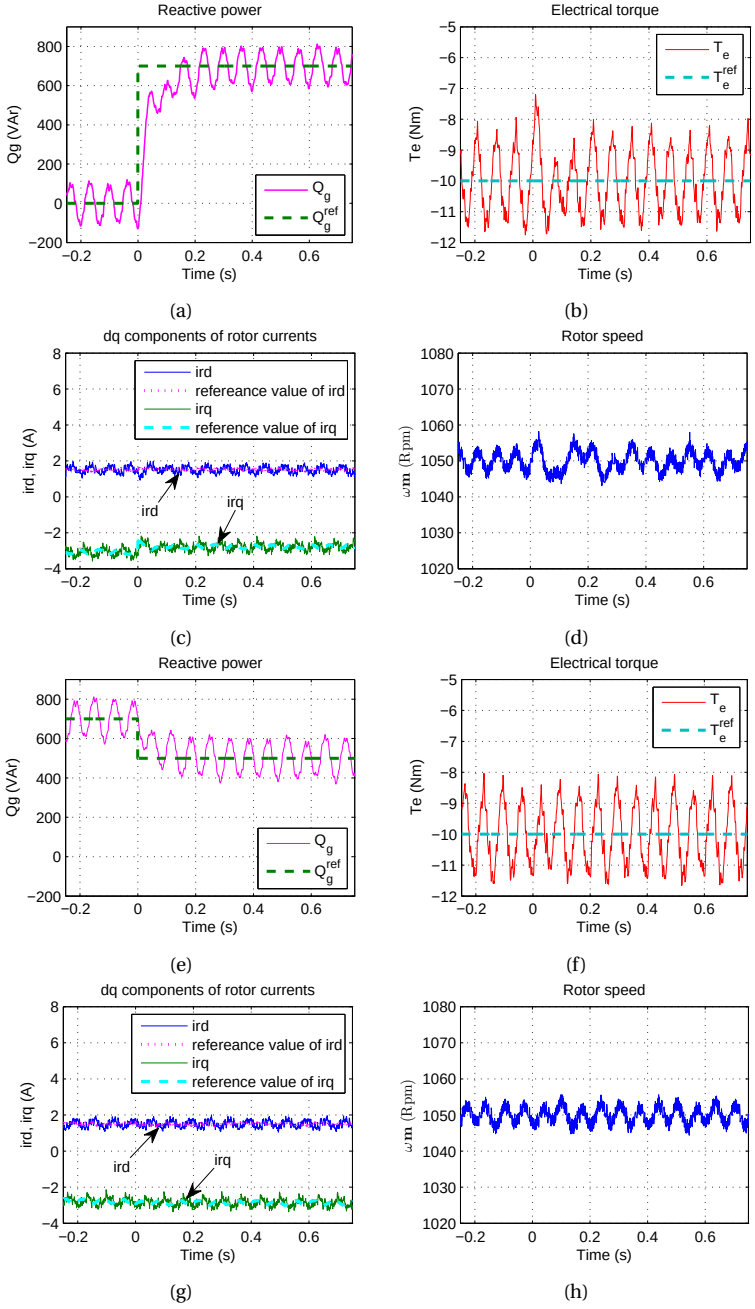

Figure 7.28: Performance of the FRT control system with step changes of reactive power from $0VAr$ to $700VAr$ at under-synchronous speed (1050rpm)

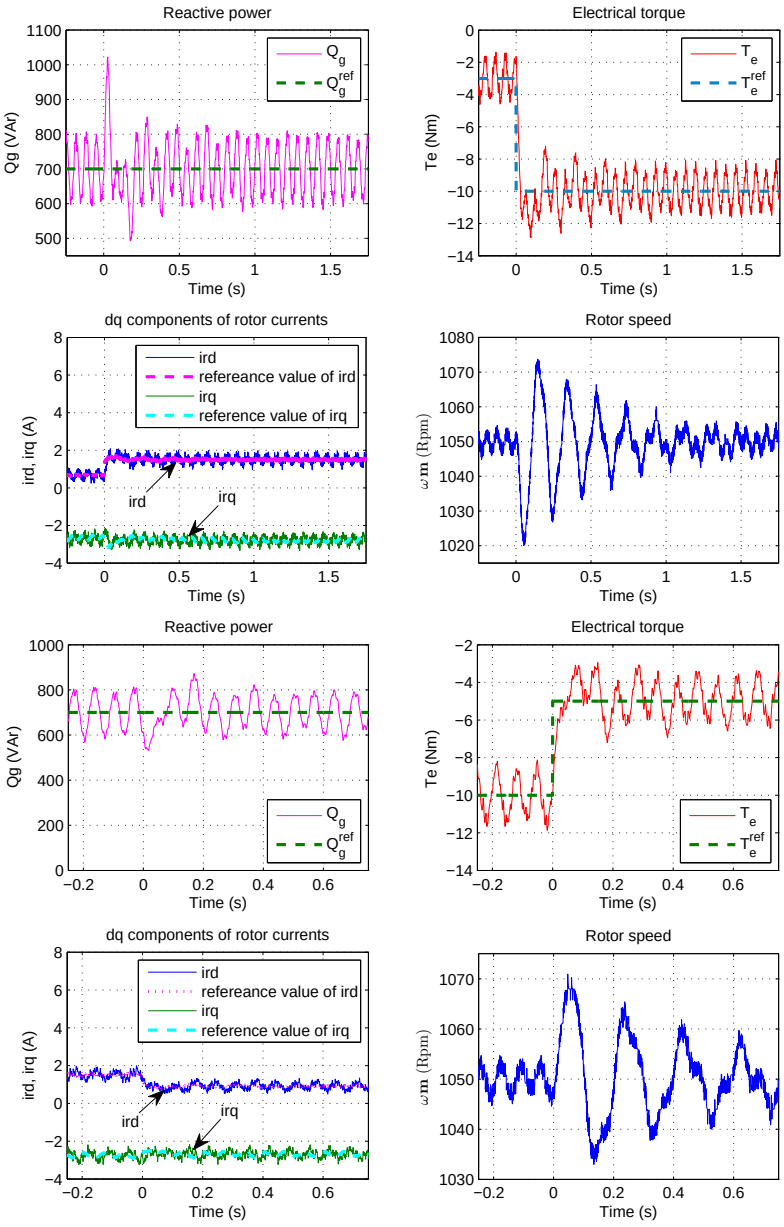

Figure 7.29: Performance of the FRT control system with step changes of electrical torque from $-3Nm$ to $-10Nm$ at under-synchronous speed (1050rpm)

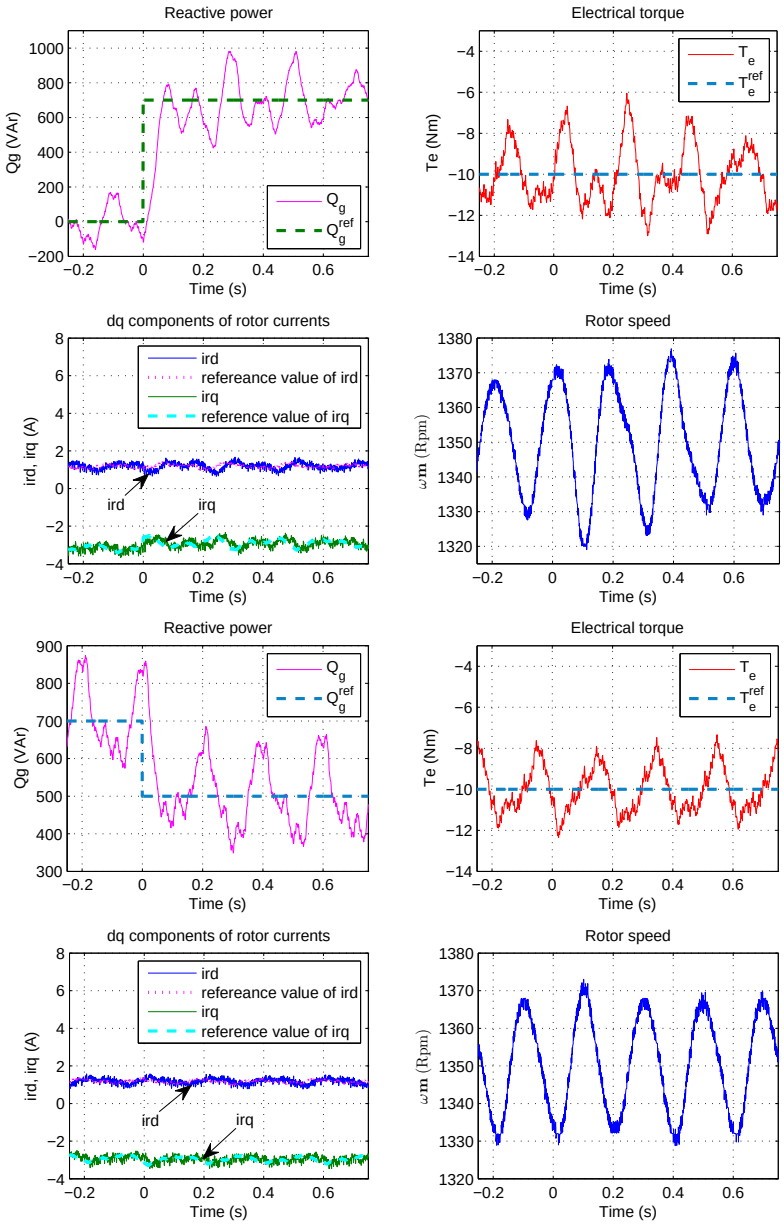

Figure 7.30: Performance of the FRT control system with step changes of reactive power from $0 VAr$ to $700 VAr$ at near-synchronous speed (1350rpm)

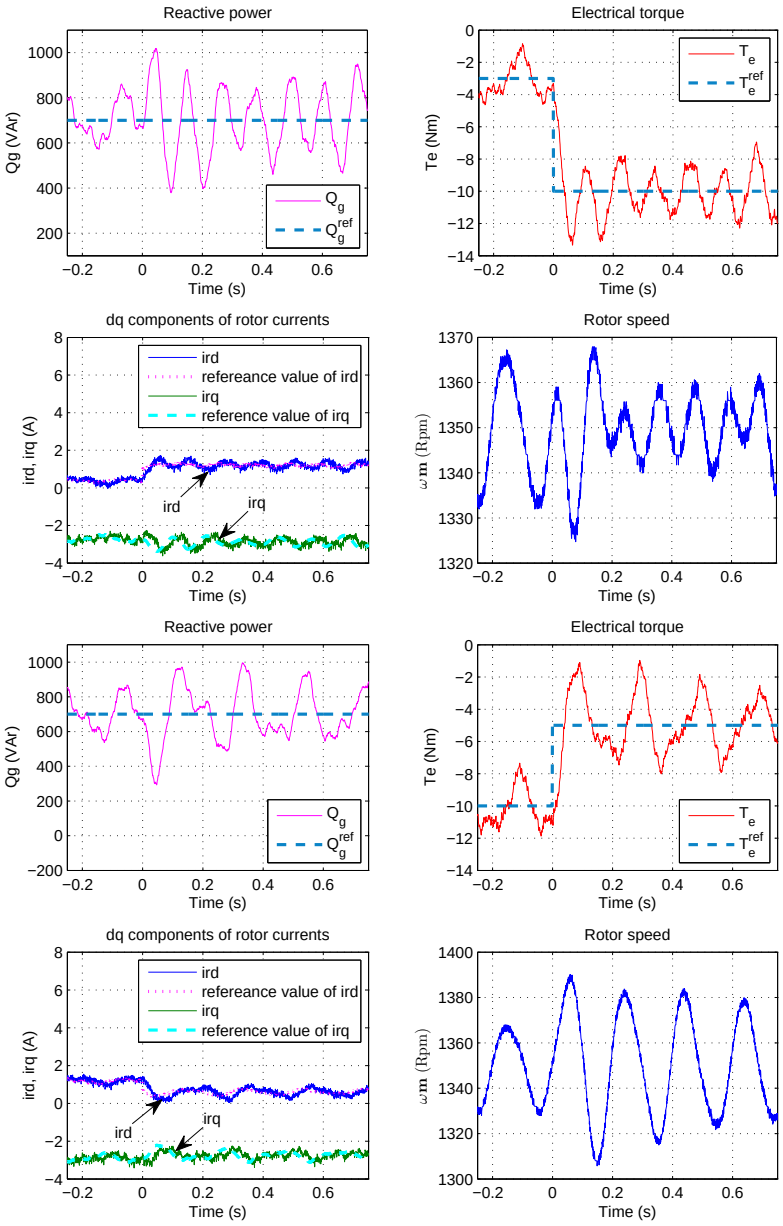

Figure 7.31: Performance of the FRT control system with step changes of electrical torque from $-3Nm$ to $-10Nm$ at near-synchronous speed (1350rpm)

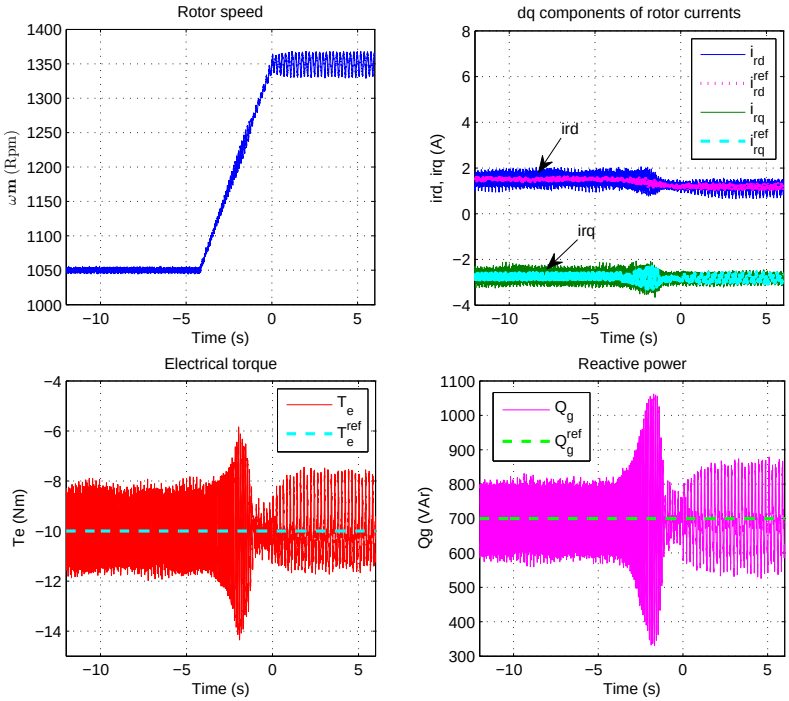

Figure 7.32: Performance of the controlled system with FRT controller for step changes of the rotor speed from $1050rpm$ to $1350rpm$

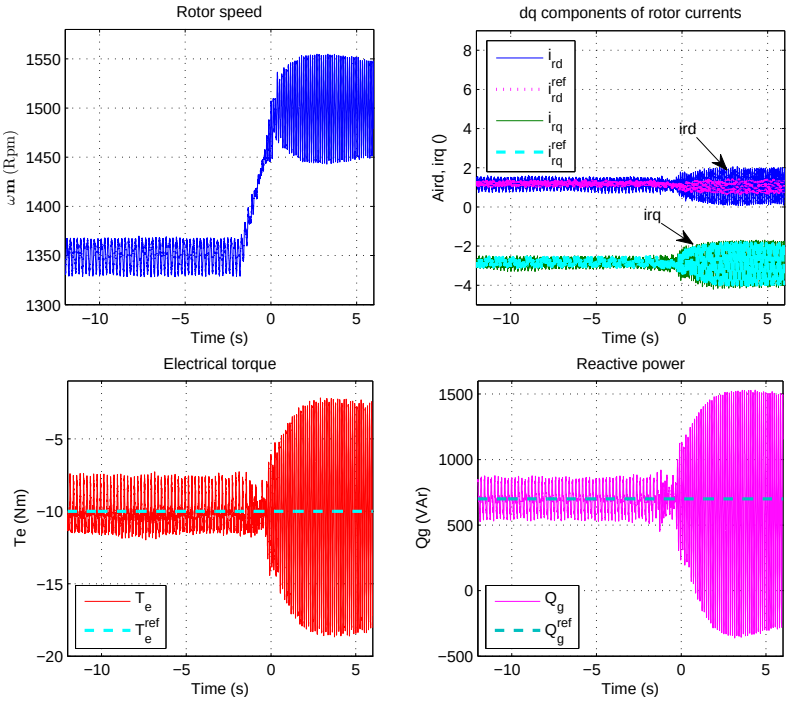

Figure 7.33: Performance of the controlled system with FRT controller for step changes of the rotor speed from $1350rpm$ to $1500rpm$

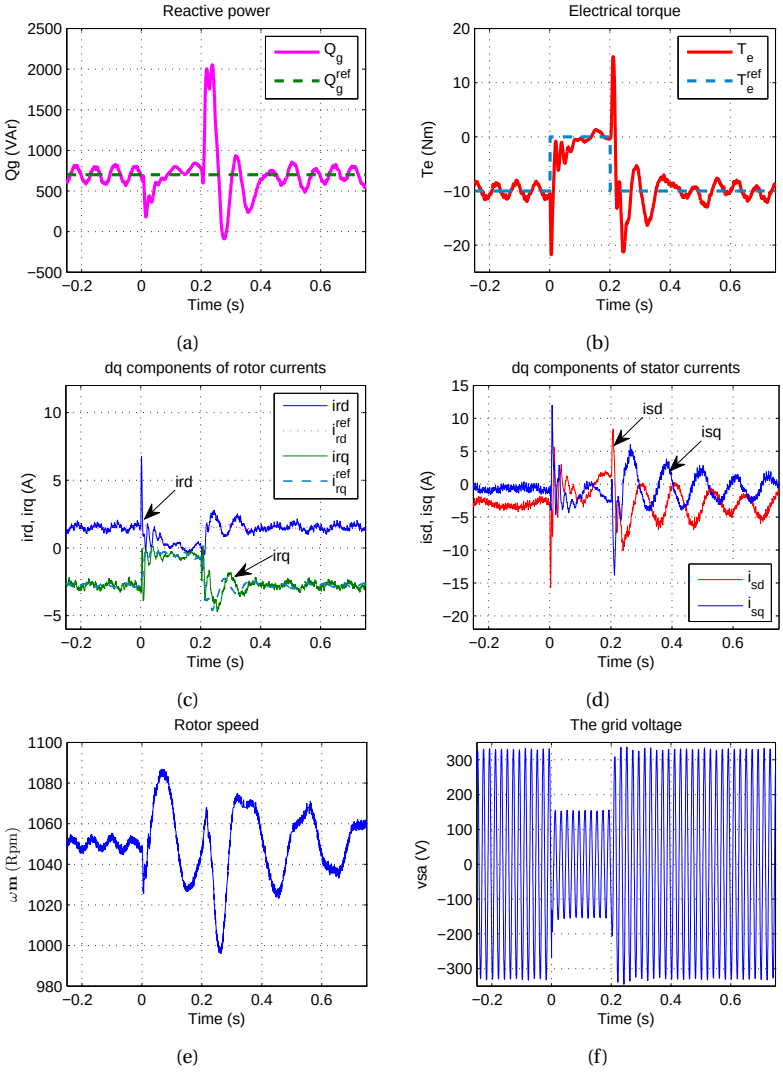

Figure 7.34: Grid voltage dips test at under-synchronous speeds of the rotor with the FRT current controller

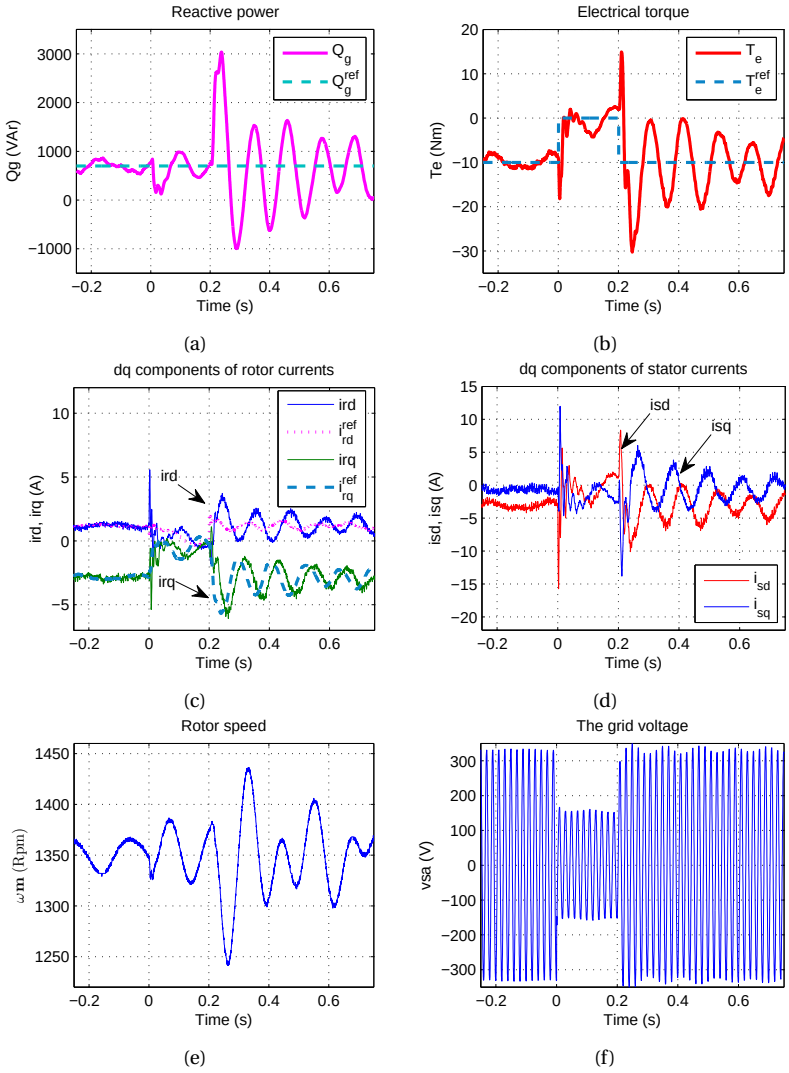

(a) (b) (c) (d) (e) (f)

Figure 7.35: The grid voltage dips test at near-synchronous speeds of the rotor with the FRT current controller

8

CONCLUSIONS AND RECOMMENDATIONS

8.1. CONCLUSIONS

The work described in this thesis has been concerned with the designs of the current controller for doubly fed induction machines where the mechanical angular speed was considered to be a measurable time-varying parameter. The objective of this study was to obtain robust dynamic performance of the controlled system with respect to changes of the mechanical rotor speed in a specified operating range and against stator voltage dips.

In the conventional design, as presented in Chapter 3, the coupling terms related to the stator voltages and flux disturbances are eliminated by using a simple feedforward compensator and the controller is constructed in each sampling period relied upon measurements of the rotor angular speed. However, this approach has the following two main disadvantages:

- The performance of the controlled system is not guaranteed over the large operating range of the rotor speed since the feedforward compensation depends highly on the accuracy of the machine inductances and the total leakage coefficient since they vary with the saturation of the machine magnetizing circuit. This was verified via the experimental results shown in Figs. 7.32, and 7.33.
- The assumption that the rotor angular speed treated as the scheduling parameter is constant during a sampling period may no longer correct for a rapid change of the rotor angular speed, especially when the grid undergoes a fault as shown in Figs. 7.34, and 7.35. Hence, the conventional approach does not ensure the performance of the controlled system for rapid variations of the rotor angular speed as well as in the presence of stator voltage dips.

The H_∞ controller designed in Chapter 4 improves the performance of the controlled system without using the feed-forward compensator. This approach reduces the sensitivity of the controlled system to changes of the machine parameters and enhances the performance of the controlled system with respect to the rotor angular speed variations in comparison with the conventional design. However, the designed H_∞ controller does not guarantee the desired performance of the controlled system with respect to rapid variations of the rotor angular speed as shown in Fig. 5.9.

The advanced control technique with LPV design is then employed in order to maintain the desired objectives for all admissible trajectories (including rapid variations) of the rotor speed in the operating range. In addition, this approach also manifests an improvement of the performance of the closed-loop system with respect to changes in the machine parameters and the stator voltage disturbance. Under variations of the machine parameters and grid voltage dips, some simulation results show that the designed LPV controller is far more robust than the conventional design with the deadbeat controller. Furthermore, oscillations in the stator and rotor currents are considerably reduced during the grid voltage faults, and the closed loop system recovers from the faults much faster than that of the deadbeat design. Therefore, since the LPV controller improves the performance of the closed-loop controlled system remarkably in comparison with the conventional scheme, the LPV design approach can be considered as a promising solution for the control of DFIMs for wind turbine applications.

For the real-time implementation, the designed continuous-time LPV controller is superseded by a sampled discrete-time LPV controller. The objective of the continuous-to-discrete time LPV controller design is to obtain a good match of the closed-loop performance of the continuous-time and the discrete-time systems for a suitable sampling rate.

The next part of the thesis deals with the robustness analysis of the closed-loop controlled system for both the LPV and deadbeat controllers. As a matter of fact, the machine parameters such as the stator, rotor, and mutual inductances are all varying with time because of changes in the machine temperature, the magnetic saturation level, and the winding current modulus. Consequently, a rigorous robustness analysis has been performed in order to systematically investigate the stability of the closed-loop system against these time-varying parameters. In this thesis, the IQC approach is employed for robust stability analysis for these rate-bounded LTV parametric uncertainties. The analysis tests are performed based on the IQC framework with the help of the YALMIP toolbox in Matlab [147]. The IQC analysis results for both the controlled system with the LPV and the deadbeat controllers are presented. The given robustness margins show that the closed-loop systems remain stable in the presence of slowly time-varying parametric uncertainties. In addition, the closed-loop system with the LPV design is more robust than that of the deadbeat design. Besides, the test results also indicate the deterioration of the stability margins if the rate-of-variations increase.

An experimental set up is presented in order to evaluate the quality of the rotor current controllers with the open and closed-loop circuits of the stator windings. The experimental tests are also performed for the variation of the rotor speed over the operating range of the DFIM. The experimental results show that the LPV controller ensures the

performance of the closed-loop system for fixed rotor speeds as well as over the rotor speed variations around ±30% of the synchronous speed. Furthermore, grid voltage dip tests of 50% of its normal value are also carried out in order to investigate robustness of the controlled system in the presence of stator voltage disturbances. Via these experiments, the advantages of the proposed LPV controller are demonstrated by means of the improvement of the damping oscillations and the faster recovery of the controlled variables during and after the fault.

The main contributions of this work are summarized as follows:

- In Chapter 3, the mathematical models of the feed-forward compensators for the stator voltage, and stator flux are derived via suitable variable transformations. This can be considered to as a supplement to the missing part in previous designs, for example in [29, 53].
- In Chapter 5, the main contribution of this chapter is a design of the discrete-time LPV controller that guarantees the performance of the closed-loop system matching that of the closed-loop system for the predesigned continuous-time LPV controller with a reasonable sampling rate. Another contribution of this chapter is the analysis of the time responses of the discrete-time LPV current controller under the step changes of the rotor currents for differential sampling frequencies.
- In Chapter 6, the main contribution is the implementation of the IQC framework to analyze the robustness of the controlled system with respect to changes in the machine inductances and the rotor angular speed. The derived stability margins for both the controlled system with the LPV and deadbeat controllers are also contributions of this chapter.
- In Chapter 7, the main contribution is the experimental validation of the proposed LPV controller. The experimental tests show that the LPV controller design fulfills all the performance requirements over the operating region of the rotor speed around ±30% of the synchronous speed.

8.2. RECOMMENDATIONS

For future works, the following topics remain open:

- In this work, the experimental tests have not been performed in order to analyze robustness of the closed-loop system with respect to machine parameter variations as presented in Chapter 6. Future work is required to investigate a more thorough analysis of the performance improvements and robustness of the controlled system under parameter changes in the normal operation as well as in the grid voltage faults on the real-time laboratory set up.
- As mentioned earlier, the grid voltage is assumed to be sinusoidal and balanced, i.e. the phase voltages are equal to each other. However, as presented in the literature, the performance of the controlled system is deteriorated if the stator windings are connected to unbalanced grid voltages. This results in an over current

of the rotor side converter and more oscillation in the dc link voltage and electromagnetic torque. Consequently, robustness of the closed-loop system with the LPV current controller should be investigated in the presence of unbalanced grid faults as presented for conventional controller designs in [155, 156, 157, 158].

- For the LPV design, the rotor speed is considered as a gain-scheduling parameter since it can be measured online while the other parameters are treated as constant parameters. However, as appearing in the DFIM model, the stator and rotor inductances, and the mutual inductance vary with the machine flux due to magnetic saturation and winding current modulus. Therefore, they can also be considered as uncertain parameters. For improving robustness of the closed-loop system with respect to these parametric uncertainties, a robust LPV control of the system should be designated in future research. This is a mixed problem of classical robust synthesis techniques and the gain-scheduling procedure [111].

- For the IQC-based robust stability analysis of the controlled system, the tests are carried out by varying the ranges of the values and rates of the parameters until getting the margins of stability. It should be emphasized that the tests are only sufficient to reveal lower bounds on the stability margins. Hence, calculating upper bounds for the robust stability margin is another interesting aspect for future work.

A

LINEAR FRACTIONAL REPRESENTATION OF THE SYSTEM

The equations (2.15) and (2.16) can be expressed as

$$\boldsymbol{E}_{rc}\dot{x}_r = \boldsymbol{A}_{rc}x_r + \boldsymbol{B}_{rc}v_{rs} \tag{A.1}$$

$$y_r = C_{rc}x_r \tag{A.2}$$

where

$$\boldsymbol{A}_{rc} = \begin{pmatrix} -L_s^2R_r - L_m^2R_s & -L_s(L_sL_r - L_m^2)(\omega-\omega_s) & L_mR_s & -L_mL_s\omega \\ L_s(L_sL_r - L_m^2)(\omega-\omega_s) & -L_s^2R_r - L_m^2R_s & L_mL_s\omega & L_mR_s \\ L_m(L_sL_r - L_m^2)R_s & 0 & -(L_sL_r - L_m^2)R_s & L_s(L_sL_r - L_m^2)\omega_s \\ 0 & L_m(L_sL_r - L_m^2)R_s & -L_s(L_sL_r - L_m^2)\omega_s & -(L_sL_r - L_m^2)R_s \end{pmatrix};$$

$$\boldsymbol{B}_{rc} = \begin{pmatrix} -L_mL_s & 0 & L_s^2 & 0 \\ 0 & -L_mL_s & 0 & L_s^2 \\ L_s(L_sL_r - L_m^2) & 0 & 0 & 0 \\ 0 & L_s(L_sL_r - L_m^2) & 0 & 0 \end{pmatrix};$$

$$\boldsymbol{E}_{rc} = L_s(L_sL_r - L_m^2)I_4 = \begin{pmatrix} L_s(L_sL_r - L_m^2) & 0 & 0 & \\ 0 & L_s(L_sL_r - L_m^2) & 0 & 0 \\ 0 & 0 & L_s(L_sL_r - L_m^2) & 0 \\ 0 & 0 & 0 & L_s(L_sL_r - L_m^2) \end{pmatrix}.$$

Let $L_s = L_{sn}(1+p_s\delta_s)$, $L_r = L_{rn}(1+p_r\delta_r)$, $L_m = L_{mn}(1+p_m\delta_m)$, where $-1 \le \delta_r, \delta_s, \delta_m \le 1$; L_{rn}, L_{sn}, and L_{mn} are nominal values of the rotor, the stator and mutual inductances; p_s, p_r, and p_m present the relative perturbations on the L_s, L_r, and L_m, respectively, we

have

$$\begin{aligned}
L_sL_r - L_m^2 &= (L_{sn}+\delta_s p_s)(L_{rn}+\delta_r p_r) - (L_{mn}+\delta_m p_m)^2 \\
&= L_{sn}L_{rn} - L_{mn}^2 + \delta_s L_{rn} p_s + \delta_s \delta_r p_s p_r + \delta_r L_{sn} p_r - \delta_m 2L_{mn} p_m - \delta_m^2 p_m^2 \\
L_s(L_sL_r - L_m^2) &= L_{sn}(L_{sn}L_{rn} - L_{mn}^2) + \delta_s(2L_{sn}L_{rn} - L_{mn}^2)p_s + \delta_s\delta_r 2L_{sn}p_s p_r \\
&\quad +\delta_s^2 L_{rn} p_s^2 + \delta_s^2\delta_r p_s^2 p_r - \delta_s\delta_m 2L_{mn}p_s p_m - \delta_s\delta_m^2 p_s p_m^2 + \delta_r L_{sn}^2 p_r \\
&\quad -\delta_m 2L_{sn}L_{mn}p_m - \delta_m^2 L_{sn} p_m^2 \\
L_m(L_sL_r - L_m^2) &= L_{mn}(L_{sn}L_{rn} - L_{mn}^2) + \delta_s L_{rn}L_{mn}p_s + \delta_s\delta_r L_{mn}p_s p_r + \delta_s\delta_m L_{rn}p_s p_m \\
&\quad +\delta_s\delta_r\delta_m p_s p_r p_m + \delta_r L_{sn}L_{mn}p_r + \delta_r\delta_m L_{sn}p_r p_m + \delta_m(L_{sn}L_{rn} - 3L_m^2)p_m \\
&\quad -\delta_m^2 3L_{mn}p_m^2 - \delta_m^3 p_m^3
\end{aligned}$$

and

$$\begin{aligned}
\boldsymbol{A}_{rc} &= A_{rn} + \delta_s A_{p01} + \delta_s^2 A_{p02} + \delta_s\delta_r A_{p03} + \delta_s^2\delta_r A_{p04} + \delta_s\delta_m A_{p05} + \delta_s\delta_m^2 A_{p06} \\
&\quad +\delta_s\delta_r\delta_m A_{p07} + \delta_r A_{p08} + \delta_r\delta_m A_{p09} + \delta_m A_{p10} + \delta_m^2 A_{p11} + \delta_m^3 A_{p12}
\end{aligned}$$

A

where

$$A_{rn} = \begin{pmatrix} -L_{sn}^2R_r - L_{mn}^2R_s & -L_{sn}(L_{sn}L_{rn} - L_{mn}^2)(\omega-\omega_s) & L_{mn}R_s & -L_{sn}L_{mn}\omega \\ L_{sn}(L_{sn}L_{rn} - L_{mn}^2)(\omega-\omega_s) & -L_{sn}^2R_r - L_{mn}^2R_s & L_{sn}L_{mn}\omega & L_{mn}R_s \\ L_{mn}(L_{sn}L_{rn} - L_{mn}^2)R_s & 0 & -(L_{sn}L_{rn} - L_{mn}^2)R_s & L_{sn}(L_{sn}L_{rn} - L_{mn}^2)\omega_s \\ 0 & L_{mn}(L_{sn}L_{rn} - L_{mn}^2)R_s & -L_{sn}(L_{sn}L_{rn} - L_{mn}^2)\omega_s & -(L_{sn}L_{rn} - L_{mn}^2)R_s \end{pmatrix}$$

$$A_{p01} = \begin{pmatrix} -2L_{sn}R_r p_s & -(2L_{sn}L_{rn} - L_{mn}^2)(\omega-\omega_s)p_s & 0 & -L_{mn}\omega p_s \\ (2L_{sn}L_{rn}(\omega-\omega_s)p_s & -2L_{sn}R_r p_s & L_{mn}\omega p_s & 0 \\ L_{rn}L_{mn}R_s p_s & 0 & -L_{rn}R_s p_s & (2L_{sn}L_{rn} - L_{mn}^2)\omega_s p_s \\ 0 & (L_{rn}L_{mn}R_s p_s & -(2L_{sn}L_{rn} - L_{mn}^2)\omega_s p_s & -L_{rn}R_s p_s \end{pmatrix}$$

$$A_{p02} = \begin{pmatrix} -R_r p_s^2 & -L_{rn}(\omega-\omega_s)p_s^2 & 0 & 0 \\ L_{rn}(\omega-\omega_s)p_s^2 & -R_r p_s^2 & 0 & 0 \\ 0 & 0 & 0 & L_{rn}\omega_s p_s^2 \\ 0 & 0 & -L_{rn}\omega_s p_s^2 & 0 \end{pmatrix}$$

$$A_{p03} = \begin{pmatrix} 0 & -2L_{sn}(\omega-\omega_s)p_s p_r & 0 & 0 \\ 2L_{sn}(\omega-\omega_s)p_s p_r & 0 & 0 & 0 \\ L_{mn}R_s p_s p_r & 0 & -R_s p_s p_r & 2L_{sn}\omega_s p_s p_r \\ 0 & L_{mn}R_s p_s p_r & -2L_{sn}\omega_s p_s p_r & -R_s p_s p_r \end{pmatrix}$$

$$A_{p04} = \begin{pmatrix} 0 & -(\omega-\omega_s)p_s^2 p_r & 0 & 0 \\ (\omega-\omega_s)p_s^2 p_r & 0 & 0 & 0 \\ 0 & 0 & 0 & \omega_s p_s^2 p_r \\ 0 & 0 & -\omega_s p_s^2 p_r & 0 \end{pmatrix}$$

$$A_{p05} = \begin{pmatrix} 0 & 2L_{mn}(\omega-\omega_s)p_s p_m & 0 & -\omega_m p_s p_m \\ -2L_{mn}(\omega-\omega_s)p_s p_m & 0 & \omega_m p_s p_m & 0 \\ L_{rn}R_s p_s p_m & 0 & 0 & -2L_{mn}\omega_s p_s p_m \\ 0 & L_{rn}R_s p_s p_m & 2L_{mn}\omega_s p_s p_m & 0 \end{pmatrix}$$

$$A_{p06} = \begin{pmatrix} 0 & (\omega-\omega_s)p_s p_m^2 & 0 & 0 \\ -(\omega-\omega_s)p_s p_m^2 & 0 & 0 & 0 \\ 0 & 0 & 0 & -\omega_s p_s p_m^2 \\ 0 & 0 & \omega_s p_s p_m^2 & 0 \end{pmatrix}$$

$$A_{p07} = \begin{pmatrix} 0 & 0 & 0 & 0 \\ 0 & 0 & 0 & 0 \\ R_s p_s p_r p_m & 0 & 0 & 0 \\ 0 & R_s p_s p_r p_m & 0 & 0 \end{pmatrix}$$

$$A_{p08} = \begin{pmatrix} 0 & 0 & 0 & 0 \\ 0 & 0 & 0 & 0 \\ L_{sn}L_{mn}R_s p_r & 0 & -L_{sn}R_s p_r & L_{sn}^2\omega_s p_r \\ 0 & L_{sn}L_{mn}R_s p_r & -L_{sn}^2\omega_s p_r & -L_{sn}R_s p_r \end{pmatrix}$$

$$A_{p09} = \begin{pmatrix} 0 & 0 & 0 & 0 \\ 0 & 0 & 0 & 0 \\ L_{sn}R_s p_r p_m & 0 & 0 & 0 \\ 0 & L_{sn}R_s p_r p_m & 0 & 0 \end{pmatrix}$$

$$A_{p10} = \begin{pmatrix} -2L_{mn}R_s p_m & 2L_{sn}L_{mn}(\omega-\omega_s)p_m & R_s p_m & -L_{sn}\omega_m p_m \\ -2L_{sn}L_{mn}(\omega-\omega_s)p_m & -2L_{mn}R_s p_m & L_{sn}\omega_m p_m & R_s p_m \\ (L_{sn}L_{rn}-3L_{mn}^2)R_s p_m & 0 & 2L_{mn}R_s p_m & -2L_{sn}L_{mn}\omega_s p_m \\ 0 & (L_{sn}L_{rn}-3L_{mn}^2)R_s p_m & 2L_{sn}L_{mn}\omega_s p_m & 2L_{mn}R_s p_m \end{pmatrix}$$

$$A_{p11} = \begin{pmatrix} -R_s p_m^2 & L_{sn}(\omega-\omega_s)p_m^2 & 0 & 0 \\ -L_{sn}(\omega-\omega_s)p_m^2 & -R_s p_m^2 & 0 & 0 \\ -3L_{mn}R_s p_m^2 & 0 & R_s p_m^2 & -L_{sn}\omega_s p_m^2 \\ 0 & -3L_{mn}R_s p_m^2 & L_{sn}\omega_s p_m^2 & R_s p_m^2 \end{pmatrix}$$

$$A_{p12} = \begin{pmatrix} 0 & 0 & 0 & 0 \\ 0 & 0 & 0 & 0 \\ -R_s p_m^3 & 0 & 0 & 0 \\ 0 & -R_s p_m^3 & 0 & 0 \end{pmatrix}$$

$$\begin{aligned} \boldsymbol{B}_{rc} &= B_{rn} + \delta_s B_{p01} + \delta_s^2 B_{p02} + \delta_s\delta_r B_{p03} + \delta_s^2\delta_r B_{p04} + \delta_s\delta_m B_{p05} + \delta_s\delta_m^2 B_{p06} \\ &\quad + \delta_s\delta_r\delta_m B_{p07} + \delta_r B_{p08} + \delta_r\delta_m B_{p09} + \delta_m B_{p10} + \delta_m^2 B_{p11} + \delta_m^3 B_{p12} \end{aligned}$$

where

$$B_{rn} = \begin{pmatrix} -L_{sn}L_{mn} & 0 & L_{sn}^2 & 0 \\ 0 & -L_{sn}L_{mn} & 0 & L_{sn}^2 \\ L_{sn}(L_{sn}L_{rn}-L_{mn}^2) & 0 & 0 & 0 \\ 0 & L_{sn}(L_{sn}L_{rn}-L_{mn}^2) & 0 & 0 \end{pmatrix}$$

$$B_{p01} = \begin{pmatrix} -L_{mn}p_s & 0 & 2L_{sn}p_s & 0 \\ 0 & -L_{mn}p_s & 0 & 2L_{sn}p_s \\ (2L_{sn}L_{rn}-L_{mn}^2)p_s & 0 & 0 & 0 \\ 0 & (2L_{sn}L_{rn}-L_{mn}^2)p_s & 0 & 0 \end{pmatrix}$$

$$B_{p02} = \begin{pmatrix} 0 & 0 & p_s^2 & 0 \\ 0 & 0 & 0 & p_s^2 \\ L_{rn}p_s^2 & 0 & 0 & 0 \\ 0 & L_{rn}p_s^2 & 0 & 0 \end{pmatrix}$$

$$B_{p03} = \begin{pmatrix} 0 & 0 & 0 & 0 \\ 0 & 0 & 0 & 0 \\ 2L_{sn}p_s p_r & 0 & 0 & 0 \\ 0 & 2L_{sn}p_s p_r & 0 & 0 \end{pmatrix}$$

$$B_{p04} = \begin{pmatrix} 0 & 0 & 0 & 0 \\ 0 & 0 & 0 & 0 \\ p_s^2 p_r & 0 & 0 & 0 \\ 0 & p_s^2 p_r & 0 & 0 \end{pmatrix}$$

$$B_{p05} = \begin{pmatrix} -p_s p_m & 0 & 0 & 0 \\ 0 & -p_s p_m & 0 & 0 \\ -2L_{mn}p_s p_m & 0 & 0 & 0 \\ 0 & -2L_{mn}p_s p_m & 0 & 0 \end{pmatrix}$$

$$B_{p06} = \begin{pmatrix} 0 & 0 & 0 & 0 \\ 0 & 0 & 0 & 0 \\ -p_s p_m^2 & 0 & 0 & 0 \\ 0 & -p_s p_m^2 & 0 & 0 \end{pmatrix}$$

$$B_{p07} = 0$$

$$B_{p08} = \begin{pmatrix} 0 & 0 & 0 & 0 \\ 0 & 0 & 0 & 0 \\ L_{sn}^2 p_r & 0 & 0 & 0 \\ 0 & L_{sn}^2 p_r & 0 & 0 \end{pmatrix}$$

$$B_{p09} = 0$$

$$B_{p10} = \begin{pmatrix} -L_{sn} p_m & 0 & 0 & 0 \\ 0 & -L_{sn} p_m & 0 & 0 \\ -2L_{sn} L_{mn} p_m & 0 & 0 & 0 \\ 0 & -2L_{sn} L_{mn} p_m & 0 & 0 \end{pmatrix}$$

$$B_{p11} = \begin{pmatrix} 0 & 0 & 0 & 0 \\ 0 & 0 & 0 & 0 \\ -L_{sn} p_m^2 & 0 & 0 & 0 \\ 0 & -L_{sn} p_m^2 & 0 & 0 \end{pmatrix}$$

$$B_{p12} = 0.$$

$$\begin{aligned} \boldsymbol{E}_{rc} \quad = \quad & E_{rn} + \delta_s E_{p01} + \delta_s^2 E_{p02} + \delta_s \delta_r E_{p03} + \delta_s^2 \delta_r E_{p04} + \delta_s \delta_m E_{p05} + \delta_s \delta_m^2 E_{p06} \\ & + \delta_s \delta_r \delta_m E_{p07} + \delta_r E_{p08} + \delta_r \delta_m E_{p09} + \delta_m E_{p10} + \delta_m^2 E_{p11} + \delta_m^3 E_{p12} \end{aligned}$$

where

$$E_{rn} = L_{sn}(L_{sn} L_{rn} - L_{mn}^2) I_4$$

$$E_{p01} = (2L_{sn} L_{rn} - L_{mn}^2) p_s I_4$$

$$E_{p02} = L_{rn} p_s^2 I_4$$

$$E_{p03} = 2L_{sn} p_s p_r I_4$$

$$E_{p04} = p_s^2 p_r I_4$$

$$E_{p05} = -2L_{mn} p_s p_m I_4$$

$$E_{p06} = -p_s p_m^2 I_4$$

$$E_{p07} = 0$$

$$E_{p08} = L_{sn}^2 p_r I_4$$

$$E_{p09} = 0$$

$$E_{p10} = -2L_{sn} L_{mn} p_m I_4$$

$$E_{p11} = -L_{sn} p_m^2 I_4$$

$$E_{p12} = 0$$

Equation (A.1) now becomes

$$(E_{rn}+\delta_s E_{p01}+\delta_s^2 E_{p02}+\delta_s\delta_r E_{p03}+\delta_s^2\delta_r E_{p04}+\delta_s\delta_m E_{p05}+\delta_s\delta_m^2 E_{p06}+\delta_s\delta_r\delta_m E_{p07}+\delta_r E_{p08}+\delta_r\delta_m E_{p09}+\delta_m E_{p10}+\delta_m^2 E_{p11}+\delta_m^3 E_{p12})\dot{x}_r = (A_{rn}+\delta_s A_{p01}+\delta_s^2 A_{p02}+\delta_s\delta_r A_{p03}+\delta_s^2\delta_r A_{p04}+\delta_s\delta_m A_{p05}+\delta_s\delta_m^2 A_{p06}+\delta_s\delta_r\delta_m A_{p07}+\delta_r A_{p08}+\delta_r\delta_m A_{p09}+\delta_m A_{p10}+\delta_m^2 A_{p11}+\delta_m^3 A_{p12})x_r + (B_{rn}+\delta_s B_{p01}+\delta_s^2 B_{p02}+\delta_s\delta_r B_{p03}+\delta_s^2\delta_r B_{p04}+\delta_s\delta_m B_{p05}+\delta_s\delta_m^2 B_{p06}+\delta_s\delta_r\delta_m B_{p07}+\delta_r B_{p08}+\delta_r\delta_m B_{p09}+\delta_m B_{p10}+\delta_m^2 B_{p11}+\delta_m^3 B_{p12})\upsilon_{rs} = (F_{rn}+\delta_s F_{p01}+\delta_s^2 F_{p02}+\delta_s\delta_r F_{p03}+\delta_s^2\delta_r F_{p04}+\delta_s\delta_m F_{p05}+\delta_s\delta_m^2 F_{p06}+\delta_s\delta_r\delta_m F_{p07}+\delta_r F_{p08}+\delta_r\delta_m F_{p09}+\delta_m F_{p10}+\delta_m^2 F_{p11}+\delta_m^3 F_{p12})\begin{pmatrix} x_r \\ \upsilon_{rs}\end{pmatrix}$$

where $F_{rn} = \begin{pmatrix} A_{rn} & B_{rn}\end{pmatrix}$; $F_{pi} = \begin{pmatrix} A_{pi} & B_{pi}\end{pmatrix}$; $i = 1..12$.

Let $\eta_r = \dot{x}_r$, $\xi_r = \begin{pmatrix} x_r \\ \upsilon_{rs}\end{pmatrix}$, we have

$$(E_{rn}+\delta_s E_{p01}+\delta_s^2 E_{p02}+\delta_s\delta_r E_{p03}+\delta_s^2\delta_r E_{p04}+\delta_s\delta_m E_{p05}+\delta_s\delta_m^2 E_{p06}+\delta_s\delta_r\delta_m E_{p07}+\delta_r E_{p08}+\delta_r\delta_m E_{p09}+\delta_m E_{p10}+\delta_m^2 E_{p11}+\delta_m^3 E_{p12})\eta_r = F_{rn}\xi_r+\delta_s F_{p01}\xi_r+\delta_s^2 F_{p02}\xi_r+\delta_s\delta_r F_{p03}\xi_r+\delta_s^2\delta_r F_{p04}\xi_r+\delta_s\delta_m F_{p05}\xi_r+\delta_s\delta_m^2 F_{p06}\xi_r+\delta_s\delta_r\delta_m F_{p07}\xi_r+\delta_r F_{p08}\xi_r+\delta_r\delta_m F_{p09}\xi_r+\delta_m F_{p10}\xi_r+\delta_m^2 F_{p11}\xi_r+\delta_m^3 F_{p12}\xi_r$$

It follows that

$$(I+\delta_s E_{rn}^{-1}E_{p01}+\delta_s^2 E_{rn}^{-1}E_{p02}+\delta_s\delta_r E_{rn}^{-1}E_{p03}+\delta_s^2\delta_r E_{rn}^{-1}E_{p04}+\delta_s\delta_m E_{rn}^{-1}E_{p05}+\delta_s\delta_m^2 E_{rn}^{-1}E_{p06}+\delta_s\delta_r\delta_m E_{rn}^{-1}E_{p07}+\delta_r E_{rn}^{-1}E_{p08}+\delta_r\delta_m E_{rn}^{-1}E_{p09}+\delta_m E_{rn}^{-1}E_{p10}+\delta_m^2 E_{rn}^{-1}E_{p11}+\delta_m^3 E_{rn}^{-1}E_{p12})\eta_r = E_{rn}^{-1}(F_{rn}\xi_r+\delta_s F_{p01}\xi_r+\delta_s^2 F_{p02}\xi_r+\delta_s\delta_r F_{p03}\xi_r+\delta_s^2\delta_r F_{p04}\xi_r+\delta_s\delta_m F_{p05}\xi_r+\delta_s\delta_m^2 F_{p06}\xi_r+\delta_s\delta_r\delta_m F_{p07}\xi_r+\delta_r F_{p08}\xi_r+\delta_r\delta_m F_{p09}\xi_r+\delta_m F_{p10}\xi_r+\delta_m^2 F_{p11}\xi_r+\delta_m^3 F_{p12})\xi_r$$

Thus

$$\begin{aligned}\eta_r &= E_{rn}^{-1}F_{rn}\xi_r+\delta_s E_{rn}^{-1}(F_{p01}\xi_r-E_{p01}\eta_r)+\delta_s^2 E_{rn}^{-1}(F_{p02}\xi_r-E_{p02}\eta_r)+\delta_s\delta_r E_{rn}^{-1}(F_{p03}\xi_r-E_{p03}\eta_r)\\ &\quad+\delta_s^2\delta_r E_{rn}^{-1}(F_{p04}\xi_r-E_{p04}\eta_r)+\delta_s\delta_m E_{rn}^{-1}(F_{p05}\xi_r-E_{p05}\eta_r)+\delta_s\delta_m^2 E_{rn}^{-1}(F_{p06}\xi_r-E_{p06}\eta_r)\\ &\quad+\delta_s\delta_r\delta_m E_{rn}^{-1}(F_{p07}\xi_r-E_{p07}\eta_r)+\delta_r E_{rn}^{-1}(F_{p08}\xi_r-E_{p08}\eta_r)+\delta_r\delta_m E_{rn}^{-1}(F_{p09}\xi_r-E_{p09}\eta_r)\\ &\quad+\delta_m E_{rn}^{-1}(F_{p10}\xi_r-E_{p10}\eta_r)+\delta_m^2 E_{rn}^{-1}(F_{p11}\xi_r-E_{p11}\eta_r)+\delta_m^3 E_{rn}^{-1}(F_{p12})\xi_r-E_{p12}\eta_r)\\ &= E_{rn}^{-1}F_{rn}\xi_r+w_1+w_3+w_6\end{aligned}$$

where

$$w_1 = \delta_s z_1$$

$$z_1 = E_{rn}^{-1}(F_{p01}\xi_r-E_{p01}\eta_r)+\delta_s E_{rn}^{-1}(F_{p02}\xi_r-E_{p02}\eta_r)+\delta_r E_{rn}^{-1}(F_{p03}\xi_r-E_{p03}\eta_r)+\delta_s\delta_r E_{rn}^{-1}(F_{p04}\xi_r-E_{p04}\eta_r)+\delta_m E_{rn}^{-1}(F_{p05}\xi_r-E_{p05}\eta_r)+\delta_m^2 E_{rn}^{-1}(F_{p06}\xi_r-E_{p06}\eta_r)+\delta_r\delta_m E_{rn}^{-1}(F_{p07}\xi_r-E_{p07}\eta_r) = E_{rn}^{-1}(F_{p01}\xi_r-E_{p01}\eta_r)+w_2+w_4+w_7 = E_{rn}^{-1}F_{p01}\xi_r-E_{rn}^{-1}E_{p01}(E_{rn}^{-1}F_{rn}\xi_r+w_1+w_3+w_6)+w_2+w_4+w_7 = (E_{rn}^{-1}F_{p01}-E_{rn}^{-1}E_{p01}E_{rn}^{-1}F_{rn})\xi_r-E_{rn}^{-1}E_{p01}w_1-E_{rn}^{-1}E_{p01}w_3-E_{rn}^{-1}E_{p01}w_6+w_2+w_4+w_7$$

Similarly

$$w_2 = \delta_s z_2$$
$$z_2 = (E_{rn}^{-1}F_{p02} - E_{rn}^{-1}E_{p02}E_{rn}^{-1}F_{rn})\xi_r - E_{rn}^{-1}E_{p02}w_1 - E_{rn}^{-1}E_{p02}w_3 - E_{rn}^{-1}E_{p02}w_6 + w_5$$
$$w_3 = \delta_r z_3 z_3 = (E_{rn}^{-1}F_{p08} - E_{rn}^{-1}E_{p08}E_{rn}^{-1}F_{rn})\xi_r - E_{rn}^{-1}E_{p08}w_1 - E_{rn}^{-1}E_{p08}w_3 - E_{rn}^{-1}E_{p08}w_6 + w_5$$
$$w_4 = \delta_r z_4 z_4 = (E_{rn}^{-1}F_{p03} - E_{rn}^{-1}E_{p03}E_{rn}^{-1}F_{rn})\xi_r - E_{rn}^{-1}E_{p03}w_1 - E_{rn}^{-1}E_{p03}w_3 - E_{rn}^{-1}E_{p03}w_6 + w_8$$
$$w_5 = \delta_r z_5 z_5 = (E_{rn}^{-1}F_{p04} - E_{rn}^{-1}E_{p04}E_{rn}^{-1}F_{rn})\xi_r - E_{rn}^{-1}E_{p04}w_1 - E_{rn}^{-1}E_{p04}w_3 - E_{rn}^{-1}E_{p04}w_6$$
$$w_6 = \delta_m z_6 z_6 = (E_{rn}^{-1}F_{p10} - E_{rn}^{-1}E_{p10}E_{rn}^{-1}F_{rn})\xi_r - E_{rn}^{-1}E_{p10}w_1 - E_{rn}^{-1}E_{p10}w_3 - E_{rn}^{-1}E_{p10}w_6 + w_{11}$$
$$w_7 = \delta_m z_7 z_7 = (E_{rn}^{-1}F_{p05} - E_{rn}^{-1}E_{p05}E_{rn}^{-1}F_{rn})\xi_r - E_{rn}^{-1}E_{p05}w_1 - E_{rn}^{-1}E_{p05}w_3 - E_{rn}^{-1}E_{p05}w_6 + w_9$$
$$w_8 = \delta_m z_8 z_8 = (E_{rn}^{-1}F_{p07} - E_{rn}^{-1}E_{p07}E_{rn}^{-1}F_{rn})\xi_r - E_{rn}^{-1}E_{p07}w_1 - E_{rn}^{-1}E_{p07}w_3 - E_{rn}^{-1}E_{p07}w_6$$
$$w_9 = \delta_m z_9 z_9 = (E_{rn}^{-1}F_{p06} - E_{rn}^{-1}E_{p06}E_{rn}^{-1}F_{rn})\xi_r - E_{rn}^{-1}E_{p06}w_1 - E_{rn}^{-1}E_{p06}w_3 - E_{rn}^{-1}E_{p06}w_6$$
$$w_{10} = \delta_m z_{10} z_{10} = (E_{rn}^{-1}F_{p09} - E_{rn}^{-1}E_{p09}E_{rn}^{-1}F_{rn})\xi_r - E_{rn}^{-1}E_{p09}w_1 - E_{rn}^{-1}E_{p09}w_3 - E_{rn}^{-1}E_{p09}w_6$$
$$w_{11} = \delta_m z_{11} z_{11} = (E_{rn}^{-1}F_{p11} - E_{rn}^{-1}E_{p11}E_{rn}^{-1}F_{rn})\xi_r - E_{rn}^{-1}E_{p11}w_1 - E_{rn}^{-1}E_{p11}w_3 - E_{rn}^{-1}E_{p11}w_6 + w_{12}$$
$$w_{12} = \delta_m z_{12} z_{12} = (E_{rn}^{-1}F_{p12} - E_{rn}^{-1}E_{p12}E_{rn}^{-1}F_{rn})\xi_r - E_{rn}^{-1}E_{p12}w_1 - E_{rn}^{-1}E_{p12}w_3 - E_{rn}^{-1}E_{p12}w_6$$

The LFR form of the plant can be expressed as in (A.3) and (A.4). The LFR representation of DFIM with the inductance uncertainties is depicted as Fig. 6.4.

$$\begin{pmatrix} \dot{x}_r \\ \hline z_1 \\ z_2 \\ z_3 \\ z_4 \\ z_5 \\ z_6 \\ z_7 \\ z_8 \\ z_9 \\ z_{10} \\ z_{11} \\ z_{12} \\ \hline y_r \end{pmatrix} = \underbrace{\left(\begin{array}{c|cccccccccccc|c} A_{rs} & I & 0 & I & 0 & 0 & I & 0 & 0 & 0 & 0 & 0 & 0 & B_{rs} \\ \hline E_{s01} & F_{u01} & I & F_{u01} & I & 0 & F_{u01} & I & 0 & 0 & 0 & 0 & 0 & F_{v01} \\ E_{s02} & F_{u02} & 0 & F_{u02} & 0 & I & F_{u02} & 0 & 0 & 0 & 0 & 0 & 0 & F_{v02} \\ E_{s03} & F_{u03} & 0 & F_{u03} & 0 & 0 & F_{u03} & 0 & 0 & 0 & I & 0 & 0 & F_{v03} \\ E_{s04} & F_{u04} & 0 & F_{u04} & 0 & 0 & F_{u04} & 0 & I & 0 & 0 & 0 & 0 & F_{v04} \\ E_{s05} & F_{u05} & 0 & F_{u05} & 0 & 0 & F_{u05} & 0 & 0 & 0 & 0 & 0 & 0 & F_{v05} \\ E_{s06} & F_{u06} & 0 & F_{u06} & 0 & 0 & F_{u06} & 0 & 0 & 0 & 0 & I & 0 & F_{v06} \\ E_{s07} & F_{u07} & 0 & F_{u07} & 0 & 0 & F_{u07} & 0 & 0 & I & 0 & 0 & 0 & F_{v07} \\ E_{s08} & F_{u08} & 0 & F_{u08} & 0 & 0 & F_{u08} & 0 & 0 & 0 & 0 & 0 & 0 & F_{v08} \\ E_{s09} & F_{u09} & 0 & F_{u09} & 0 & 0 & F_{u09} & 0 & 0 & 0 & 0 & 0 & 0 & F_{v09} \\ E_{s10} & F_{u10} & 0 & F_{u10} & 0 & 0 & F_{u10} & 0 & 0 & 0 & 0 & 0 & 0 & F_{v10} \\ E_{s11} & F_{u11} & 0 & F_{u11} & 0 & 0 & F_{u11} & 0 & 0 & 0 & 0 & 0 & I & F_{v11} \\ E_{s12} & F_{u12} & 0 & F_{u12} & 0 & 0 & F_{u12} & 0 & 0 & 0 & 0 & 0 & 0 & F_{v12} \\ \hline C_{rs} & 0 & 0 & 0 & 0 & 0 & 0 & 0 & 0 & 0 & 0 & 0 & 0 & 0 \end{array}\right)}_{P_r} \begin{pmatrix} x_r \\ \hline w_1 \\ w_2 \\ w_3 \\ w_4 \\ w_5 \\ w_6 \\ w_7 \\ w_8 \\ w_9 \\ w_{10} \\ w_{11} \\ w_{12} \\ \hline v_{rs} \end{pmatrix} \tag{A.3}$$

$$
\begin{pmatrix} w_1 \\ w_2 \\ \hline w_3 \\ w_4 \\ w_5 \\ \hline w_6 \\ w_7 \\ w_8 \\ w_9 \\ w_{10} \\ w_{11} \\ w_{12} \end{pmatrix}
=
\underbrace{\left(\begin{array}{cc|ccc|ccccccc}
\delta_s I_4 & 0 & 0 & 0 & 0 & 0 & 0 & 0 & 0 & 0 & 0 & 0 \\
0 & \delta_r I_4 & 0 & 0 & 0 & 0 & 0 & 0 & 0 & 0 & 0 & 0 \\
\hline
0 & 0 & \multicolumn{3}{c|}{\multirow{3}{*}{$\delta_s I_{12}$}} & 0 & 0 & 0 & 0 & 0 & 0 & 0 \\
0 & 0 & & & & 0 & 0 & 0 & 0 & 0 & 0 & 0 \\
0 & 0 & & & & 0 & 0 & 0 & 0 & 0 & 0 & 0 \\
\hline
0 & 0 & 0 & 0 & 0 & \multicolumn{7}{c}{\multirow{8}{*}{$\delta_m I_{28}$}} \\
0 & 0 & 0 & 0 & 0 & & & & & & & \\
0 & 0 & 0 & 0 & 0 & & & & & & & \\
0 & 0 & 0 & 0 & 0 & & & & & & & \\
0 & 0 & 0 & 0 & 0 & & & & & & & \\
0 & 0 & 0 & 0 & 0 & & & & & & & \\
0 & 0 & 0 & 0 & 0 & & & & & & &
\end{array}\right)}_{\Delta_r}
\begin{pmatrix} z_1 \\ z_2 \\ \hline z_3 \\ z_4 \\ z_5 \\ \hline z_6 \\ z_7 \\ z_8 \\ z_9 \\ z_{10} \\ z_{11} \\ z_{12} \end{pmatrix}
\tag{A.4}
$$

where

$$E_{s01} = E_{rn}^{-1} A_{p01} - E_{rn}^{-1} E_{p01} E_{rn}^{-1} A_{rn}$$
$$E_{s02} = E_{rn}^{-1} A_{p02} - E_{rn}^{-1} E_{p02} E_{rn}^{-1} A_{rn}$$
$$E_{s03} = E_{rn}^{-1} A_{p08} - E_{rn}^{-1} E_{p08} E_{rn}^{-1} A_{rn}$$
$$E_{s04} = E_{rn}^{-1} A_{p03} - E_{rn}^{-1} E_{p03} E_{rn}^{-1} A_{rn}$$
$$E_{s05} = E_{rn}^{-1} A_{p04} - E_{rn}^{-1} E_{p04} E_{rn}^{-1} A_{rn}$$
$$E_{s06} = E_{rn}^{-1} A_{p10} - E_{rn}^{-1} E_{p10} E_{rn}^{-1} A_{rn}$$
$$E_{s07} = E_{rn}^{-1} A_{p05} - E_{rn}^{-1} E_{p05} E_{rn}^{-1} A_{rn}$$
$$E_{s08} = E_{rn}^{-1} A_{p07} - E_{rn}^{-1} E_{p07} E_{rn}^{-1} A_{rn}$$
$$E_{s09} = E_{rn}^{-1} A_{p06} - E_{rn}^{-1} E_{p06} E_{rn}^{-1} A_{rn}$$
$$E_{s10} = E_{rn}^{-1} A_{p09} - E_{rn}^{-1} E_{p09} E_{rn}^{-1} A_{rn}$$
$$E_{s11} = E_{rn}^{-1} A_{p11} - E_{rn}^{-1} E_{p11} E_{rn}^{-1} A_{rn}$$
$$E_{s12} = E_{rn}^{-1} A_{p12} - E_{rn}^{-1} E_{p12} E_{rn}^{-1} A_{rn}$$
$$F_{v01} = E_{rn}^{-1} B_{p01} - E_{rn}^{-1} E_{p01} E_{rn}^{-1} B_{rn}$$
$$F_{v02} = E_{rn}^{-1} B_{p02} - E_{rn}^{-1} E_{p02} E_{rn}^{-1} B_{rn}$$
$$F_{v03} = E_{rn}^{-1} B_{p08} - E_{rn}^{-1} E_{p08} E_{rn}^{-1} B_{rn}$$
$$F_{v04} = E_{rn}^{-1} B_{p03} - E_{rn}^{-1} E_{p03} E_{rn}^{-1} B_{rn}$$
$$F_{v05} = E_{rn}^{-1} B_{p04} - E_{rn}^{-1} E_{p04} E_{rn}^{-1} B_{rn}$$
$$F_{v06} = E_{rn}^{-1} B_{p10} - E_{rn}^{-1} E_{p10} E_{rn}^{-1} B_{rn}$$
$$F_{v07} = E_{rn}^{-1} B_{p05} - E_{rn}^{-1} E_{p05} E_{rn}^{-1} B_{rn}$$
$$F_{v08} = E_{rn}^{-1} B_{p07} - E_{rn}^{-1} E_{p07} E_{rn}^{-1} B_{rn}$$
$$F_{v09} = E_{rn}^{-1} B_{p06} - E_{rn}^{-1} E_{p06} E_{rn}^{-1} B_{rn}$$
$$F_{v10} = E_{rn}^{-1} B_{p09} - E_{rn}^{-1} E_{p09} E_{rn}^{-1} B_{rn}$$

$$F_{v11} = E_{rn}^{-1} B_{p11} - E_{rn}^{-1} E_{p11} E_{rn}^{-1} B_{rn}$$
$$F_{v12} = E_{rn}^{-1} B_{p12} - E_{rn}^{-1} E_{p12} E_{rn}^{-1} B_{rn}$$
$$F_{u01} = -E_{rn}^{-1} E_{p01}$$
$$F_{u02} = -E_{rn}^{-1} E_{p02}$$
$$F_{u03} = -E_{rn}^{-1} E_{p08}$$
$$F_{u04} = -E_{rn}^{-1} E_{p03}$$
$$F_{u05} = -E_{rn}^{-1} E_{p04}$$
$$F_{u06} = -E_{rn}^{-1} E_{p10}$$
$$F_{u07} = -E_{rn}^{-1} E_{p05}$$
$$F_{u08} = -E_{rn}^{-1} E_{p07}$$
$$F_{u09} = -E_{rn}^{-1} E_{p06}$$
$$F_{u10} = -E_{rn}^{-1} E_{p09}$$
$$F_{u11} = -E_{rn}^{-1} E_{p11}$$
$$F_{u12} = -E_{rn}^{-1} E_{p12}$$
$$C_{rs} = \begin{pmatrix} 1 & 0 & 0 & 0 \\ 0 & 1 & 0 & 0 \end{pmatrix};$$

B

ELECTRICAL MACHINE CHARACTERISTICS

B.1. PARAMETERS FOR A REAL DOUBLY-FED INDUCTION MACHINE

Doubly-fed induction machine parameters referred to the stator side [66]:

Rated power	$620kW$
Stator voltage	$690V$ (phase-phase)
Moment of inertia	$150kgm^2$
Stator resistance	$R_s = 0.0107\Omega$
Rotor resistance	$R_s = 0.0264\Omega$
Stator inductance	$L_s = 0.0166H$
Rotor inductance	$L_r = 0.0168H$
Mutual inductance	$L_m = 0.0163H$

B.2. PARAMETERS FOR A LABORATORY SCALE DOUBLY-FED INDUCTION MACHINE

Laboratory-scale doubly-fed induction machine parameters referred to the stator side:

- Rated power: $4kW$
- Stator voltage: $230/400V$ (Δ/Y)
- Rotor voltage: $950V$

- Rotor current: $2.7A$
- Rated speed: $1440rpm$
- Moment of inertia: $0.032kgm^2$
- Stator resistance: $R_s = 1.070\Omega$
- Rotor resistance: $R_s = 1.32\Omega$
- Stator leakage inductance: $L_{\sigma s} = 0.0066H$
- Rotor leakage inductance: $L_{\sigma r} = 0.0098H$
- Mutual inductance: $L_m = 0.1601H$

B.3. INDUCTION MOTOR

The induction motor parameters referred to the stator side:

- Rated power: $11kW$
- Stator voltage: $330V$ (Δ)
- Rated current: $25A$
- Rated speed: $3000rpm$
- Operating frequency: $102Hz$
- Power factor: 0.87

C

THE EXPERIMENTAL PLATFORM

C.1. THE ALPHA-COMBO SYSTEM

The ALPHA-COMBO system consists of the DSpace Multi-processor system and peripheral cards. The DSpace Multi-processor ALPHA-COMBO system includes:

- The Master DSP DS1003 used for input/output tasks.
- The slave processor DS1004 used for calculation tasks.

The peripheral cards include

- Card DS2201 contains 20 analog to digital (AD) converters with a 12-bit resolution, $\pm 10V$, and a time conversion of $32.4\mu s$; 8 digital to analog (DA) converters with a 12-bit resolution, $\pm 10V$; a 6 channels PWM module with frequency from 0.01Hz up to 1MHz.
- Card DS1501 provides a single PWM channel; a three-phase PWM generation with inverted and non-inverted PWM outputs.

C.2. THE POWER MODULE

The power module BUS623 (Baumueller - Germany) is connected with the DSpace Multi-processor ALPHA-COMBO system via an interface card. It has the following properties:

- The DC-link voltage: $v_{DC} = 0..685V$, $v_{DC}^{max} = 760V$.
- The DC-link capacitor: $C_{DC} = 1470F$.

- The rated power: 14KVA.
- The rated current: 20A.
- The maximum current: 30A.
- The switching frequency: 3..8KHz.

BIBLIOGRAPHY

[1] Global Wind Energy Council. *Global wind 2015 report*. Brussels, Belgium, 2015.

[2] European Wind Energy Association. *Wind in power 2014 European statistics*. Brussels, Belgium, 2015.

[3] B.L. Capehart. *Encyclopedia of Energy Engineering and Technology*. CRC, 2007.

[4] AWEA Data Services. *U.S. Wind Industry First Quarter 2015 Market Report*. American Wind Energy Association, 2015.

[5] A. Miller, E. Muljadi, and D.S. Zinger. A variable speed wind turbine power control. *IEEE Transactions on Energy Conversion*, 12:181–186, 1997.

[6] T. Lund, P. Sorensen, and J. Eek. Reactive power capability of a wind turbine with doubly fed induction generator. *John Wiley and Sons*, 2007.

[7] M. Yamamoto and O. Motoyoshi. Active and reactive power control for doubly-fed wound rotorinduction generator. *IEEE Transactions on Power Electronics*, 6:624–629, 1991.

[8] Y. Tang and L. Xu. A flexible active and reactive power control strategy for avariable speed constant frequency generating system. *IEEE Transactions on Power Electronics*, 10:472–478, 1995.

[9] D.C.-Gaona, E.L.M-Goytia, and O.A-Lara. Fault ride-through improvement of DFIG-WT by integrating a two-degrees-of-freedom internal model control. *IEEE Transactions on Industrial Electronics*, 60 No. 3:1133–1145, 2013.

[10] Y. Zhang, J. Hu, and J. Zhu. Three-vectors-based predictive direct power control of the doubly fed induction generator for wind energy applications. *IEEE Transactions on Power Electronics*, 29 No. 7:3485–3500, 2014.

[11] A.E.-Naggar and I. Erlich. Fault current contribution analysis of doubly fed induction generator-based wind turbines. *IEEE Transactions on Energy Conversion*, 30 No. 3:874–882, 2015.

[12] J.P. da Costa, H. Pinheiro, T. Degner, and G. Arnold. Robust controller for DFIGs of grid-connected wind turbines. *IEEE Transactions on Industrial Electronics*, 58 No. 9:4023–4038, 2011.

[13] D.D. Reigosa, F. Briz, C. Blanco, and J.M. Guerrero. Sensorless control of doubly fed induction generators based on stator high-frequency signal injection. *IEEE Transactions on Industry Applications*, 50 No. 5:3382–3391, 2014.

[14] R. Datta and V. T. Ranganathan. A method of tracking the peak power points for a variable speed wind energy conversion system. *IEEE Transactions on Energy Conversion*, 18:163–168, 2003.

[15] A. Petersson, L. Harnefors, and T. Thiringer. Evaluation of current control methods for wind turbines using doubly fed induction machines. *IEEE transactions on Power Electronics*, 20:227–235, 2005.

[16] S. Peresada, A. Tilli, and A. Tonielli. Power control of a doubly fed induction machine via output feedback. *Control Engineering Practice*, 12:41–57, 2004.

[17] R. Pena, J. C. Clare, and G. M. Asher. Doubly fed induction generator using back-to-back PWM converters and its application to variable speed wind energy generation. *IEE Proceedings on Electric Power Applications*, 143:231–241, 1996.

[18] A. Tapia, G. Tapia, J. X. Ostolaza, and J. R. Saenz. Modeling and control of a wind turbine driven doubly fed induction generator. *IEEE Transactions on Energy Conversion*, 18:194–204, 2003.

[19] B. Hopfensperger, D.J. Atkinson, and R. A. Lakin. Stator flux oriented control of a double-fed induction machine with and without position encoder. *IEE Proc.-Electr. Power Appl.*, 147:241–250, 2000.

[20] C. J. Ramos, A. P. Martins, A. S. Araujo, and A. S. Carvalho. Current control in the grid connection of the double-output induction generator linked to a variable speed wind turbine. *28th Annual Conference of the Industrial Electronics Society*, 2:979–984, 2002.

[21] C. Batlle, A.D.-Cerezo, and R. Ortega. A stator voltage oriented PI controller for the doubly-fed induction machine. *American Control Conference*, pages 5438–5443, 2007.

[22] M.K. Bourdoulis and A.T. Alexandridis. Direct power control of DFIG wind systems based on nonlinear modeling and analysis. *IEEE Journal of Emerging and Selected Topics in Power Electronics*, 2 No. 4:764–775, 2014.

[23] R. Cardenas, R. Pena, S. Alepuz, and G. Asher. Overview of control systems for the operation of DFIGs in wind energy applications. *IEEE Transactions on Industrial Electronics*, 60 No. 7:2776–2798, 2013.

[24] S. Tamalouzt, T. Rekioua, and R. Abdessemed. Direct torque and reactive power control of grid connected doubly fed induction generator for the wind energy conversion. *International Conference on Electrical Sciences and Technologies in Maghreb (CISTEM)*, 2014.

[25] J. Mohammadi, S. Vaez-Zadeh, S. Afsharnia, and E. Daryabeigi. A combined vector and direct power control for DFIG-based wind turbines. *IEEE Transactions on Sustainable Energy*, 5 No. 3:767–775, 2014.

[26] B. Singh and N.K. Swami Naidu. Direct power control of single VSC-based DFIG without rotor position sensor. *IEEE Transactions on Industry Applications*, 50 No. 6:4152–4163, 2014.

[27] M.F. Iacchetti, G.D. Marques, and R. Perini. Torque ripple reduction in a DFIG-DC system by resonant current controllers. *IEEE Transactions on Power Electronics*, 30 No. 8:4244–4254, 2015.

[28] R. Franco, C. E. Capovilla, R. V. Jacomini, J. A. T. Altuna, and A. J. Sguarezi Filho. A deadbeat direct power control applied to doubly-fed induction aerogenerator under normal and sag voltages conditions. *40th Annual Conference of the IEEE Industrial Electronics Society (IECON)*, pages 1906–1911, 2014.

[29] P.N. Lan. *Linear and nonlinear control approach to doubly-fed induction generators in wind power generation.* PhD thesis, TU Dresden, 2006.

[30] C. Wang and G. Weiss. Self-scheduled LPV control of a wind driven doubly-fed induction generator. *IEEE Conference on Decision and Control*, pages 1246–1251, 2006.

[31] C. Wang and G. Weiss. Linear parameter varying control of a doubly fed induction generator based wind turbine with primary grid frequency support. *International Journal of Robust and Nonlinear Control*, 2013.

[32] S. George and M. Rita. Loop-shaping H_∞ control for a doubly fed induction motor. *12th European Conference on Power Electronics and Applications*, 2007.

[33] S. Georges, M. Rita, P.-D. Maria, and D. De Bernard. Mixed sensitivity H_∞ control of doubly fed induction motor. *IEEE International Symposium on Industrial Electronics*, pages 1300–1304, 2007.

[34] P. Nicolas, N Ammar, M. Eric, and L. Jean-Paul. Sliding mode control of a doubly-fed induction generator. *12th European Conference on Power Electronics and Applications*, 2007.

[35] P.-E. Vidal and M.P. David. Flux sliding mode control of a doubly fed induction machine. *European Conference on Power Electronics and Applications*, 2005.

[36] R. G.-D.-Valle, M.C.-Pfeifer, and D.B.-Sole. Sliding mode control of a doubly fed induction generator supplying an isolated RL load. *10th IEEE International Power Electronics Congress*, 2006.

[37] S. Drid, M. Tadjine, and M.-S.N.-Said. Robust backstepping vector control for the doubly fed induction motor. *IET Control Theory and Applications*, 1:861–868, 2007.

[38] W. Leonhard. *Control of electrical drives.* Springer, 1996.

[39] D. W. Novotny and T. A. Lipo. *Vector Control and Dynamics of AC Drives.* Oxford University Press, USA, 1996.

[40] S. Peresada, A. Tilli, and A. Tonielli. Indirect stator flux-oriented output feedback control of a doubly fed induction machine. *IEEE Transactions on Control Systems Technology*, 11:875– 888, 2003.

[41] I. Erlich, H. Wrede, and C. Feltes. Dynamic behavior of DFIG-based wind turbines during grid faults. *Power Conversion Conference (PCC) , Nagoya, Japan*, pages 1195–1200, 2007.

[42] B. Xie, B. Fox, and D. Flynn. Study of fault ride-through for DFIG based wind turbines. *Electric Utility Deregulation, Restructuring and Power Technologies conference*, 1:411–416, 2004.

[43] A. Petersson. *Analysis, Modeling and Control of Doubly-Fed Induction Generators for Wind Turbines*. PhD thesis, Chalmers University of Technology, 2005.

[44] J. Morren and S. W. H. de Haan. Ridethrough of wind turbines with doubly-fed induction generator during a voltage dip. *IEEE Transactions on energy conversion*, 20:435–441, Jun 2005.

[45] J. Lopez, P. Sanchis, X. Roboam, and L. Marroyo. Dynamic behavior of the doubly fed induction generator during three-phase voltage dips. *IEEE Transactions on Energy Conversion*, 22:709–717, 2007.

[46] T. Sun, Z. Chen, and F. Blaabjerg. Voltage recovery of grid-connected wind turbines with DFIG after a short-circuit fault. *Power Electronics Specialists Conference, PESC*, 3:1991–1997, 2004.

[47] A. M. Trzynadlowski. *The Field Orientation Principle in Control of Induction Motors*. Springer, 1994.

[48] H. A. Toliyat and S. Campbell. *DSP-Based electromechanical motion control*, volume 3. CRC Press, 2004.

[49] Texas Instruments. *Clarke and Park Transforms on the TMS320C2xx*. Application Report, 1997.

[50] J.W. Finch. Scalar and vector: a simplified treatment of induction motor control performance. *IEE Colloquium on Vector Control Revisited, London, UK*, 1998.

[51] J.A. Santisteban and R.M. Stephan. Vector control methods for induction machines: an overview. *IEEE Transactions on Education*, 44:170–175, 2001.

[52] A. Petersson, L. Harnefors, and T. Thiringer. Comparison between stator-flux and grid-flux-oriented rotor current control of doubly-fed induction generators. *IEEE 35th Annual Power Electronics Specialists Conference, PESC04*, 1:482–486, 2004.

[53] N. P. Quang, A. Dittrich, and A. Thieme. Doubly-fed induction machine as generator: control algorithms with decoupling of torque and power factor. *Electrical Engineering (Archiv fur Elektrotechnik)*, 80:325–325, 1997.

[54] J.B. Ekanayake, L. Holdsworth, Wu XueGuang, and N. Jenkins. Dynamic modeling of doubly fed induction generator wind turbines. *IEEE Transactions on Power Systems*, 18:803–809, 2003.

[55] W. Hofmann and A. Thieme. Control of a double-fed induction generator for windpower plants. *Power Quality Proceedings PCIM'98, Nurnberg*, pages 275–282, 1998.

[56] P. Kundur. *Power System Stability and Control.* McGraw-Hill Education, 1994.

[57] N.P. Quang and J.-A. Dittrich. *Vector Control of Three-Phase AC Machines: System Development in the Practice.* Springer Berlin Heidelberg, 2008.

[58] F. Blaabjerg and Z. Chen. *Power Electronics for Modern Wind Turbines.* Morgan and Claypool Publishers, 2006.

[59] E. Koutroulis and K. Kalaitzakis. Design of a maximum power tracking system for wind-energy-conversion applications. *IEEE Transactions on Industrial Electronics*, 53:486–494, 2006.

[60] R. J. Simoes, M. G. Bose, and B. K. Spiegel. Fuzzy logic based intelligent control of a variable speed cage machine wind generation system. *IEEE Transactions on Power Electronics*, 12:87–95, 1997.

[61] M. R. Patel. *Wind and Solar Power Systems.* CRC Press, 1999.

[62] S. Heier. *Grid integration of wind energy conversion systems.* John Wiley and Sons, 1998.

[63] D. P. Molenaar. *Cost-effective Design and Operation of Variable Speed Wind Turbines.* PhD thesis, Delft University Press, 2003.

[64] F.D. Bianchi, H. De Battista, and R.J. Mantz. *Wind Turbine Control Systems: Principles, Modelling and Gain Scheduling Design.* Springer, 2006.

[65] I. Cadirci and M. Ermis. Double-output induction generator operating at subsynchronous and supersynchronous speeds: steady-state performance optimisation and wind-energy recovery. *IEE Proceedings-B*, 139:429–442, 1992.

[66] P. N. Lan, N. P. Quang, and P. Buechner. A non-linear control algorithm for improving performance of wind generator using doubly-fed induction generator. *European Wind Energy Conference, Athen*, 2006.

[67] K.S. Rongve, B.I.Naess, T.M. Undeland, and T. Gjengedal. Overview of torque control of a doubly fed induction generator. *Power Tech Conference Proceedings, Bologna*, 3, 2003.

[68] M.M. Fahmy and J. O'Reilly. Dead-beat control of linear discrete-time systems. *International Journal of Control*, 37:685–705, 1983.

[69] A. Emami-Naeini and G. Franklin. Deadbeat control and tracking of discrete-time systems. *IEEE Transactions on Automatic Control*, 27:176–181, 1982.

[70] R. Ottersten. *On Control of Back-to-Back Converters and Sensorless Induction Machine Drives*. PhD thesis, Chalmers University of Technology, 2003.

[71] B.H. Kenny and R.D. Lorenz. Stator- and rotor-flux-based deadbeat direct torque control of induction machines. *IEEE Transactions on Industry Applications*, 39:1093–1101, 2002.

[72] T. G. Habetler, F. Profumo, M. Pastorelli, and L. M. Tolbert. Direct torque control of induction machines using space vector modulation. *IEEE Transactions on Industry Applications*, 28:1045–1053, 1992.

[73] J. Maes and J. Melkebeek. Discrete time direct torque control of induction motors using back-emf measurement. *The IEEE Industry Applications Conference*, 1:407–414, Oct 1998.

[74] G. Buja, M. Candela, and R. Menis. A novel direct control scheme for SVM inverter-fed induction motor drives. *Proceedings of the IEEE International Symposium on Industrial Electronics*, 3:1267–1272, 1999.

[75] D. Casadei, G. Serra, and A. Tani. Analytical investigation of torque and flux ripple in DTC schemesfor induction motors. *International Conference on Industrial Electronics*, 2:552–556, 1997.

[76] B. Porter. Deadbeat control of linear multivariable discrete-time systems. *Electronics Letters*, 9:83–84, 1973.

[77] K. Ogata. *Discrete-Time Control Systems*, volume 2. Prentice Hall, 1994.

[78] N. P. Quang and A. Dittrich. *Praxis der feldorientierten Drehstromantriebsregelungen*. Expert-Verlag, 2nd, 1999.

[79] K. J. Astrom and B. Wittenmark. *Computer Controlled Systems: Theory and Design*. Prentice Hall, 28 Feb 1997.

[80] J. H. Chang and B. K. Kim. Minimum-time minimum-loss speed control of induction motors underfield-oriented control. *IEEE Transactions on Industrial Electronics*, 44:809–815, 1997.

[81] R. Datta and V. T. Ranganathan. Decoupled control of active and reactive power for a grid-connected doubly-fed wound rotor induction machine without position sensors. *Proceedings of IEEE Industry Applications Conference, Phoenix, USA*, 4:2623–2630, 1999.

[82] Y. Zhao and H. Kimura. Dead-beat control with robustness. *International Journal of Control*, 43:1427–1440, 1986.

[83] Y. Zhao and H. Kimura. Multivariable dead-beat control with robustness. *International Journal of Control*, 47:229–255, 1988.

[84] H. K. Tam and J. Lam. Robust deadbeat pole assignment with gain constraints: an LMI optimization approach. *Optimal Control Applications and Methods*, 21:243–256, 2000.

[85] D. Nesic. *Dead-Beat Control for Polynomial Systems.* PhD thesis, Australian National University, Canberra, Australia, 1996.

[86] Y. Zhao and H. Kimura. Two-degrees-of-freedom dead-beat control system with robustness. *International Journal of Control*, 48:303–315, 1988.

[87] J. Lam, H. K. Tso, and N. K. Tsing. Robust deadbeat regulation. *International Journal of Control*, 67:587–602, 1997.

[88] A. Casavola. Robust ripple-free deadbeat control design. *International Journal of Control*, 72:564–573, 1999.

[89] Y. Funahashi and H. Katoh. Robust-tracking deadbeat control. *International Journal of Control*, 56:213–225, 1992.

[90] L. Harnefors and H. P. Nee. Model-based current control of ac machines using the internal modelcontrol method. *IEEE Transactions on Industry Applications*, 34:133–141, 1998.

[91] F. Briz, M. W. Degner, and R. D. Lorenz. Analysis and design of current regulators using complex vectors. *Thirty-Second IAS Annual Meeting, New Orleans, LA, USA*, 2:1504–1511, 1997.

[92] Q. Yu, L. Norum, T. Undeland, and S. Round. Investigation of dynamic controllers for a unified power flow controller. *International Conference on Industrial Electronics*, 3:1764–1769, 1996.

[93] D. R. Seidl, D. A.Kaiser, and R. D. Lorenz. One-step optimal space vector pwm current regulation using a neural network. *Industry Applications Society Annual Meeting, Denver, CO, USA*, 2:867–874, 1994.

[94] A. M. Hava, S. Sul, R. J. Kerkman, and T. A. Lipo. Dynamic overmodulation characteristics of triangle intersection PWM methods. *IEEE Transactions on Industry Applications*, 35:896–907, 1999.

[95] J.-W. Choi, H.-W. Kim, and S.-K. Sul. New current control concept: minimum time current control ininduction machine drive. *Int. Con. on Industrial Industrial Electronics, IECON, Orlando, FL, USA*, 1:311–316, 1995.

[96] J.-W. Choi, H.-W. Kim, and S.-K. Sul. Design of fast response current controller using d-q axis cross-coupling. *22nd International Conference on Industrial Electronics, Taipei, Taiwan*, 2:1187–1192, Aug 1996.

[97] J. Jung and K. Nam. A dynamic decoupling control scheme for high-speed operation ofinduction motors. *IEEE Transactions on Industrial Electronics*, 46:100–110, 1999.

[98] Y. Long, H. Miyagi, and K. Yamashita. Windmill power systems controller design using H_∞ theory. *IEEE International Conference on Systems, Man, and Cybernetics*, 5:3490–3495, 2000.

[99] C. Wang and G. Weiss. Self-scheduled LPV control of a wind driven doubly-fed induction generator. *IEEE Conference on Decision and Control*, pages 1246–1251, 2006.

[100] A. Makouf, M. E. H. Benbouzid, D. Diallo, and N. E. Bouguechal. Induction motor robust control: An H_∞ control approach with field orientation and input-output linearizing. *The 17th annual conference of the IEEE industrial electronics society*, 2:1406–1411, 2001.

[101] D. Fodor and R. Toth. Speed sensorless linear parameter variant H_∞ control of the induction motor. *IEEE Conference on Decision and Control*, 4:4435– 4440, 2004.

[102] E. Prempain, I. Postlethwaite, and A. Benchaib. A linear parameter variant H_∞ control design for an induction motor. *Control Engineering Practice*, 10:633–644, 2002.

[103] J.D. Bendtsen and K. Trangbaek. Discrete-time LPV current control of an induction motor. *IEEE Conference on Decision and Control*, 6:5903–5908, 2003.

[104] K. Trangbek. *Linear Parameter Varying Control of Induction Motors*. PhD thesis, Aalborg University, Denmark, 2001.

[105] C. W. Scherer and S. Weiland. *Linear Matrix Inequalities in Control*. Lecture Notes, Delft University of Technology, 2005.

[106] G. Balas, R. Chiang, A. Packard, and M. Safonov. *Robust control toolbox for use with Matlab*, volume 3. The MathWorks, 2005.

[107] K. Zhou and P. P. Khargonekar. An algebraic Riccati equation approach to H_∞ optimization. *Systems and Control Letters*, 11:85–91, 1988.

[108] J. G. Van Antwerp and R. D. Braatz. A tutorial on linear and bilinear matrix inequalities. *Journal of Process Control*, 10:363–385, 2000.

[109] P. Gahinet and P. Apkarian. A linear matrix inequality approach to H_∞ control. *Int. J. Robust and Nonlinear Contr.*, 4:421–448, 1994.

[110] C. W. Scherer. *Theory of Robust Control*. Lecture Notes, Delft University of Technology, 2001.

[111] P. Apkarian and P. Gahinet. A convex characterization of gain-scheduled H_∞ controllers. *IEEE Transactions on Automatic Control*, 40:853–864, 1995.

[112] C.W. Scherer. Robust mixed control and LPV control with full block scalings. *Advances in LMI Methods in Control, SIAM*, pages 187–208, 1999.

[113] P. Gahinet. Explicit controller formulas for LMI-based H_∞ synthesis. *Automatica*, 32:1007–1014, 1996.

[114] C. W. Scherer. Mixed H_2/H_∞ control for time-varying and linear parametrically-varying systems. *International Journal of Robust and Nonlinear Control*, 6:929–952, 1996.

[115] S. Skogestad and I. Postlethwaite. *Multivariable feedback control - Analysis and design*. John Wiley and Sons, 1996.

[116] P. Apkarian, P. Gahinet, and G. Becker. Self-scheduled H_∞ control of linear parameter varying systems: a design example. *Automatica*, 31:1251–1261, 1995.

[117] S. Bennani, D.M.C. Willemsen, and C.W. Scherer. Robust LPV control with bounded parameter rates. *AIAA Guidance, Navigation, and Control Conference, New Orleans, LA*, pages 1080–1089, 1997.

[118] P. Apkarian and R.J. Adams. Advanced gain-scheduling techniques for uncertain systems. *IEEE Transactions on Control Systems Technology*, 6:21 – 32, 1998.

[119] P. Gahinet, A. Nemirovski, A. J. Laub, and M. Chilali. *LMI Control Toolbox for use with Matlab*, volume 1. The Mathworks, 1995.

[120] H. Nguyen Tien, C. W. Scherer, and J. M. A. Scherpen. Robust performance of self-scheduled LPV control of doubly-fed induction generator in wind energy conversion systems. *12th European Conference on Power Electronics and Applications, EPE2007, Aalborg, Denmark*, 2007.

[121] H. Nguyen Tien, C. W. Scherer, and J. M. A. Scherpen. Discrete-time linear parameter varying control of doubly-fed induction generators. *International Symposium on Electrical Engineering, ISEE2007, VietNam*, pages 266–273, 2007.

[122] L.S. Shieh, X.M. Zhao, and J.L. Zhang. Locally optimal-digital redesign of continuous-time systems. *IEEE Transactions on Industrial Electronics*, 36:511–515, 1989.

[123] B.C. Kuo and D.W. Peterson. Optimal discretization of continuous-data control system. *Automatica*, 9:125–129, 1973.

[124] A.H.D. Markazi and N. Hori. Discretisation of continuous-time control systems with guaranteed stability. *IEE Proceedings on Control Theory and Applications*, 142:323–328, 1995.

[125] R.A. Kennedy and R.J. Evans. Digital redesign of a continuous controller based on closed loop performance. *IEEE Conference on Decision and Control*, 3:1898–1901, 1990.

[126] T. Hagiwara, H. Umeda, and M. Sawada. Discretization of continuous-time controllers based on the hilbert-schmidt norm of the sampled-data frequency response. *IEEE Conference on Decision and Control*, pages 4891–4898, 2006.

[127] P. Apkarian. On the discretization of LMI-synthesized linear parametervarying controllers. *Automatica*, 33 No. 4:655–661, 1997.

[128] H. Nguyen Tien, C.W. Scherer, J.M.A. Scherpen, and V. Muller. Linear parameter varying control of doubly fed induction machines. *IEEE Transactions on Industrial Electronics*, 63 No. 1:216–224, 2016.

[129] S.Peresada, A.Tilli, and A.Tonielli. Robust output feedback control of a doubly-fed induction machine. *IEEE Annual Conference of industrial Electronics Society IECON99*, pages 1348–1354, 1999.

[130] E. Laroche, Y. Bonnassieux, H. Abou-Kandil, and J. P. Louis. Controller design and robustness analysis for induction machine-based positioning system. *Control Engineering Practice*, 12:757–767, 2004.

[131] P. Gahinet, P. Apkarian, and M. Chilali. Affine parameter-dependent lyapunov functions and real parametric uncertainty. *IEEE Transactions on Automatic Control*, 41:436–442, 1996.

[132] W. M. Haddad and V. Kapila. Robust stabilization for continuous-time systems with slowlytime-varying uncertain real parameters. *IEEE Transactions on Automatic Control*, 43:987–992, 1998.

[133] A. Megretski and A. Rantzer. System analysis via integral quadratic constraints. *IEEE Transactions on Automatic Control*, 42:819–830, 1997.

[134] A. Helmerssonn. An IQC-based stability criterion for systems with slowly varying parameters. *14th World Congress of IFAC, Beijing, China*, pages 525–530, 1999.

[135] P. M. Young, M. P. Newlin, and J. C. Doyle. μ analysis with real parametric uncertainty. *Proceedings of the 30th IEEE Conference on Decision and Control*, 2:1251–1256, 1991.

[136] A. Packard and J. C. Doyle. The complex structured singular value. *Automatica*, 29:71–109, 1993.

[137] J. Doyle, A. Packard, and K. Zhou. Review of LFTs, LMIs, and μ. *Proceedings of the 30th IEEE Conference on Decision and Control*, 2:1227–1232, 1991.

[138] A. Helmersson. *Methods for robust gain scheduling*. PhD thesis, Linkoping University, 1995.

[139] R. Braatz, P. Young, J.C. Doyle, and M. Morari. Computational complexity of μ calculation. *IEEE Transactions on Automatic Control*, 39:1994–1996, 1994.

[140] P.M. Young and J.C. Doyle. Properties of the mixed μ problem and its bounds. *IEEE Transactions on Automatic Control*, 41:155–159, 1996.

[141] G.J. Balas, J.C. Doyle, K. Glover, A. Packard, and R. Smith. *μ-Analysis and synthesis toolbox for use with Matlab*, volume 3. The mathworks, 2001.

[142] U. Jonsson and A. Rantzer. Systems with uncertain parameters-time-variations with bounded derivatives. *IEEE Conference on Decision and Control*, 3:3074–3079, 1994.

[143] H. Koroglu and C. W. Scherer. Robust stability analysis for structured uncertainties with bounded variation rates. *16th IFAC World congress*, 2005.

[144] A. Rantzer. On the Kalman-Yakubovich-Popov lemma. *Systems and Control letters*, 28:7–10, 1996.

[145] H. Koroglu and C. W. Scherer. Robust stability analysis against perturbations of smoothly time-varying parameters. *IEEE Conference on Decision and Control*, pages 2895 – 2900, 2006.

[146] G. Balas, R. Chiang, A. Packard, and M. Safonov. *Robust Control Toolbox*. The Mathworks, 2006.

[147] J. Lofberg. YALMIP: a toolbox for modeling and optimization in matlab. *IEEE International Symposium on Computer Aided Control Systems Design, Taipei, Taiwan*, pages 284–289, 2004.

[148] G. Yuan, J. Chai, and Y. Li. Vector control and synchronization of doubly fed induction wind generator system. *Power Electronics and Motion Control Conference*, 2:886– 890, 2004.

[149] R. Pena, R. Cardenas, J. Proboste, G. Asher, and J. Clare. Sensorless control of doubly-fed induction generators using a rotor-current-based MRAS observer. *IEEE Transactions on Industrial Electronics*, 55:330–339, 2008.

[150] I. Park, K. Lee, and D. Kim. Control method of a doubly-fed induction generator with automatic grid synchronization. *IEEE Annual Conference on Industrial Electronics*, pages 4254–4259, 2006.

[151] Y. Liao, L. Ran, G.A. Putrus, and K.S. Smith. Evaluation of the effects of rotor harmonics in a doubly-fed induction generator with harmonic induced speed ripple. *IEEE Transaction on Energy Conversion*, 18:508–515, 2003.

[152] M.E. Elshiekh, D.A. Mansour, and A.M. Azmy. Improving fault ride-through capability of DFIG-based wind turbine using superconducting fault current limiter. *IEEE Transactions on Applied Superconductivity*, 23 No. 3, 2013.

[153] P.-H. Huang, M.S. El Moursi, and S.A. Hasen. Novel fault ride-through scheme and control strategy for doubly fed induction generator-based wind turbine. *IEEE Transactions on Energy Conversion*, 30 No. 2:635–645, 2014.

[154] H. Jia-bing and H. Yi-kang. Dynamic modelling and robust current control of wind-turbine driven DFIG during external ac voltage dip. *Zhejiang University Press*, 7:1757–1764, 2006.

[155] T. Brekken, N. Mohan, and T. Undeland. Control of a doubly-fed induction wind generator under unbalanced grid voltage conditions. *European Conference on Power Electronics and Applications*, 2005.

[156] C.H. Ng, L. Ran, and J. Bumby. Unbalanced-grid-fault ride-through control for a wind turbine inverter. *IEEE Transactions on Industry Applications*, 44:845–856, 2008.

[157] T. Brekken and N. Mohan. A novel doubly-fed induction wind generator control scheme for reactive power control and torque pulsation compensation under unbalanced grid voltage conditions. *Electronics Specialist Conference*, 2:760–764, 2003.

[158] N. Mohan T.K.A. Brekken. Control of a doubly fed induction wind generator under unbalanced grid voltage conditions. *IEEE Transaction on Energy Conversion*, 22:129–135, 2007.

SUMMARY

The linear control of doubly-fed induction machines (DFIMs) in wind power systems normally encounters the problems in variations of the rotor mechanical angular speed and other time-varying parameters. However, better performance requirements against changes in the machine parameters and exogenous inputs are desired. This can be achieved by appropriate controller design for the DFIM. Furthermore, since the stator windings of the DFIM in the regular configuration of the variable speed wind turbines are directly connected to the grid, the robustness of the controlled system under the effects of grid voltage dips is an important aspect of the controller design. The control system should maintain operation and reduce oscillations as much as possible during grid voltage faults, and normal operation of the DFIM should be re-established as soon as the fault is cleared.

This thesis focuses on the use of *linear matrix inequalities* (LMIs) for analysis and synthesis of current controllers for doubly fed induction machines in wind power systems. The design is aimed at improving the robust dynamic performance of the controlled system in a wide range of mechanical rotor speed variations as well as reducing the effect of stator voltage dips when the grid undergoes a fault. A rigorous robustness analysis based on the *integral quadratic constraints* (IQCs) approach is presented for evaluating and comparing the robustness of the controlled system with respect to the changes in the machine inductances and the rotor angular speed for both the *linear parameter varying* (LPV) approach and the conventional one with a deadbeat controller design.

In the first part of this thesis, including Chapter 2 and 3, we present the mathematical models of the DFIM and the grid, the working principle of a wind power system with doubly-fed induction machine, and several investigations of open-loop characteristics of the DFIM. The application of the deadbeat control technique is employed to design the current controllers for both the generator and the grid sides. Robustness of the controlled system with respect to parameter variations and the impact of the stator voltage dips on the system performance are investigated via a number of simulation results.

The necessary background for linear parameter varying controller synthesis is introduced in Chapter 4. We first review the H_∞-synthesis of linear time-invariant systems in which H_∞-constraints are transformed into linear matrix inequalities by using the so-called bounded real lemma. We then provide the polytopic approach for synthesizing gain-scheduled H_∞ controllers as an extension of the H_∞-synthesis technique for a class of affine parameter-dependent systems whose time-varying parameters are measured online. The objective of this approach is to ensure stability and performance of the closed-loop system for all admissible parameter trajectories.

In Chapter 5 we apply the synthesis technique presented in Chapter 4 to design robust parameter-independent H_∞ and self-scheduled LPV controllers for the DFIM. The purpose of the design is to reduce the sensitivity of the controlled system to changes of the machine parameters and to ensure the desired objectives in the wide operating range of the rotor angular speed. As we present in the next part of this chapter, the performance of the closed-loop system with the H_∞ controller is deteriorated for both constant and fast parameter variations of rotor angular speeds. While the designed LPV controller exhibits a highly robust dynamic performance for all admissible trajectories of the rotor angular speed over the operating range. Furthermore, in comparison with the conventional deadbeat design, the LPV controller manifests an improvement of the performance of the closed-loop system with respect to changes in the machine parameters and the stator voltage disturbance. For the real-time implementation of the LPV controller, we present the trapezoidal technique that guarantees a good match between the closed-loop performance of the continuous-time and the discrete-time systems for a consistent sampling frequency.

The next part of the thesis is devoted to the robustness analysis of the closed-loop controlled system for both the LPV and deadbeat controllers. In Chapter 6, a systematical robustness analysis with the integral quadratic constraints approach is employed for investigating the stability of the system against *rate-bounded linear time-varying* (LTV) parametric uncertainties. The test results presented in this chapter indicate the robustness margins of the closed-loop systems in the presence of slowly time-varying parametric uncertainties and the deterioration of the stability margins when the rate-of-variations is increased.

The experimental set up of the LPV and deadbeat-like controllers is presented in Chapter 7. The experimental results show that the LPV controller fulfills all the performance requirements of the closed-loop system for frozen and varying rotor speeds around ±30% of the synchronous speed. When the grid voltage dips, the proposed LPV controller demonstrates a good damping of electrical torque and reactive power as well as an ability of fast recovery of the rotor currents during and after the fault. The experimental results also indicate the performance improvement of the controlled system with the LPV current controller in comparison with that of the deadbeat-like controller.

SAMENVATTING

Gewoonlijk wordt lineaire regeling van dubbelgevoede inductiemachines (doubly-fed induction machines, DFIM's) in windenergiesystemen gebruikt om problemen bij variaties van de mechanische hoeksnelheid van de rotor en andere tijdvariabele parameters op te lossen. Betere prestatie-eisen tegen schommelingen in de parameters van het mechanisme en exogene ingangen zijn echter wenselijk. Dit kan worden bereikt met behulp van een geschikt regelaarontwerp voor de DFIM. Aangezien in de gebruikelijke configuratie van windturbines met variabele snelheid de statorwikkelingen van de DFIM direct verbonden zijn met het elektriciteitsnetwerk, is de robuustheid van het geregelde systeem, die wordt beïnvloed door inzinkingen in de netspanning, een belangrijk aspect van het regelaarontwerp. Het besturingssysteem moet tijdens storingen in de netspanning doorwerken en oscillaties zoveel mogelijk beperken, de normale werking van de DFIM moet zo spoedig mogelijk worden hersteld als de storing is opgelost.

Dit proefschrift richt zich op het gebruik van *linear matrix inequalities* (LMI's) voor analyse en synthese van huidige controllers voor dubbelgevoede inductiemachines in windenergiesystemen. Het ontwerp is gericht op het verbeteren van de robuuste dynamische prestaties van het geregelde systeem in een breed scala van mechanische rotorsnelheidsvariaties en op het verminderen van het effect van dips in de statorspanning als er een storing is in het elektriciteitsnetwerk. Wij stellen een rigide robuustheidsanalyse gebaseerd op de *integral quadratic constraints* (IQC's) benadering voor om de robuustheid van het geregelde systeem te beoordelen en te vergelijken met betrekking tot veranderingen in de zelfinductie van de machine en de rotorhoeksnelheid voor zowel de *linear parameter varying* (LPV) aanpak en de conventionele aanpak met een *deadbeat*-regelaarontwerp.

In het eerste deel van dit proefschrift, waaronder hoofdstukken 2 en 3, presenteren we de wiskundige modellen van de DFIM en het elektriciteitsnetwerk, het werkprincipe van een windenergiesysteem met dubbelgevoede inductiemachine en diverse onderzoeken naar *open loop* karakteristieken van de DFIM. De *deadbeat*-regeltechniek wordt gebruikt om de huidige regelaars voor zowel de kant van de generator als van het elektriciteitsnetwerk te ontwerpen. Robuustheid van het geregelde systeem met betrekking tot parametervariaties en de invloed van inzinkingen in de statorspanning op de systeemprestaties worden onderzocht met behulp van simulatieresultaten.

De noodzakelijke achtergrond voor *linear parameter varying* regelaarsynthese wordt in hoofdstuk 4 geïntroduceerd. We bestuderen eerst de H_∞-synthese van lineaire tijdinvariante systemen waarin H_∞-beperkingen omgezet worden in *linear matrix inequalities* door gebruik te maken van het zogenaamde *bounded real lemma*. Vervolgens introduceren we de polytopische aanpak voor de synthese van *gain-scheduled* H_∞-regelaars, dit kan worden gezien als uitbreiding van de H_∞-synthese techniek voor een klasse van

affine parameterafhankelijke systemen waarvan de tijdvariërende parameters *online* worden gemeten. Het doel van deze aanpak is om de stabiliteit en de prestaties van het *closed loop*-systeem voor alle toelaatbare parametertrajecten te garanderen.

In hoofdstuk 5 passen we de synthesetechniek uit hoofdstuk 4 toe om robuuste parameterafhankelijke H_∞- en *self-scheduled* LPV-regelaars voor de DFIM te ontwerpen. Het doel van het ontwerp is om de gevoeligheid voor veranderingen van parameters van het geregelde systeem te verminderen en om de gewenste vereisten in het brede werkgebied van de rotorhoeksnelheid te garanderen. In het volgende deel van dit hoofdstuk laten we zien dat de prestaties van het *closed loop*-systeem met de H_∞-regelaar zowel voor constante als snelle parametervariaties van rotorhoeksnelheden achteruitgaan. De nieuw ontworpen LPV-regelaar toont zeer robuuste dynamische prestaties voor alle toelaatbare trajecten van de rotorhoeksnelheid over het werkbereik. In vergelijking met het conventionele *deadbeat*-ontwerp laat de LPV-regelaar daarnaast een verbetering zien van de prestatie van het closed loop-systeem met betrekking tot veranderingen in de parameters van het mechanisme en in het statorvoltage. Voor de *real time* implementatie van de LPV regelaar presenteren we de trapezoïdale techniek die zorgt voor een goede overeenstemming tussen de *closed loop* prestaties van continue- en discrete-tijdsystemen voor consistente bemonsteringsfrequenties.

Het volgende deel van het proefschrift is gewijd aan de robuustheidsanalyse van het *closed loop* geregelde systeem voor zowel de LPV- als de *deadbeat*-regelaars. In hoofdstuk 6 wordt een systematische robuustheidsanalyse met *integral quadratic constraints* benaderd om de stabiliteit van het systeem met betrekking tot *rate-bounded linear time varying* (LTV) parametrische onzekerheden te onderzoeken. De testresultaten die in dit hoofdstuk worden gepresenteerd laten de robuustheidsmarges van *closed loop*-systemen bij trage tijdvariërende parametrische onzekerheden zien en tonen de achteruitgang van de stabiliteitsmarges als de variatiesnelheid toeneemt.

De experimentele opstelling van de LPV- en deadbeat-achtige regelaars volgt in hoofdstuk 7. De experimentele resultaten tonen aan dat de LPV-regelaar voldoet aan alle prestatievereisten van het *closed loop*-systeem voor bevroren en variërende rotatiesnelheden rond ±30% van de synchrone snelheid. Als de netspanning inzakt, laat de voorgestelde LPV-regelaar een goede demping van het elektrische koppel en het reactief vermogen zien, evenals het vermogen van snel herstel van de rotorstromen tijdens en na de storing. De experimentele resultaten wijzen ook op prestatieverbetering van het geregelde systeem met de huidige LPV-regelaar in vergelijking met die van de *deadbeat*-achtige regelaar.

LIST OF PUBLICATIONS

5. **H. Nguyen Tien, C.W. Scherer, J.M.A. Scherpen, and V. Muller**, *Linear parameter varying control of doubly fed induction machines*, IEEE Transac- tions on Industrial Electronics, 63 No. 1:216–224, 2016.

4. **H. Nguyen Tien, C. W. Scherer, and J. M. A. Scherpen** , *IQC-based robust stability analysis for LPV control of doubly-fed induction generators*, The 10th International Conference on Control, Automation, Robotics and Vision, ICARCV, Hanoi, Vietnam, 2008.

3. **H. Nguyen Tien, C. W. Scherer, and J. M. A. Scherpen**, *Robust performance of self-scheduled LPV control of doubly-fed induction generator in wind energy conversion systems*, 12th European Conference on Power Electronics and Applications, Aalborg, Denmark, 2007.

2. **H. Nguyen Tien, C. W. Scherer, and J. M. A. Scherpen**, *Discrete-time linear parameter varying control of doubly-fed induction generators*, International Symposium on Electrical Engineering, ISEE, Vietnam, 2007.

1. **H. Nguyen Tien, C. W. Scherer, and J. M. A. Scherpen** , *Self-scheduled LPV controller synthesis for doubly-fed induction generators* , Wind power Conference and Exhibition, Los Angeles, USA, 2007.

PROPOSITIONS

1. The conventional deadbeat controller does not guarantee the robustness of the closed-loop system with respect to perturbations of the plant without sacrificing the lower settling time. [This thesis]
2. The linear parameter varying design ensures a good performance in terms of robustness with respect to machine parameter uncertainties and to rotor speeds. [This thesis]
3. The selected discretization method and sampling interval heavily influence the replacement of an existing continuous-time controller by an equivalent discrete-time controller. [This thesis]
4. The stability analysis within the integral quadratic constraint framework can take the bounds on both the values and the rate-of-variation of the parameters into account. [This thesis]
5. When the grid undergoes a fault, the rotor currents with the linear parameter varying controller recover their nominal values faster than that of the deadbeat controller. [This thesis]
6. Wind is the breath of life due to the fact that, without wind, humankind will be threatened with extinction.
7. You can forgive others easier if you do not forgive yourself easily.
8. Confronting the inevitability as soon as you can is a shortcut to get it over.
9. Losing hope at the most difficult moments can be the highest barrier to your success.
10. Working on a PhD research is like playing in a football match. At the very end of the match, as all the players are exhausted, the team with the leading goals wishes the match might end sooner while its opponent, on the contrary, wishes to have more time.
11. Criticism on the first page is always problematic. Knowing how to accept it can enlighten the rest of your working story.
12. Destiny is nothing but an initial condition of the equations for one's life.

These propositions are regarded as opposable and defendable, and have been approved as such by the promotors prof. dr. ir. J. Hellendoorn, prof. dr. ir. J. M. A. Scherpen and prof. dr. C. W. Scherer.

ABOUT THE AUTHOR

Nguyen Tien Hung was born on January 01, 1968 in Thainguyen, Vietnam. He took his undergraduate program at Thai Nguyen University of Technology where he received his Bachelor degree in electrical engineering in 1991. In 1992, he started his career as a lecturer and researcher at the department of electrical machinery, Thainguyen University of Technology. In 1997, he obtained the Master degree of electrical engineering from Hanoi University of Science and Technology, Vietnam. In the same year, he was appointed as a head of electrical machine division, electrical engineering faculty, Thainguyen University of Technology. In 2004, he started his PhD research at the Delft Center for Systems and Control, Delft University of Technology. The research was sponsored by the Ministry of Education and Training, Vietnam via Project 322. During his PhD study he received graduate certificates from the Dutch Institute for Systems and Control. In 2013, he went back to work for Thainguyen University of Technology at the division of Electrical Engineering, Faculty of International Training.